2011

Experimental and Numerical Evaluation of the behaviour of laterally-loaded non slender piles

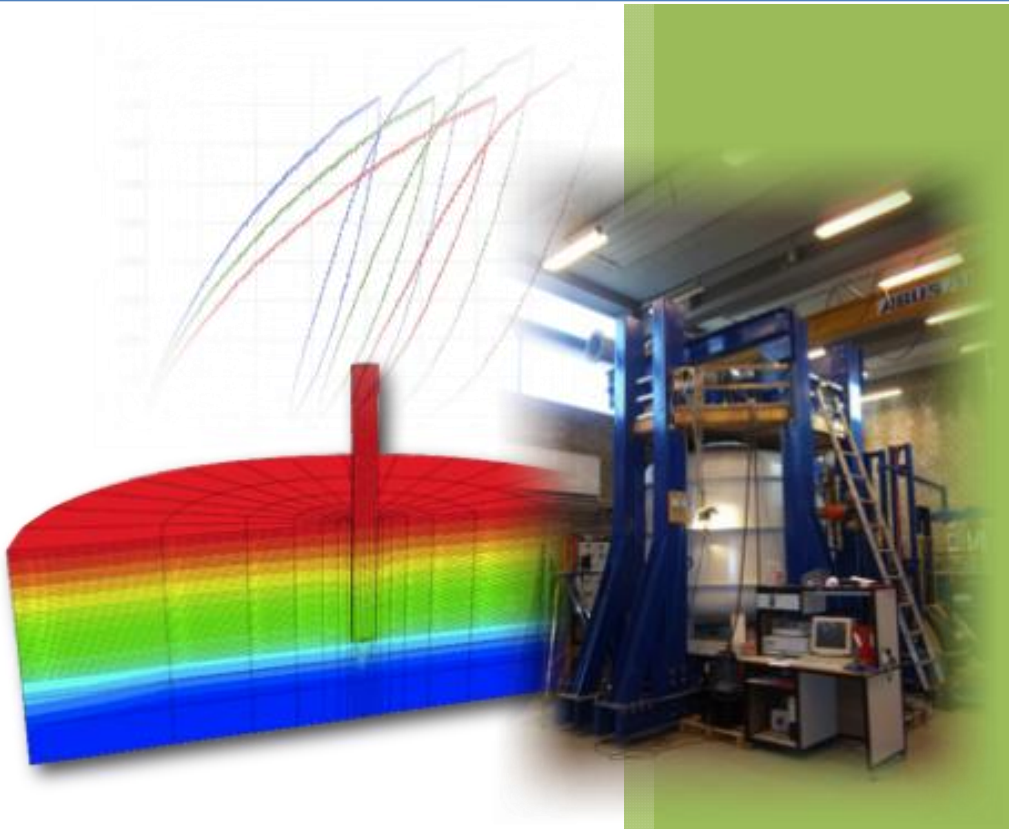

ALEJANDRO BOROBIA MORENO

LINAS MIKALAUSKAS

JOSE LUIS TROYA DÍAZ

17 th of June 2011

M.Sc. in Structural Civil Engineering

10th semester – M.Sc.
Sohngårdsholmsvej 57 9000 Aalborg
+45 96 35 80 80
http://www.bsn.aau.dk

Title:

"Experimental and Numerical Evaluation of the behaviour of laterally-loaded non slender piles"

Written by:

Alejandro Borobia Moreno _____

Linas Mikalauskas _____

Jose Luis Troya Díaz _____

(Graduate Students, Department of Civil Engineering, Aalborg University, Denmark)

Supervisors:

Professor Lars Bo Ibsen

PhD Fellow Søren P. H. Sørensen

(Department of Civil Engineering, Aalborg University, Denmark)

Project Period:

1st February 2011 - 17th of June 2011

Completed: 17th of June 2011

Copies printed: 6

Number of pages: 70

Number of pages (appendix): 178

PREFACE

This report is a product of group B105's project work during the 10th semester of the master degree of Structural and Civil Engineering at Aalborg University. The project is completed within the period of 1st of February 2011 to the 17th of June 2011 under the supervision of Lars Bo Ibsen and Søren P. H. Sørensen. The report is prepared and made in accordance and compliance of the current curriculum of the 10th semester in Civil Engineering.

The project is based on the theme ***"Experimental and Numerical Evaluation of the behaviour of laterally- loaded non slender piles"***. The aim of the project is to provide the knowledge to apply advanced experimental and numerical methods to analyse the lateral soil resistance related to load-displacement of monopiles under pressure.

The project report consists of two parts, the main project and the appendix. The appendix is divided into A, B, C, D, E, F, G, H, I and J which are found at the end of the report and whose contents are explained in the index.

The main project consists of an introduction, three articles concerning experimental testing, dimensionless analysis of the results and numerical modelling by FLAC^{3D} and Plaxis 3D 2010 and a concluding chapter including some directions for future research.

An experimental and a numerical evaluation of the pile behaviour for laterally loaded non-slender piles is carried out through the project. The experimental tests have been conducted on instrumented piles situated in a pressure tank. Hence, *p-y* curves have been determined based on the strain gauge measurements. The numerical simulations have been carried out by means of FLAC^{3D} and Plaxis 3D 2010 employing 3 different material models, i.e. Mohr-Coulomb, Hardening soil and Hardening soil Small Strain material models.

A dimensionless analysis is also performed in order to obtain a general relation for the lateral displacement of the pile and the lateral load applied.

The project report uses the Harvard method of bibliography with the name of the source author and year of publication after the text, for example: Zaaijer and Tempel (2006). The lists of all the sources of reference are found in the bibliography list which can be found in the end of the report, sorted by alphabetic order.

Group B-105

June 17/2011

SUMMARY

Offshore wind turbines are a highly competitive source of renewable energy. The development of these offshore installations has advanced quickly, therefore the elaboration of a specific regulation and theoretical method for the design of wind turbine foundations is needed.

Several types of foundation concepts can be employed for offshore wind turbines, i.e. gravitational foundation, monopile foundation, bucket foundation, tripod foundation, etc. For water depths of 15 to 30 m, the monopile foundation concept has been employed in many projects. The focus of this report is therefore on monopile foundations. The goal of the project has been to understand and investigate the uncertainties in the design method currently being used for monopile foundations. Small-scale tests have been carried out in a pressure tank with the objective of minimising small-scale effects. Afterwards, these tests have been modelled by means of three dimensional numerical methods by the programs FLAC^{3D} and Plaxis 3D 2010. A dimensionless analysis is realised through the project with the goal of analysing the soil exponent and deriving a general equation which relates the lateral load to the lateral displacement of the pile. A full-scale model is also modelled in Plaxis 3D 2010 and FLAC^{3D}.

The method followed to design monopile foundations in sand is based on the *p-y* curve method, but this method does not fit the requirements of the monopile foundations properly. The reason of the problem is that *p-y* curve formulations were developed for lateral loaded piles with higher diameters and slenderness ratios, designed for offshore petroleum industry, where most of the discoveries were located in areas with soft clays primarily, extended later to the knowledge of the behaviour in sands.

Therefore, the methods developed for the oil industry, the jag piles, are based on slender piles with different geometries and properties than the wind turbine monopiles, such as the slenderness ratio. Slenderness ratios for wind turbine monopiles are considered less than 10, due to the fact that they have bigger diameter and shorter embedded length than the jags piles, which are considered slender piles.

Another uncertainty in the actual method is that the different diameters of the piles and the initial stiffness have not been taken into account due to the fact that they are designed regarding to the ultimate limit state, where it has been assumed that possible initial deformations of the soil are not included in the calculations. Thereby, in the service limit state, the initial stiffness is very important for the design of monopile foundations. In the case that the monopile rotates a bigger angle than the maximum allowed by API design regulations, the efficiency of the wind turbines decreases.

The experimental tests are realised on a monopile with strain gauges installed on it which can measure the strain at eleven different levels through the embedded length of the pile. In total 22 tests with different slenderness ratios and pressure levels are carried out since 2009, but only 10 have been conducted by Borobia, Mikalauskas and Troya during the present year. Afterwards, the same tests have been modelled numerically by FLAC^{3D} and Plaxis 3D 2010 in order to analyse the possible uncertainties between different methods and a dimensionless analysis is performed to derive a general equation which relates the lateral displacement of the pile with the load applied.

SUMMARY IN SPANISH

Las turbinas eólicas situadas lejos de la costa, son una fuente energética con una alta competitividad en el ámbito de las energías renovables. El desarrollo de estas instalaciones alejadas de la costa ha crecido muy rápidamente. De este modo, la elaboración de una regulación específica y un método analítico para el diseño de los cimientos de dichas turbinas eólicas es necesaria.

Existen varios tipos de cimentaciones que pueden ser empleadas para turbinas eólicas en el mar: cimentación gravitacional, cimentación "monopila", cimentación de succión y cimentación en trípode, entre otras. Para profundidades marinas entorno a 15-30 m, la cimentación monopila ha sido empleada en muchos proyectos reales. Por esta razón, este proyecto está centrado en las cimentaciones "monopila". El objetivo de del mismo es entender e investigar las incertidumbres en el actual método de diseño usado para el diseño de cimentaciones en monopila.

Experimentos a pequeña escala han sido llevados a cabo en un tanque de presión, con el objetivo de minimizar los efectos de escala. Dichos tests experimentales han sido modelados más tarde mediante tres métodos numéricos tridimensionales gracias a los programas FLAC^{3D} y Plaxis 3D 2010. Un análisis adimensional es realizado durante el proyecto, con el objetivo de analizar el exponente del suelo y derivar una ecuación general que relacione la fuerza lateral con el desplazamiento lateral de la monopila. Un prototipo de monopila a escala real es también modelado en los programas Plaxis 3D 2010 y FLAC^{3D}.

El método usado para el diseño de cimentaciones monopila en arena, está basado en el método de las curvas *p-y*. Sin embargo este método no se adapta a los requerimientos de las monopilas adecuadamente. La razón del problema es que las formulaciones de las curvas *p-y* fueron desarrolladas para monopilas cargadas lateralmente con diámetros y radios de esbeltez más grandes, diseñados para las plataformas petrolíferas de la industria del petróleo. Además, estas regulaciones de diseño fueron desarrolladas para la industria del petróleo en áreas donde las arcillas blandas predominaban, y luego estos conocimientos fueron extendidos al comportamiento de las monopilas en arena.

Los métodos desarrollados para la industria del petróleo, concretamente para las "jag piles", están basados en monopilas esbeltas con diferente geometría y propiedades que las modernas monopilas de las turbinas eólicas. La mayor diferencia es el radio de esbeltez, el cual, para las monopilas de las turbinas eólicas es considerado menor de 10, debido a que tienen mayor diámetro y menor longitud embebida en el fondo marino que las "jag piles".

Otra incertidumbre en el actual método de diseño, es que los diferentes diámetros de las monopilas y la rigidez inicial del fondo marino no son tenidas en cuenta, debido a que están diseñadas de acuerdo al "Estado límite último", donde se asume que posibles deformaciones iniciales del suelo no son incluidas en los cálculos. De esta forma, en el "estado límite último", la rigidez inicial del fondo marino es muy importante para el diseño de cimentaciones en monopila. En el caso de que la monopila rotase un ángulo mayor del máximo permitido por las regulaciones de diseño API y DNV (American Petroleum Industry y Det Norske Veritas), la eficiencia de las turbinas eólicas marinas decrecería.

Los experimentos son realizados en una monopila con sensores de deformación instalados sobre ella, en ambos lados. Dichos sensores, pueden medir la deformación en 11 niveles a lo largo de la longitud embebida de la pila. En total 22 experimentos con diferentes radios de esbeltez y niveles de presión son llevados a cabo desde el año 2009, sin embargo, sólo 10 han sido realizados por Borobia, Mikalauskas y Troya, durante el año presente. Después de haber finalizado los experimentos, los mismos son modelados por dos programas numéricos tridimensionales anteriormente mencionados: FLAC^{3D} y Plaxis 3D 2010, con el objetivo de analizar las posibles incertidumbres entre los diferentes métodos empleados al usar los programas, y un análisis adimensional es llevado a cabo para obtener una ecuación general que relacione el desplazamiento lateral de la pila con la carga aplicada.

TABLE OF CONTENTS

PREFACE
SUMMARY
MAIN REPORT

Chapter 1. Introduction **1**

1.1 Overview of foundation's types 4
1.1.1 Monopile foundations 4
1.1.2 Gravity-based foundations 5
1.1.3 Jacket-monopile hybrids and tripods 5
1.1.4 Suction Bucket Foundations 6
1.2 Aim of the thesis 7
1.3 General idea of experimental and numerical methods 7
1.3.1 Experimental tests at Aalborg University laboratory 7
1.3.2 Numerical modelling by $FLAC^{3D}$ 8
1.3.3 Numerical modelling by Plaxis 3D 9
1.4 Triaxial tests 10
1.5 Dimensionless analysis 11

Chapter 2. Small-Scale Testing of Static Laterally-Loaded non slender piles in cohesionless sand **13**

2.1 Introduction 15
2.2 Tests overview 16
2.3 Calibration of the pile 16
2.4 Installation of the pile 16
2.5 Preparation of the soil 17
2.6 Test setup 18
2.7 Test results 19
2.7.1 Load-displacement relationship 19
2.7.2 Lateral deflection of the pile 19
2.7.3 Bending moment distribution 20
2.7.4 P-y curves 21
2.7.5 Uncertainties in the computed p-y curves 23
2.8 Analysis of initial stiffness 23
2.9 Conclusions 24

Chapter 3. Dimensionless analysis of Small-Scale tests subjected to static lateral loading in cohesionless sand **27**

3.1 Introduction 29
3.2 Tests overview 30
3.3 Installation of the pile 30
3.4 Test setup 31
3.5 Dimensionless analysis 31
3.6 Triaxial tests 36

3.7 Extrapolation of the Small-Scale parameters to a prototype 38
3.8 Conclusions 39

Chapter 4. Numerical modelling of laterally-loaded monopiles in cohesionless sand **41**

4.1 Introduction 43
4.2 Laboratory Test Setup 44
4.3 Small-Scale Numerical Modelling 44
4.3.1 FLAC^{3D} Modelling procedure 44
4.3.2 Plaxis 3D 2010 modelling procedure 46
4.4 Comparison of FLAC^{3D} and Plaxis 3D 48
4.5 Comparison of Mohr-Coulomb, Hardening Soil and Hardening Soil Small Strains Model 49
4.5.1 Introduction to material models 49
4.5.2 Load-displacement relationship 50
4.6 Calibration of Small Scale tests 53
4.6.1 Evaluation of lateral deflection 54
4.6.2 Evaluation of Bending Moments 54
4.6.3 Evaluation of p-y curves 55
4.7 Experimental and numerical results of small-scale tests 55
4.7.1 Evaluation of Bending Moments distribution 55
4.7.2 Evaluation of deflection distribution 56
4.7.3 Evaluation of p-y curves 57
4.8 Full Scale Models 58
4.9 Conclusions 60

Chapter 5. Concluding Remarks **61**

5.1 Lateral pile deflection 63
5.2 Variation of initial stiffness, E_{py}* with depth 64
5.3 Sensitivity of initial stiffness to varying pile embedded length and changing overburden pressure 64
5.4 Variation of soil resistance with overburden pressure and slenderness ratio 64
5.5 Sensitivity of bending moment distribution to varying embedded pile length and changing overburden pressure 64
5.6 Small-scale effects 65
5.7 Variation of soil exponent with pile diameter, overburden pressure and slenderness ratio 65
5.8 General equation for the lateral movement of the pile and extrapolation of the small-scale model parameters 66
5.9 Constitutive Material Models 66
5.10 Directions for Future Research 67
5.10.1 Experimental Work 67
5.10.2 Numerical Work 68

Appendices **71**

Bibliography **249**

CHAPTER 1

INTRODUCTION

In the following chapter the motivation for this project will be described followed by a presentation of the problems to be handled. This leads to the scope for the project, which will be answered through the report.
A short description about the different methods and offshore wind turbine foundations is presented and the different foundation choices are explained.
An overview about offshore wind turbine foundations, the importance of their development for the future and the different methods used to analyse them through the project is described in this Chapter.

The evolution of wind farms from land-based to offshore locations is gradual but surely significant. Stronger winds, better technologies, less impact on real estate values and on the nature, makes offshore wind power an important side of the wind power industry in its attempts to meet the high electricity demands of heavily populated coastal areas.

To date, most offshore wind farms have been installed in shallow waters just off the coast and locations have been dictated by the shallowness of the sea bottom because the foundation technology has focused on a limited depth solution. This is also due to the fact that the actual offshore foundations are a lot cheaper in shallow water depths than in deep depths. Innovation Consulting is working on a design that will eventually push the depth threshold to 120 m of water using 'conventional' technology from the oil and gas industry where jack-up platforms have been in use for a number of years. The proposed designs are purpose built jack-ups using the same principles as those in the oil and gas industry. World Wind Energy Association (2010).

The Danish wind power industry has grown uninterruptedly to its current level. Up scaling and technological advances have made it possible to produce approximately 100 times more electricity at the newest wind turbines (up to 2 MW of unitary power) than at the first modern versions. The previsions show that in the following years the offshore wind turbines will be able to produce 5 MW of unitary power. The most recent wind turbines have been built higher and higher (for instance at Horn Revs II they reach a height of 70 m) , which has meant that, for visual reasons and in consideration of potential neighbours onshore, it has become attractive for the wind power industry to prioritise locating wind turbines offshore. Danish Energy Authority (2005).

Europe continues playing the leading role in the global market, Germany and United Kingdom as the largest domestic markets, although the market in United Kingdom is growing strongly, especially with respect to large offshore wind farms. The American market also seems to have impressive potential, cf. Figure 1.1.

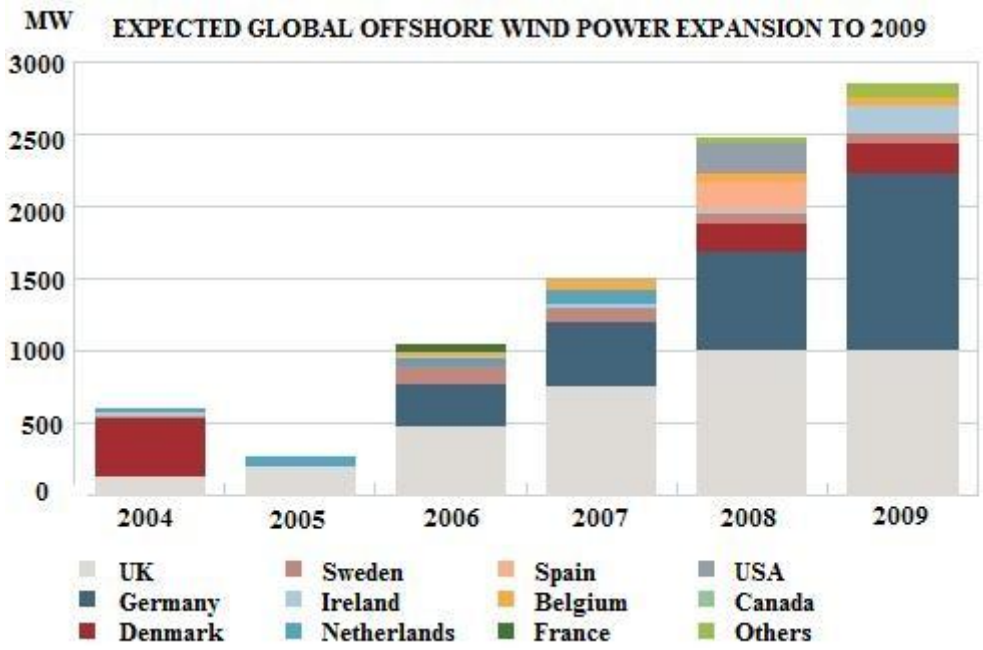

Figure 1.1: Expected global offshore wind power expansion to 2009. Danish Wind Industry Association (2008)

For instance, in Denmark, the Horns Reef I offshore wind farm, constructed in 2002, comprises 80 wind turbines capable of an annual production corresponding to the consumption of 150.000 households. The European Commission requires that 30 % of the total Danish energy consumption shall be covered by the renewable energy in 2020 (currently 20% of the Danish energy consumption is covered by offshore wind turbines). As a step towards reaching this goal, a large extension of Horns Reef I offshore wind farm by 91 new wind turbines, named Horns Reef II, was constructed in 2009. Being capable of an annual production corresponding to the consumption of 200.000 households, Horns Reef II is the world's largest wind farm up to date. DONG energy (2010).

Denmark has been leading in the development of wind energy since the early 1980s. Due to this, the level of knowledge in the area is high. Combining this knowledge with the favourable sea and wind conditions near the Danish coast, Denmark has significant wind energy potential which can be seen in Figure 1.2 where it is shown the Danish wind farms which are in operation, under construction, planned, and under consideration.

In order for wind turbines to be set up in Denmark or in Danish waters they, and the foundation used, must first be approved according to the Danish Energy Authority's technical approval scheme. This scheme, which has been in place since the beginning of the 1980s, is intended to ensure that wind turbines and their foundations are constructed and installed in agreement with regulations governing safety, energy and quality. Danish Energy Authority (2005).

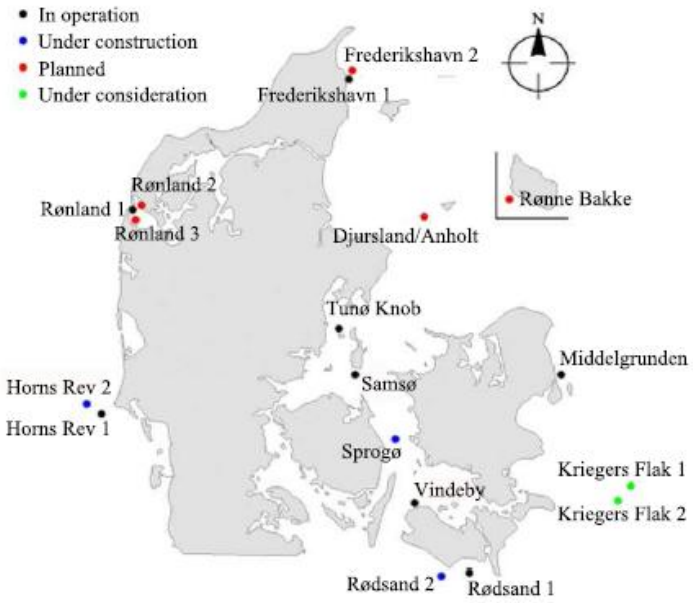

Figure 1.2: Danish wind farms in operation, under construction, planned and under consideration Sørensen et. al (2009)

There are a number of different aspects connected to a wind farm project. This project focuses on the design of the foundation for the wind turbines. As previously mentioned, keeping the overall cost of the project as low as possible is of great interest. General experience indicates that the costs of the foundations constitutes around 30% to 40% of the total costs. This emphasises the essentiality of optimising the cost of the foundation. Danish Energy Authority, 2005.

In this pursuit, alternative solutions for foundations become attractive. In the advance of the foundation technology it is basically possible to consider four different kinds of typologies depending on the water depth and soil characteristics. In the following, a small concept description of each kind of foundation is given in order to create a general idea.

However, this report is focused only on monopile foundations with the aim of analysing the behaviour of this kind of foundation when the overburden pressure and the slenderness ratio vary, in order to be able to understand the possible uncertainties in the theoretical formulation developed for slender monopiles from the oil industry.

1.1. Overview of foundation types

Basically four foundation types are in use and developed nowadays: Monopiles, Jacket-monopiles-hybrids, gravity based foundations and suction bucket foundations. A short introduction of these foundation types are given in the following, as well as advantages and disadvantages of each kind of foundation.

1.1.1 The monopile foundation

It is a simple construction. The foundation consists of a steel monopile with a diameter between 3.5 and 4.5 meters. The pile is driven some 15 to 30 meters into the seabed depending on the type of soil. The monopile foundation is effectively extending the turbine tower under water and into the seabed.

An important advantage of this foundation is that no preparations of the seabed are necessary. On the other hand, it requires heavy piling equipment as well as scour protection, and the foundation type is not suitable for locations with many large boulders in the seabed. If a large boulder is encountered during piling it is possible to drill down to the boulder and blast it with explosives. In evaluation of soil resistance against pile loads, the following factors shall be considered. DNV (2007):

- Shear strength characteristics.
- Deformation properties and in-situ stress conditions of the foundation soil surrounding the pile.
- Method of installation
- Geometry of installation
- Type of loads.

Figure 1.3: Sketch of a monopile foundation

Figure 1.4: Sketch of a gravity-based foundation

1.1.2 Gravity-based foundation

The purpose of a gravity based foundation is to use its mass and width to keep the wind turbine stable. It is an adaptable solution in shallow water. The gravity based foundation consists of a large concrete frame in which gravel and stones are added for extra stability.

The gravity based foundation is resting on the seabed and therefore the horizontal forces on the wind turbine are absorbed by shear stresses between the seabed and the foundation. The function of a gravity based foundation is to utilize its mass to withstand the horizontal and overturning forces from wind and waves. The base of a foundation of this type will be around 14 by 15 m (or a diameter of 15 m for a circular base) for water depths from 4 to 10 m. The weight used to be around 1000 tonnes, depending on the construction materials and if it is necessary to add pack ice protection like in the North Sea.

Seabed preparation should be done before installation of the foundation, silt has to be removed and a smooth horizontal bed of shingles has to be prepared by divers.

1.1.3 Jacket-monopile hybrids and tripods

Designs of jacket monopiles tend to rely on technology used by the oil and gas industry. This technology is generally used at deeper depths and has not been used on many wind turbine projects to date.

The jacket-monopile hybrid structure is a three-legged jacket structure in the lower section connected to a monopile in the upper part of the water column, all made of cylindrical steel tubes. The base width and the pile penetration depth can be adjusted to suit the actual soil conditions.

Figure 1.5: Photo of tripod foundation. Dajin Industries.

The tripod is a standard three-legged structure made of cylindrical steel tubes. The central steel shaft of the tripod makes the transition to the wind turbine tower.

The tripod can have either vertical or inclined pile sleeves. Inclined pile sleeves are used when the structure is to be installed with a jack-up drilling rig, cf. Figure 1.5.

The base width and pile penetration depth can be adjusted to suit the actual environmental and soil conditions. These types of structures are well suited for sites with water depth ranging from 20 to 50 meters. DNV (2007).

The advantage of the three-legged model is that it is suitable for larger water depths further from shore where the wind is stronger furthermore the projects can be invisible from the shoreline lowering the chances of opposition. Cost efficiency may be one of the biggest challenges facing deep water offshore technology.

1.1.4 Suction-bucket foundations

Figure 1.6: Photo of a bucket foundation. Dong Energy & Aalborg

Suction bucket foundations are tubular steel foundations, which distribute the loads from the centre column to the edge of the bucket, cf. Figure 1.6.

The wind turbine tower is connected to the centre pile above mean sea level. The steel bucket consists of vertical steel skirts extending down from a horizontal base resting on the soil surface.

The bucket is installed by applying suction, and the hydrostatic pressure difference and the deadweight cause the bucket to penetrate the soil. This benign installation procedure allows the buckets to be connected to the rest of the structure before installation, enabling a reduction in steps of the installation procedure. DNV (1992).

In the design of offshore foundations it is important to take into account the scour phenomenon, since it usually appears after installing the wind turbine foundation. Scour is a type of erosion that can occur around an offshore foundation, and can cause a significant amount of soil to be removed. Scour holes can reach depths of double the diameter of the foundation. Scour especially develops at locations with tidal currents and where the soil consists of sand or silty-sand. Scour occurs due to the effect of the foundation on the local flow pattern and the velocity of this flow. Scour around a monopile is caused by current and waves and scour protection becomes an important and necessary actuation in offshore foundations. However, in this project scour is not considered, since it has been focused on other fields explained in the next sections. Zaaijer and Tempel (2006).

1.2 Aim of the thesis

Monopile foundations are the most employed type of foundation for offshore wind turbines, thereby this report is focused on the evaluation and analysis of monopile foundations. This is also due to the non-validation of the design procedure for big pile foundations.

A fundamental study of soil response of piles subjected to lateral loads in sand is conducted. Stress paths for selected soil elements around a pile subjected to lateral loads are investigated experimentally and numerically. The effects of pile properties (stiffness, diameter, slenderness ratio) and soil properties (friction angle, density index and soil dilation) are also analysed.

The aim is to compare the *p-y* curves obtained experimentally and numerically, and establish some conclusions and knowledge which can solve the uncertainties generated by the API and DNV regulations, and provide results to develop a specific formulation for non-slender monopiles. A dimensionless analysis will be also carried out, with the purpose of studying the variation of the soil exponent, and be able to derive a general equation which describes the lateral behaviour of the pile. Prosperine K. Peralta (2010).

This thesis is mostly focused on the dimensionless analysis and numerical modelling by means of FLAC^{3D} and Plaxis 3D 2010, since an analytical and experimental analysis was performed during 9th semester.

1.3 General Idea of experimental and numerical methods

The procedure followed to conduct and establish the knowledge for each method is explained in each chapter but a basic description of each method is presented in the following:

1.3.1 Experimental tests at Aalborg University laboratory

Twenty-two small-scale tests have been carried out since 2009 by different students at Aalborg University Laboratory: 6 tests by Sørensen et al. (2009), 6 by Rousse and Thomassen (2010) and 10 by Borobia, Mikalauskas and Troya (2010 and 2011). However, the same test setup and soil preparation has been used through the 22 small-scale tests.

A pressure tank is used for the performance of the mentioned tests which allows to increase the effective stresses in the soil by the help of a rubber membrane placed inside the tank, cf. Figure 1.7.

The sand inside the tank is well known due to previous triaxial tests realised at Aalborg University laboratory, cf. Ibsen and Bødker (1994). To verify that the tests are conducted in homogeneous soil conditions, six CPT's (Cone penetration tests) are carried out at different positions in the tank.

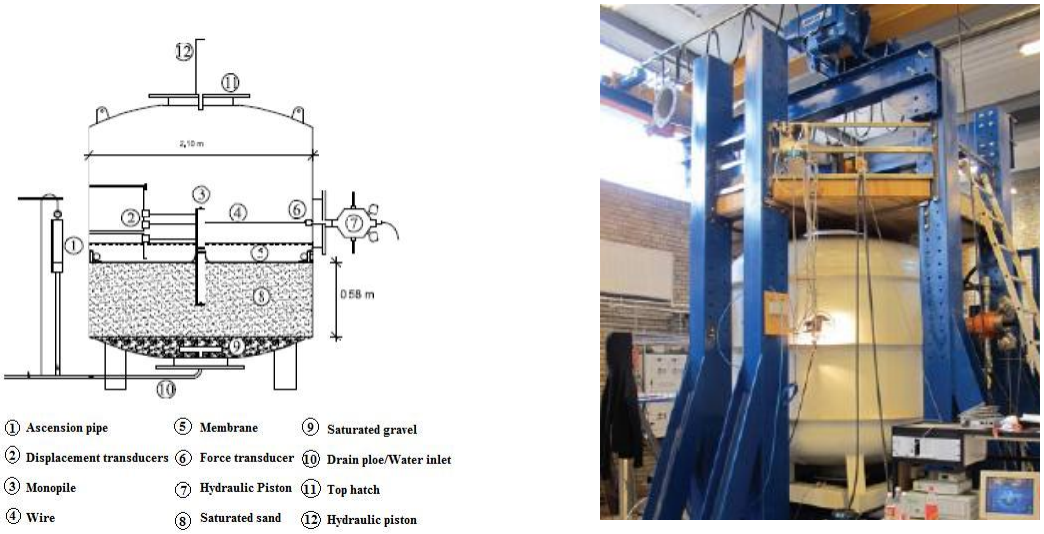

Figure 1.7: Left: Cross-section view of the test setup cf. Sørensen et al. (2009). Right: Photo of the pressure tank.

Three displacement transducers which proportionate information of horizontal displacement above the soil surface when the pile is subjected to a horizontal load, are attached to the pile, cf. Figure 1.7, left.

The pile is loaded horizontally at the same level of the displacement transducer placed in the middle. The pressure is applied constantly and homogeneously to the entire soil surface within a plastic membrane with dimensions equal to the inner dimension of the tank. The tests are carried out on two different close-ended piles provided with eleven strain gauges on each side, a total of 22 strain gauges in the pile. The strain gauges provide live measurements of the strain, therefore stress at eleven different levels in the soil can be derived.

Within this strain data, the deflection of the pile, bending moment distribution and soil resistance at each level can be computed. Thus, the *p-y* curves, which represent the non-linear relation between the soil resistance of the soil and the lateral deflection of the pile can be obtained and then, be analysed comparing the results obtained by different methods and commercial software.

1.3.2 Numerical Modelling by FLAC^{3D}

FLAC^{3D} is a numerical modelling program for advanced geotechnical problems where continuum analysis is necessary in three dimensions. The program utilizes an explicit Finite Difference formulation that can model complex mechanical behaviours not suitable for Finite Elements method. FLAC^{3D} manual (2009).

The purpose of using the commercial software FLAC^{3D} is to create a numerical model (cf. Figure 1.8) with the same conditions as the experimental tests. The input for the

numerical program is the soil parameters obtained by the CPT's, the pile geometry, overburden pressure of each test and lateral displacement of the pile.

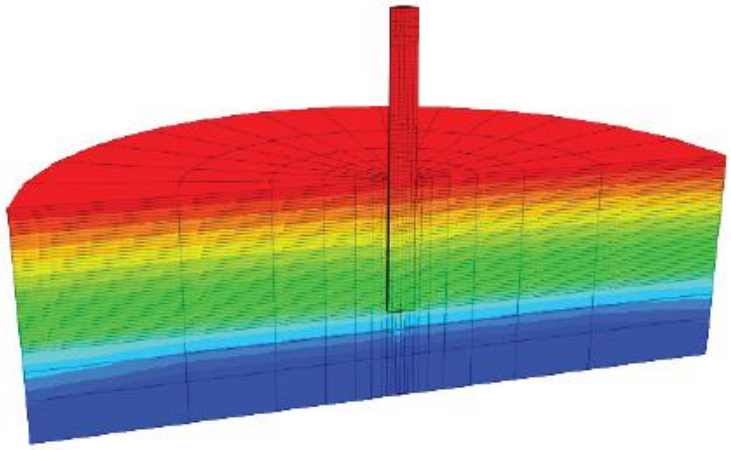

Figure 1.8: Model geometry generated by FLAC^{3D}

With the test results, the FLAC^{3D} models are calibrated in order to obtain the right numerical approach and to be able to compare to the experimental results and to the models generated by Plaxis 3D 2010.

The output of the program provides the soil resistance, lateral deflection, and force applied at different levels. The output depends on the initial setup, i.e. generation of the grid and number of steps. A further explanation is given in Appendix F.

Furthermore, a full-scale model is generated in FLAC^{3D} in order to analyse how a real monopile with real dimensions behaves when it is submitted to lateral loading in a typical offshore location with layered soil.

1.3.3 Numerical Modelling by Plaxis 3D 2010

Plaxis 3D 2010 is a commercial three dimensional finite element program used to perform deformation and stability analysis for various types of geotechnical structures such as foundations, anchors and sheet piles. Plaxis 3D is an implicit element solver relating forces and displacements by demanding equilibrium in every point in the model. In contrast to FLAC^{3D}, Plaxis 3D is a static solver, meaning that inertial forces are omitted.

The numerical models in Plaxis 3D, cf. Figure 1.9, are modelled with the same parameters as in FLAC^{3D} using as input data the soil parameters obtained by the CPT's, pile geometry and overburden pressure of each test. The aim of the Plaxis 3D model is to compare the results to the ones obtained by FLAC^{3D} and to analyse the behaviour of the numerical models based on the experimental tests.

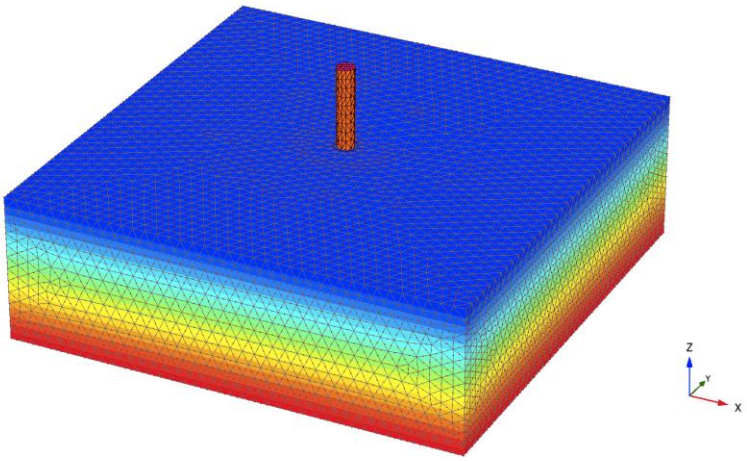

Figure 1.9: Plaxis 3D model geometry.

Results of load-displacement relationship, bending moment distribution, zero deflection point and *p-y* curves along the pile length are obtained. Furthermore, a full-scale model is modelled with the same geometrical and geotechnical parameters as used in an ABAQUS model done by L. Kellezi and P. B. Hansen (2003). This full-scale model corresponds to a real offshore wind turbines project carried out in Horns Rev II.

The results of the full-scale model obtained by Plaxis 3D are compared to the results of the same model obtained by FLAC^{3D} in order to verify the accuracy of these commercial software programmes and find out which one gives more accurate results when comparing to the experimental results. For a further explanation and details of Plaxis 3D modelling see Appendix G.

1.4 Triaxial tests

Triaxial tests were previously carried out at Aalborg University Laboratory with the purpose of analysing how the soil behaves when confining pressure is applied. The soil is compressed in the three directions yielding in a significant volumetric strain (the height of the specimen decreases). It is assumed that the behaviour of the soil specimen represents the behaviour of the entire soil, cf. Figure 1.10.

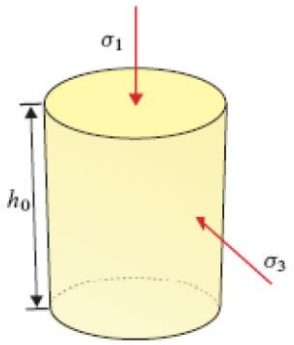

Figure 1.10: Soil specimen subjected to compression in the three directions

The purpose of these triaxial tests is to obtain the soil exponent, *k*, cf. Appendix D, from the stress-strain relationship of the soil, and be able to compare it to the one obtained by the small-scale tests. The triaxial tests are also employed to compute the characteristic line which defines the transition between the elastic behaviour and the plastic behaviour of the soil to have an idea of the force to be applied in the small-scale tests, cf. Figure 1.11. Gudehus and Hettler.

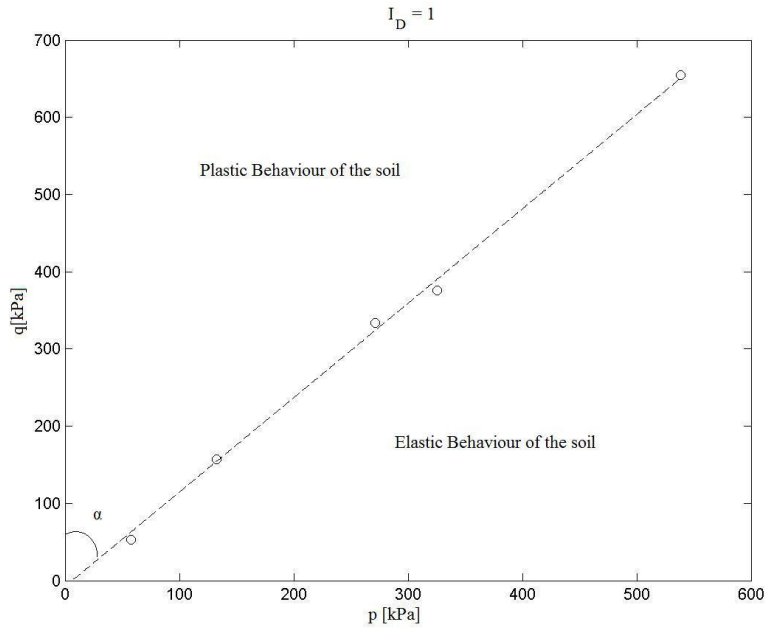

Figure 1.11: Characteristic line of Baaskarp Sand no.15. $I_D = 1$.

Furthermore, an analysis of the variation of the characteristic friction angle and peak friction angle with the density index is realised through the project, cf. Appendix C.

1.5 Dimensionless analysis

A dimensionless analysis is performed by means of the Π-factors. A general relation of the lateral displacement of the monopile and the force applied is obtained depending on the soil exponent, density index and pile properties. Prosperpine K. Peralta (2010).

The soil exponent, k, is obtained by the small-scale tests and its validity is checked by comparing the result obtained by small-scale tests to the one obtained by means of the triaxial tests. An analysis of the variation of the soil exponent depending on the slenderness ratio and the overburden pressure level is carried out, cf. Chapter 3.

CHAPTER 2

SMALL-SCALE TESTING OF STATIC LATERALLY LOADED NON-SLENDER PILES IN COHESIONLESS SAND

Small-Scale testing of Static Laterally loaded Non-Slender Monopiles in cohesionless Sand

Alejandro Borobia Moreno[1]; Linas Mikalauskas[1]; Jose Luis Troya Díaz[1]

Aalborg University, March 2011

Abstract

A monopile is often employed as the foundation for offshore wind turbines. The design regulations propose to use the Winkler model approach in the design of monopiles, employing *p-y* curves to describe the soil-pile interaction. The currently adopted *p-y* curves are based on experiments on flexible piles with diameters up to 2 meters and higher slenderness ratios than used for modern wind turbines. A monopile foundation for an offshore wind turbine typically behaves rigidly, has diameters of 4-6 m and slenderness ratios lower than 10. The aim of this paper is to analyse the behaviour of non-slender aluminium piles situated in fully saturated sand. Small-scale tests are conducted in a pressure tank at Aalborg University. Hereby, the effective stresses of the soil can be increased minimizing uncertainties regarding soil parameters. An analysis of the variation of the initial stiffness is performed. Finally, some conclusions are drawn as well as some directions for future research.

1 Introduction

Up to date, monopile foundations are the most common kind of foundation when designing offshore wind turbines. The *p-y* curve method based on design regulations such as API, 1993 and DNV, 1992 is often used as basis for the design of monopiles. However, it is considered by many researches (Therzagui (1955), Vesic (1961), Lesny and Wiemann (2006), etc.) as inaccurate and incomplete since it is based on tests conducted at Mustang Island with slenderness ratio of L/D = 34.4, cf. Cox et al. (1974) and validated through a series of tests on flexible piles, Murchison and O'neill, 1984. Firstly, it was developed for jag piles in the oil industry for primarily clays and then extended to sand.

Modern wind turbines have a slenderness ratio of $L/D < 10$, exhibiting a rigid behaviour when they are subjected to lateral loading. The recommended *p-y* curves do not take into account the slenderness ratio. This fact justifies the aim of carrying out several small-scale tests with varying slenderness ratio at different pressure levels by the use of a pressure tank. The objective is to reduce the scale effects by increasing the effective stresses of the soil, implying a reduction in the uncertainties regarding soil parameters.

This paper presents an overview of the obtained results and focuses on the effect of varying slenderness ratio and changing overburden pressure.

[1] Graduate student, Dept. of Civil Engineering. Aalborg University, Denmark.

2 Tests overview

Full-scale tests are expensive and time consuming, reason for why ten quasi-static small-scale tests are conducted at Aalborg University Laboratory. The tests are conducted on piles with a diameter of D = 80 mm and D = 100 mm, changing slenderness ratio, L/D, and different overburden pressures, P_0, with the objective of reducing the small scale effects which usually appear in this kind of experiments, such as uncertainties when obtaining soil parameters. The pile is a closed-ended pile with 22 strain gauges placed along its length (except for the pile of D = 100 mm and tests 8, 9 and 10) and a constant wall thickness of 5 mm. An overview of all the tests can be shown in table 1:

Test no.	D [mm]	P_0 [KPa]	L/D	Strain Gauges
Test 1	100	50	5	No
Test 2	80	0	5	22
Test 3	80	50	5	22
Test 4	80	50	6	22
Test 5	80	100	4	22
Test 6	80	100	5	22
Test 7	80	100	6	22
Test 8	80	50	3	No
Test 9	80	0	3	No
Test 10	80	100	3	No

Table 1: Test programme

3 Calibration of the pile

Strain gauges installed on the pile show live measurements of the strain along the pile axis. In order to obtain reliable values of the bending moment, a calibration of the pile is done. When calibrating the pile, it is supported at two points and two loads are applied at different times and positions in 10 loading steps, cf. Figure 1. Bending moment can be computed analytically, and then related to the strain as figure 2 shows.

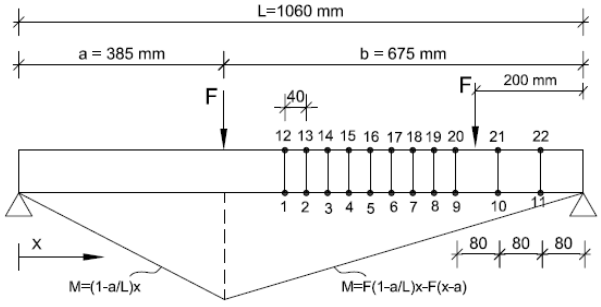

Figure 1: Sketch of the calibration of the pile

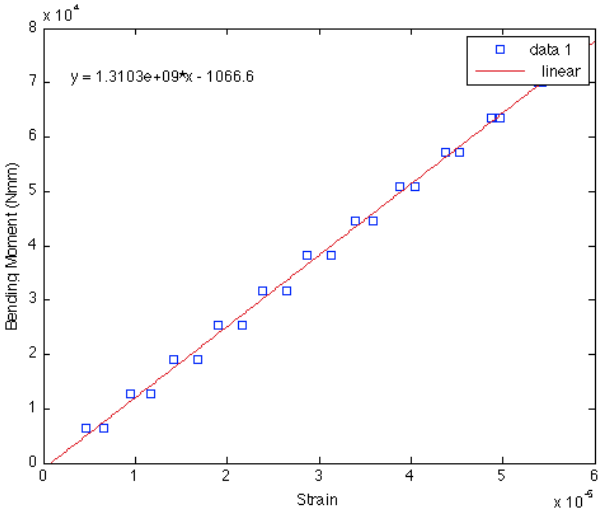

Figure 2: Analytical Bending Moment – Strain

The data points are fitted by a straight line which slope, k_g, is called the strain gauge factor, later used to obtain experimentally the bending moment as equation 1 states:

$$M(x) = k_g \cdot \varepsilon \qquad (1)$$

4 Installation of the pile

The pile is installed by the help of a hydraulic piston placed on the top hatch of the tank, and it is driven into fully saturated sand with embedded lengths of 240 mm, 320 mm, 400 mm, 480 mm and 500 mm, cf. Figure 3.

Figure 3: Installation of the pile

After the installation of the pile a standard preparation of the soil for all the tests has been performed.

5 Preparation of the soil

Baaskarp sand no.15 brought from Sweden is used for all the tests, characterised by the properties shown in table 2:

BAASKARP SAND No. 15	
Specific grain density d_s	2,64
Maximum void ratio e_{max}	0,858
Minimum void ratio e_{min}	0,549

Table 2: Baaskarp Sand No.15

The large grains are rounded while the small grains have sharp edges. The sand consists of quarts, but also contains feldspar and biotite.

The soil has been vibrated previous to the tests with the purpose of achieving homogeneous properties. It consists of three steps:

- Water flow in the upwards direction (i=0.9) with the objective of loosening up the soil.
- Random pre-vibration of the soil in the surroundings of the pile.
- Systematic vibration procedure by the help of a wooden plate with holes, cf. Figure 4.

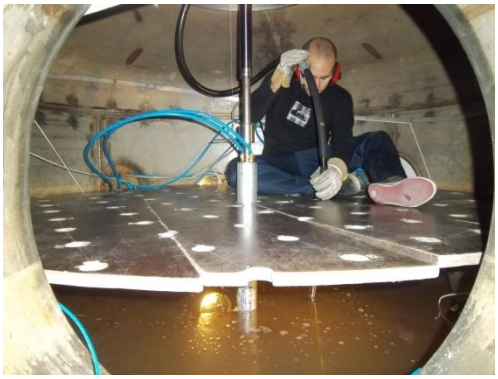

Figure 4: Systematic vibration of the soil previous to the tests.

To verify the homogeneity of the soil and calculate the soil parameters 6 CPT's were carried out at 6 different positions in the tank. Since Baaskarp Sand no.15 is considered cohesionless, only tip resistance is measured by the cone, cf. Figure 5.

Figure 5: Cone penetration test

The density index, I_D, and the unit weight of the soil, γ', are obtained by iteration using equations 2 to 5:

$$\gamma' = \frac{d_s - 1}{1 + e_{insitu}} \cdot \gamma_w \quad (2)$$

$$\sigma_1' = \gamma' \cdot x \quad (3)$$

$$I_D = c_2 \cdot \left(\frac{\sigma_1'}{q_c^{c_1}}\right)^{c_3} \quad (4)$$

$$I_D = \frac{e_{max} - e_{insitu}}{e_{max} - e_{min}} \cdot 100 \quad (5)$$

Where γ_w is the unit weight of the water, x defines the depth and c_1 and c_2 are fitting constants. The rest of the soil parameters are obtained based on previous triaxial tests realized at Aalborg University and the relation between the density index and the friction angle proposed by Schmertmann (1978).

An average of the soil parameters derived for Baaskarp Sand no.15 are shown in table 3 for tests 1 to 7.

Test no.	φ_{tr}[°]	ψ_{tr} [°]	I_D [%]	γ' [kN/m^3]	E_0 [MPa]
1	49.92	17.56	87.20	10.33	29.96
2	52.70	17.03	84.57	10.27	[-]
3	47.26	15.70	77.91	10.15	25.15
4	48.26	16.09	79.85	10.18	26.12
5	45.46	15.45	76.60	10.12	36.54
6	45.67	16.06	79.66	10.18	38.85
7	45.54	15.84	78.59	10.15	38.00

Table 3: Estimated soil parameters

Notice that for tests 8, 9 and 10, it was decided not to carry out any CPT's, since the slenderness ratio considered was L/D = 3 and thus, the embedded length of the pile leads to 240 mm, which only allows to conduct

CPT's of 10 cm depth. For this reason, the CPT's interpretation is not reliable enough for these 3 tests, and it is preferred to use an averaged value of the density index of 83% for further calculations.

6 Test setup

The tests are carried out inside a pressure tank with a height of 2.5 m and a diameter of 2.1 m, cf. Figure 6. The purpose is to reduce small-scale effects, such as the variation of the friction angle with the stress level.

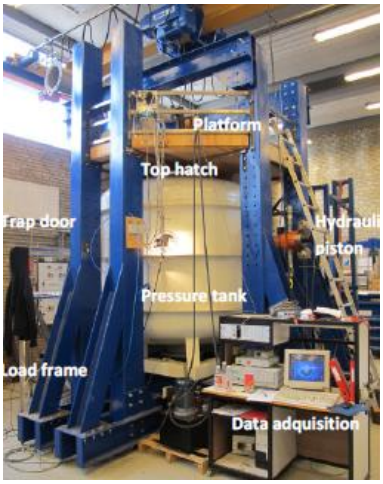

Figure 6: Pressure tank at Aalborg University

Inside the tank, a 0.58 m thick layer of sand was located and also a layer of highly permeable gravel below it was placed with the objective of being able to lead out water out of the tank easily in the case that it was necessary.

Measuring devices are lead out of openings in the tank side and connected to a spider which is also plugged to the computer shown in figure 6.

The 10 tests carried out inside the pressure tank have a similar setup, consisting of three displacement transducers attached at three different heights over the soil surface (-265 mm, -370 mm, -480 mm), cf. Figure 7. The pile is pulled out by a wire connected at the same height as the displacement transducer placed in the middle (-370 mm) and at the same time attached to a force transducer capable of producing a force up to 20 kN when the hydraulic piston moves. Figure 8 shows an outside view of the hydraulic piston.

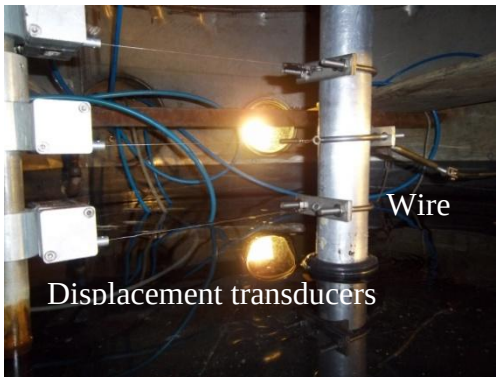

Figure 7: Displacement transducers

Figure 8: Hydraulic piston

In order to increase the effective vertical stresses homogeneously, and to reduce the vertical water flow, a rubber membrane is placed on the soil surface, cf. Figure 9.

Since the membrane is not completely tight, air can penetrate through leaks in the membrane increasing the pore pressure. The dynamic viscosity of water is approximately 55 times higher than for air, so some water must be poured in the tank, reaching a level of approximately 16 cm above the membrane. Hereby, the leaking is minimized.

In order to maintain a hydrostatic pore pressure in the soil, an ascension pipe is used, cf. Figure 10.

Figure 9: Rubber membrane over the soil surface

Figure 10: Ascension Pipe

The mechanism of controlling the hydrostatic pressure is realised by means of the ascension pipe. When the water column increases, some water is lead out of the tank through a drain on the bottom of it, directly to the sewer.

7 Test results

7.1 Load-displacement relationship

The test programme described in Table 1 is designed to analyse the behaviour of the pile when the slenderness ratio and the pressure level vary. This criterion will be followed through all the results presented.

In the following graphs, cf. Figures 11 and 12, the lateral displacement of the pile at the height of the hydraulic piston is shown for L/D = 3, 4, 5, 6 and P_0 = 0, 50, 100 kPa, corresponding to tests 5, 6, 7, 10 and 2, 3, 6 respectively.

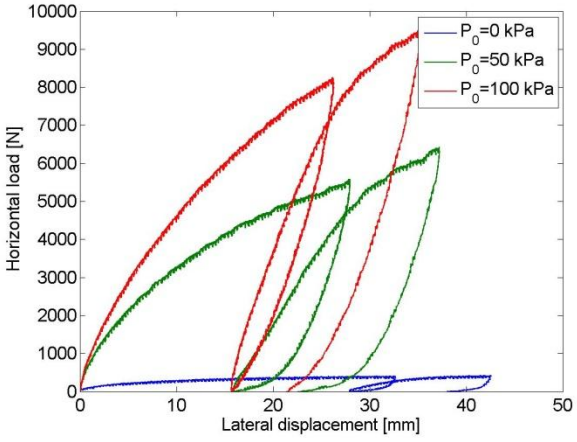

Figure 11: Lateral displacement at -370 mm for P_0 = 0, 50, 100 kPa and L/D = 5

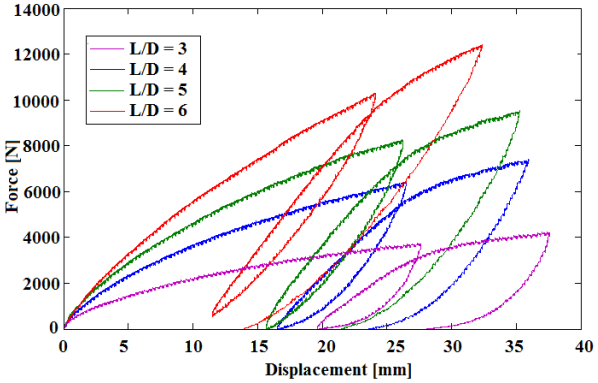

Figure 12: Lateral displacement at -370 mm for P_0= 100 kPa and L/D = 3, 4, 5, 6.

As it was expected, either the higher overburden pressure applied inside the tank or a higher slenderness ratio is considered, a bigger force is required to pull out the pile. In order to reach the same lateral displacement at the height of the second displacement transducer a higher force is applied. For instance, the highest force registered is around 12 kN for P_0 = 100 kPa and L/D = 6.

On the other hand, the minimum force was found to be around 0.4 kN for P_0 = 0 and L/D = 5.

The soil is loaded, unloaded and reloaded again, meaning that plastic deformations occur after the first loading. Figures 11 and 12 show how plastic deformations decrease when either the pressure level or the slenderness ratio increase, meaning a more elastic behaviour of the soil.

Due to the increasing overburden pressure the curvature of the line is higher because of a higher dilation of the soil. In general, the higher the slenderness ratio or the overburden pressure is, the lower lateral deflection is experienced by the pile.

7.2 Lateral deflection of the pile

Lateral deflection of the pile shows in all the cases that for the slenderness ratios considered (L/D = 4, 5, 6) and the different pressure levels (P_0 = 0, 50, 100 kPa) the pile exhibits a rigid behaviour, experimenting negative deflections due to the existence of a rotation point. Figures 13 and 14 show how the rotation point varies with the overburden pressure and slenderness ratio.

Lateral deflection is computed experimentally by equation 6 using some boundary condi-

tions measured by the displacement transducers above the soil surface (constant rotation above the second displacement transducer, known lateral deflection at displacement transducer 2, similar rotation and displacement at the soil surface).

The deflection variation along the depth is represented against depth in figures 13 and 14. Notice that it is not possible to represent the deflection variation for *L/D* = 3 since these tests were carried out without any strain gauges.

$$y(x) = \iint \frac{M(x)}{E \cdot I_{zz}} dx \cdot dx \qquad (6)$$

Furthermore, the pile behaves more flexibly when either the pressure level is increased or the slenderness ratio considered is higher. However, it always remains inside the rigid limits, which is in accordance with the criterion showed in equations 7 and 8. DNV-OS-J101 (October, 2007).

$$\frac{L}{D} < 10 \qquad (7)$$

$$\frac{L}{D} > 10 \qquad (8)$$

When the slenderness ratio considered is lower than 10 the pile behaves rigidly, whereas a flexible behaviour of the pile is adopted when the slenderness ratio is higher than 10.

Criteria based on the bending stiffness and the embedded length can also be used to verify whether the monopiles behave flexibly (when equation 9 is fulfilled) or rigidly (equation 10 is verified) as it is expressed in the following, cf. Poulus and Hull (1989):

$$L < 1.48 \cdot \left(\frac{E_p \cdot I_P}{E_S} \right)^{0.25} \qquad (9)$$

$$L > 4.44 \cdot \left(\frac{E_p \cdot I_P}{E_S} \right)^{0.25} \qquad (10)$$

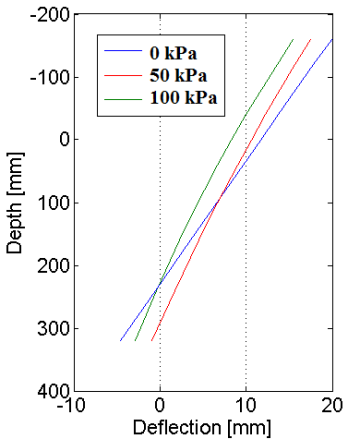

Figure 13: Depth-deflection for P_0 = 0, 50, 100 kPa

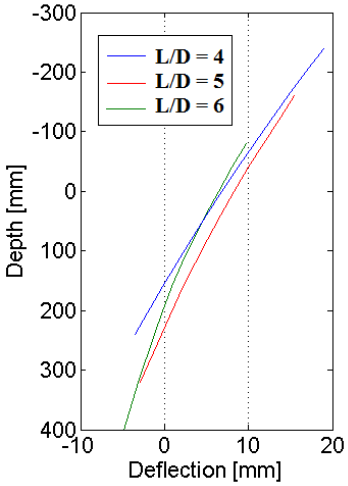

Figure 14: Depth-deflection for *L/D* = 4, 5 and 6

The depth of the rotation point is found to vary for the different tests. This is due to the higher force which is applied to the pile when either the overburden pressure or the slenderness ratio increases.

7.3 Bending moment distribution

Bending moment distribution along the embedded length of the pile is analysed in the following regarding to varying overburden pressure and changing slenderness ratio. 11 levels along the depth of the pile are considered, corresponding to the depths where every pair of strain gauges is located. A linear distribution of the bending moment is obtained above the soil surface, whereas a 5th degree polynomial has been used to fit the data points through all the embedded length of the pile. Figure 15 shows the moment distribution for 5 time steps during the first loading for test no.2 (*D* = 80 mm, *L/D* = 5, P_0 = 0 kPa).

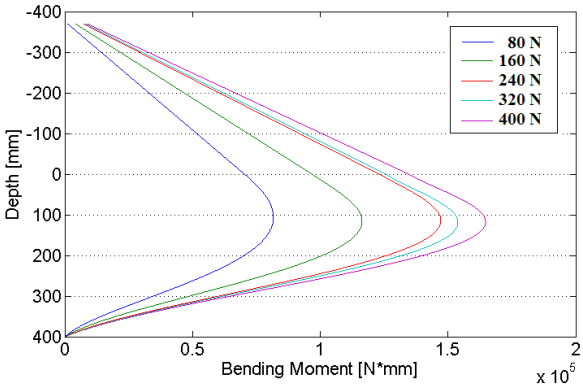

Figure 15: Bending moment distribution for 5 time steps, test no. 2 (P_0 = 0 kPa, L/D = 5)

The bending moment is found to be very sensitive to the lateral load applied, increasing very rapidly. The peaks of the bending moment curves are located between the soil surface and 100 mm depth. The moment decreases until a value of zero N ·mm at the pile toe in all the cases. Figures 16 and 17 show the bending moment distribution along the depth for different overburden pressures and slenderness ratios.

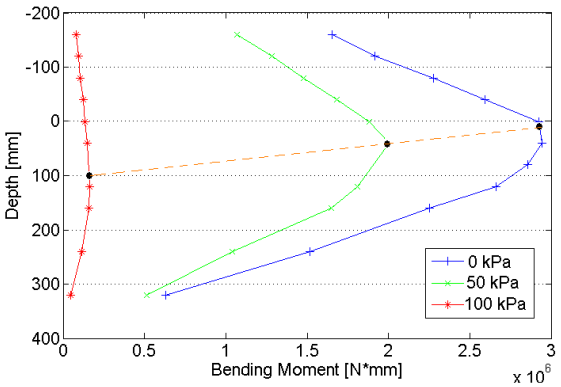

Figure 16: Bending Moment distribution for P_0 = 0, 50, 100 kPa, L/D = 5

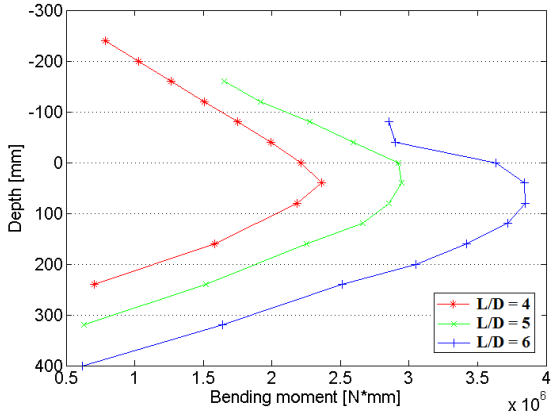

Figure 17: Bending Moment distribution for L/D = 4, 5, 6 and P_0 = 100 kPa

Regarding Figure 16, for a pressure level of 0 kPa, the pile behaves almost like a rigid body, and it behaves more flexibly when the overburden pressure increases since the force needed to be applied to reach the same displacement at the height of the hydraulic piston is bigger. Furthermore, as the dashed orange line shows, the peaks of the moment curves are located closer to the soil surface when the P_0 considered is higher.

It can be concluded that the bending moment is very sensitive to the overburden pressure variation, increasing drastically when P_0 also does.

Of high importance it is also the variation of the bending moment with the considered slenderness ratio. It is also affected by L/D, but not as drastically as the overburden pressure does, cf. Figure 17. Notice that the blue distribution adopts a strange distribution above the soil surface which is due to a wrong measurement by the strain gauges placed at that depth level.

Both parameters (P_0 and L/D) affect in a similar way to the bending moment, due to the fact that the pile is subjected to a higher lateral load when any of these two parameters become higher.

The bending moment has not been computed for the last 3 tests, since no strain gauges were considered.

7.4 *p-y* curves

The actual design criterion for monopile foundations is based on Winkler model approach which uses *p-y* curves method to represent the pile-soil interaction. In *p-y* curves, the soil resistance and the lateral displacement of the pile are related non-linearly.

Lateral displacement is computed as equation 6 shows, applying the four previously mentioned boundary conditions obtained by the displacement transducers above the soil surface.

Soil resistance is directly obtained from the bending moment distribution as equation 11 states:

$$p(x) = \frac{d^2 M(x)}{dx^2} \qquad (11)$$

Piecewise Polynomial fitting curve method is used to derive the resistance of the soil, p, Yang & Liang (2006).

P-y curves corresponding to different overburden pressures and a constant slenderness ratio of L/D = 5 are presented in figures 18, 19 and 20. It is expected to obtain higher values of soil resistance when the overburden pressure increases since the soil is more compacted and offers a higher resistance against the movement of the pile.

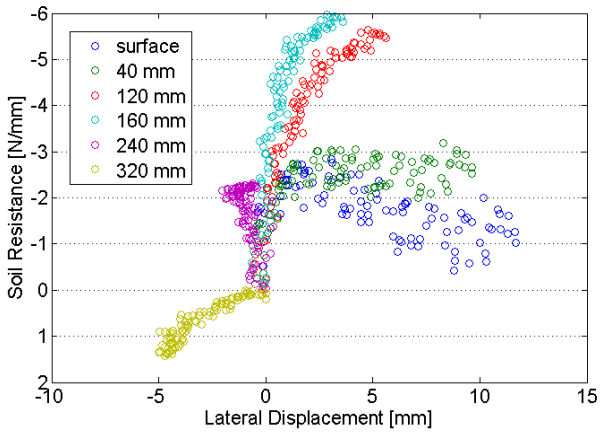

Figure 18: *p-y* curves for test 2, P_0 = 0 kPa, L/D = 5

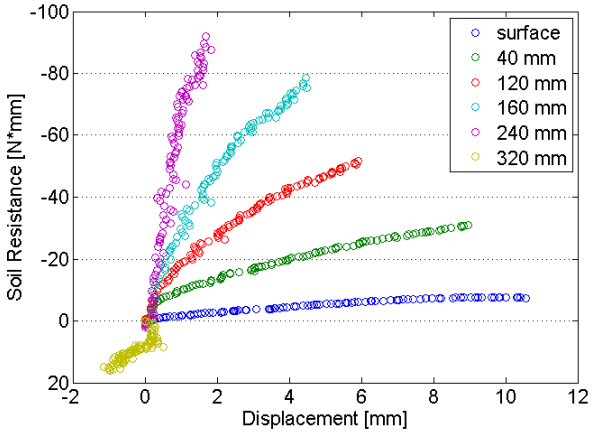

Figure 19: *p-y* curves for test 3, P_0 = 50 kPa, L/D = 5

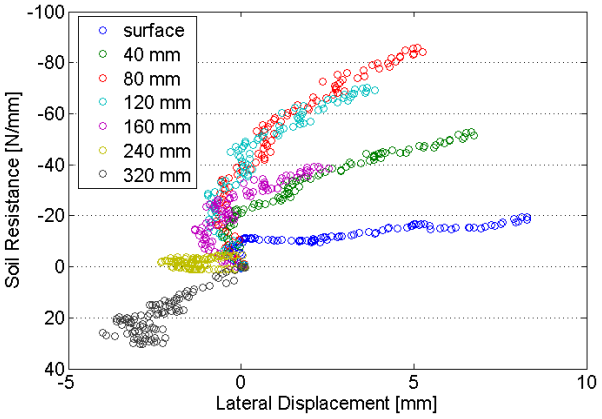

Figure 20: *p-y* curves for test 6, P_0 = 100 kPa, L/D = 5

Based on the experimental *p-y* curves obtained from the tests carried out at Aalborg University Laboratory the soil resistance increases significantly when the effective stress level rises. For instance, at the soil surface the lowest value of ultimate soil resistance is obtained, reaching 2, 10 and 20 N/mm for 0, 50 and 100 kPa respectively.

There are some curves which point to positive values of the soil resistance meaning that those depths are below the zero deflection point.

Focusing on detail in the graphs, the rotation point is found to increase in depth when the overburden pressure applied is higher.

On the other hand, it is shown for an increasing slenderness ratio how the soil resistance decreases, cf. Figures 21 to 23. This behaviour is expected since a raise in L/D means an increment in the embedded length. The more embedded length is considered, the more length is to distribute the strength of the soil, yielding into a decrement in soil resistance.

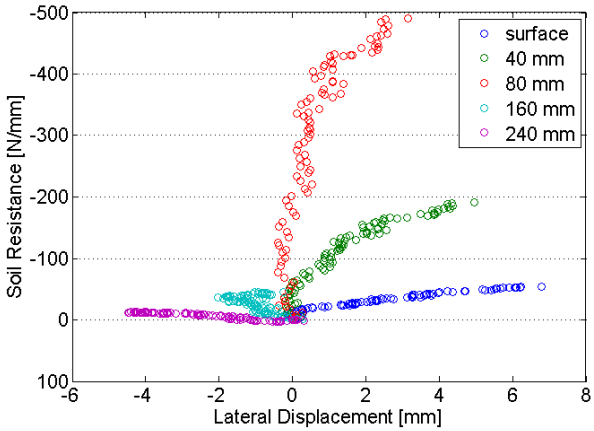

Figure 21: *p-y* curves for test 5, P_0 = 100 kPa, L/D = 4

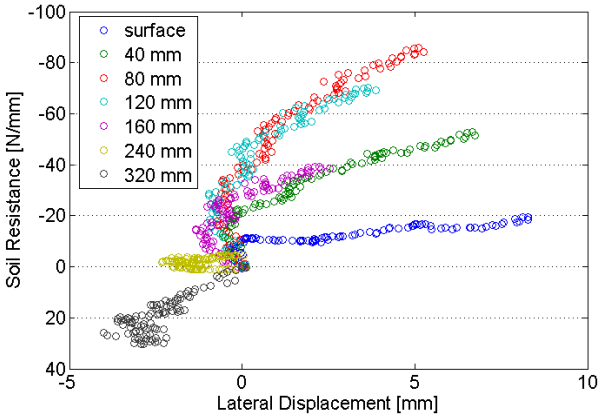

Figure 22: *p-y* curves for test 6, P_0 = 100 kPa, L/D = 5

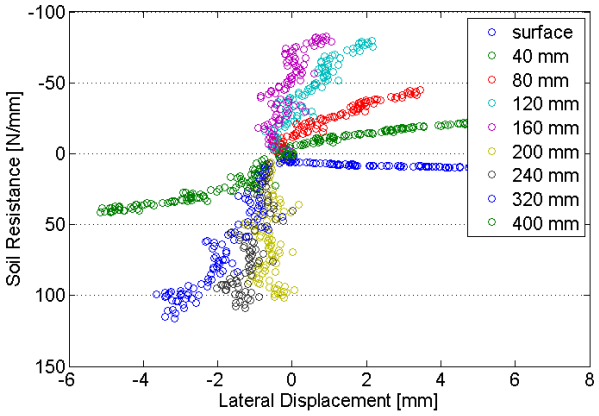

Figure 23: *p-y* curves for test 7, P_0 = 100 kPa, *L/D* = 6

Notice that more depth levels in the pile are considered for higher slenderness ratios when computing *p-y* curves, since more embedded pile length is driven into the soil and more strain gauges are in contact with it. The soil surface shows the lowest value of soil resistance, reaching values of 50, 20 and nearly 0 N/mm for *L/D* = 4, 5 and 6 respectively. The rotation point is found to decrease in depth when the slenderness ratio increases.

7.5 Uncertainties in the computed *p-y* curves

The *p-y* curves obtained experimentally are in general difficult to fit by a polynomial function, since some of them show uncorrelation and the *p-y* data points are quite disperse and unreliable. This is due to the inefficiency when using the Piecewise polynomial fitting curve method when computing the soil resistance.

However, not all of them are inaccurate. The *p-y* curves obtained for the highest overburden pressure (100 kPa) show a better distribution, and thus a better shape, due to the uncertainties observed for low pressure levels, such as the overestimated value of the friction angle.

In all the *p-y* curves plots, the *p-y* curves which are computed near the rotation point show a strange shape, due to the suddenly change in the sign of soil resistance, since the pile exhibits a total rigid-body motion. Thus, these *p-y* curves are considered unreliable.

Some of the *p-y* curves show negative displacements in the beginning, cf. Figure 22, which is not reasonable, and thus the initial stiffness cannot be computed in those *p-y* curves.

8 Analysis of initial stiffness

The initial stiffness defined as the stiffness of the soil for small deflections as equation 12 reads, is found to increase in all the cases with depth, and also with the variation of the stress level, cf. Figures 24 and 25. DNV-OS-J101 (October, 2007).

$$E_{py}^{*} = \left.\frac{\partial p(y)}{\partial y}\right|_{y=0} = k \cdot x \qquad (12)$$

Where *k* is the initial subgrade reaction modulus and *x* denotes the depth along the embedded length of the pile. Graphically, the initial stiffness is defined as the tangent of the initial part of the *p-y* curve shown in figures 24 to 26.

API (1993) and DNV (1992) design regulations state that the variation of the initial stiffness is dependent on depth but not on the pile properties or the overburden pressure. However, it is shown in figure 25 the variation of the initial stiffness when the pressure level increases.

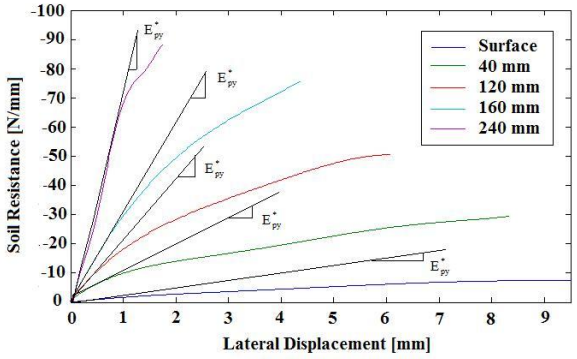

Figure 24: Variation of initial stiffness with depth, P_0 = 50 kPa, *L/D* = 5

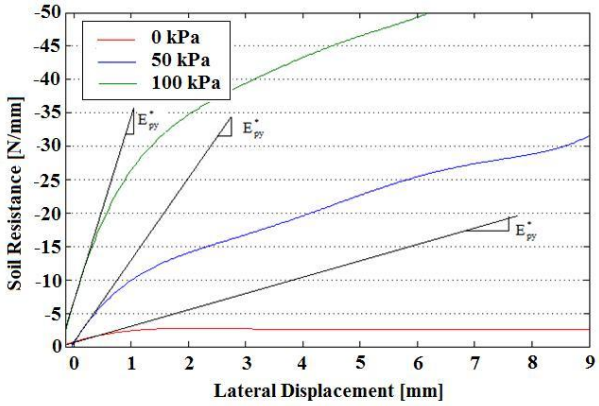

Figure 25: Variation of initial stiffness with overburden pressure level, *L/D* = 5, *x* = 40 mm

The initial stiffness tends to decrease when the slenderness ratio increases, showing the opposite behaviour when P_0 gets higher, cf. Figure 26.

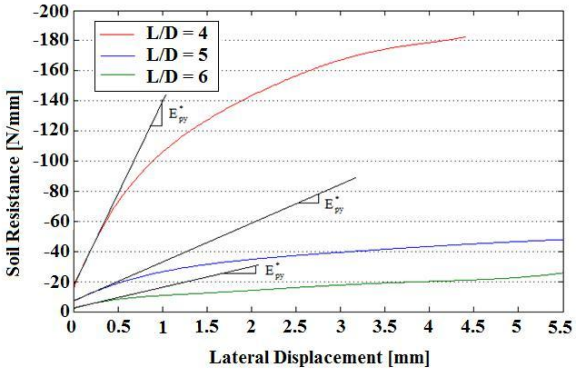

Figure 26: Variation of initial stiffness with slenderness ratio, P_0 = 100 kPa, x = 40 mm

Furthermore, the design regulations are based on the assumption that the initial stiffness varies linearly with depth being in disaccordance with the results obtained at Aalborg University Laboratory, resulting in a non-linear variation of the initial stiffness with depth, cf. Figure 27.

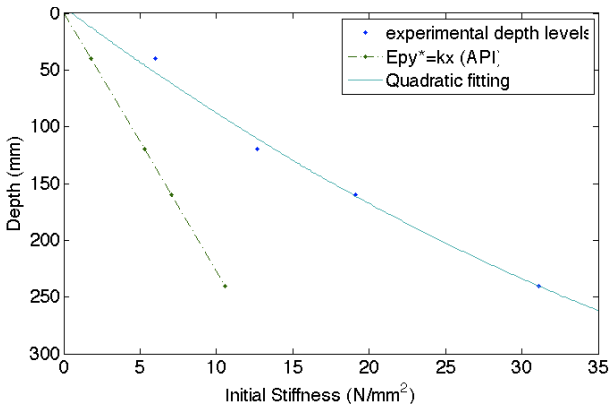

Figure 27: Variation of initial stiffness with depth, test no. 2

It was expected to obtain a non-linear variation of the initial stiffness, based on previous research, however the results obtained at Aalborg University Laboratory show a significant change in the initial stiffness adopting a quadratic fitting.

9 Conclusions

- The deflection of the pile consists of a rigid body motion. The pile rotates around a zero deflection point in all the cases (L/D = 3, 4, 5 and 6).

- Overburden pressure, P_0, and slenderness ratio, L/D, affect in the same way to the lateral deflection of the pile, y. The larger P_0 or L/D become, the lower lateral deflection is experimented by the pile.

- When applying overburden pressure, effective stresses in the soil, increase, and as a result the pile behaves more flexibly.

- Soil resistance is very sensitive to depth and overburden pressure variation, increasing rapidly when depth or pressure increase.

- When the pressure is kept constant and the slenderness ratio increases the soil resistance decreases.

- The bending moment, $M(x)$, is very sensitive when the pressure and the slenderness ratio are increased, since it rises very quickly. For an overburden pressure of 0 kPa, the pile behaves almost like a rigid body. Additionally, when the pressure increases, the maximum bending moment occurs closer to the soil surface. This fact is due to the increase of effective stresses in the soil. Consequently, when the overburden pressure increases, the bending moment also becomes higher, and as a result the pile behaves more flexibly.

- The soil has a linear elastic behaviour in the initial part of the p-y curves, and the initial stiffness, E_{py}^*, increases when overburden pressure is being added. This means that when the pressure increases, the vertical effective stresses also increase and the soil will experiment less deformation, because of Hooke's Law.

- One assumption made is that the initial stiffness is independent of the pile properties, however, the tests carried out at Aalborg University laboratory, show the opposite. Initial stiffness decreases for big slenderness ratios, which is a function of the diameter. This observation is not in accordance with the recommendations provided by the design regulations, such as API or DNV.

- The initial stiffness is assumed to vary linearly with depth according to API and DNV. However, the test results indicate that its variation is not linear.

- Some scale effects related to scaling appeared. However, the results obtained show that scaling effects were minimized.

- The test conducted at low stress level show uncertainties due to the fact that the friction angle is a parameter with a strong relationship with the stress level of the soil.

- Numerical modelling was processed only for small-scale tests. In future research these models and conclusions should be extrapolated to full-scale models.

References

Andersen A., Madsen E., and Schaarup-Jensen. 1998. *Eastern Scheldt Sand. Baaskarp Sand no.15. Data Report 9701*

API. 1993. *Recommended practice for Planning, Designing and Constructing Fixed Offshore Platforms - Working Stress design*. American Petroleum Institute.

Cox et al. 1974. *Field testing of laterally loaded piles in sand.*

DNV. 1992. *Foundations. Det Norske Veritas. Classification Notes No. 30.4*

Hanne R. Roesen, Thomassen Kristina. 2010. *Small-Scale Laterally Loaded Non-Slender Monopiles*

Ibsen L. B. Hanson M., Hjort. T. and Thaarup M. 2009. *MC-Parameter Calibration for Baaskarp Sand no.15*.

Murchinson and O'neill. 1984. *Evaluation of p-y relationships in sand.*

Reese L. C. and Van Impe W. F. 2001. *Single Piles and Pile Groups under Lateral Loading*. A. A. Balkema, Rotterdam, Brookfiel.

Sørensen S. P. H., Kristian T. Brødbæk and Martin Møller. 2009. *Evaluation of Load-Displacement Relationships for Large-Diameter Piles.* Aalborg University.

Yang and Liang. 2006. *Methods for deriving p-y curves from instrumented lateral load tests.*

CHAPTER 3

DIMENSIONLESS ANALYSIS OF SMALL-SCALE TESTS SUBJECTED TO STATIC LATERAL LOADING IN COHESIONLESS SOILS

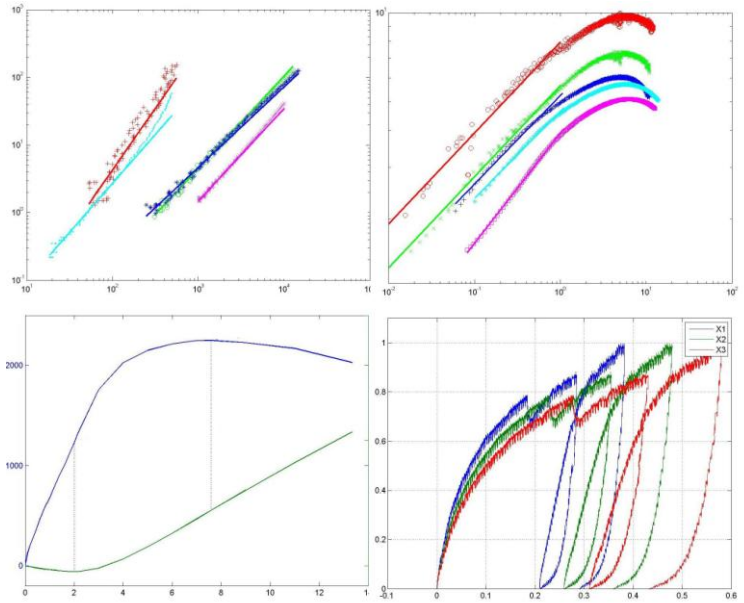

Dimensionless analysis of Small-Scale Tests subjected to static lateral loading in cohesionless soil

Alejandro Borobia Moreno[1]; Linas Mikalauskas[1]; Jose Luis Troya Díaz[1]

Aalborg University, April 2011

Abstract

Twenty two small-scale tests concerning monopiles subjected to static lateral loading have been conducted at Aalborg University from 2009 to 2011 by different students taking into account varying slenderness ratios (L/D = 3, 4, 5 and 6) and different overburden pressures (0 kPa, 50 kPa, 100 kPa). Based on these tests, a dimensionless analysis is carried out. The results are investigated, sorted and compared regarding to the variation of overburden pressure and slenderness ratio. Some load-displacement normalized graphs are represented in logarithmic scale and the data points are fitted by the so called Power Law. Previously to the small-scale tests, some triaxial tests were performed on Baaskarp sand no.15 at different confining pressures which are also compared to the monopile small-scale tests carried out since 2009. Finally, a general equation which describes the lateral displacement of the small-scale tests is derived, as well as some conclusions of the performed analysis.

1 Introduction

Up to date, monopile foundations are the most employed type of foundation for offshore wind turbines. The *p-y* curve method based on design regulations such as API (1993) and DNV (1992) is often used as basis for the design of monopiles, however it is considered by many researchers as inaccurate and incomplete, cf. Borobia et al. (March, 2011).

Full-scale test models are very expensive and time consuming, reason for why 22 quasi-static small-scale models have been performed at Aalborg University Laboratory by different students since 2009 until the current date.

When this kind of tests are realised, small-scale effects usually appear. In order to reduce these small-scale effects, the tests are carried out inside a pressure tank, increasing the effective stresses, and thus reducing the uncertainties when the soil parameters are obtained, due to the strong dependency of the friction angle on the effective stress level.

Furthermore, some triaxial tests previously performed at Aalborg University on the same kind of sand (Baaskarp sand no. 15) are compared to the behaviour of the soil for the 22 quasi-static tests taken into account for this analysis. These tests were carried out by Sørensen et al. (2009), Roessen and Thomassen (2010) and Borobia et al. (March, 2011).

This paper presents an overview of the results obtained for the 22 small-scale tests and a dimensionless analysis is realized based on the comparison between small-scale tests and previous triaxial tests carried out at Aalborg University.

---

[1] Graduate student, Dept. of Civil Engineering. Aalborg University, Denmark.

It is focused on the load-displacement normalized relationship, being compared and analysed regarding to the varying slenderness ratio and changing overburden pressure. Therefore, an analysis of the variation of the soil exponent is performed. Gudehus and Hettler (1983).

2 Tests overview

The main characteristics of the 22 small-scale tests carried out at Aalborg University are presented in table 1. The test programme is conducted on piles with diameters of D = 40, 60, 80, 100 mm, changing slenderness ratio (L/D = 3, 4, 5, 6) and different overburden pressures (P_0 = 0, 50, 100 kPa). The piles are closed-ended piles, some of them with strain gauges attached, and some of them without. A constant wall thickness of 5 mm is used for the 4 piles.

Test number	D [mm]	P_0 [kPa]	L/D	Strain gauges
Test 1	40	0	5	No
Test 2	40	50	5	No
Test 3	40	100	5	No
Test 4	60	0	5	10
Test 5	60	50	5	10
Test 6	60	100	5	10
Test 7	80	0	3	No
Test 8	80	50	3	No
Test 9	80	100	3	No
Test 10	80	100	4	22
Test 11	80	0	5	22
Test 12	80	50	5	22
Test 13	80	100	5	22
Test 14	80	0	5	10
Test 15	80	50	5	10
Test 16	80	100	5	10
Test 17	80	50	6	22
Test 18	80	100	6	22
Test 19	100	0	5	No
Test 20	100	50	5	No
Test 21	100	50	5	No
Test 22	100	100	5	No

Table 1: Test programme.

Tests 1 to 3 and tests 19, 21 and 22 were performed by Roessen and Thomassen (2010). Tests 14 to 16 and 4 to 6 were carried out by Sørensen et al. (2009) and the 10 remaining tests were conducted by Borobia et al. (March, 2011).

3 Installation of the pile

The pile is installed by the help of a hydraulic piston placed on the top hatch of the tank, and it is driven into fully saturated sand with embedded lengths of 200, 240, 300, 320, 400, 480 and 500 mm, cf. Figure 1.

Figure 1: Installation of the pile

After the installation of the pile, a standard preparation of the soil for all the tests must be performed as it is fully explained in Borobia et al (March, 2011).

To verify the homogeneity of the soil and calculate the soil parameters 6 CPT's were carried out at 6 different positions. Since Baaskarp Sand no.15 is considered cohesionless, only tip resistance is measured by the cone, cf. Figure 2.

Figure 2: Cone penetration test

The density index, I_D, and the unit weight of the soil, γ', are obtained by iteration using equations 1 to 4:

$$\gamma' = \frac{d_s - 1}{1 + e_{insitu}} \cdot \gamma_w \qquad (1)$$

$$\sigma_1' = \gamma' \cdot x \qquad (2)$$

$$I_D = c_2 \cdot \left(\frac{\sigma_1'}{q_c^{c_1}} \right)^{c_3} \qquad (3)$$

$$I_D = \frac{e_{max} - e_{insitu}}{e_{max} - e_{min}} \cdot 100 \qquad (4)$$

Where γ_w is the unit weight of the water, x defines the depth and c_1 and c_2 are fitting constants. The rest of the soil parameters are obtained based on previous triaxial tests realized at Aalborg University and the relation between the density index and the friction angle proposed by Schmertmann (1978), cf. Figure 3.

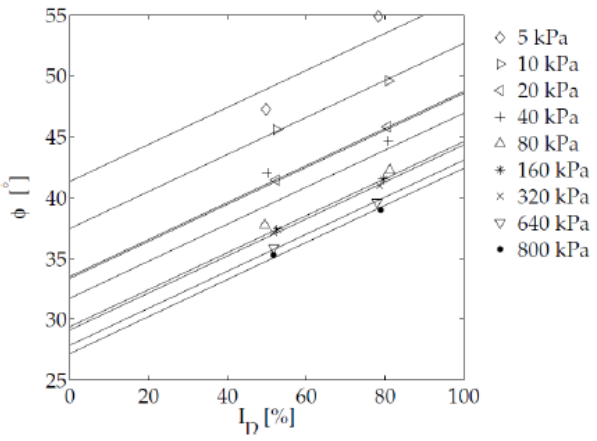

Figure 3: Schmertmann Relation based on triaxial tests, Schmertmann (1978)

An average of the soil parameters derived for Baaskarp Sand no.15 in all the tests are reflected in table 2.

Notice that for tests 7, 8 and 9 corresponding to a slenderness ratio of *L/D* = 3, it was decided not to carry out the CPT's since the embedded length is only 240 mm and the CPT cone could only penetrate 10 cm, which is not deep enough to rely on these CPT's. Thus, an averaged density index of I_D = 83 % is assumed for the calculation of the rest of the parameters in these tests (the range of I_D varies from 75% to 91%).

Test no.	φ_{tr}[°]	ψ_{tr}[°]	I_D [%]	γ' [kN/m^3]	E_0 [MPa]
1	54.4	20.4	91.0	10.4	[-]
2	50.4	19.1	89.0	10.4	38.6
3	48.0	18.6	91.0	10.40	57.2
4	52.6	18.1	79.0	10.2	[-]
5	48.5	16.9	79.0	10.2	25.4
6	45.9	16.2	79.0	10.2	41.1
7	52.6	18.2	83.0	10.3	[-]
8	49.5	17.9	83.0	10.2	27.6
9	49.7	17.0	83.0	10.2	44.4
10	45.5	15.5	76.6	10.1	36.5
11	52.7	17.0	84.6	10.3	[-]
12	47.3	15.7	77.9	10.2	25.2
13	45.7	16.1	79.7	10.2	38.9
14	52.2	17.5	76.0	10.1	[-]
15	45.1	15.3	75.0	10.1	37.4
16	48.3	16.7	78.0	10.1	24.9
17	48.3	16.1	79.9	10.2	26.1
18	45.5	15.8	78.6	10.2	38.0
19	53.7	19.6	86.0	10.3	[-]
20	49.9	17.6	87.2	10.3	30.00
21	50.3	19.0	89.0	10.4	38.2
22	47.7	18.3	90.0	10.4	55.6

Table 2: Averaged soil parameters obtained by Sørensen et al. (2009), Roessen and Thomassen (2010) and Borobia et al. (2011)

4 Test setup

The tests are carried out inside a pressure tank with a height of 2.5 m and a diameter of 2.1 m. The objective of the pressure tank is to increase the effective stresses, which are very significant when calculating the soil parameters, specially the friction angle which strongly depends on the stress level. It is observed that the friction angle is overestimated for low values of the pressure level.

Thus, the rest of the parameters also depend on the effective stresses, since all of them are related by equations 1 to 4 and also by the equations presented by Schemertmann, 1978.

A full description of all the test setup can be found in Borobia, Mikalauskas and Troya, March 2011.

5 Dimensionless Analysis

The normalised load-deflection relationship shown in figures 4 to 6 represents only the first loading of the 10 tests realised at Aalborg University by Borobia et al. (March,

2011), the 6 tests carried out by Roessen and Thomassen (2010) and the 6 tests performed by Sørensen et al. (2009) respectively.

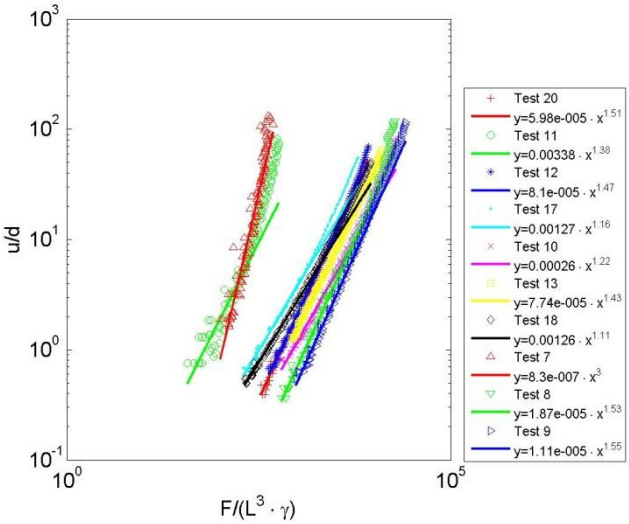

Figure 4: Normalised load-deflection for tests carried out by Borobia et al. (2011)

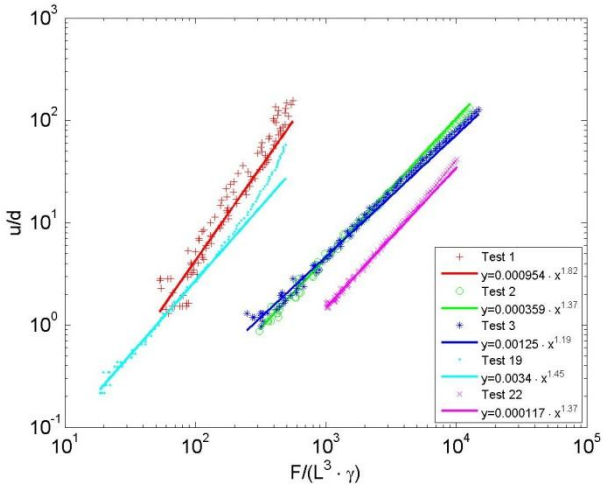

Figure 5: Normalised load-deflection for tests performed by Roessen and Thomassen (2010)

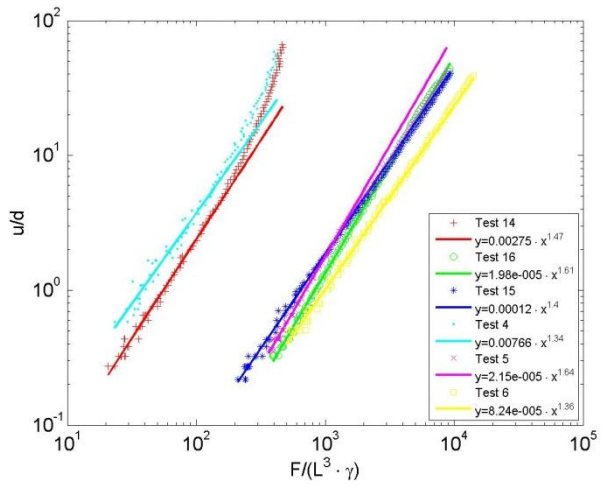

Figure 6: Normalised load-deflection for tests carried out by Sørensen et al. (2009)

For piles subjected to static loading, and assuming the validity of the power law, cf. Prosperine K. Peralta (2010), the pile displacement can be expressed as a potential function, cf. Equation 5, where *C* is a constant dependent on the pile geometry and soil properties and α denotes the exponent of the lateral load on a pile.

$$\frac{y}{L} = C \cdot \left(\frac{H}{\gamma \cdot L^3} \right)^{\alpha} \qquad (5)$$

According to Dietrich (1983) and Hettler (1981) assuming a rigid behaviour of the pile, α is inversely proportional to *k* which is the soil exponent obtained from the triaxial tests previously performed at Aalborg University, cf. Equation 6.

$$\alpha_{rigid} = \frac{1}{k} \qquad (6)$$

Regarding to the data points shown in all the figures through this dimensionless analysis, only the points which are linearly distributed are fitted by a straight line, obtaining the exponent of the lateral load, α, and thus the soil exponent, *k*, by means of equation 6, assuming a rigid-pile system.

Table 3 shows how the exponent of the lateral load, α, and the analytically computed soil exponent, *k*, vary for the different tests carried out in the last two years by different students at Aalborg University Laboratory. The diameter and overburden pressure are expressed in mm and kPa respectively.

Notice that for this analysis, test no. 21 has been ignored, since some problems with the hydraulic piston appeared, and the initial loading is too small to be considered, cf. figure 7.

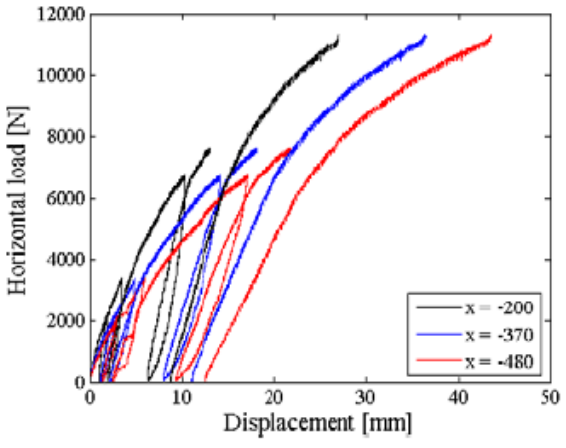

Figure 7: Load-deflection plot for test no.21

Test no.	D	L/D	P_0	α	k
1	40	5	0	1.82	0.55
2	40	5	50	1.37	0.73
3	40	5	100	1.19	0.84
4	60	5	0	1.34	0.74
5	60	5	50	1.64	0.61
6	60	5	100	1.36	0.73
7	80	3	0	3.00	0.33
8	80	3	50	1.53	0.65
9	80	3	100	1.55	0.65
10	80	4	100	1.22	0.82
11	80	5	0	1.38	0.72
12	80	5	50	1.43	0.70
13	80	5	100	1.43	0.70
14	80	5	0	1.47	0.68
15	80	5	50	1.40	0.72
16	80	5	100	1.61	0.62
17	80	6	50	1.16	0.87
18	80	6	100	1.11	0.90
19	100	5	0	1.45	0.69
20	100	5	50	1.51	0.66
21	100	5	50		
22	100	5	100	1.37	0.73

Table 3: Variation of α and k for all the tests

The maximum variation in the exponent of the lateral load on a pile is found to be 39% corresponding to tests 1 and 18, carried out at different pressures (0 kPa and 100 kPa). The same behaviour occurs to the soil exponent, k, since it is directly related to α by equation 6.

The tendency of the data in figures 4 to 6 show a linear tendency, but slightly curved in the upper part of it. This behaviour could be due to the dilation of the soil which varies depending on the overburden pressure and the slenderness ratio.

More similar slopes of the straight lines in the load-deflection relationship are obtained for the tests carried out at the same pressure level, cf. Figures 8 to 10 and tables 4 to 6.

However, for the tests realised without any overburden pressure applied, the results are more uncorrelated due to the inaccuracy when calculating the friction angle and the young's modulus of elasticity for small pressure levels, cf. Figure 8.

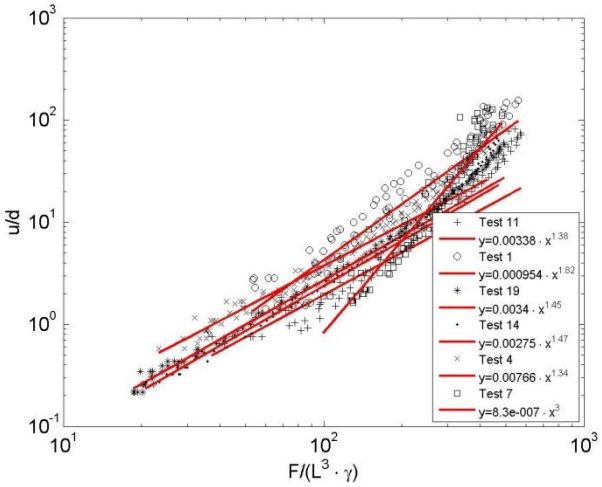

Figure 8: Normalised load-deflection for tests carried out at P_0 = 0 kPa

D	L/D	P_0	C	α	k
40	5	0	$9.54 \cdot 10^{-4}$	1.82	0.55
60	5	0	$7.66 \cdot 10^{-3}$	1.34	0.74
80	3	0	$8.30 \cdot 10^{-7}$	3.00	0.33
80	5	0	$3.38 \cdot 10^{-3}$	1.38	0.72
80	5	0	$2.75 \cdot 10^{-3}$	1.47	0.68
100	5	0	$3.40 \cdot 10^{-3}$	1.45	0.69

Table 4: Variation of α for P_0 = 0 kPa

A maximum variation of k with a value of 26.4 % is obtained for the tests carried out at 0 kPa for a constant value of L/D = 5.

It is also observed that for a slenderness ratio of L/D = 3 a value of k = 0.33 is obtained, which is not reasonable.

For this reason, the tests carried out without any overburden pressure applied are considered unreliable. The averaged soil exponent is computed for 0 kPa, considering a constant L/D = 5, yielding a value of k = 0.67. Figure 9 shows the dimensionless load-displacement for a pressure level of 50 kPa.

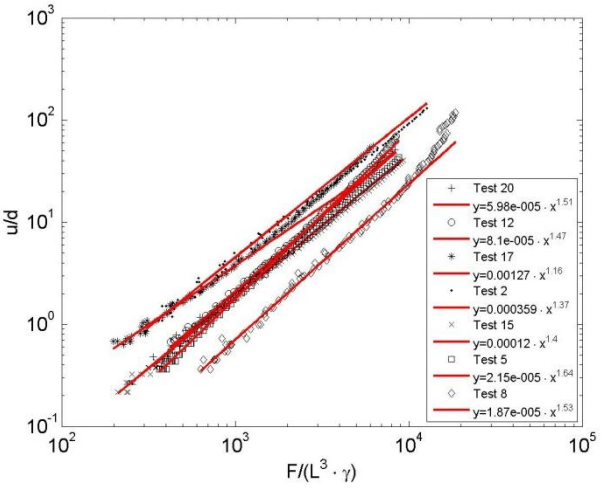

Figure 9: Normalised load-deflection for tests performed at P_0 = 50 kPa

D	L/D	P_0	C	α	k
40	5	50	$3.59 \cdot 10^{-4}$	1.37	0.73
60	5	50	$2.15 \cdot 10^{-5}$	1.64	0.61
80	3	50	$1.87 \cdot 10^{-5}$	1.53	0.65
80	5	50	$8.45 \cdot 10^{-5}$	1.43	0.70
80	5	50	$1.20 \cdot 10^{-4}$	1.40	0.72
80	6	50	$1.27 \cdot 10^{-3}$	1.16	0.87
100	5	50	$5.98 \cdot 10^{-5}$	1.51	0.66

Table 5: Variation of α and k for P_0 = 50 kPa

The maximum variation of the exponent of the lateral load on a pile subjected to a pressure level of 50 kPa for a constant L/D = 5, is found to be 14.8 % which is lower than for 0 kPa. The averaged soil exponent is found to be k = 0.69, which is slightly higher than for 0 kPa. Moreover, for a slenderness ratio of L/D = 6 it is obtained a high value of the soil exponent k = 0.87, which is considered unreliable since it is very elevated compare to the rest.

For the maximum overburden pressure applied in the tests (100 kPa), the highest variation experienced by k is found to be 26.1 % for a constant L/D = 5, cf. Figure 10 and table 6.

The averaged soil exponent for a constant L/D = 5 reaches a value of k = 0.72, which is higher than for 0 kPa and 50 kPa.

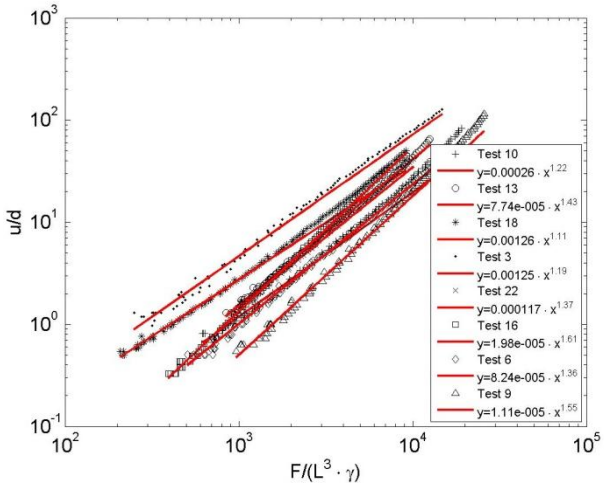

Figure 10: Normalised load-deflection for tests carried out at P_0 = 100 kPa

D	L/D	P_0	C	α	k
40	5	100	$1.25 \cdot 10^{-3}$	1.19	0.84
60	5	100	$8.24 \cdot 10^{-5}$	1.36	0.73
80	3	100	$1.11 \cdot 10^{-5}$	1.55	0.65
80	4	100	$2.60 \cdot 10^{-4}$	1.22	0.82
80	5	100	$7.74 \cdot 10^{-5}$	1.43	0.70
80	5	100	$1.98 \cdot 10^{-5}$	1.61	0.62
80	6	100	$1.26 \cdot 10^{-3}$	1.11	0.90
100	5	100	$1.17 \cdot 10^{-4}$	1.37	0.73

Table 6: Variation of α and k for P_0 = 100 kPa

Regarding the three pressure levels, in general, higher values of the soil exponent are found when the overburden pressure level increases, with averaged values of k = 0.67, 0.69, and 0.72 for 0, 50 and 100 kPa respectively.

It can be concluded that the overburden pressure makes the exponent of the lateral load to decrease, and thus the soil exponent increases, meaning lower lateral deflection experienced by the pile when the pressure level increases.

Four different diameters were considered for all the small-scale tests carried out at Aalborg University (40, 60, 80 and 100 mm), and its influence when calculating the soil exponent is shown in figures 11 to 14 and tables 7 to 10.

Figure 11 shows agreement with the fact of increasing k for higher values of overburden pressure. The averaged value of the soil exponent for D = 40 mm is found to be k = 0.71, cf. Table 7.

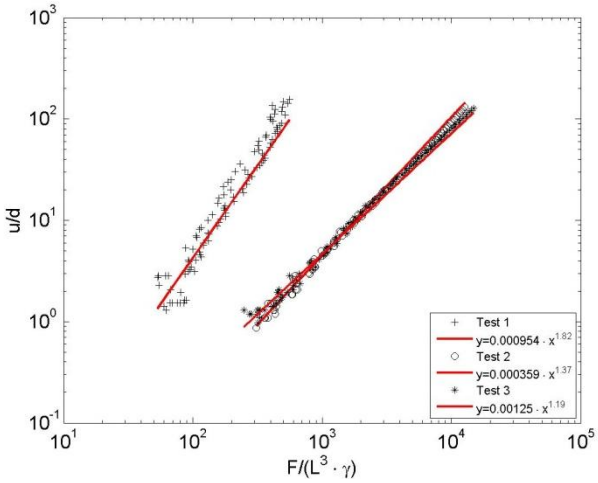

Figure 11: Normalised load-deflection D = 40 mm and P_0 = 0, 50 and 100 kPa

D	*L/D*	P_0	*C*	*α*	*k*
40	5	0	$9.54 \cdot 10^{-4}$	1.82	0.55
40	5	50	$3.59 \cdot 10^{-4}$	1.37	0.73
40	5	100	$1.25 \cdot 10^{-3}$	1.19	0.84

Table 7: Variation of α and *k* for *D* = 40 mm

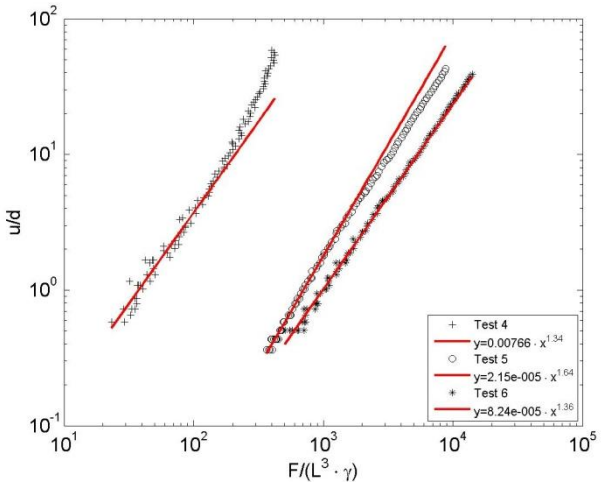

Figure 12: Normalised load-deflection *D* = 60 mm and P_0 = 0, 50 and 100 kPa

D	*L/D*	P_0	*C*	*α*	*k*
60	5	0	$7.66 \cdot 10^{-3}$	1.34	0.74
60	5	50	$2.15 \cdot 10^{-5}$	1.64	0.61
60	5	100	$8.24 \cdot 10^{-5}$	1.36	0.73

Table 8: Variation of α and k for *D* = 60 mm

Based on Figure 12, uncertainties are shown again for the test carried out at 0 kPa, since it is expected to obtain the lowest value of *k*. An averaged value of *k* = 0.69 is found for *D* = 60 mm.

Figure 13 represents the normalised load-displacement relationship for *D* = 80 mm.

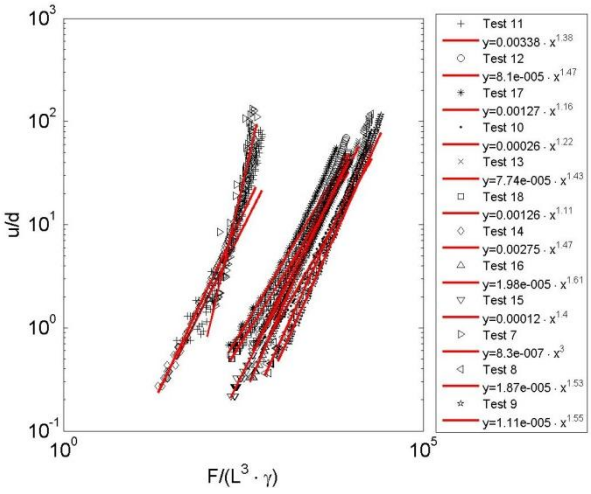

Figure 13: Normalised load-deflection *D* = 80 mm and P_0 = 0, 50 and 100 kPa

D	*L/D*	P_0	*C*	*α*	*k*
80	3	0	$8.30 \cdot 10^{-7}$	3.00	0.33
80	3	50	$1.87 \cdot 10^{-5}$	1.53	0.65
80	3	100	$1.11 \cdot 10^{-5}$	1.55	0.65
80	4	100	$2.60 \cdot 10^{-4}$	1.22	0.82
80	5	0	$3.38 \cdot 10^{-3}$	1.38	0.72
80	5	50	$8.45 \cdot 10^{-5}$	1.43	0.70
80	5	100	$7.74 \cdot 10^{-5}$	1.43	0.70
80	5	0	$2.75 \cdot 10^{-3}$	1.47	0.68
80	5	50	$1.20 \cdot 10^{-4}$	1.40	0.72
80	5	100	$1.98 \cdot 10^{-5}$	1.61	0.62
80	6	50	$1.27 \cdot 10^{-3}$	1.16	0.87
80	6	100	$1.26 \cdot 10^{-3}$	1.11	0.90

Table 9: Variation of α and k for *D* = 80 mm

An averaged value of the soil exponent is computed for *D* = 80 mm, obtaining *k* = 0.68.

It can be noticed that for tests with similar characteristics carried out in two different years (2009 and 2011) it is obtained correlation between the results. For instance, for tests 11 and 14 (*D* = 80 mm, *L/D* = 5 and 0 kPa) it is obtained values of *k* = 0.72 and *k* = 0.68, respectively. Tests 12 and 15 (*D* = 80 mm, *L/D* = 5 and 50 kPa) also show similar results of the soil exponent, *k* = 0.70 and 0.72, respectively.

Figure 14 shows the variation of the lateral load exponent and the soil exponent for a diameter of *D* = 100 mm.

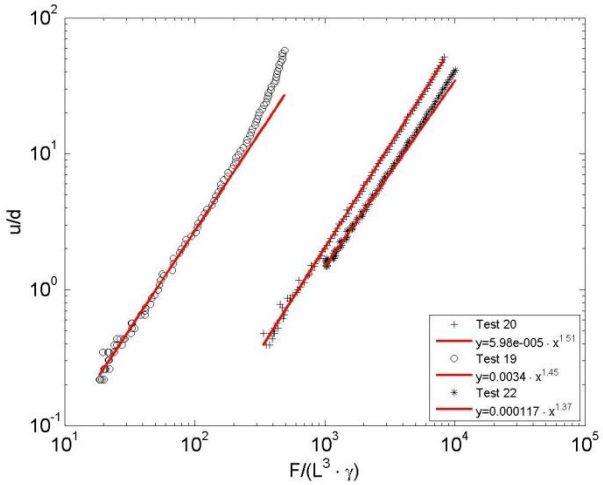

Figure 14: Normalised load-deflection *D* = 100 mm and P_0 = 0, 50 and 100 kPa.

D	*L/D*	P_0	*C*	*α*	*k*
100	5	0	$3.40 \cdot 10^{-3}$	1.45	0.69
100	5	50	$5.98 \cdot 10^{-5}$	1.51	0.66
100	5	100	$1.17 \cdot 10^{-4}$	1.37	0.73

Table 10: Variation of α and k for *D* = 100 mm

It is obtained averaged values of the soil exponent of 0.71, 0.69, 0.68 and 0.69 for D = 40, 60, 80 and 100 mm respectively. Since these values are very similar from each other, it can be considered that the soil exponent is independent of the pile diameter, with an averaged value of k = 0.69

However, the influence of the slenderness ratio is difficult to analyse, since most of the tests were carried out with a slenderness ratio of L/D = 5 and thus, its influence cannot be analysed.

In general, an average value of the load exponent is computed for the three pressure levels being independent of the diameter of the pile, yielding 0.67, 0.69 and 0.72 corresponding to overburden pressure levels of 0 kPa, 50 kPa and 100 kPa and an averaged density index of I_D = 82.4 %.

For a rigid pile system, a constant value of $\alpha = 1/k$ is assumed, being a soil constant which only depends on the stress level and can be derived from the triaxial tests previously carried out at Aalborg University on Baaskarp sand no. 15. Thereafter, these values are analysed and then compared to the values obtained by means of the small-scale tests.

6 Triaxial tests

Some triaxial tests were performed at Aalborg University Laboratory with the purpose of analysing how the soil behaves when confining pressure is applied. Four different void ratios were employed, corresponding to density indexes of I_D = 1, 0.8, 0.51, 0.025 and many different confining pressures σ_c were used for each density index.

However, in order to compute and compare the calculated soil exponents, k, by means of the small-scale tests, to the ones obtained by the triaxial tests, only the data corresponding to a density index of 80% is used, since an averaged density index of I_D = 82.4 % is obtained from the 22 tests carried out at the Geotechnical Laboratory. Furthermore, the maximum overburden pressure applied inside the tank for the small-scale tests was 100 kPa. By means of the lateral earth pressure coefficient at rest, the relation defined by equation 7 shows the maximum confining pressure to be considered in the triaxial tests, yielding 27 kPa.

$$\sigma_c = (1 - \sin\varphi) \cdot \sigma_1 \qquad (7)$$

In figure 15 it can be observed how a triaxial test is carried out and stresses in the three directions were applied on the soil specimen.

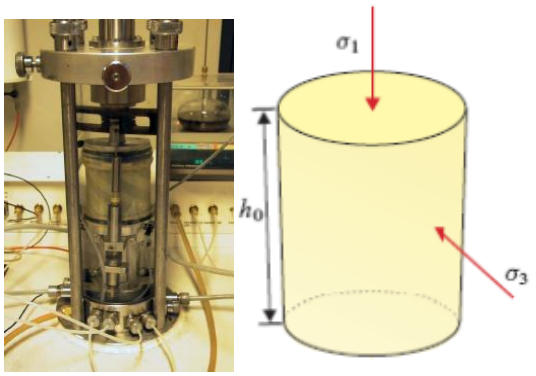

Figure 15: Triaxial test on the left and sketch of soil specimen on the right.

The purpose of performing this kind of tests is to determine the mechanical properties of the soil assuming that the soil specimen represents the behaviour of the entire soil, and the properties obtained through these small-scale tests are reliable enough to extrapolate them to full-scale.

Figure 16 shows the stress-strain relationship for the triaxial tests in a double-logarithmic scale, where the data points are fitted again by the power law and the exponent is found to be the soil exponent, k.

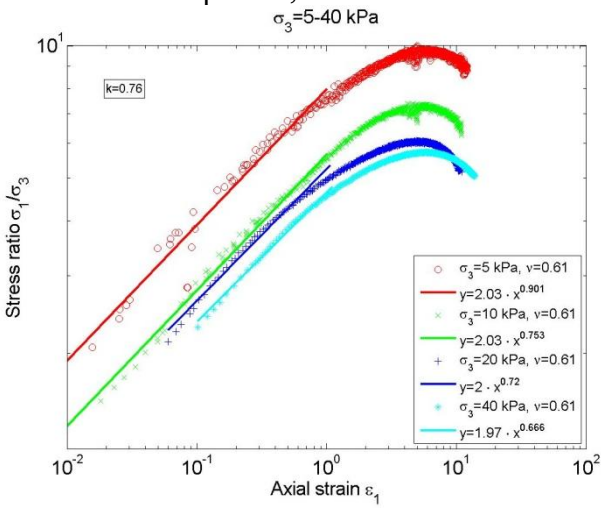

Figure 16: Stress-Strain relation in the triaxial tests for different confining pressures

Figure 16 shows disagreement between the soil exponent calculated by small-scale tests and triaxial tests for low confining pressures. It is obtained values of k = 0.90, 0.75, 0.72

and 0.67 for confining pressures of 5 kPa, 10 kPa, 20 kPa and 40 kPa, respectively. Thus, only the soil exponent computed for an overburden pressure of 100 kPa in the small-scale tests is considered reliable (k = 0.72), corresponding to a confining pressure computed by equation 7 of approximately 27 kPa.

This result was expected, since previous triaxial tests carried out at Aalborg University showed uncorrelation for low confining pressures when calculating the friction angle, cf. Figure 3.

This k is assumed to be a soil constant, only depending on the stress level, and the static pile test results show that the power law of the force-displacement curve can to a large extent be verified using small-scale models.

The degree of influence of the applied horizontal load on a pile system can be predicted using the soil exponent, k. The displacement of a rigid pile will increase with the applied horizontal load amplitude to the power of $1/k$. Thus, the load function is given by the power law expressed by equation 8:

$$f_H = \left(\frac{H}{\gamma \cdot L^3} \right)^{1/k} \qquad (8)$$

Based on equation 5, the coefficient C is dependent on the geometry of the pile and the soil density, thus the Π-products are independent of the pile bending stiffness, yielding:

$$C = f\left(\frac{d}{L}, e \right) = f_d \cdot f_e \qquad (9)$$

Thus, the dimensionless displacement can be represented by equation 10 reading:

$$\frac{y}{L} = f_d \cdot f_e \cdot f_H \qquad (10)$$

In cohesionless soils, the density of the soil has a significant effect on the pile displacement, y, since soil resistance to the static load along the length of the pile is dependent on this parameter. The function f_e can be calculated by means of f_n proposed by Hettler (1981):

$$f_n \approx \frac{1}{1 + 5 \cdot 10^4 \cdot \left[\left(\frac{n_{ref}}{n} \right)^{10^{-3}} - 1 \right]} \qquad (11)$$

The soil porosity is related to the void ratio by equation 12 and considering $e_{ref} = e_{max}$ = 0.858, corresponding to the loosest state of Baaskarp sand no. 15, and a void ratio of e = 0.60 for an averaged density index of 85% , f_n is found to be 0.0874 and it is assumed constant for further calculations.

$$n = \frac{e}{1+e} \qquad (12)$$

This means that the total lateral pile displacement should decrease by approximately 87% for I_D = 0.85 when compared to the maximum pile displacement in a loose cohesionless soil (when f_n = 1).

Since the bending stiffness (EI) of the pile system can be ignored for rigid piles, the general displacement equation for rigid pile systems can further be described according to equation 13, where the only unknown function is f_d. cf. Appendix D.

$$\frac{y}{L} = \left(\frac{H}{\gamma \cdot L^3} \right)^{1/k} \cdot 0.0874 \cdot f_d \qquad (13)$$

Taking only into account the soil exponents computed for a pressure level of 100 kPa, and based on equation 13, four linear functions for f_d can be obtained for the four diameters used through all the tests (40 mm, 60 mm, 80 mm, 100 mm), corresponding to tests 3, 6, 13 and 22, cf. Figure 17.

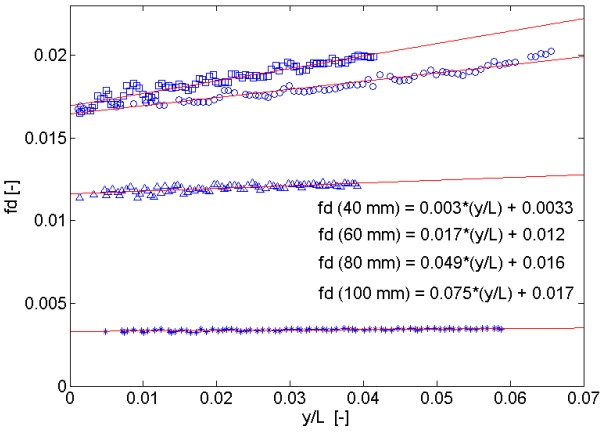

Figure 17: Variation of f_d with the normalised displacement

The four linear functions adopt the form of a straight line with a common shape for the four tests considered as shown in equation 14:

$$f_d = a \cdot \frac{y}{L} + b \qquad (14)$$

According to the four different equations obtained for f_d for each pile diameter, and substituting each f_d in equation 13, four implicit

dimensionless equations to describe the lateral deflection of the pile for the four different diameters (40, 60, 80, 100 mm) can be computed, being f_n = 0.0874, cf. Equation 15 to 18 respectively.

$$\frac{y}{L}=\left(\frac{H}{\gamma \cdot L^3}\right)^{1/k} \cdot f_n \cdot \left(0.003 \cdot (\frac{y}{L}) + 0.0033\right) \quad (15)$$

$$\frac{y}{L}=\left(\frac{H}{\gamma \cdot L^3}\right)^{1/k} \cdot f_n \cdot \left(0.017 \cdot (\frac{y}{L}) + 0.012\right) \quad (16)$$

$$\frac{y}{L}=\left(\frac{H}{\gamma \cdot L^3}\right)^{1/k} \cdot f_n \cdot \left(0.049 \cdot (\frac{y}{L}) + 0.016\right) \quad (17)$$

$$\frac{y}{L}=\left(\frac{H}{\gamma \cdot L^3}\right)^{1/k} \cdot f_n \cdot \left(0.075 \cdot (\frac{y}{L}) + 0.017\right) \quad (18)$$

These four equations are obtained for four different diameters (D = 40, 60, 80 and 100 mm). However, the goal is to obtain only a general equation which can describe the dimensionless lateral displacement of a pile as a function of the density index of the soil, its pile diameter, force applied, unit weight of the soil, soil exponent and embedded length of the pile. This equation will adopt the form shown in equation 19:

$$\frac{y}{L}(I_D, D, H, \gamma, k, L)$$

$$\frac{y}{L}=\left(\frac{H}{\gamma \cdot L^3}\right)^{1/k} \cdot \left(0.0874 \cdot a(D) \cdot \frac{y}{L} + b(D)\right) \quad (19)$$

Therefore, the coefficients a and b can be represented as a function of the pile diameter, cf. Figures 18 and 19.

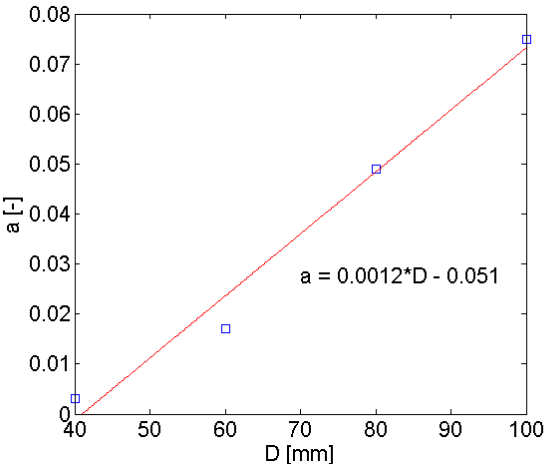

Figure 18: Variation of a with the diameter of the pile

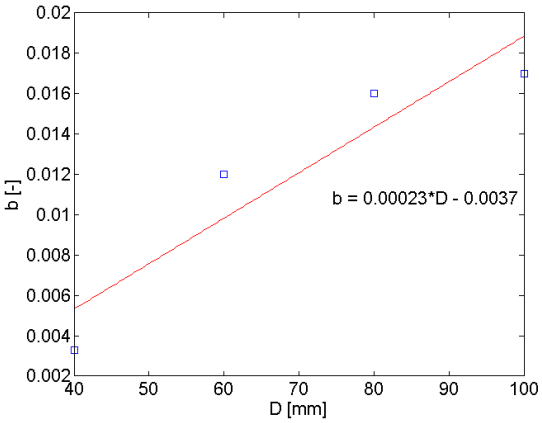

Figure 19: Variation of b with the diameter of the pile

Substituting $a(D)$ and $b(D)$ in equation 19, the general dimensionless implicit equation which can describe the lateral displacement of the pile at the height of the hydraulic piston and taking f_n = 0.0874, reads:

$$\frac{y}{L}=\left(\frac{H}{\gamma \cdot L^3}\right)^{1/k} \cdot f_n \cdot \left(\begin{array}{l}(0.0012 \cdot D - 0.051) \cdot \frac{y}{L} + \\ + \left(2.3 \cdot 10^{-4} \cdot D - 0.0037\right)\end{array}\right) \quad (20)$$

7 Extrapolation of Small–Scale parameters to a Prototype

An extrapolation of the parameters from the small-scale test to a full-scale model is realised in this section. Due to the uncertainties observed when calculating the friction angle for low stress levels, only the tests carried out with an overburden pressure of 100 kPa are chosen to extrapolate the parameters. Thus, model pile parameters of tests 3, 6, 13 and 22 (100 kPa, D = 40, 60, 80 and 100 mm, respectively) and extrapolated parameters to a prototype are shown in table 11.

	II-products	**Model Pile Parameters**	**Prototype Parameters**
Test 3	f_d = 0.0033	D = 0.04 m	D = 2.2 m
		L = 0.2 m	L = 10.1 m
	f_n = 0.0874	γ = 10.4 kN/m^3	γ = 10.4 kN/m^3
	f_H = 4.604	H = 300 N	H = 4.9MN
Test 6	f_d = 0.0121	D = 0.06 m	D = 3.29 m
		L = 0.3 m	L = 16.43 m
	f_n = 0.0874	γ = 10.2 kN/m^3	γ = 10.2 kN/m^3
	f_H = 5.850	H = 1000 N	H = 16.4MN
Test 13	f_d = 0.016	D = 0.08 m	D = 4.38 m
		L = 0.4 m	L = 21.9 m
	f_n = 0.0874	γ = 10.2 kN/m^3	γ = 10.2 kN/m^3
	f_H = 2.675	H = 1300 N	H = 21.3MN
Test 22	f_d = 0.0173	D = 0.1 m	D = 5.48 m
		L = 0.5 m	L = 27.4 m
	f_n = 0.0874	γ = 10.4 kN/m^3	γ = 10.4 kN/m^3
	f_H = 2.861	H = 2800 N	H = 45.9MN

Table 11: Variation of α and k for D=100 mm

A scaling factor of λ = 0.01826 is used, according to the defined scaling laws defined in Appendix D.

The lateral load, *H*, taken into account for the extrapolation of the model parameters corresponds to the reached force when a maximum rotation allowed by the API regulations of 0.25˚occurs.

Notice that an averaged density index of 85% is considered in all the cases, yielding to the same Π-product, f_n in the four tests considered for the extrapolation, and a load eccentricity of h = 370 mm is used in the calculations.

Furthermore, two full-scale models are modelled numerically in order to analyse the real behaviour of a typical monopile offshore foundation, cf. Borobia, Mikalauskas and Troya (May, 2011).

8 **Conclusions**

- Soil parameters derived for the 22 quasi-static tests showed correlation between them; decreasing the value of the friction angle when the overburden pressure gets higher; yielding to a more accurate value of the friction angle for high overburden pressure levels (typical offshore locations rarely have a friction angle above 40 degrees).

- The exponent of the lateral load, α, can be computed by means of the double logarithmic-scale graphs, obtained as the slope of the straight line which fits the data points in the normalised load - lateral deflection graphs.

- The models are assumed to be rigid-pile systems where the soil exponent, *k*, is directly related to the exponent of the lateral load by means of equation 6.

- Averaged values of the soil exponent, *k*, of 0.71, 0.69, 0.68 and 0.69 are obtained for diameters of 40, 60, 80 and 100 mm, respectively. Due to the similarity of the results obtained for the 4 diameters considered, it can be assumed that the soil exponent is independent of the pile diameter, with an averaged value of k = 0.69.

- Averaged values of the soil exponent for the three overburden pressure levels applied at Aalborg University Laboratory were found to be k = 0.67, 0.69 and 0.72 for 0 kPa, 50 kPa and 100 kPa, respectively. This leads into a significant sensitivity of the soil exponent regarding the overburden pressure. The higher the overburden pressure level is, the higher soil exponent is obtained, meaning a lower lateral deflection experienced by the pile when the pressure level increases.

- The soil exponent is assumed to be a soil constant which only depends on the stress level, and it is independent of the pile properties, such as the pile diameter. Thus, the soil exponent can be obtained by means of triaxial tests.

- Disagreement between the soil exponent calculated by small-scale tests and triaxial tests for low confining pressures is observed. Due to the uncertainties observed when calculating the soil parameters for low stress levels and the uncorrelation found between small-scale tests and triaxial tests, only the soil exponent computed for an overburden pressure of 100 kPa in the small-scale tests is considered reliable (k = 0.72), corresponding to a confining pressure in the triaxial tests of 27 kPa.

- The influence of the slenderness ratio cannot be analysed, since most of the tests were conducted with a slenderness ratio of L/D = 5, and thus, its influence is difficult to observe.

- It is assumed the validity of the Power Law, which states that the lateral displacement of the pile is a function of the density index of the soil, pile diameter, force applied, unit weight of the soil, soil exponent and embedded length of the pile. Therefore, a general implicit equation which describes the lateral displacement of the pile is obtained by means of the Π-products, cf. Appendix D.

- An extrapolation of the model parameters to full-scale parameters is carried out based on the scaling laws shown in Appendix D. An averaged value of I_D = 85% and a lateral load, *H*, corresponding to the maximum rotation allowed by API design regulations (0.25˚) have been used in the calculations.

References

Chia-Chen Fang, James H. Long. 2005. *Assesment of existing methods for predicting soil response of laterally loaded piles in sand.*

Cox et al. 1974. *Field testing of laterally loaded piles in sand*

G. Gudehus and A. Hettler. 1983. *Model Studies of Foundations in Granular Soil.*

Hanne R. Roesen, Kristina Thomassen. 2010. *Small-Scale Laterally Loaded Non-Slender Monopiles*

Lars Bo Ibsen. 2009. *Soil Testing.* Aalborg University

L.B Ibsen, P.V. Lade. 1998. *The role of the characteristic line in static soil behavior.*

Prosperpine K. Peralta. 2010. *Investigations on the behavior of large diameter piles under long-term lateral cyclic loading in cohesion-less soil.*

Søren P. H. Sørensen, Kristian T. Brødbæk and Martin Møller. 2009. *Evaluation of Load-Displacement Relationships for Large-Diameter Piles.* Aalborg University.

CHAPTER 4

NUMERICAL MODELLING OF LATERALLY-LOADED MONOPILES IN COHESIONLESS SAND

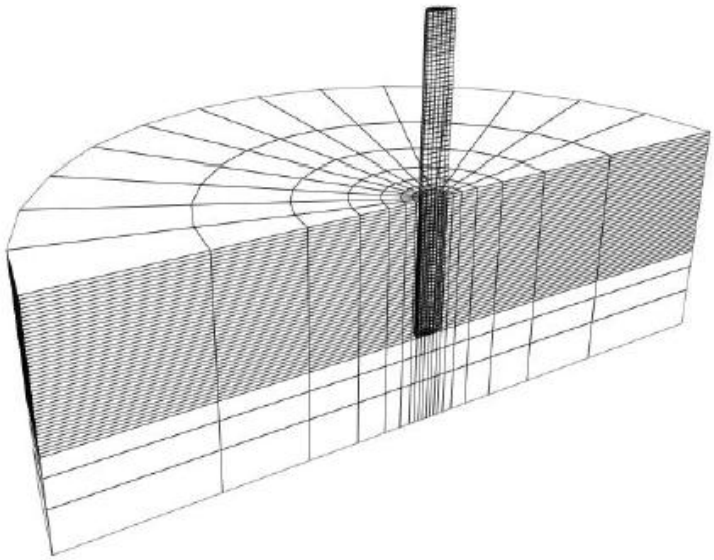

Numerical modelling of laterally-loaded non-slender monopiles in cohesionless sand

Alejandro Borobia Moreno[1]; Linas Mikalauskas[1]; Jose Luis Troya Díaz[1]

Aalborg University, May 2011

Abstract

A monopile is often employed as the foundation for offshore wind turbines. These piles are subjected to lateral loads generated by wind and waves, leading to significant lateral loads and overturning bending moments. The current method for the design of offshore wind turbines is the Winkler Model approach in which the soil resistance acting against the pile wall, *p*, is modelled by means of *p-y* curves. However, this method, and the recommended *p-y* curves are developed for jag-piles for the oil-industry, primarily developed for soft clays and then extended to sand. These jag-piles have higher slenderness ratios than modern wind turbines ($L/D > 10$) due to higher embedded lengths and lower diameters (less than 2 meters). In contrast, modern wind turbines have diameters of 4-6 m and $L/D < 10$. For this reason, uncertainties appear when using the *p-y* curve method in the design of monopiles. This paper consists of a numerical evaluation performed by two commercial three dimensional numerical programs: FLAC^{3D} and Plaxis 3D 2010. Mohr-Coulomb cut-off material model is used to compare the results obtained by both three dimensional programs. Moreover, two more material models: Hardening Soil model and Hardening Soil small strains model are employed in order to analyse and compare the accuracy of using one of them regarding the experimental results. The numerical modelling is then compared with small-scale laboratory tests. Furthermore, one full-scale monopile previously analysed in ABAQUS by Kellezj and Hansen (2003) is modelled by means of FLAC^{3D} and Plaxis 3D 2010 to analyse the real behaviour of a monopile foundation.

1 Introduction

The actual design of laterally-loaded monopiles, employed as foundation for offshore wind turbines, is the Winkler model approach based on the *p-y* curve method and following the design regulations of the petroleum industry: API (1993) and DNV (1992). However, they are considered as inaccurate and incomplete when designing monopile foundation for offshore wind turbines, cf. Borobia et al. (March, 2011). Several uncertainties in the method are found, such as the linear variation of the initial stiffness of the *p-y* curves with depth or its non-dependency on the pile properties.

These uncertainties are generated due to the fact that design regulations are based on some tests conducted on two slender flexible piles with $L/D = 34.4$, in contrast to modern monopiles which have a slenderness ratio $L/D \approx 5$, Cox et al. (1974).

Full-scale tests are expensive and time consuming, therefore numerical modelling becomes interesting to be performed. Further, small-scale tests have been conducted experimentally at the Aalborg University Geotechnical Laboratory by Borobia et al. (March, 2011).

[1] Graduate Student, Dept. of Civil Engineering, Aalborg University.

Thus, seven small-scale models with the same characteristics as the experimental tests are modelled numerically by means of two commercial three dimensional numerical programs: FLAC^{3D} and Plaxis 3D 2010.

Three different material models are employed in order to analyse which one represents a better approach of the real behaviour of the soil when a monopile foundation is installed and submitted to a lateral load:

- Mohr-Coulomb tension cut-off model
- Hardening Soil model
- Hardening Soil small strains model

Furthermore, one full-scale model previously conducted by Kellezj and Hansen (2003) with the help of another numerical program (ABAQUS) is modelled by FLAC^{3D} and Plaxis 3D 2010, with L = 21 m, D = 4 m and a layered soil with varying friction angle from 21.6 to 44.3 degrees.

Through this paper an evaluation and a comparison of the results obtained by FLAC^{3D} and Plaxis 3D 2010, taking into account the three material models previously mentioned, is presented.

2 Laboratory Test Setup

Quasi-static laboratory tests have been conducted by Troya et al. (March, 2011) with two closed-ended aluminium pipe piles with the outer diameter of D = 80, 100 mm with different slenderness ratios (L/D = 3 – 6) and subjected to different overburden pressures (P_0 = 0, 50, 100 kPa). Seven of these tests were chosen to be modelled numerically. Each test parameters are given in Table 1.

Test no.	D [mm]	L/D	P_0 [kPa]
Test 1	100	5	50
Test 2	80	5	0
Test 3	80	5	50
Test 4	80	6	50
Test 5	80	4	100
Test 6	80	5	100
Test 7	80	6	100

Table 1: Tests' geometries and overburden pressures

Input parameters for the soil in the models are taken the same as found in the small-scale tests by CPT's. The values of these parameters are given in Table 2.

Test no.	φ_{tr}[°]	ψ_{tr}[°]	γ' [kN/m^3]	E_0 [MPa]
Test 1	49.92	17.56	10.33	29.96
Test 2	52.70	17.03	10.27	9
Test 3	47.26	15.70	10.15	25.15
Test 4	48.26	16.09	10.18	26.12
Test 5	45.46	15.45	10.12	36.54
Test 6	45.67	16.06	10.18	38.85
Test 7	45.54	15.84	10.15	38.00

Table 2: Mechanical soil parameters obtained in the laboratory

3 Small-scale numerical modelling

3.1 FLAC^{3D} modelling procedure

A 3D model is generated with FLAC^{3D} which uses explicit finite difference method. Geometry is modelled to match the exact conditions as measured in the laboratory tests, cf. Tab. 1.

As the geometry is symmetrical, only a half of the test setup is created. At first, the soil is generated and the volume near the pile is meshed into smaller elements as the stresses have greater variation in these zones. To have correct model conditions an interface is generated at the soil-pile interaction. This allows separation and sliding between two materials. These elements are attached to the face of a soil surface. On the appearance of contact with the pile each interface node characterizes sliding properties, normal and shear stiffnesses between the materials. The pile is embedded to the soil after generating all the elements. A number of around 6500 elements is used in the model, as this number was found to be appropriate by convergence tests. Final model geometry is shown in figure 1.

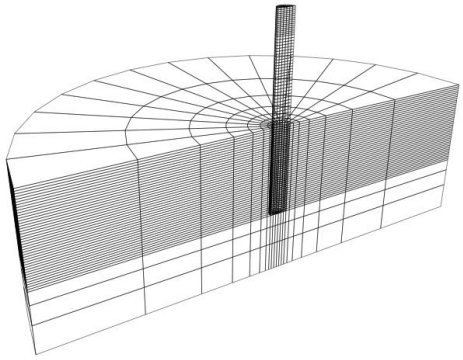

Figure 1. Final model geometry

A solid pile is used instead of a hollow to simplify the model; therefore equivalent Young's modulus and density have to be used.

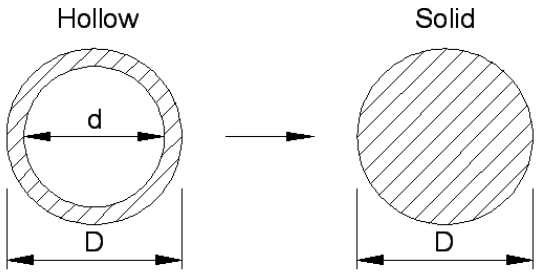

Figure 2. Hollow and solid pile cross-sections

$$E_{solid} = \frac{E_{hollow} \cdot I_{hollow}}{I_{solid}} \qquad (1)$$

$$\rho_{solid} = \frac{\rho_{hollow} \cdot A_{hollow}}{A_{solid}} \qquad (2)$$

The Poisson's ratio (ν = 0.33) and hence the shear stiffness for aluminium are not scaled due to negligible effect to the results.

Interface properties have a great influence to the results. They are described by the following parameters given in table 3. These values of the parameters were chosen so that numerical load-displacement curves would show the best approach to the experimental.

Friction angle	φ_{tr} [˚]	36.8 – 38.7
Cohesion	c_{int} [kPa]	0.001
Dilation angle	ψ_{tr} [˚]	0
Normal stiffness	k_n [MPa]	100 x E_0
Shear stiffness	k_n [MPa]	100 x E_0

Table 3: Interface properties

The friction angle is calculated by formula 3, where φ_{tr} is the internal friction angle for sand.

$$\varphi_{tr}' = \tan^{-1}\left(2/3 \cdot \tan(\varphi_{tr})\right) \qquad (3)$$

Mohr-Coulomb material model with tension cut-off is used to represent relations in the sand. This model describes the soil stress-strain behaviour in an elastic-plastic state. The elastic part is described by Hooke's law whereas in the plastic part the strain is described as a sum of elastic and plastic strains. An elastic, isotropic model is used for the monopile. In this case, stress-strain relationship is described by the Hooke's law. Null model is used for the rest of the volume – the part above the soil. In this type of material stresses are automatically set to zero.

Boundary conditions are modelled to match the real conditions in the tank. Three different conditions are assigned to different parts of the model, cf. Fig 3.

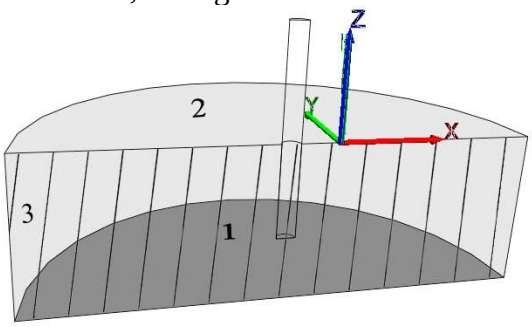

Figure 3. Model boundaries: 1-bottom of the pressure tank, 2- pressure tank walls, 3-symmetry plane

All nodes in the bottom of the model (1) are fixed in x, y and z directions. Nodes in vertical part which simulate the pressure tank walls (2) are fixed in x and y directions. Nodes in the symmetry plane (3) are fixed in the y direction.
Initial conditions are assigned by applying densities, gravity loading and overburden pressure for model elements. The horizontal pressure is defined by use of the coefficient of horizontal earth pressure at rest K_0=1-$sin(\varphi_{tr})$, valid for normally consolidated soil.

As in the laboratory tests the deflection is applied to the pile instead of the force. Velocity is applied to the nodes at 370 mm height above the soil surface. It is increased slowly to avoid any dynamic response in the model which would make the inertia effects dominant. A steady-state response is achieved in the system by using more than a million time steps.

To ensure quasi-static solution of the model, motion equations have to be damped. Significant uniform motion is apparent as velocity loading is applied and the velocity will not change sign in most of the nodes. Therefore the combined damping is used. In this mechanism damping depends on the unbalanced force sign variation and it is more appropriate for rigid-body motion systems.

Bending moments, *M*, are calculated at different levels of embedded pile by formula:

$$M = \sigma_{zz,i} \cdot A_i \cdot x_i \qquad (4)$$

Where $\sigma_{zz,i}$ is the vertical normal stress for element *i*, A_i is the area of the element *i*, x_i is the x coordinate of the center of element *i*.
The soil resistance along the pile, p_x, is calculated by equation:

$$p_x = \int T_x dC \qquad (5)$$

Where T_x is the x-component of the total stress and *C* is the pile circumference.

3.2 **Plaxis 3D 2010 modelling procedure**

Plaxis 3D 2010 is a commercial three-dimensional finite element program used to perform deformation and stability analysis for various types of geotechnical structures such as foundations. The program uses a convenient graphical user interface that enables users to generate a model quickly and easily.

Plaxis 3D is an implicit element solver relating forces and displacements by demanding equilibrium in every point in the model. From the equations of equilibrium the weak formulation of the continuum problem is obtained by means of virtual work. In contrast to FLAC^{3D}, Plaxis 3D is a static solver, meaning that inertial forces are omitted.

The generation of a three-dimensional finite element model is based on the small-scale model geometry. The program, in contrast with FLAC^{3D}, does not allow using symmetry simplifications and moreover, does not allow curved outer boundaries, only square boundaries. Therefore a whole model has been created.

The monopile is modelled as a closed-ended hollow pile, as the monopile used in the laboratory, with the geometry shown in table 1.

For the soil volume, the outer boundaries of the model are set to the dimension of the soil volume in the pressure tank. Hence, the side length is 2.10 meters and the depth of the soil is set to 0.58 meters. The lateral load is applied as a punctual load in the centre of the cross section of the top pile and the overburden pressure is simulated as a distributed load in all surface area of the model. In figure 5 the mesh of the small-scale model can be appreciated for test number 7.

Along all boundaries Plaxis 3D automatically imposes a set of fixities corresponding to a free ground surface and a fully fixed bottom. All vertical boundaries are fixed in the direction of their normal.

The structural surfaces of the monopile are modelled as plates, which are 6-noded wedge triangle elements with 6 degrees of freedom in each node, i.e. three translational and three rotational degrees of freedom. These plates allow the shearing, bending and axial deformation. The top and bottom plates are created with higher thickness than the mantle of the cylinder to avoid transversal deformations when the lateral load is applied.

In Plaxis 3D 2010, 3 different Material models have been employed to model and analyze the small-scale tests.

A traditional Mohr Coulomb failure criterion with tension cut-off is used for the small-scale models since the same material model is employed in FLAC^{3D}. Furthermore, Hardening soil and Hardening soil small strain models are employed in order to compare the effect of more advance material models.

Mohr Coulomb model with tension cut-off describes perfectly elastic-plastic soil behaviour and no tension is allowed for the soil. Further explanation is given in Appendix I.

The soil elements are generated by means of 10-noded tetrahedral elements. This type of element has three translational degrees of freedom in each node. The program offers a three-dimensional mesh generation feature, which can be carried out for various mesh densities in different surfaces. A convergence test is made in order to establish the optimal density mesh with which the horizontal displacement remains constant if the density mesh increases.

Interfaces are attached to the plate elements for an accurate interaction of the soil-structure behaviour. To each interface the program assigned a 'virtual thickness', which is used to calculate the stiffness properties of the interface. However in the finite element formulation, the coordinates of each node pair are identical, which means that the element has a zero thickness. Hence, a pair of nodes is found with the same coordinates. Interfaces are composed of 12-node interface elements. Interface elements consist of six pairs of nodes, compatible with the 6-noded triangular side of a soil element or plate element. Each node has three translational degrees of freedom and it is numerically integrated using 3 point Gauss integration. The aim of these interface nodes is to allow slipping and gapping by means of differential displacements between the node pairs.

The interface stiffness and strength can be defined depending on the kind of analysis, and it is controlled by the parameter $R_{inter.}$ In general, for real soil-structure interaction the interface is weaker and more flexible than the surrounding soil, which means that the value of R_{inter} should be smaller than 1. However, it is possible to find a suitable value of R_{inter} by the following relationships, cf. Eq. 6 to 8:

$$\tan(\varphi_i) = R_{inter} \cdot \tan(\varphi_s) \qquad (6)$$

$$E_i = R_{intern}^2 \cdot E_s \qquad (7)$$

$$G_i = R_{intern}^2 \cdot G_s \qquad (8)$$

Where:

φ_i	Friction angle of the interface [°] Obtained by equation 3
φ_s	Friction angle of the soil [°]
E_i	Young's Modulus Interface [kN/m^2]
E_S	Young's Modulus soil [kN/m^2]
G_i	Shear Modulus interface [kN/m^2]
G_S	Shear Modulus soil [kN/m^2]

According to equation 6, a value of R_{inter} is calculated for every test since it changes with different frictions angles. The coefficients of earth pressure at rest, $K_{0,X}$ and $K_{0,Y}$ are also determined for every test, cf. Tab. 4. Plaxis 3D requires an input value for cohesion, even if the soil is considered cohesionless, therefore a very small value is introduced.

Test no.	R_{inter} interface	Poisson's ratio	Cohesion [kPa]	K_{0X} , K_{0Y}
1	0.4664	0.23	0.001	0.2349
2	0.4223	0.23	0.001	0.2045
3	0.5122	0.23	0.001	0.2656
4	0.4946	0.23	0.001	0.2538
5	0.5455	0.23	0.001	0.2872
6	0.5415	0.23	0.001	0.2847
7	0.5440	0.23	0.001	0.2863

Table 4: Specific input mechanical parameters for Mohr Coulomb models in Plaxis 3D

When the interface is elastic, both slipping (relative movement parallel to the interface) and gapping or overlapping (i.e. relative displacements perpendicular to the interface) can be expected to occur.

Therefore interfaces are created around the mantle of the cylinder and in the bottom of the pile, to simulate the toe-kick effect that appears due to the rigid motion of the non-slender pile. Figure 4, shows the interface surrounding.

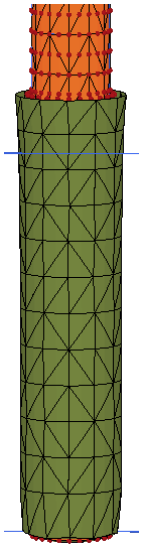

Figure 4. Interface (green mesh) attached to the monopile. The interface is surrounded only in the embedded part of the pilel

In the calculation stage, the K_0-procedure is employed. The initial vertical stresses are computed using the submerged unit weight. The horizontal stresses are computed using the coefficient of horizontal earth pressure at rest, $K_0=1-sin(\varphi_{tr})$ for normally consolidated soil. Following the initial phase, a second phase, called the installation phase, is initiated. In the installation phase the foundation is

"constructed", the plate and interface surfaces are activated. The 3rd phase involves the creation of the distributed load on the soil surface (cf. Figure 5 for the model in phase 3 with the overburden pressure applied.), which corresponds to the overburden pressure simulation. Afterwards the lateral load is applied in the centre of the top plate of the pile. The load is applied using different load intervals, and each interval corresponds to a different phase.

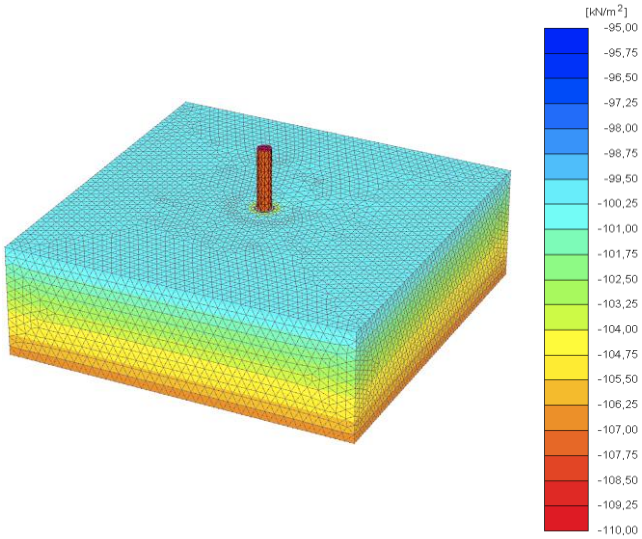

Figure 5. Plaxis 3D Model boundaries, test 7 P_0=100kPa. Total stresses in z-direction

4 Comparison of FLAC^{3D} and Plaxis 3D

Seven different tests have been conducted by means of FLAC^{3D} and Plaxis 3D using the Mohr-Coulomb material model. Obtained results from both models are compared including load-displacement relationship, bending moment distribution, pile deflection and soil resistance along the embedded pile length, as well as the *p-y* curves. Only a comparison of one of the test results is presented, which is representation for the other tests, that can be found in the Appendix H.

In order to see if the models follow the conditions in the small scale tests in the laboratory, load – displacement curves at the force application level of the pile are compared cf. Fig. 6. Both models show disagreement with the experimental test, but FLAC^{3D} shows a better approach as the displacement for the same load is observed closer to the experimental.

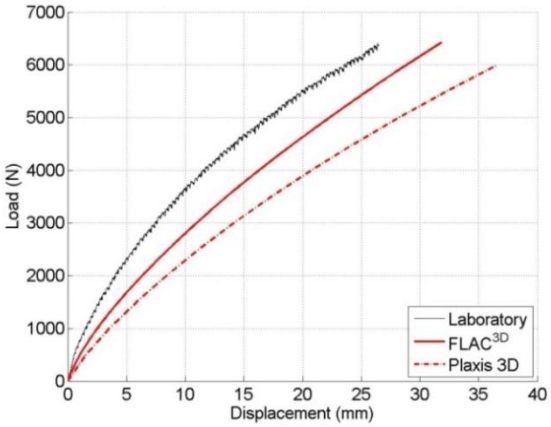

Figure 6. Load – displacement at force application level for test 5

Bending moment distribution shows similar behaviour – the peak moment values are located in the same depth and are found closer to the soil surface with higher force applied, cf. Fig. 7. However there is a mismatch in the bending moment values. Same as in load - displacement stiffer soil behaviour was appreciated by the FLAC^{3D}.

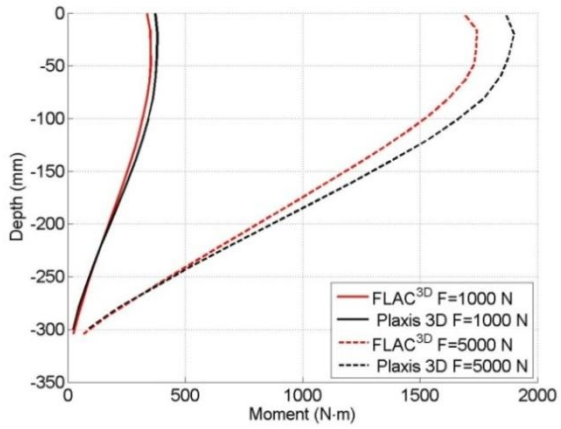

Figure 7. Moment distribution along the embedded pile length for test 5

Both models prove a rigid-body motion with a zero displacement point at the same depth, cf. Fig 8. However, same as in the bending moment distribution uncertainties are found regarding the displacement values.

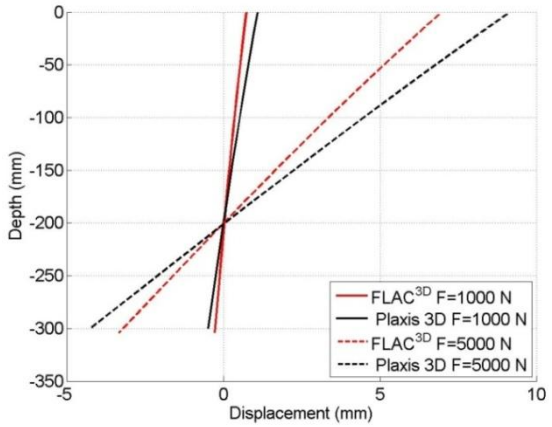

Figure 8. Displacement distribution along the embedded pile length for test 5

Soil resistance distribution along the embedded pile length is presented in the figure 9. A good match of the curves is found when the pile experiences a small load in contrast with the curves obtained when the pile experiences bigger load, where uncertainties are found in the first 100 mm of the soil. In Plaxis 3D the curve reaches the maximum of 100 N/mm, while FLAC^{3D} shows 140 N/mm for the same depth.

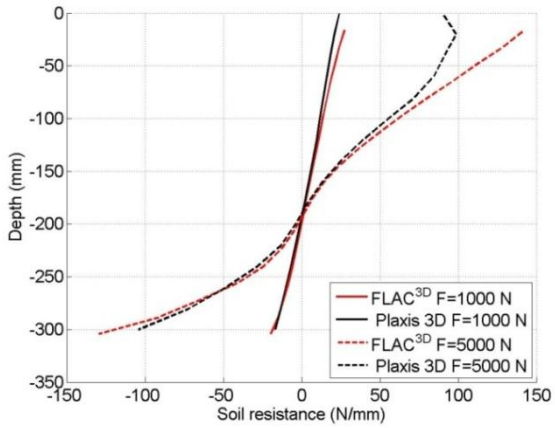

Figure 9. Soil resistance distribution along the embedded pile length for test 5

This is in accordance with the *p-y* curves, cf. Fig. 10. In the shallow depths of the soil, where the soil resistance is close or equal to ultimate resistance, the difference between the values is high and it decreases with the depth. Moreover the initial subgrade reaction modulus is found to be smaller in the Plaxis 3D model. Due to these reasons, more conservative results are appreciated by Plaxis 3D in the previous plots.

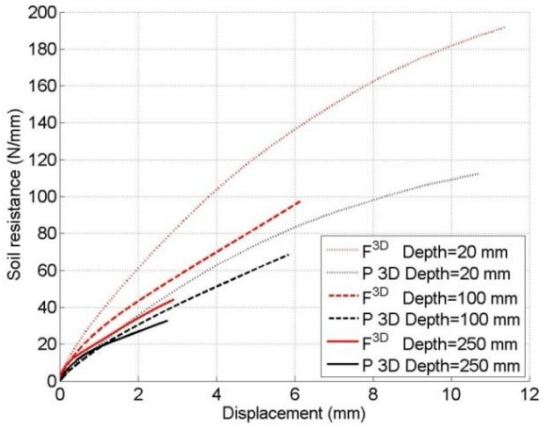

Figure 10. *p-y* curves for test 5

In general, it was found that using Mohr-Coulomb constitutive models in Plaxis 3D and FLAC^{3D} gives overestimated results; due to the fact that Young's modulus is not stress dependant and only initial value (E_0) is used for the whole stress-strain curve.
Even though the same material model (Mohr-Coulomb) and input parameters were used, significant difference is observed between the programmes.
It was found that Plaxis 3D has more underestimated results than the FLAC^{3D} especially with higher forces applied. This is because FLAC^{3D} model shows stiffer behaviour due to the higher values of the soil resistance in the *p-y* curves, especially in the shallow soil depths.

5 Comparison of Mohr-Coulomb, Hardening Soil and Hardening Soil Small Strain models

5.1 Introduction to material models

As it was found in the previous section, using Mohr-Coulomb material model gives high uncertainties. Therefore it is in the interest to analyse if other material models would give better results.

Three different material models have been employed in Plaxis 3D to model the small-scale tests and analyse the load-displacement behaviour using the experimental load-displacement relationship as a referent. Three Material models are: the traditional Mohr-Coulomb model, Hardening soil model and Hardening soil small-strain model. It is considered drained conditions in all the simulations. The basic principal difference between Mohr coulomb and the hardening soil models can be appreciated in figure 11.

The Mohr-Coulomb model is a linear-elastic, perfect plastic model (blue line) and the Hardening Soil model describes work curve of the soil in a more realistic manner (red curve).

In contrast to an elastic perfectly-plastic model, the yield surface of a hardening plasticity model is not fixed in principal stress space, but it can expand due to plastic straining.

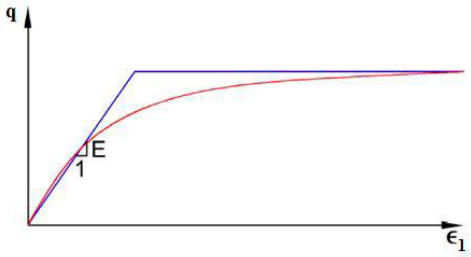

Figure 11. Basic difference between Mohr Coulomb (Blue line) and Hardening soil (Red curve) models

Mohr-Coulomb model does not take into account stress dependency or stress path dependency on stiffness. The model considers the initial Young's Modulus constant and independent of the variation of effective stresses. In contrast, the Hardening soil small strain model incorporates strain dependence on stiffness modulus, simulating the different reaction of soils from small strains. In the loading and unloading, the strain range in which soils can be considered truly elastic (i.e. where they recover from applied straining almost completely) is very small. With increasing strain amplitude, soil stiffness decays nonlinearly.

The parameters used for the Mohr Coulomb model are specified in table 2, where the Young's Modulus employed is E_0. Same parameters are used in the Hardening soil model and Hardening soil small strains model with additional parameters in table 5.

Test no.	E_{50}^{ref} [kN/m^2]	E_{ur}^{ref} [kN/m^2]	m [-]	E_{oed}^{ref} [kN/m^2]
1	57235	171706	0.58	44027
2	53812	161438	0.58	41394
3	45840	137521	0.58	35262
4	48061	144184	0.58	36970
5	44386	133160	0.58	34143
6	47840	143520	0.58	36800
7	46609	139828	0.58	35854

Table 5: Specific input mechanical parameters for Hardening soil models in Plaxis 3D

Where:

E_{50}^{ref}	Secant stiffness in standard drained triaxial test	[kN/m^2]
E_{ur}^{ref}	Unloading/reloading stiffness	[kN/m^2]
E_{oed}^{ref}	Tangent stiffness for primary oedometer loading	[kN/m^2]
m	Power for stress level dependency on stiffness	[-]

The Hardening soil small strain models have extra parameters for the small strain stiffness cf. Tab. 6.

Test no.	G_0^{ref} kN/m^2]	$\gamma_{0,7}$ (10^{-5}) [-]
1	82454	28,4
2	82354	21,7
3	82104	27.63
4	82177	27.87
5	82057	35.95
6	82170	35.97
7	82130	35.96

Table 6: Additional input mechanical parameters for Hardening soil small strains models in Plaxis 3D

Where:

G_0^{ref}	Reference shear modulus at very small strains	[kN/m^2]
$\gamma_{0,7}$	Shear strain at which	[-]
G_s	Secant shear modulus $G_s = 0{,}722 G_0$	[kN/m^2]

For further details of Hardening soil and Hardening soil small strain model employed, a deeper explanation of the theory and the procedure for obtaining the parameters of the model is written in Appendix I.

5.2 **Load-Displacement relationship**

In order to validate the results obtained by Plaxis 3D, the load-deflection relationships are plotted within the experimental results. In figure 12 load-displacement curves from 2 different numerical approaches with different material models are compared with experimental.

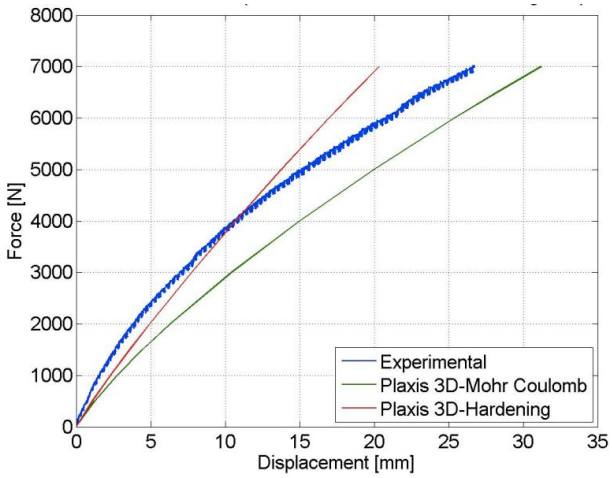

Figure 12. Comparison load-displacement curves for the 2 different material models, test 4

Analysing the graph, the load-displacement relationship obtained using the Mohr-Coulomb model tends to underestimate the load, giving a higher lateral displacement; hence the Young's modulus of the soil is smaller than the real stiffness of the soil in the small-scale test at the laboratory.

However, when the Hardening soil material model is employed, the load-deflection relationship fits better the experimental results, especially in the first half of the loading. In the second half of the loading, the model tends to overestimate the soil stiffness, giving less ultimate lateral displacement. This behaviour occurs due to the fact that in the Hardening soil material model, the values of Young's modulus has a dependence on the stress-strain state, cf. Fig. 13.

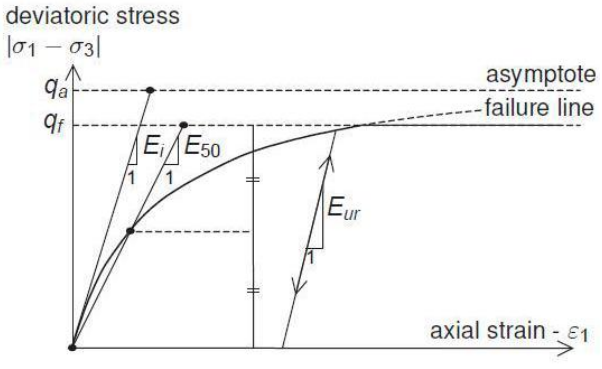

Figure 13. Young's modulus dependency on stress and strain (Plaxis 3D manual)

Therefore at the beginning of the loading, small strain and stress gives a more accurate value of Young's modulus. However, with high stresses and strains the Young's modulus becomes higher, causing the soil to be stiffer and smaller values of the lateral displacement.

In figure 14, the Young's Modulus distribution of unloading and reloading, E_{ur}, is plotted for the last phase of test number 4, when the entire load has been applied.

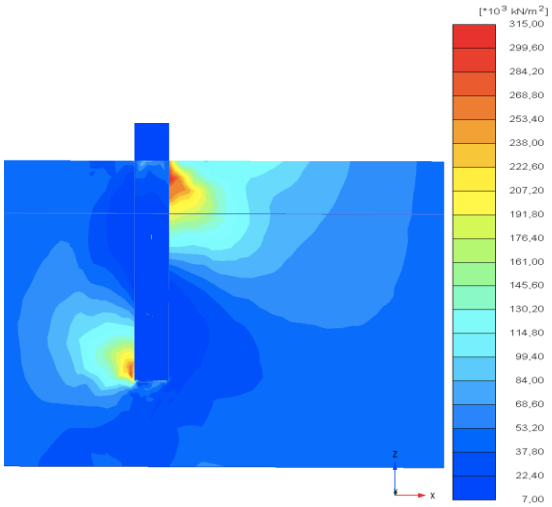

Figure 14. Young's modulus distribution of unloading and loading in test 4

It is important to highlight the increment of the Young's Modulus when the pile deflection creates high levels of stress and strain. In test number 4 the input parameter of Young's Modulus of unloading and reloading referent, E_{ur}^{ref} is calculated as 3 times E_{50}^{ref} giving a value around 144 MN/m^2.

As it can be appreciated in the figure 14, when the total load is applied the values of E_{ur} are much higher than the E_{ur}^{ref}, around 315 MN/m^2 in the areas of maximum stress, giving higher values of Young's Modulus. Therefore it is proved that due to the stiffness dependency on stress-strain path, the Hardening soil model provides higher values of Young's Modulus for high stress-strain paths. Hence, the result is a stiffer soil in the model than in the experimental case, reason for why the numerical load-displacement graph shows for the same force slightly smaller displacement than the experimental curve.

When the Hardening soil small strains model is employed, cf. Fig. 15, the results are slightly better compared to the other 2 models, since the improved stiffness of the soil for small strains in the beginning of the loading.

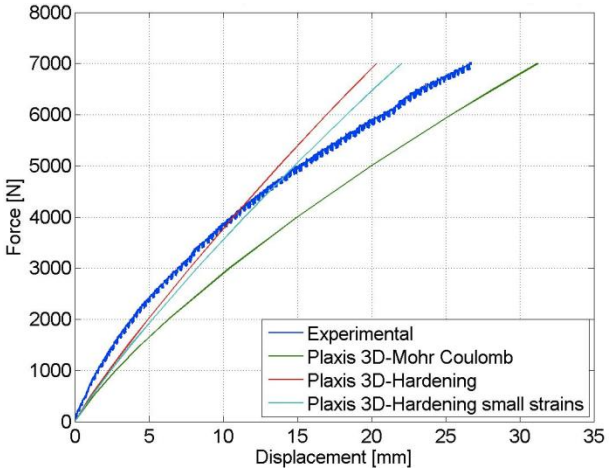

Figure 15. Comparison load-displacement curves for the 3 different materials models, test 4

However, the model still does not fit properly the experimental curve, as the Young's modulus has a big dependency on high stress-strain level. Nevertheless, the results can be considered accurate compared to the experimental results, since it is not expected to obtain exactly the same path of load-displacement due to the uncertainties while conducting the laboratory tests and obtaining the mechanical soil parameters.

For a better understanding of Hardening small strains model, figure 16 shows nonlinear decay of the soil stiffness, with higher strain amplitude. Plotting soil stiffness against *log* (strain) yields characteristic "S-shaped" stiffness reduction curves.

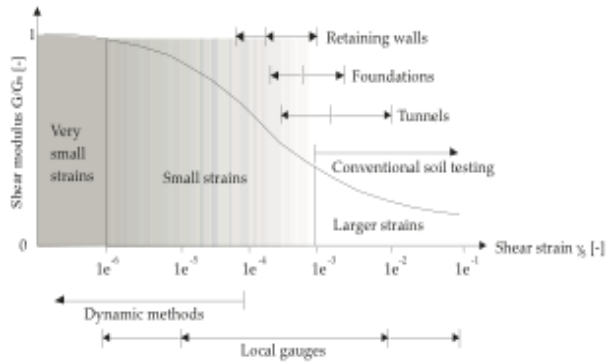

Figure 16. Characteristic stiffness-strain behaviour of soil with typical strain ranges for laboratory tests and structures. Plaxis 3D manual (2010)

Observing the characteristic shear strains it turns out that at the minimum strain which can be reliably measured in classical laboratory tests, i.e. triaxial tests (γ_s around $1e^{-4}$), soil stiffness is often decreased to less than half its initial value.

Therefore Hardening soil small strains model takes into account very small soil stiffness and it shows non-linear dependency on strain amplitude.

With this improvement it is expected that analysing the load-displacement graph for very small strains, the Hardening small strain model gives higher values of stiffness than the Hardening material model. In figure 17 the load-deflection curve is zoomed-in in the zone of small displacements, in order to be able to see if what it has been explained can be observed in the model.

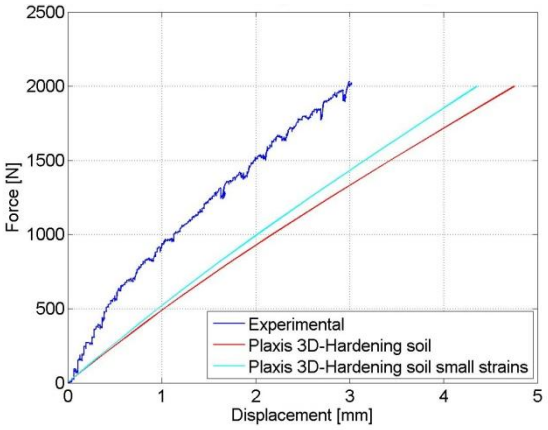

Figure 17. Zoom of the small lateral displacement zone in test number 6

As it was expected, the Hardening soil small strains gives smaller lateral displacement compared to the Hardening soil, when the soil is in low stress-strain state, cf. Fig. 17 and 18 respectively.
The behaviour observed in tests number 4 and 6 is representative for the other tests, cf. Appendix H.

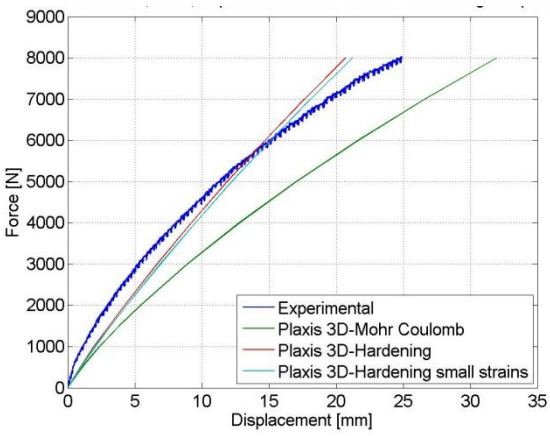

Figure 18. Comparison load-deflection curves for the 3 different materials models, test 6

In conclusion, the Mohr-Coulomb model seems to be simple model to simulate the soil behaviour. It is computationally light and

recommended when conducting an initial numerical analysis of soil behaviour. It is a first order model that does not take into account stress dependency or stress path dependency on stiffness. The model describes the failure state quite well when using effective values, friction angle and cohesion, but is insufficient when the load-displacement is compared with the experimental results.

The Hardening soil model becomes more realistic and accurate, since the model describes a better approach of the work curve. However it is important to take into account the stiffness dependency on stress-strain path, which could result too high values of Young's Modulus.

As an improvement of the Hardening soil model, the Hardening soil Small strains model gives better results in the beginning of the loading, due to the better approach in the small stress-strain path. However, the models do not offer a great difference when compared to the Hardening soil model but still are slightly better. Perhaps in another kind of simulation, where not so high strain values are reached, the Hardening soil small strain model could provide a better approach.

6 Calibration of small-scale tests

It is in the interest to compare results obtained numerically and experimentally. It was chosen to compare FLAC^{3D} models as they showed better approach than Plaxis 3D. However it was found in section 4 that laboratory tests and FLAC^{3D} models do not follow the same conditions as the load-displacement curves do not fit. In order to be able to compare the results, calibration of the tests has to be done, which is based on changing soil parameters until the load-displacement curves match (values of E_0 and φ_{tr} are regulated). Increasing the elasticity modulus calls bigger values of horizontal load for the same displacement and increasing the friction angle decreases the curve asymptote. In figures 19 and 20 the numerical and experimental load-displacement curves at different load transducer levels (265 mm, 370 mm, 480 mm) for test 5 are presented before and after the calibration respectively.

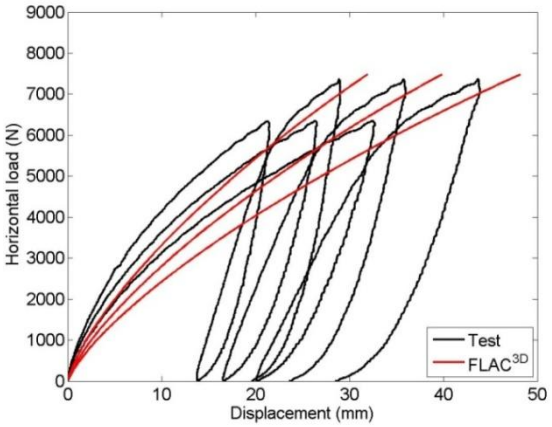

Figure 19. Load-displacement curves before calibration for test 5

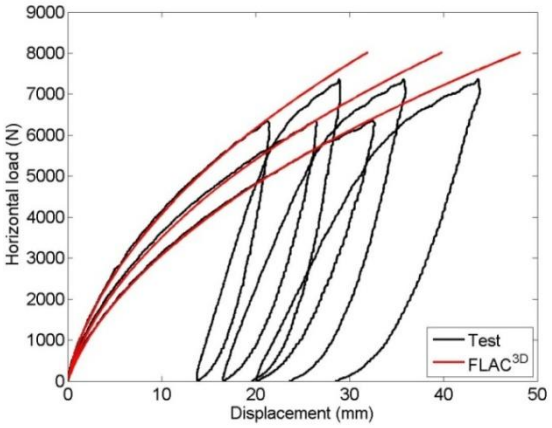

Figure 20. Load-displacement curves after calibration for test 5

The soil parameters after models calibration are given in the table 7.

Test no.	φ_{tr} [°]	E_0 [MPa]
Test 1	40.00	48.00
Test 2	40.00	7.00
Test 3	33.00	62.00
Test 4	35.00	49.00
Test 5	38.00	59.00
Test 6	36.00	60.00
Test 7	40.00	58.00

Table 7: Calibrated soil properties for each test

After the models have been calibrated, results from different tests are compared in the following sections.

6.1 **Evaluation of lateral deflection**

Deflection of the embedded pile is computed, when the displacement of the pile at 370 mm above the soil surface is 10 mm and 35 mm. The deflections along the pile length are plotted at the different overburden pressure levels. As it is seen in lateral deflection plots, cf. Fig. 21, the pile behaves rigidly as the rotation point changes very slightly, even though more flexible pile behaviour is observed with greater pressure levels.

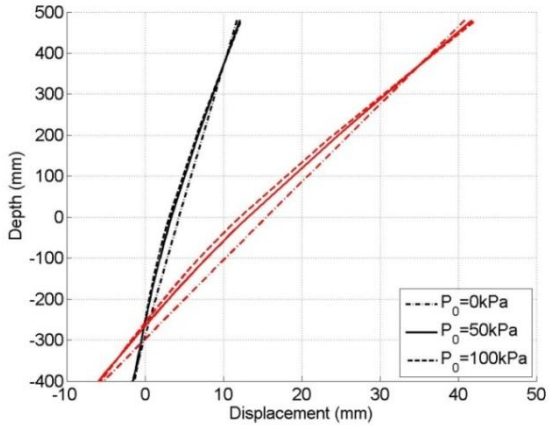

Figure 21. Lateral pile deflection with depth for different P_0, when the displacement of the pile at 370 mm is 10 mm (black) and 35mm (red)

For higher slenderness ratios the pile rotation point tends to increase in depth, moreover the pile shows more flexible behaviour, cf. Fig. 22.

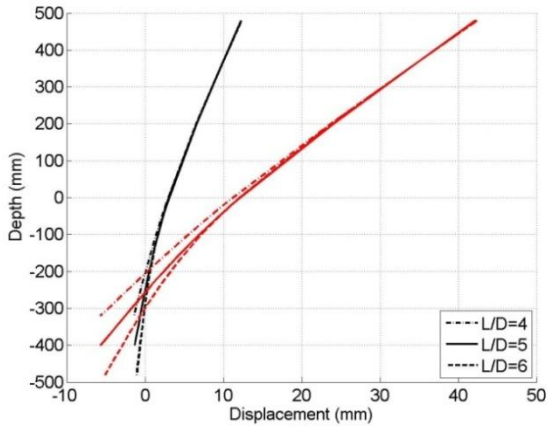

Figure 22. Lateral pile deflection with depth for different slenderness ratios, when the displacement of the pile at 370 mm above the soil surface is 10 mm (black) and 35 mm (red)

6.2 **Evaluation of bending moments**

Like the deflection, the bending moment distribution is computed along the pile length. Results are plotted in figure 23. It is observed that the maximum bending moment position is different in all the tests and is dependent on the overburden pressure. With higher values of the pressure, the maximum bending moment is located closer to the soil surface.

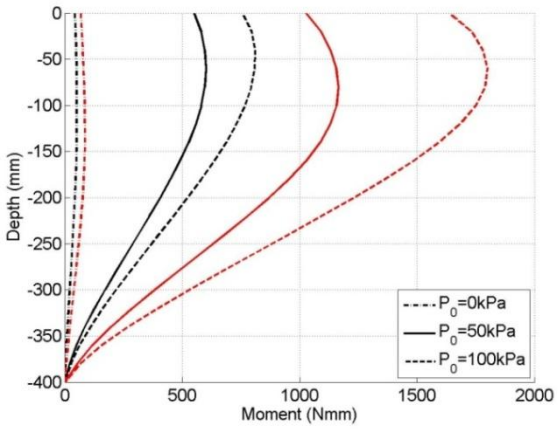

Figure 23. Bending moment distribution with depth for different overburden pressures, when the displacement of the pile at 370 mm above the soil surface is 10 mm (black) and 35 mm (red)

In figure 24 bending moment distribution of different pile slenderness ratios are shown. As slenderness ratio becomes higher, larger bending moment values are observed and the peaks of the curves tend to be deeper in the soil.

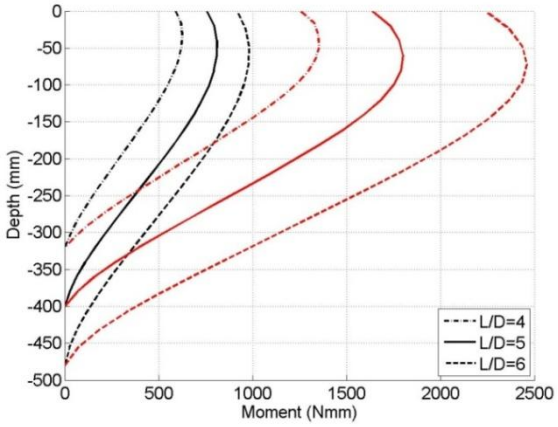

Figure 24. Bending moment distribution with depth for different slenderness ratios, when the displacement of the pile at 370 mm above the soil surface is 10 mm (black) and 35 mm (red)

6.3 Evaluation of *p-y* curves

In figures 25 to 28 the soil resistance and *p-y* curves are plotted for different pressure levels. It can be noted that for the test without overburden pressure the maximum soil pressure is located at the depth of approximately 150 mm. And the initial stiffness at this level tends to increase respectively. At next range up to the rotation point the soil pressure tends to decrease with the depth as well as the initial subgrade reaction modulus (E^*_{py}). At the last part until the pile foot soil resistance and E^*_{py} tend to increase with the depth.

$$E^*_{py} = \left.\frac{dp}{dy}\right|_{y=0} \qquad (9)$$

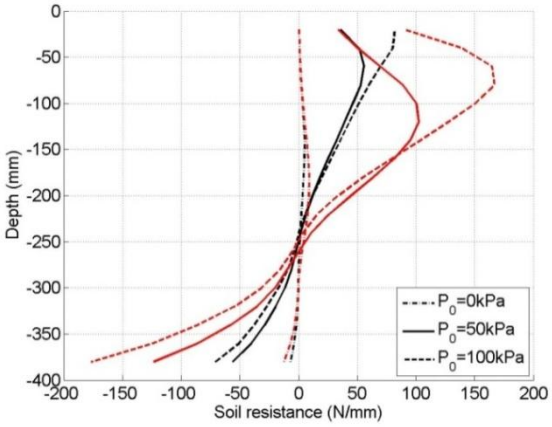

Figure 25. Soil resistance distribution with depth for different overburden pressures, when the displacement of the pile at 370 mm above the soil surface is 10 mm (black) and 35mm (red)

In the tests with overburden pressures the soil pressure tends to decrease from the soil surface to the pile rotation point and increase from that point up to the pile foot. Respectively does the E^*_{py} so it shows that the E^*_{py} depends of the stress state.

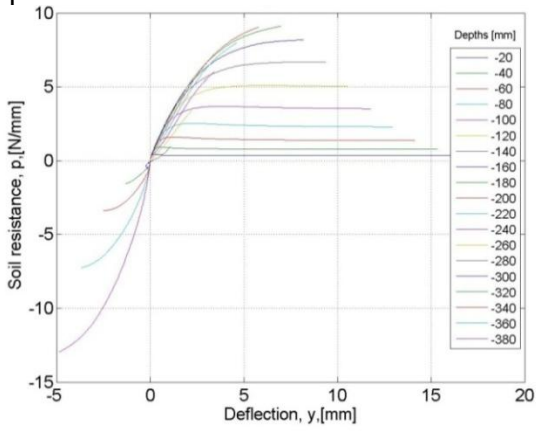

Figure 26. *p-y* curves test 2 (P_0=0 kPa)

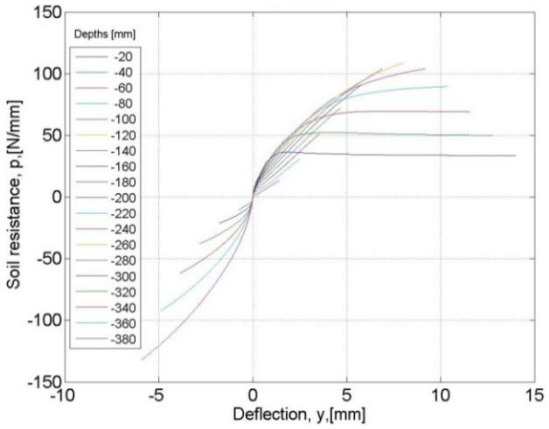

Figure 27. *p-y* curves test 3 (P_0=50 kPa)

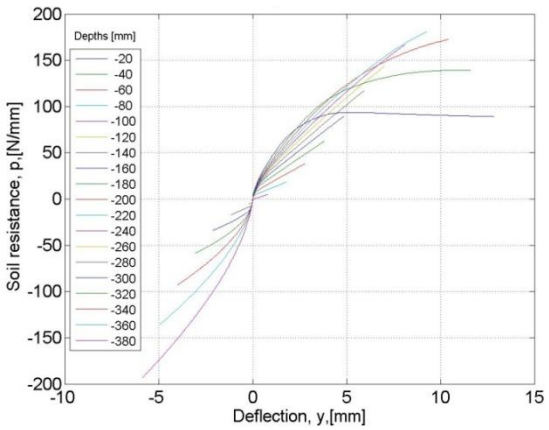

Figure 28. *p-y* curves test 6 (P_0=100 kPa)

7 Experimental and numerical results of small-scale tests

The purpose of this section is to compare the numerical (FLAC^{3D}) and experimental results and make the conclusions if the small scale tests and numerical models work by same principles. This is done by comparing the depth-deflection, moment distribution and *p-y* curves from different tests.

Numerical models are calibrated by means of experimental tests, which are described in section 6. Therefore, no comparison of load-deflection plots between experimental and numerical methods are carried out.

7.1 Evaluation of bending moments distribution

The bending moments obtained by FLAC^{3D} are compared to the ones obtained from the small-scale tests in the laboratory. In figure 29 the results without the overburden pressure are presented.

In this case the bending moments do not match, especially with smaller loading values. However, the peaks of the curves are observed at same depths for both numerical and experimental work results. In this case the biggest uncertainty is that as the friction angle, φ_{tr}, is highly dependable on the stress level and the density index, I_D, which were calculated from the CPT's.

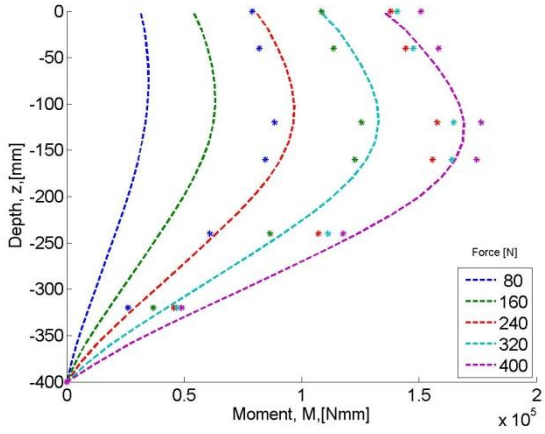

Figure 29. Moment distribution along depth at different force levels for test 2 (dots represent the results from the experimental tests)

In the tests with overburden pressure the moment curves fit much better – the shape and the peaks of the curves are similar, cf. Fig. 30 to 31. The maximum bending moment position is different in all the tests and is dependent on the overburden pressure. Both numerical and experimental results show that with higher values of the pressure, the maximum bending moment is observed closer to the soil surface due to the increase of the soil resistance.

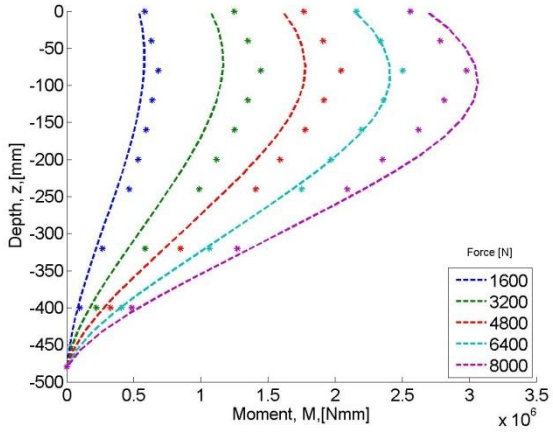

Figure 30. Moment distribution along depth at different force levels for test 4 (dots represent the results from the experimental tests)

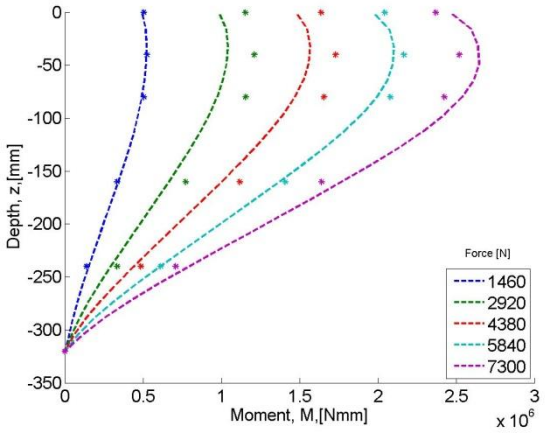

Figure 31. Moment distribution along depth at different force levels for test 5 (dots represent the results from the experimental tests)

7.2 Evaluation of deflection distribution

Pile deflections along the depth obtained by FLAC^{3D} and the small-scale tests are compared. However, same as in the bending moment comparison, disagreements are found in the test without the overburden pressure, cf. Fig. 32. In this instance neither the rotation angle of the pile, nor the pile rotation point match.

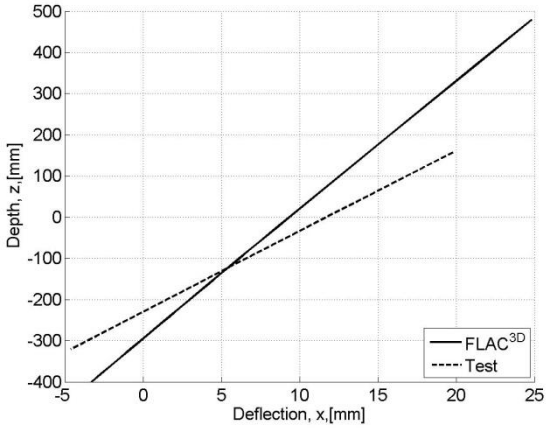

Figure 32. Deflection distribution along depth at maximum force for test 2

The deflection plots fit better in the tests with the overburden pressure as the deflection values, pile rotation points and the pile rotation angles are similar, cf. Fig. 33 to 35.

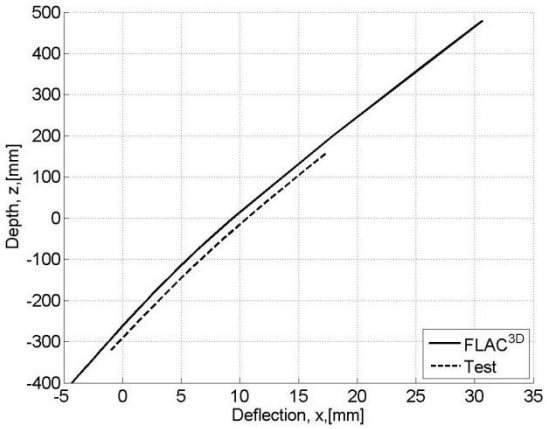

Figure 33. Deflection distribution along depth at maximum force for test 3

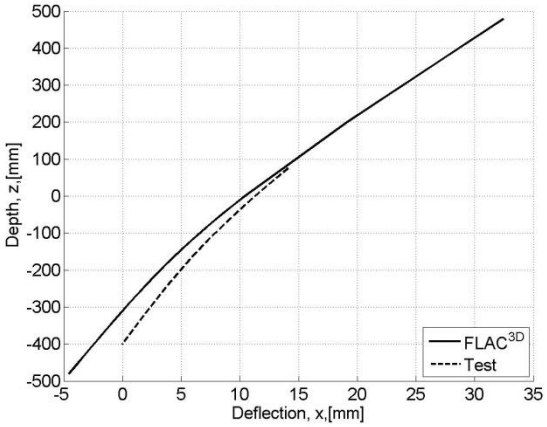

Figure 34. Deflection distribution along depth at maximum force for test 4

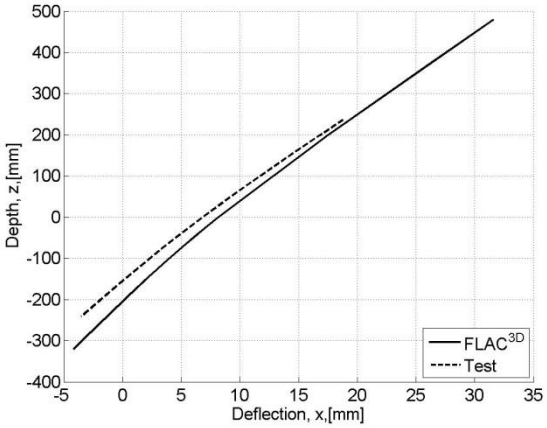

Figure 35. Deflection distribution along depth at maximum force for test 5

Although some uncertainties are observed in the comparison, the results are considered to be reasonable; therefore following remarks can be made.

The deflection of the pile consists of a rigid body motion. The pile rotates around a zero deflection point. More flexible behaviour inside the rigid limits can be observed with an increase of the pressure or the slenderness ratio.

7.3 Evaluation of *p-y* curves

The *p-y* curves obtained by FLAC^{3D} are compared to the ones obtained from small-scale tests in the laboratory. Although the shape and the distribution along the depth of the curves are correct, there is no reasonable relation between the curves in any of the tests, cf. Fig. 36 to 39. Soil resistance values from the experiments are lower compared to the ones obtained by numerical modelling and this difference gets higher as the overburden pressure level rises. The initial stiffnesses of the experimental curves are observed to be either higher than the FLAC^{3D} curves or lower without any reliance to the slenderness ratio or overburden pressure. This could be due to the mathematical and experimental errors while obtaining the experimental curves.

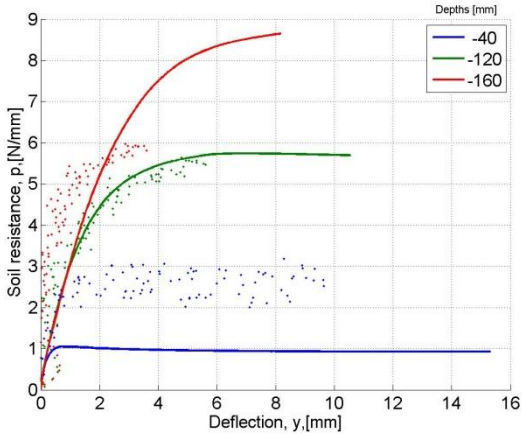

Figure 36. *p-y* curves for test 2

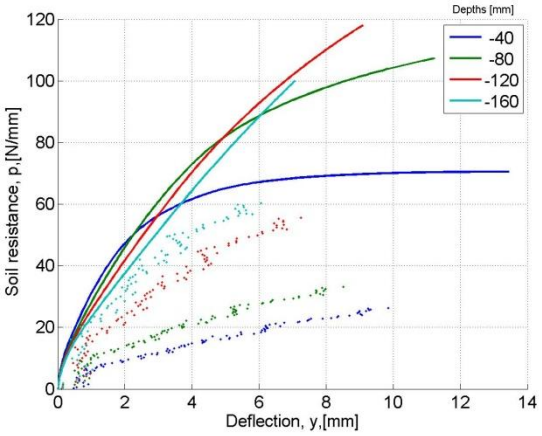

Figure 37. *p-y* curves for test 4

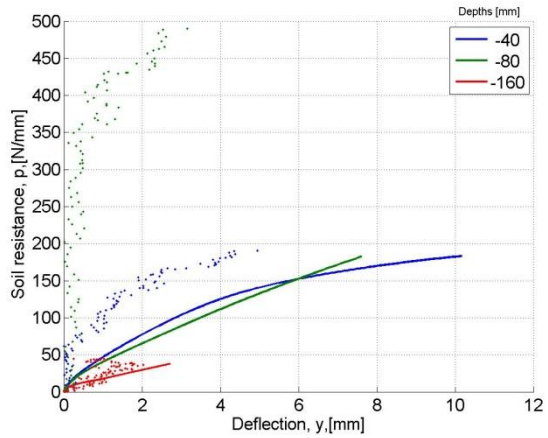

Figure 38. *p-y* curves for test 5

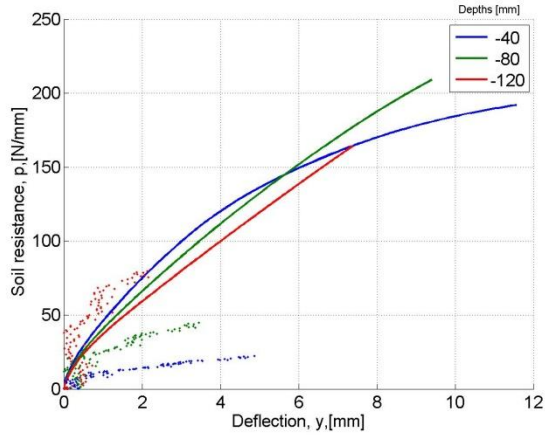

Figure 39. *p-y* curves for test 7

The comparisons show that in the tests with the overburden pressure bending moment distributions and depth-displacement plots match the FLAC^{3D} results well. As expected results show some uncertainties in the test without the overburden pressure as in this case the friction angle, φ_{tr}, is highly dependable on the stress level and the density index.

It is approved by both, the numerical and the experimental results that with higher values of the pressure, the maximum bending moment is observed closer to the soil surface due to the increase of the soil resistance.

The deflection of the pile consists of a rigid body motion. Even when the pressure and the slenderness ratio increase, the pile rotates around a zero deflection point. Therefore, the pile behaves more flexibly inside the rigid limits.

However the *p-y* curves show disagreement between the numerical and the experimental results in all the tests. As the curves obtained by the FLAC^{3D} have logical tends, it can be stated, that the experimental *p-y* curves are not reasonable.

8 Full Scale Models

It has been shown in Section 4 that FLAC^{3D} fits the experimental results better in comparison with Plaxis 3D. In order to see if these programs behave in the same way in the full-scale, a comparison of FLAC^{3D}, Plaxis 3D and additionally an ABAQUS model is presented.

Kellezi and Hansen (2003) have simulated a monopile foundation at Horns Rev subjected to static lateral load. The analysis was performed by means of the three-dimensional numerical program ABAQUS assuming drained soil conditions and Mohr Coulomb material model. The soil conditions, shown in table 8 have been also employed in Plaxis 3D and FLAC^{3D} in order to ensure the same conditions in all numerical models.

Depth (m)	E (kN/m^2)	γ' (kN/m^3)	φ (°)	ψ (°)	υ
1	31800	10	42	12	0.3
3.5	57100	10	43.5	13.5	0.3
5.5	52534	10	42.5	12.5	0.3
6.5	44100	10	41.7	11.7	0.3
7	58200	10	43.2	13.2	0.3
8.5	72170	10	44.3	14.3	0.3
10	52950	10	43.1	13.1	0.3
11.5	35400	10	40.3	10.3	0.3
12.5	23530	10	37.2	7.2	0.3
13.5	13600	10	33.8	3.8	0.3
20	3135	7	21.6	0	0.3
21	12950	7	31.2	1.2	0.3
42	36800	10	37.8	7.8	0.3

Table 8: Geometric and mechanical parameters for the soil after Kellezi and Hansen (2003)

All layers consist of sand except two layers of organic sand characterised by a small effective density and low strength, located at a depth from 13.5 to 21 meters.

The outer boundaries of the full-scale models in Plaxis 3D and FLAC^{3D} are used as it is in ABAQUS model. However, as the width of the soil is not given, it is determined to use the suggested values by Abbas et al. (2008) and in Sørensen et al. (2009). The width of the soil mass is set to 40 times the diameter of the pile and the bottom boundary is set to the last layer depth.
It is important for the full-scale model, that the bottom and vertical boundaries are locat-

ed in a distance from the foundations large enough to avoid interference with the failure zone around the foundation. If the boundaries interfered with the failure zone it would strengthen the soil. This issue has been examined; in conclusion, the purpose is that the chosen geometry does not pose any problems in the deformed mesh area.

The material model employed in the three numerical models is Mohr-Coulomb isotropic hardening/ softening, since it was employed by Kellezi and Hansen (2003) in the ABAQUS model. It is very important to ensure that the initial conditions are the same in all the different models in order to be able to compare the results.

The geometry and material properties for the pile are based on a preliminary pile design, which consists of a 4 m diameter and 22 m embedded pile length, composed for four different sections, cf. Fig. 40, with the following parameters:

E_{steel}	210E6	[kN/m^3]
γ_{steel}	78.5	[kN/m^3]
υ	0.3	[-]

Table 9: Mechanical parameters for the monopile after Kellezi and Hansen (2003)

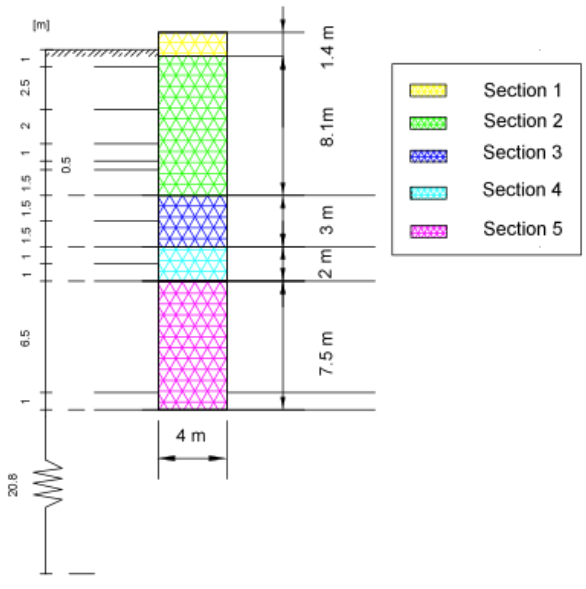

Figure 40. Full-scale monopile sections and distribution of the different layers of soil

The extreme static horizontal load is H = 2503 kN and the bending moment M = 84983 kNm are acting at the seabed level. In order to simulate the same conditions, in the models by means Plaxis 3D and FLAC^{3D}, a lateral force is applied with an eccentricity of 34 meters above the soil surface creating a moment of the same magnitude.

To be able to apply the load at that specific eccentricity, the pile is extended until 34 meters above the soil surface, giving low values of density to the extra section of the pile to make the weight of the foundation as low as possible, similar to the ABAQUS and Plaxis models. The stiffness of the extended pile section is used as in section 1.

In Plaxis 3D, the pile is modelled as a closed-ended hollow steel pile tube. It is considered to behave linearly elastic and it is modelled as a cylindrical structure. In FLAC^{3D} a solid pile is used with equivalent pile stiffness and density, which are calculated by the formulas described in the section 3.1, cf. Eq. 1 and 2. The geometry of each section is:

Sections	Depth (m)	Walls thickness (mm)
Section 1	1.4	50
Section 2	9.1	54
Section 3	12.4	50
Section 4	14.7	40
Section 5	22	30

Table 10: Geometrical parameters for the monopile in Plaxis 3D model.

In figure 41 load-displacement relationship is presented. The behaviour of FLAC^{3D} and Plaxis 3D is found to be similar as it was in small-scale models. In the beginning of the curves FLAC^{3D} shows stiffer behaviour, while Plaxis 3D and ABAQUS have similar results. However with larger displacement Plaxis 3D shows bigger uncertainties than FLAC^{3D} in comparison with ABAQUS.

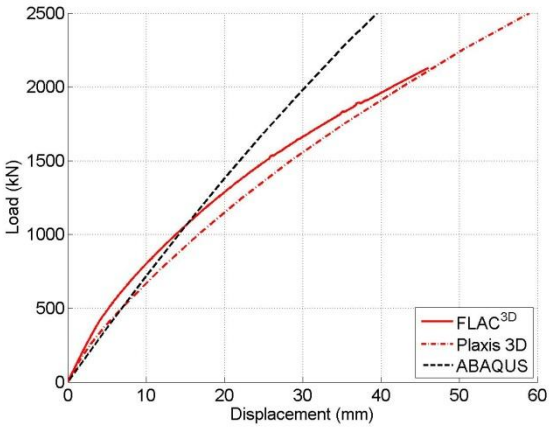

Figure 41. Load-displacement curves for different numerical models.

9 Conclusions

In this paper numerical analysis of laterally loaded small-scale and large-scale monopiles in cohesionless soils is presented. Results of three dimensional numerical programs FLAC^{3D} and Plaxis 3D have been compared using experimental results as reference. As Plaxis 3D shows high uncertainties in the comparison using a Mohr-Coulomb material model, a deeper analysis of material models has been conducted. Meanwhile FLAC^{3D} is calibrated to the small-scale tests carried out at Aalborg University Laboratory. Finally full-scale models are simulated with the same characteristics according to Kellezi and Hansen (2003) ABAQUS model. The general conclusions are:

- Both, in small-scale and large-scale model comparison between FLAC^{3D} and Plaxis 3D it was found that with Mohr-Coulomb material model, Plaxis 3D overestimates the displacement and underestimates the soil resistance.

- Comparing material models by Plaxis 3D, Hardening soil shows more accurate results than Mohr-Coulomb.

- Hardening soil model slightly overestimates the values of Young's modulus in high stress-strain states, when compared to the experimental results, which is found to be reasonable, due to uncertainties while obtaining the soil parameters. However, the curvature of the Hardening soil model was expected to be higher.

- Hardening soil small strain model provides a better approach in the small stress-strain path, giving slightly better results. However, the difference between the models was found to be very small, therefore, it can be concluded that it is not worth using Hardening soil small-stain model for non-slender statically loaded monopile analysis.

- Comparison of FLAC^{3D} calibrated model and experimental tests show similar results of bending moment distributions and depth-displacement plots. As expected results show some uncertainties in the test without the overburden pressure as in this case the friction angle, φ_{tr}, is highly dependable on the stress level and the density index, I_D.

- It is proved that with higher values of the pressure, the maximum bending moment is observed closer to the soil surface due to the increase of the soil resistance.

- The deflection of the pile consists of a rigid body motion. Even when the pressure and the slenderness ratio increase, the pile rotates around a zero deflection point. Therefore, the pile behaves more flexibly but inside the rigid limits.

References

API. 1993. *Recommended practice for Planning, Designing and Constructing Fixed Offshore Platforms - Working Stress design*. American Petroleum Institute.

Borobia A., Mikalauskas L. and Troya J. L. 2011. *Small-Scale testing of Static Laterally loaded Non-Slender Monopiles in Cohesionless Sand*. Department of Civil Engineering. Aalborg University.

DNV. 1992. Foundations. Det Norske Veritas. Classification Notes No. 30.4

FLAC^{3D} 4.0 manual. 2009. *Fast Lagrangian Analysis of Continua in 3 Dimensions*. Itasca Consulting Group Inc., Minneapolis, Minnesota, USA.

Kellezi L. and Hansen P. B. 2003. *Static and dynamic analysis of an offshore mono-pile windmill foundation*. Lingby. Denmark.

Plaxis 3D 2010 Manual, Brinkgreve R. B. J., Engin E. and Swolfs W. M. (edt.), 2010.

Møller M., Brødbæk K. T. and S. P. H. Sørensen. 2009. *Numerical Evaluation of Load-Displacement Relationships for Non-Slender Monopiles in Sand*. Department of Civil Engineering. Aalborg University.

Thomassen K., Roesen H. R., Ibsen L. B., and S. P. H. Sørensen. 2010. *Small-Scale Testing of Laterally Loaded Non-Slender Monopiles in sand.* Department of Civil Engineering. Aalborg University.

CHAPTER 5

CONCLUDING REMARKS

An overview of all the numerical, experimental and dimensionless analysis done through the project is outlined. Concluding remarks for the results obtained by the numerical and experimental approaches are drawn, as well as some conclusions concerning the dimensionless analysis and interpretation of triaxial results. A general equation describing the lateral displacement of the pile, based on the experimental tests carried out at Aalborg University, is found. Finally, some directions for future research are recommended.

The actual method for the design of offshore wind turbine foundations is the p-y curve method proposed by API (1993) or DNV (1992), although it shows some inaccuracies and uncertainties such as the variation of the initial stiffness or the validity of this method for cohesionless sand, since it was primarily developed for soft clays. The purpose of this thesis has been to evaluate the pile behaviour, including the p-y curve method for non-slender monopiles in cohesionless sand. The evaluation has been carried out in three steps:

- **Experimental work:** Twenty-two small scale tests have been performed at Aalborg University since 2009 until the current date. The previous results obtained by other students (Sørensen et al. (2009) and Roessen and Thomassen (2009)) at Aalborg University Laboratory, and the results obtained by means of the 10 small scale tests carried out by Borobia, Mikalauskas and Troya during 2010 and 2011, form a complete set of tests with the scope of analysing p-y curves, bending moment distribution, and load-displacement relationship. Additionally, the laboratory tests have been used to calibrate numerical models in FLAC^{3D} and also an elaboration of numerical models by PLAXIS^{3D}. The tests were carried out successfully inside a pressure tank at Aalborg University laboratory, minimising the scale effects which are often introduced in small-scale tests, such as the overestimation of the friction angle for low stress levels. The conducted tests were realised on closed-ended aluminium piles, with diameters of 40 mm, 60 mm, 80 mm and 100 mm, varying overburden pressure from 0 kPa to 100 kPa, different slenderness ratios L/D = 3,4,5,6 and a constant wall thickness of 5 mm. The closed-ended piles with diameters of 60 mm and 80 mm had strain gauges attached on both sides of the pile, in order to give live

measurements of the strain when the piles were pulled out by the hydraulic piston. The computed p-y curves were acceptable, however some uncertainties were also observed in the measurements realised by the strain gauge devices.

- **Numerical models:** Small scale laterally-loaded monopiles with the same characteristics as in the experimental tests have been simulated by means of the commercial three dimensional numerical programs FLAC^{3D} and Plaxis 3D, with the purpose of analyse the accuracy of these programs and compare the numerical results to the experimental results. Three material models have been used for the numerical analysis: Mohr-Coulomb with tension cut-off, Hardening soil model and Hardening soil small strains model. The comparison between FLAC^{3D} and Plaxis 3D results, when the Mohr-Coulomb model is employed, shows a clear overestimation of lateral displacement by Plaxis 3D, giving an underestimation of soil resistance. The soil in the numerical modelling by FLAC^{3D} is stiffer than in Plaxis 3D, thus smaller values of curvature are obtained for the pile, giving smaller bending moment distribution compared to Plaxis 3D, also meaning smaller values of the soil resistance in the p-y curves.

  Due to the simplicity of the Mohr-Coulomb model, a deeper analysis employing other two material models becomes interesting. As it was expected, more accurate results with Hardening Soil material model are obtained, since it is a more complex method which takes into account the stiffness dependency on the stress-strain path. The hardening soil small strains model is an improvement of the Hardening model due to the fact that it gives a better approach when concerning small strains. However, the differences between the results are not high, perhaps caused because the pile deflection creates high strains, and the region of small strains is very small compared on large strains region.

  Some uncertainties were found in the tests without overburden pressure. In this case the friction angle, φ_{tr} is highly dependable on the stress level and the density index I_D. It is proved that with higher values of the pressure, the maximum bending moment is observed closer to the soil surface due to the increase of the soil resistance.

  Furthermore, a full-scale model, with the same characteristics as Kellezi and Hansen (2003) ABAQUS model is also modelled by FLAC^{3D} and Plaxis 3D in order to verify the validity of the numerical modelling when a full-scale model is conducted. As it was found out in the small-scale tests, Plaxis 3D overestimates the lateral displacement when it is compared to FLAC^{3D} results, according also with the full-scale model, where a similar behaviour is obtained. Nevertheless, the results obtained by FLAC^{3D} and Plaxis 3D for the full-scale test are considered more accurate than for the small-scale tests, but both of them overestimated the lateral displacement regarding the ABAQUS model.

- **Dimensionless analysis:** Based on the 22 small-scale tests carried out at Aalborg University from 2009 until 2011, a dimensionless analysis was conducted. The results are investigated, sorted and compared regarding the varying pile diameter, changing overburden pressure and the different slenderness ratios used in the tests. Some load-displacement normalised graphs in double logarithmic scale have been obtained, and the data points shown in these graphs were fitted by the so called Power Law in order to obtain the exponent of the lateral load, and thus the soil exponent (k). [G. Gudehus and A. Hettler (1988)].

  Some triaxial tests previously carried out at Aalborg University were also used to compute the soil exponent at different confining pressure levels by the help of stress-strain graphs, and then it has been compared to the one obtained in the different small-scale tests, obtaining a more reliability in the soil exponent obtained for higher pressure levels. Additionally, by means of the Π-factors, and based on the Buckingham's theorem (c.f. Appendix D), a general, implicit, dimensionless equation is derived to describe the lateral behaviour of the pile for the different pile diameters and embedded lengths when it is submitted to a horizontal load. Finally, based on the scaling laws shown in Appendix D, an extrapolation of the model parameters to a full-scale model was realised, however the results are found to overestimate the reality.

The main findings of the project are summarised in the following, based on the experimental and numerical results described in the previous chapters.

5.1. Lateral pile deflection

The piles used at the laboratory and numerical modelling had a slenderness ratio of L/D = 3, 4, 5, 6 and behaved rigidly when they were influenced by the lateral load, even though when the overburden pressure and the slenderness ratio were increased, the bending moment became also larger, and thus, the piles behaved more flexibly, but still inside the rigid behaviour.

Overburden pressure, $P_{0,}$ and slenderness ratio, *L/D,* affect in the same way to the lateral deflection of the pile, *y*. The larger P_0 or *L/D* become, the lower lateral pile deflection is experienced by the pile.

5.2. Variation of initial stiffness E_{py}* with depth

Based on design regulations API (1993) and DNV (1992), E_{py}* increases linearly with depth and they do not take into account the pile properties when computing the initial stiffness. However, this assumption was not verified by numerical and experimental simulations, which showed a non-linear distribution of the initial stiffness along the embedded length of the pile, and E_{py}* decreases when the slenderness ratio increases. c.f. Chapter 2.

5.3. Sensitivity of E_{py}* to varying embedded pile length and changing overburden pressure.

The tests carried out at Aalborg University laboratory showed that the initial stiffness decreases for high slenderness ratios and increases for higher values of the pressure level. The analysis of the numerical models indicated that E^*_{py} is dependent on the slenderness ratio and overburden pressure, as E^*_{py} increases with a growth of these parameters. This observation is not in accordance with the recommendations in the design regulations, such as API or DNV.

5.4. Variation of soil resistance with overburden pressure and slenderness ratio

It was shown by experimental and numerical models, that when overburden pressure was applied, the soil resistance, *p*, increases, due to a higher compaction of the soil, and as a result the pile behaves more flexibly, but always inside the rigid limits.

On the other hand, when the pressure is constant and the slenderness ratio increases, the opposite behaviour occurs to the soil resistance, it decreases.

5.5. Sensitivity of bending moment distribution to varying embedded pile length and changing overburden pressure.

The bending moment, *M(x),* is very sensitive when the pressure and the slenderness ratio are increased, since it rises very quickly. For an overburden pressure of 0 kPa, the pile behaves almost like a rigid body. When the pressure is increased to 50 kPa, the bending moment experiences a change of 10 times larger than for 0 kPa for the same pile displacement. Additionally, when the pressure increases, the maximum bending moment occurs closer to the soil surface. This finding indicates that the relative increase in soil resistance is more significant near the soil surface than at the pile toe.

Even though the pile behaves more flexibly when the bending moment increases, the deflection of the pile still consists of a rigid body motion. The pile rotates around a zero deflection point.

5.6. Small-scale test effects

When small-scale tests are performed, usually small-scale effects appear, such as uncertainties when calculating the soil parameters for low stress levels. The CPT's carried out in the Geotechnical Laboratory at Aalborg University were realised taking into account the pressure levels applied by the help of the pressure tank and the rubber membrane (0 kPa, 50 kPa and 100 kPa). Lower values of the friction angle were obtained when the overburden pressure increases, yielding to a more realistic value of the friction angle when the stress level increases, since in real offshore locations it is rarely above 40 degrees.

5.7. Variation of the soil exponent with pile diameter, overburden pressure and slenderness ratio.

The exponent of the lateral load (α) was computed by means of the double logarithmic-scale graphs obtained as the slope of the straight line which fits the data points in the normalised load-lateral deflection graphs. The models are assumed to be rigid-pile systems where the soil exponent (k) is directly related to the exponent of the lateral load. cf. Chapter 3.

Very similar values of the soil exponent are found for the different diameters (40 mm, 60 mm, 80 mm and 100 mm). Therefore, it is assumed that the soil exponent is independent of the pile diameter, and it is only a function of the stress level in the soil.

Averaged values of the soil exponent for the three different pressure levels were computed, showing only agreement between the soil exponents obtained by the triaxial with a confining pressure of approximately 27 kPa and an overburden pressure of P_0 = 100 kPa in the small-scale tests. This result was expected, since some uncertainties were observed when calculating the friction angle for low stress levels. For this reason it was decided to ignore the soil exponent computed for 0 kPa and 50 kPa, and it was only taken into account the averaged soil exponent computed for 100 kPa, independent of the pile diameter (k = 0.72).

For this reason the soil exponent can be considered as a soil constant which does not depend on the pile properties but it is a function of the stress level of the soil.

The influence of the slenderness ratio cannot be analysed properly, due to the small variation of L/D. Most of the tests (16/22) were conducted with a slenderness ratio L/D = 5, and wrong conclusions might be drawn from this analysis.

5.8 General equation for the lateral movement of the pile and extrapolation of the small-scale model parameters.

Based on the 22 small-scale tests, assuming the validity of the Power Law, and with the help of the Π-factors, a general implicit dimensionless equation was derived to describe the lateral displacement of the pile as a function of the load applied, unit weight of the soil, soil exponent, and pile properties such as pile diameter and embedded length. cf. Appendix D.

Furthermore, some geometrical scaling laws were defined in order to extrapolate the small-scale model parameters to a full-scale prototype, by the use of a scaling factor set to $\lambda = 0.01826$.

5.9 Constitutive materials models.

Based on the numerical analysis using FLAC^{3D} and Plaxis 3D 2010, the material model employed has a high influence in the results. It is also remarkable the importance of the employed mechanical soil parameters, since the soil stiffness is very sensitive to their variation, and thus, it can affect the results drastically.

The variation of friction angle and initial Young's Modulus affects to the curvature and slope of the load-deflections curves. Increasing the values of friction angle produces less curvature, and increasing the initial Young's Modulus, the slope of the load-deflection curve tends also to increase. Furthermore in cohesionless soils, in which very small values (near to zero) of cohesion are expected, the strength of the soil depends uniquely on friction angle. Therefore it is clear the importance of employing a precise friction angle in the numerical approach.

The constitutive materials models used to approximate the stress-strain behaviour of the soil shows the importance of the Young's Modulus employed in each model. In Mohr-Coulomb, the initial Young's Modulus is defined since the beginning and remains constant and independent of the stress-strain path during the linear elastic part, which has proved to be very inaccurate, giving an overestimation of the lateral displacement compared to the experimental curve. Employing more advanced constitutive material models, the approach of the stress-strain curve is considerable better. Hardening Soil model employs a more accurate work curve to simulate the stress-strain path of the soil. c.f. Appendix I. The Young's Modulus is not constant and there are not perfectly elastic and plastic regions in contrast to Mohr-Coulomb model.

It is very important to be aware of the Young's Modulus dependency on the stress-strains path, meaning that the stiffness of the soil depends on the effective stresses state. It is proved that the model fits better the experimental load-displacement curve, but also for large stress-strains the values of the Young's Modulus become too high, giving as a result too stiff soil which underestimates the value of lateral displacement compared to the experimental curve.

The Hardening Soil small strains can be considered as an improvement of the Hardening soil material model, since it takes into account the stiffness dependency in the small strains regions. This dependency means, that for very small strains which cannot be measured in laboratory by regular techniques as for instance triaxial test, the shear strain values are higher than in normal strains, almost double. Therefore, the stiffness of the soil when very small strains occur is much higher, giving a better approach of the experimental curve. This issue has been analysed, and slightly higher values of lateral displacement for small displacements are obtained using Hardening small strains regarding the Hardening soil results. Such a small difference is due to the fact that the region of small strains, where it is expected to give a better approach, is very small compared to the region where strains are created by the monopile when it is submitted to lateral loading.

5.10. Directions for future research

The review presented through this project about load-deflection, bending moment distribution, p-y curves method, dimensionless analysis and numerical modelling is only valid for offshore wind turbine foundations in homogeneous, dense, cohesionless sands, since *Baskarp sand No. 15* was used in the tests. Similar analyses are to be performed in layered soils, and in different types of soils.

Cyclic loading is of high interest to be analysed, due to cyclic loading from wind and waves, and only static loading was considered through this project. It may involve a study of the entire wind turbine system.

The effect of scour is a good topic to be evaluated, and develop strategies to avoid this kind of erosion. Also more analyses are to be performed including a large range of pile diameters.

5.10.1. Experimental work

Large-scale tests are very expensive and time consuming, reason for why 22 small-scale tests were carried out at Aalborg University laboratory. Some effects related to scaling usually appear in this kind of tests, but the results obtained show that the scaling effects were minimised by the help of the pressure tank.

At the moment there are no well-documented large-scale tests available, so small-scale tests are of high importance in order to predict the soil-pile interaction for slender laterally loaded monopiles.

The piles used in the tests are closed-ended piles, which is in contrast with the reality because usually open-ended piles are used as monopile foundations. Some factors such as sleeve friction are neglected, since no sand is inside the closed-ended pile. This decision was taken in order to prevent possible damages to the strain gauges and the cables which are inside the pile.

The pressure tank used to increase the stress level in the soil was subjected to 1 bar of pressure, but future tests must contain higher pressure levels in order to simulate more realistic offshore locations with a more realistic and lower friction angle, due to the overestimation of the friction angle for low pressure levels.

5.10.2. Numerical work

Two different numerical programs, FLAC^{3D} and Plaxis^{3D} 2010 have been employed in the numerical analysis of laterally-loaded monopiles in cohesionless sand. Even if FLAC^{3D} is considered as explicit finite element program and Plaxis^{3D} 2010 is a finite element program, it is assumed that for a large number of elements and in case of static analysis, both programs should give similar results. However, the results have a high dependency on the material model employed in the simulation. It is recommended for an initial numerical analysis of soil behaviour to use the Mohr-Coulomb material model, since it is computationally light and requires the basic mechanical soil parameters. It is a first order model that does not take into account stress dependency or stress path dependency on stiffness. The model describes the failure state quite well when using effective values, friction angle and cohesion, but is insufficient when the load-displacement is compared with the experimental results.

Therefore, for a deeper analysis and more accuracy of the soil behaviour, it is necessary to employ more complex models such as Hardening soil material model. This is a more complex model with the advantage that the model describes a better approach of the work curve and takes into account the stiffness dependency on stress-strain path. However, it is important to be aware that it could provide high values of soil resistance for high values of stress-strain, making the soil stiffer than in the real case.

Hence, the Hardening soil model is more realistic and accurate, but also needs as an input more mechanical parameters, which requires deeper geotechnical studies as triaxial test analysis.

Depending on the kind of numerical analysis, Hardening soil small strains material model can be a better approach than the Hardening soil model. For instance, when analysing monopiles submitted to cyclic loading, small strains are generated in the soil,

and the Hardening soil model small strains offers a better approach of the Young's Modulus concerning the stress-strain state.

Nevertheless, in the analysis of monopiles submitted to static lateral displacements, the Hardening soil small strains seems to give slightly better results than the Hardening soil, but also requires more mechanical soil parameters such as the small strain shear modulus and the secant shear modulus obtained by more complex dynamic techniques.

For this reason, it is acceptable to use Mohr-Coulomb cut-off or Hardening Soil Model, however it could be interesting to perform a deeper analysis regarding Hardening soil small strains, which could firstly include obtaining the *p-y* curves, bending moment and soil resistance distribution along the embedded pile length. Moreover, it could be interesting to employ this material model for long-term cyclic loading, where small strains are constantly present.

APPENDICES

Appendix A. Test setup **75**

A.1 Introduction to the laboratory 75
A.2 Pressure tank 78
A.3 Increasing the effective stresses 81
A.4 Constant hydrostatic pore pressure 82
A.5 Calibration of the pile 83

Appendix B. Soil preparation and derivation of soil parameters **87**

B.1 Initial soil preparation for the test 87
B.2 Preparation of the soil for the pile installation 87
B.3 Soil procedure after installation of the pile 88
B.4 Cone Penetration Tests at the laboratory 89
B.5 CPT's calculations and results 91
B.5.1 Baskarp sand no. 15 92
B.5.2 Calculation of the parameters 92
B.5.3 Interpretation of the CPT's 95

Appendix C. Interpretation of Triaxial Test results **99**

C.1 Introduction 99
C.2 Triaxial tests description 99
C.3 Interpretation of Triaxial test results 100
C.4 Triaxial test results 105

Appendix D. Scaling Small-Scale Models of Monopiles in Sand **109**
D.1 Introduction 109
D.2 Dimensional analysis and similitude theories 110
D.3 Constitutive Law 111
D.4 The Power Law 112
D.5 Π-Products derived for the load-displacement equation 114
D.6 Similitude Laws 115

Appendix E. Presentation of Experimental Results **119**

E.1 Interpretation of strain gauge measurements 119
E.1.1 Calculation of soil resistance by piecewise polynomial fitting method 121
E.1.2 Lateral deflection of the pile 122
E.2 Test 1 125
E.3 Test 2 126
E.4 Test 3 128
E.5 Test 4 131
E.6 Test 5 134
E.7 Test 6 136
E.8 Test 7 139
E.9 Test 8 142
E.10 Test 9 142
E.11 Test 10 142

Appendix F. Generation of FLAC^{3D} models **143**

F.1 General Introduction to FLAC^{3D} 143
F.2 Model generation steps 144
F.3 Geometry generation 144
F.3.1 Soil generation 144
F.3.2 Interface generation 145
F.3.3 Pile generation 147
F.4 Pile installation 148
F.5 Material models 149
F.6 Boundary and initial conditions 149
F.7 Damping 151
F.8 Numerical stability 151
F.9 Deflection application 151
F.10 Bending moment and soil resistance calculation 152

Appendix G. Numerical modeling by Plaxis3D **153**

G.1 Introduction to Plaxis3D 2010 153
G.2 Generation of the Model 155

G.2.1 Model Geometry 155
G.2.2 Model boundary fixities 156
G.2.3 Interface 156
G.2.4 Material assignment 158
G.2.4.1 Mohr-Coulomb Model 158
G.2.4.2 Hardening Soil Model 160
G.2.4.3 Hardening Soil Small Strain Model 162
G.2.5 Mesh Generation 163
G.2.6 Convergence Test 164
G.2.7 Calculation Phase 165
G.3 Generation of the full-scale model 165
G.4 Postprocesing of results 168
G.5 Bending Moment and Soil Resistance Calculation 170

Appendix H. Numerical Results **173**

H.1 FLAC^{3D} Results (Not Calibrated) 173
H.1.1 Test 1 173
H.1.2 Test 2 175
H.1.3 Test 3 177
H.1.4 Test 4 179
H.1.5 Test 5 181
H.1.6 Test 6 183
H.1.7 Test 7 185
H.2 FLAC^{3D} Results (Calibrated) 187
H.2.1 Test 1 187
H.2.2 Test 2 189
H.2.3 Test 3 191
H.2.4 Test 4 193
H.2.5 Test 5 195
H.2.6 Test 6 197
H.2.7 Test 7 199
H.3. Numerical Results by Plaxis 3D 2010 201
H.3.1 Test 1 201
H.3.2 Test 2 202
H.3.3 Test 3 202
H.3.4 Test 4 203

H.3.5 Test 5 204
H.3.6 Test 6 205
H.3.7 Test 7 206
H.4. Comparison of FLAC^{3D} and Plaxis 3D 2010 208
H.4.1 Test 1 208
H.4.2 Test 2 209
H.4.3 Test 3 210
H.4.4 Test 4 211
H.4.5 Test 5 213
H.4.6 Test 6 215
H.4.7 Test 7 216
H.5. Comparison of FLAC^{3D} and Experimental Results 219
H.5.1 Evaluation of Bending Moment Distribution 219
H.5.2 Evaluation of deflection Distribution 222
H.5.3 Evaluation of *p-y* curves 225

Appendix I. Material models **229**

I.1 Mohr-Coulomb Tension cut-off model 229
I.2 Hardening Soil Model 232
I.2.1 Hyperbolic relationship for standard drained triaxial tests 233
I.2.2 Approximation of the hyperbola by the Hardening Soil Model 234
I.2.3 Plastic Volumetric Strain for Triaxial states of stress 237
I.2.4 Dilatancy cut-off 238
I.2.5 Yield surface in the Hardening Soil model 239
I.2.6 Hardening Soil Model with Small-Strain Stiffness 240

Appendix J. Difficulties when conducting tests **243**

APPENDIX A

TEST SETUP

Twenty two small-scale tests with different diameter and overburden pressure are performed in the Geotechnical Engineering laboratory at Aalborg University, in order to investigate the effect of changing overburden pressure and slenderness ratio in the pile behaviour, for non-slender piles (L/D < 10). In this appendix, the test setup is described.

A.1. Introduction to the laboratory

Different types of tests are carried out, using various pile diameters (40, 60, 80 and 100 mm), different overburden pressures (0, 50 and 100 kPa), changing slenderness ratio (L/D = 3, 4, 5 and 6), and a constant wall thickness of 5 mm. An overview of all the tests performed is shown in table A.1.

From test 4 to 6 and from test 10 to 18, strain gauges are attached on both sides of the pile in two different layouts, with the purpose of measuring the strains at different depths of the pile, produced by the horizontal load, cf. Figures A.1 and A.2:

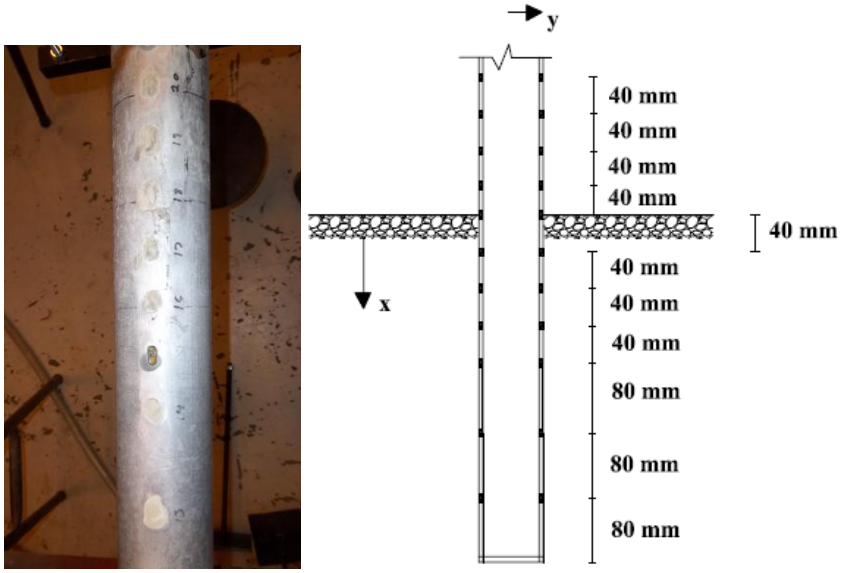

Figure A.1: Strain gauges mounted on the pile for tests 10 to 13, 17 and 18.

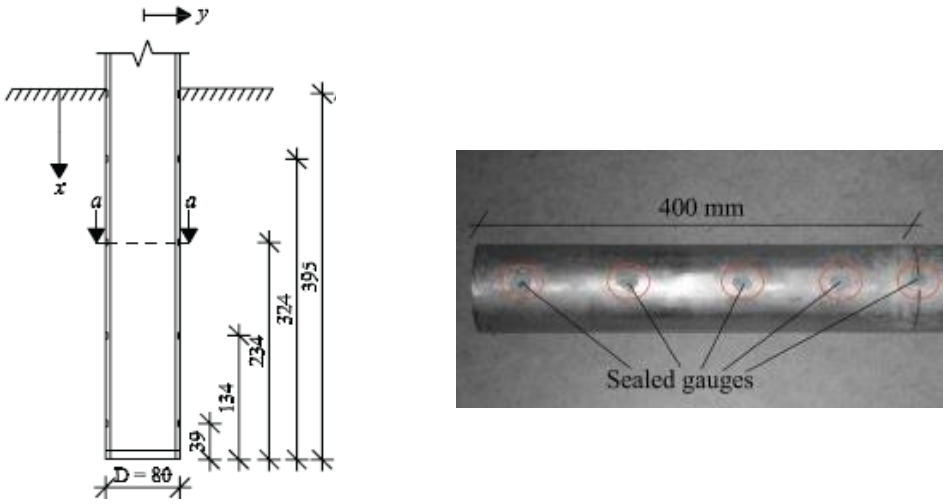

Figure A.2: Strain gauges mounted on the pile for tests 4 to 6 and 14 to 16

	***D* [mm]**	***L/D***	***P*$_0$ [kPa]**	**S.G.**
Test 1	40	5	0	No
Test 2	40	5	50	No
Test 3	40	5	100	No
Test 4	60	5	0	10
Test 5	60	5	50	10
Test 6	60	5	100	10
Test 7	80	3	0	No
Test 8	80	3	50	No
Test 9	80	3	100	No
Test 10	80	4	100	22
Test 11	80	5	0	22
Test 12	80	5	50	22
Test 13	80	5	100	22
Test 14	80	5	0	10
Test 15	80	5	50	10
Test 16	80	5	100	10
Test 17	80	6	50	22
Test 18	80	6	100	22
Test 19	100	5	0	No
Test 20	100	5	50	No
Test 21	100	5	50	No
Test 22	100	5	100	No

Table A.1: Overview of the Small-scale tests carried out at Aalborg University

This strain is directly related to the stress (by Hooke's Law), which is later used to compute the bending moment distribution through the whole length of the pile, *M(x)*.

The lateral loading is produced by a hydraulic piston positioned 370 mm above the soil surface. The load is transferred to the pile by a force transducer connected by a wire to the pile, which is pulled in the direction of the hydraulic piston, cf. Figure A.3.

The lateral displacements of the pile at different levels are measured by three displacement transducers positioned above the soil surface. As it can be observed in figure A.4, the wire is placed at the same level as force transducer 2.

Figure A.3: Hydraulic piston

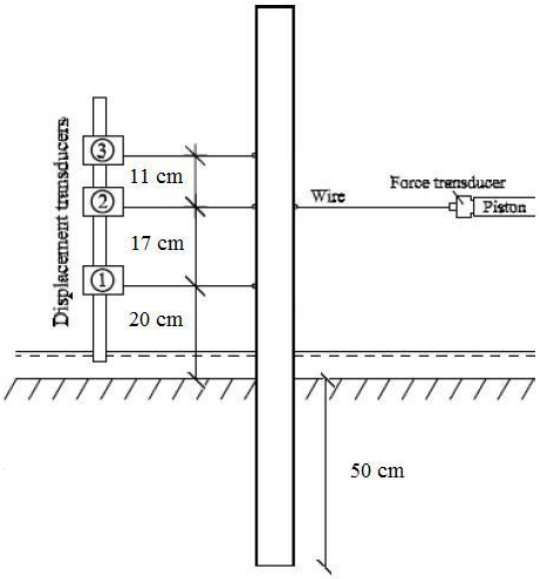

Figure A.4: Location of displacement transducers and wire

In figure A.4 it is shown the initial position of the displacement transducers, however, displacement transducer number 1 is moved 6.5 cm upper after test 2, to be able to increase the water level a few centimetres more. This decision was taken with the purpose of keeping the water level as highest as possible, cf. Figure A.5:

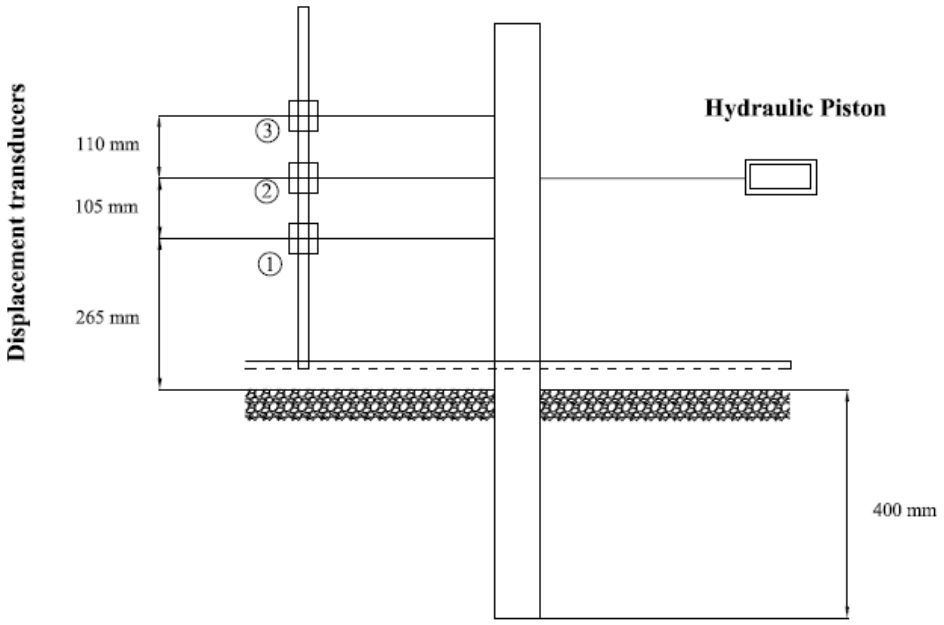

Figure A.5: New location of the displacement transducers

A.2. Pressure tank

The pressure tank is manufactured by Bergla Maskinfabrik in Brønderslev, Denmark, and its purpose is to increase the effective stresses of the soil to avoid uncertainties when obtaining the soil parameters, due to the strong relationship of the friction angle with the stress level and thus also the rest of the parameters. The dimensions of the tank are 2.5 m of height and a diameter of 2.1 m. The tank is installed in a load-frame over a reinforced foundation with no connection to the surrounding floor. A platform is mounted on the top of the tank to make easier the preparation of the tests which will be carried out in the tank, cf. Figure A.6.

To be able to enter the tank, to install the pile and prepare the soil, a trapdoor on the side of the tank is placed, cf. Figure A.7. A top hatch is used for the installation of the hydraulic piston, cf. Figure A.8, which is used for the installation of the pile, for conducting the cone penetration tests and keeping the pile in an upright position while the vibration of the soil is being done.

Measuring devices are led out of openings in the tank side, and connected to a spider which is also plugged to the computer, providing the output data which can be shown through the computer screen, cf. Figure A.9.

A 580 mm thick layer of Baskarp Sand No. 15 is placed in the pressure tank above a layer of highly permeable gravel. During the tests the sand is fully saturated, keeping the water table approximately 20 cm above the soil.

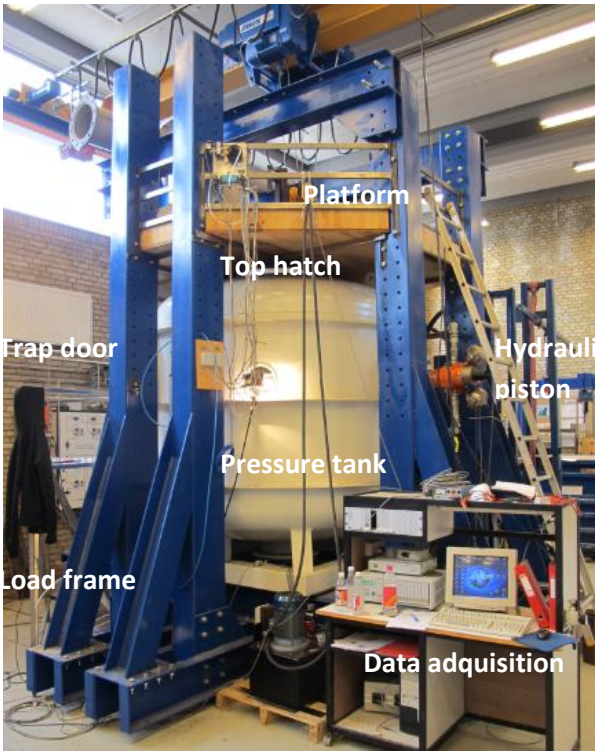

Figure A.6: Layout of pressure tank at Geotechnical laboratory at Aalborg University

Figure A.7: Trapdoor to access into the tank

Figure A.8: Top hatch for the installation of the hydraulic piston.

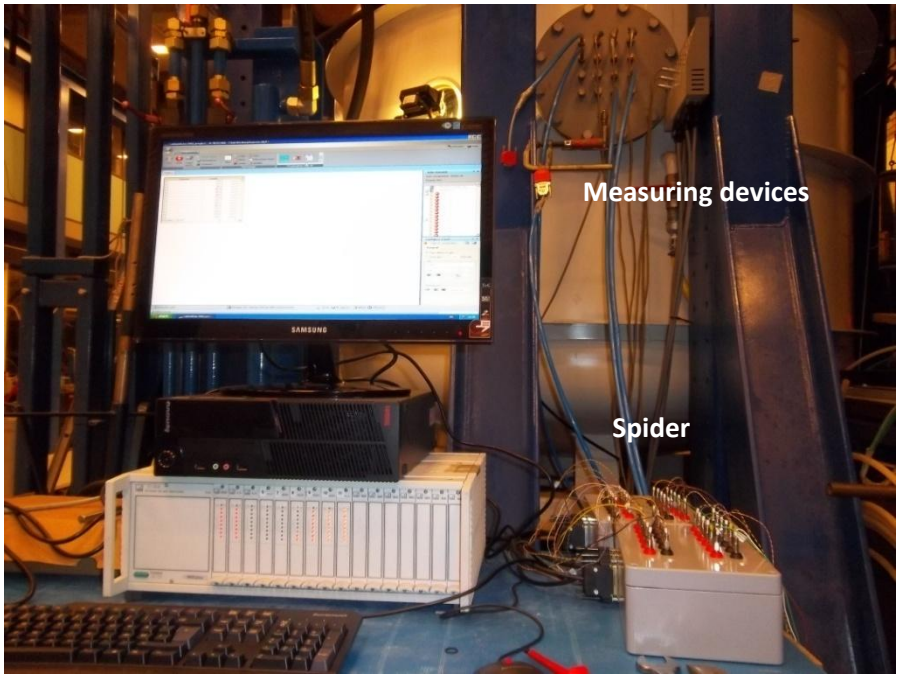

Figure A.9: Measuring devices connected to a spider and connected to a computer

A cross section of the final setup with all its elements and the thickness of the layers is shown in figure A.10:

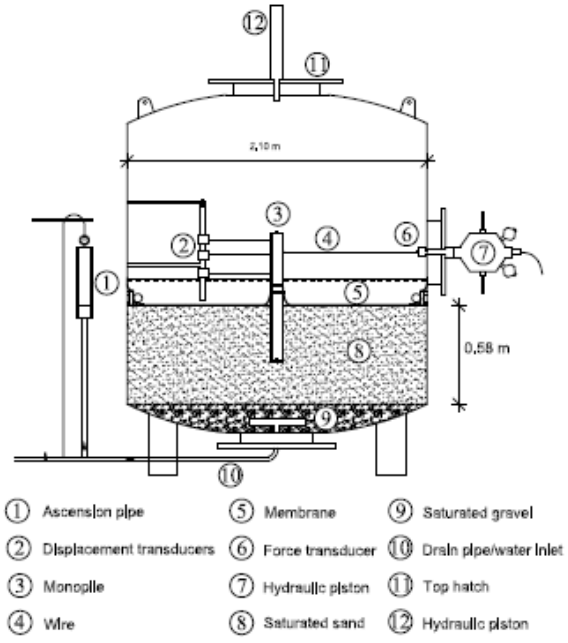

Figure A.10: Cross-sectional view of the test setup [Sørensen, 2008]

A.3. Increasing the effective stresses

In order to increase the effective vertical stresses corresponding to the applied air pressure, a rubber membrane is placed on the soil surface cf. Figure A.11.

Figure A.11: Rubber membrane to increase the effective pressure

This method increases the effective vertical stresses without increasing the pore pressure in the soil. Along the outer perimeter of the membrane, a vertical rubber band is attached to it, with the purpose of a perfectly placement of the membrane, and in order to minimize the risk of gaps between the membrane and the tank, cf. Figure A.12.

With the purpose of reducing the risk of water flowing through the joint between the tank wall and the membrane, a rubber skirt is glued to the side of the tank, and placed above the rubber band.

Finally, the rubber band and the mouldings are pressed against the tank wall by a fire hose filled with water and air with a pressure of approximately 7 bar, cf. Figure A.13.

Figure A.12: Mouldings attached to the membrane.

Figure A.13: Fire hose pushing the mouldings against the wall.

A.4. Constant hydrostatic pore pressure

Since the membrane is not completely tight, air can flow through leaks in the membrane, and increase the pore pressure. The dynamic viscosity of water is approximately 55 times higher than for air, so water must be poured in the tank, reaching a level of approximately 16 cm above the membrane, cf. Figure A.15.

This level should be kept constant, in order to maintain a hydrostatic pore pressure in the soil by the use of an ascension pipe connected to the tank, cf. Figure A.14.

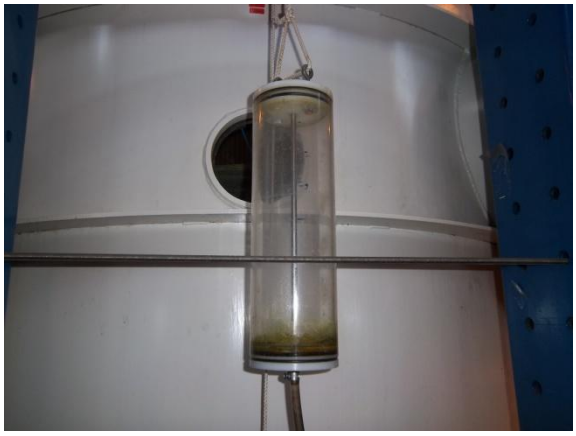

Figure A.14: Ascension Pipe

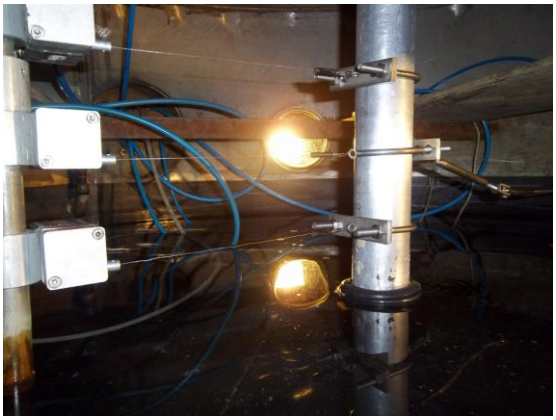

Figure A.15: Water above the membrane

The mechanism of controlling the pore pressure is very simple. When the water column in the ascension pipe increases, water is lead out of the tank through a drain in the bottom of it, and is conducted directly to the sewer.

Due to the volumetric strains when applying the overburden pressure a maximum water volume of around 60 litres/hour was found to pass through gaps between the membrane and the pressure tank.

This water flow can be measured by the help of the ascension pipe. There are two marks in the ascension pipe separated 15 cm each other, and its diameter is D = 13 cm.

The water velocity through the gaps is defined as equation A.1 shows:

$$v = \frac{V}{t} = \frac{\pi \cdot D^2 \cdot H}{4 \cdot t} \qquad \text{(A.1)}$$

Where

V	The volume of the ascension pipe [dm^3]
D	Diameter of the ascension pipe [dm]
H	Height the ascension pipe [dm]
t	Time [h]

A.5. Calibration of the pile

The piles used in the tests are made from aluminium, with a wall thickness of 5 mm. Strain gauges from HBM of the type K-LY43-3/120 are placed in 11 levels as it is shown in figure A.16.

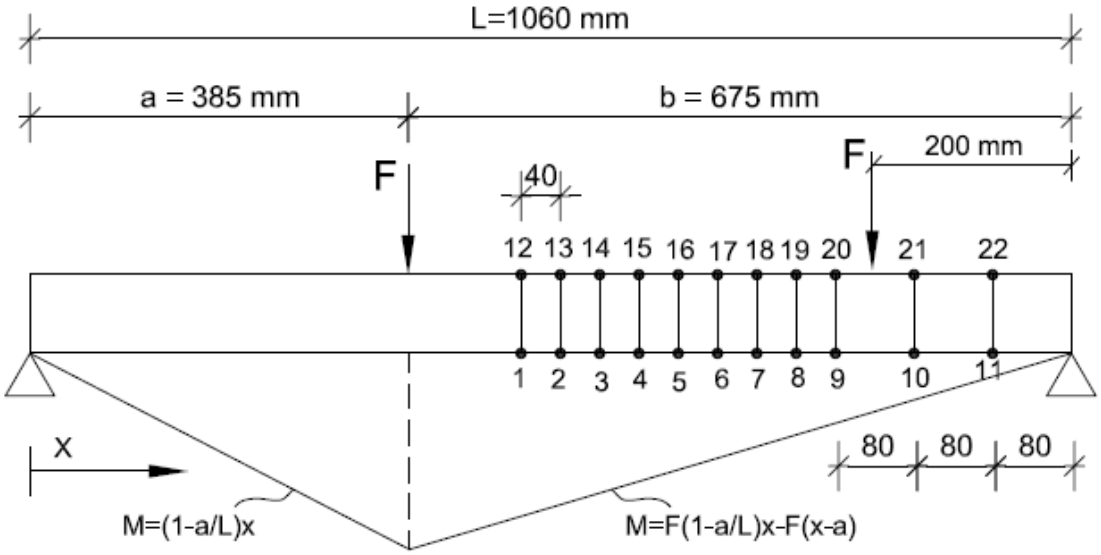

Figure A.16: Strain gauges placed on the pile in 11 depth levels

Before installing the pile inside the pressure tank, a calibration of the strain gauges must be done. It implies the calculation of the calibration factors, k_g, for each one of the strain gauges, in order to relate the strain measurements to the bending moment, cf. Figure A.17.

Figure A.17: Load applied at 385 mm from the left support

The calibration is realised in 5 steps:

1. Pile supported by two simple supports in both edges.
2. Two loads in 12 steps of 10 kg each are applied (1200 N): at 385 mm from the left support and at 675 mm from the right one, cf. Figure A.17.
3. Based on the bending moment distribution for a double supported pile shown in figure A.16, bending moment and strain (obtained along the loading and unloading time) can be plotted together, in order to get a relation between them, cf. Figure A.18.
4. Linear regression is used to fit a straight line through the points.
5. The slope of this straight line is defined as the calibration factor of the strain gauge, k_g.

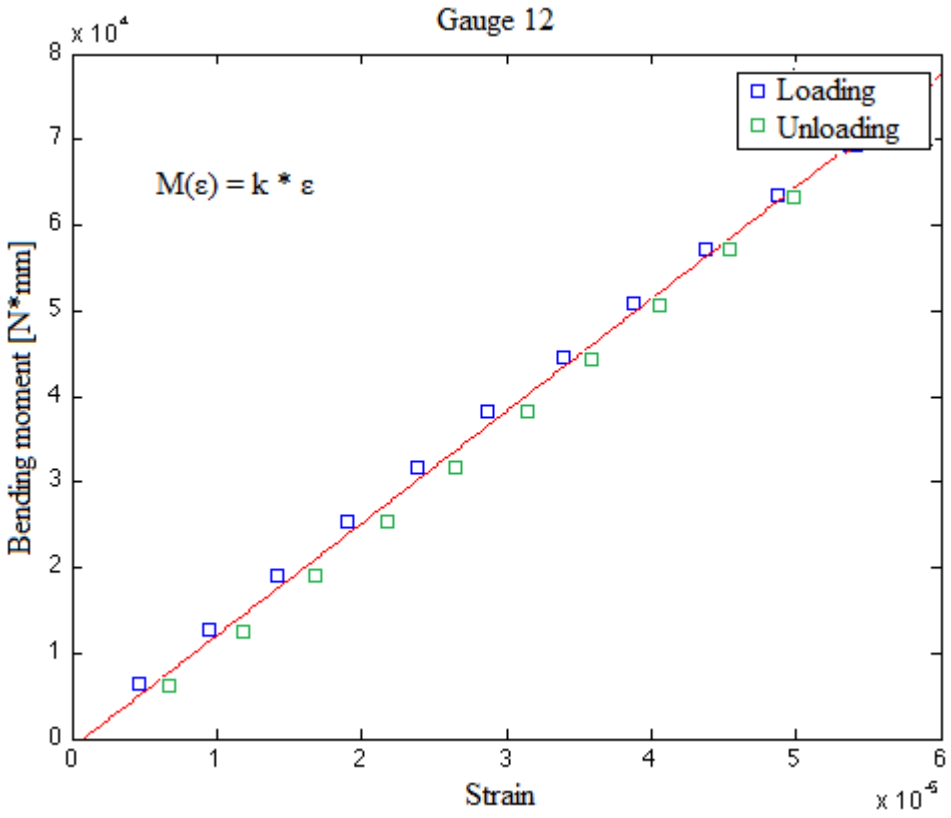

Figure A.18: Example of calibration factor, k_g, obtained from the calibration

$$M(\varepsilon) = k \cdot \varepsilon$$

The gauges are covered with a protective coating in order to protect them from the water, and to be able to measure the strain at that fixed levels. The strain gauges are installed in milled grooves as shown in figure A.19. The depth, width and length of the mill outs are approximately 2, 6 and 10 mm, for each gauge respectively. This fact is discarded in order to carry out the calculations for each pile.

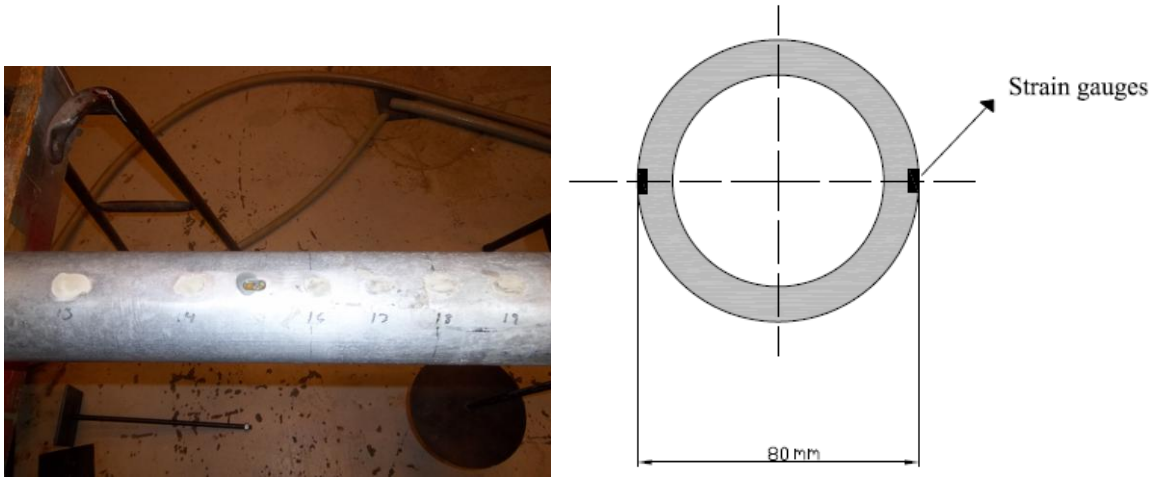

Figure A.19: Strain gauges installed on the pile and cross section at a measurement level

Calibration factors used through tests 10 to 13, 17 and 18 carried out in the laboratory in 2010 and 2011 can be observed in Table A.2:

Calibration factors [N · mm]	
$k_1 = 1.3624 \cdot 10^9$	$k_{12} = 1.4376 \cdot 10^9$
$k_2 = 1.4489 \cdot 10^9$	$k_{13} = 1.4426 \cdot 10^9$
$k_3 = 1.3946 \cdot 10^9$	$k_{14} = 1.4237 \cdot 10^9$
$k_4 = 1.4265 \cdot 10^9$	$k_{15} = 1.4153 \cdot 10^9$
$k_5 = 1.3206 \cdot 10^9$	$k_{16} = 1.3602 \cdot 10^9$
$k_6 = 1.4425 \cdot 10^9$	$k_{17} = 1.3543 \cdot 10^9$
$k_7 = 1.4396 \cdot 10^9$	$k_{18} = 1.3555 \cdot 10^9$
$k_8 = 1.4236 \cdot 10^9$	$k_{19} = 1.3819 \cdot 10^9$
$k_9 = 1.3162 \cdot 10^9$	$k_{20} = 1.3816 \cdot 10^9$
$k_{10} = 1.4389 \cdot 10^9$	$k_{21} = 1.4484 \cdot 10^9$
$k_{11} = 1.3968 \cdot 10^9$	$k_{22} = 1.5756 \cdot 10^9$

Table A.2: Calibration factors for all the strain gauges used in tests 10 to 13, 17 and 18, numbered from 1 to 22.

APPENDIX B

SOIL PREPARATION

In the following chapter the procedure to prepare the soil is explained. The laboratory tests are carried out in a pressure tank partly filled with Baskarp sand No. 15. Basically, the monopile is installed in the sand, then the soil is vibrated and afterwards 6 cone penetration tests (CPT) are carried out. Then the membrane is placed, the overburden pressure is added and the pile is loaded with a horizontal load. The purpose of the soil preparation is to ensure that the soil is homogenous, saturated and with similar basic parameters in each CPT with the aim of having similar conditions in all the tests and also to be able to model similar sand characteristics in the numerical models by FLAC^{3D} and Plaxis 3D.

B.1 Initial soil preparation for the test

The laboratory tests are carried out in a pressure tank. The pressure tank can stand air pressures up to two bars corresponding to the pressure conditions at depths down to 20 m, but in our tests the maximum pressure reached is one bar. In the following, the literature Sørensen et al. (2008) and Ibsen et al. (2009) are used.

The tank is filled with a 58 cm thick layer of Baaskarp sand No. 15. This type of sand is used, because it was used in previous tests in the laboratory.

Before testing the pile, it is important to ensure that the soil is in the right conditions. It is necessary to avoid having air captions inside the soil and to carry out the tests in saturated conditions and homogeneous compaction.

CPT's must be realised, in order to verify that a homogenous compaction of the soil has been attained and to determine the soil parameters needed as input in FLAC^{3D} and Plaxis 3D.

B.2 Preparation of the soil for the pile installation

In all the tests, before the installation of the pile, an upward gradient of magnitude 0.9 is applied in order to minimize the pressure at the bottom of the pile and through the pile surface.

Afterwards, a layer of water above the soil surface of around 5 cm depth is added with the purpose of avoiding possible air captions in the sand. A random pre-vibration is

conducted with the intention of reorder and compact the sand surrounding the pile.

This random pre-vibration reduces the effect that appears when the pile is unplugged in order to have homogeneous initial conditions before the installation.

B.3 Soil procedure after installation of the pile

Once the pile has been installed successfully, a procedure to ensure the right characteristics of the soil before carrying out the tests has to be followed.

Again, an upwards gradient of magnitude 0.9 is applied during five minutes before the vibration. The sand must be vibrated, cf. Figure B.1. This is done with the attempt to achieve compact and homogenous sand before any testing is initiated.

Regarding to the gradient, it is important to appreciate in the piezometer, cf. Figure B.2, where the initial watertable level is and then add the corresponding gradient depending on the initial watertable level to ensure that the correct gradient magnitude 0.9 is being applied. The gradient should not be very high because it may create water channels in the sand and if it is very small it will not loosen up the sand properly. Kristensen & Pedersen (2007).

Figure B.1: Vibrator machine. Watertable 5 cm avobe the surface

Figure B.2: Photo of the piezometer used to measure the gradient magnit

5 cm of water are poured into the tank, cf. Figure B.1, in order to avoid mixing the sand with air during vibration. The vibration will eliminate the effects of previous experiments and remove old air captions in the soil. Additionally, the soil around the pile is loosened up during installation, which is also re-compacted during the vibration. The pile is retained by the hydraulic piston during vibration to avoid moving the pile accidentally, cf. Figure B.4. To achieve a uniform vibration, a plate with holes is placed inside the pressure tank. The plate is shown in figure B.3.

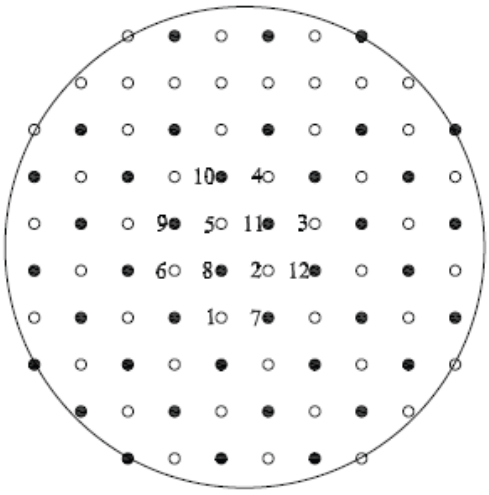

Figure B.3: Sketch of the plate. Sørensen (2008). Numerated holes are used to re-compact the soil after installation

Figure B.4: Plate installed inside the tank, pile fixed to the hydraulic piston.

The procedure followed for the vibration with the plate of the figure B.3 is explained:

- The sand is loosened up by an upward gradient of 0.9.
- Vibration in the numbered holes.
- Vibration in the black holes.
- Vibration in the white holes.

This procedure is realised twice, therefore the sand is loosened in between the two vibration procedures

It is important the vibration of the numbered holes, because after the installation of the pile the soil has failed.

The vibration following the numerated procedure has the objective of minimizing the soil failure. It approximates the coefficient of horizontal earth pressure, K_0 for the surrounding area of the pile to the coefficient of the rest sand inside the tank.

When the soil is prepared for testing, CPT's are carried out in order to verify the compaction and homogeneity of the sand and to determine the effective unit weight, friction and dilation angle, secant modulus of elasticity and relative density of Baaskarp sand No. 15. The procedure of the CPT's is explained in the next.

B.4 Cone Penetration Tests at the laboratory

In order to ensure soil homogeneity and to obtain a similar average of the soil parameters, 6 CPT's are carried out. The Cone penetration tests used at the laboratory are different as the ones used in reality in a natural scale cone penetration test.

In the laboratory, the CPT, cf. Figure B.5, only measures the tip resistance but not the

sleeve friction and pore pressure, due to the fact that in cohesionless soils such as sand it is possible to omit the sleeve friction.

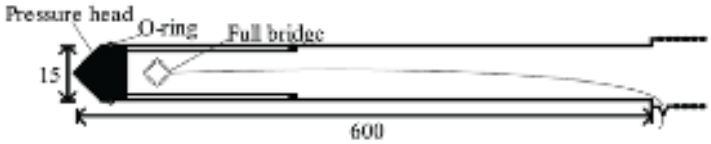

Figure B.5: Sketch of the tip cone of the CPT. Sørensen (2008)

A full bridge strain gauge placed in the cone head measures the tip resistance, cf. Fig. B.5.

The locations for the 6 CPT's are shown in the figure B.6.

CPT's 1 to 4 are performed at 50 cm from the centre of the pile in four different positions.

CPT's 5 and 6 are done at 20 cm from the centre of the pile, in order to test the soil surrounding the pile and perpendicular to the load wire. The reason of this distribution is not to alter the soil in the wire direction, because is the most important part as the soil resistance is evaluated at this side.

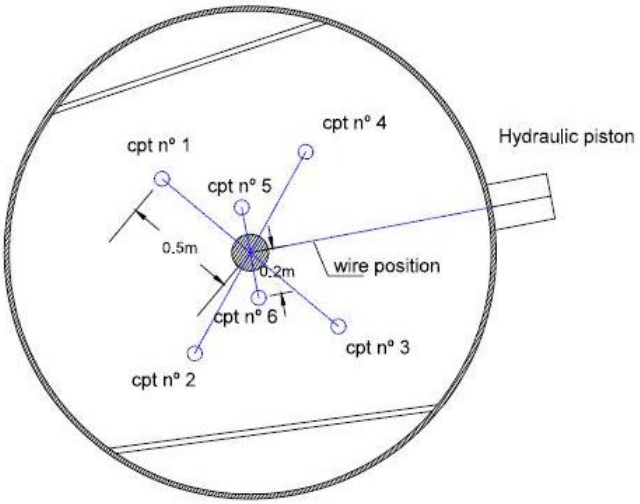

Figure B.6: A sketch of the CPT's distributions inside the tank

The CPT-device is mounted in a structure made for the tank's dimensions and attached to the hydraulic piston, to ensure that the CPT-device is moving constantly in a straight vertical direction into the soil, and it is not embedded with a rotation and inclination, cf. Figures B.7 and B.8.

Figure B.7: CPT during the test inside the tank

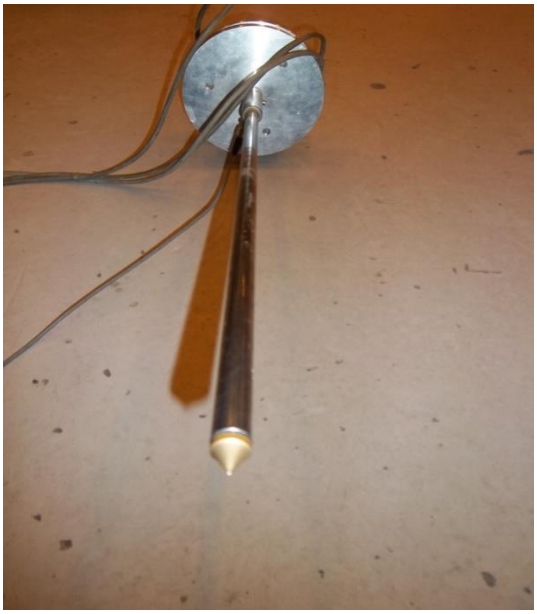

Figure B.8: CPT cone head

The embedded length in each CPT test depends on the embedded length of the pile and it has been carried out as close as the structure can be to the top pile in each test.

B.5 CPT's calculations and results

In order to analyse the data obtained in each CPT, the method used is explained and the possible uncertainties are discussed. To verify that the CPT have been conducted properly and the results are reliable, the values are compared with the results found by Sørensen (2008) to ensure that we have similar conditions in order to compare results of this experimental test with the results of previous pile tests at Aalborg University laboratory.

The parameters obtained from the CPT's are:

Effective unit weight	γ' [F/L^3]
Friction angle	φ [º]
Dilatancy angle	ψ_{tr} [º]
Relative density	I_D [-]
Initial stiffness	E_0 [F/L^2]

B.5.1 Baaskarp sand no. 15

The soil used in the pressure tank is fully saturated Baaskarp Sand No. 15. This sand is well known at Aalborg University, since it has been object of several previous tests. The sand is graded sand from Sweden. The large grains are rounded while the small grains

have sharp edges. The sand consists of quarts, but also contains feldspar and biotite. A distribution of the grains found by sieve analysis can be seen in figure B.9:

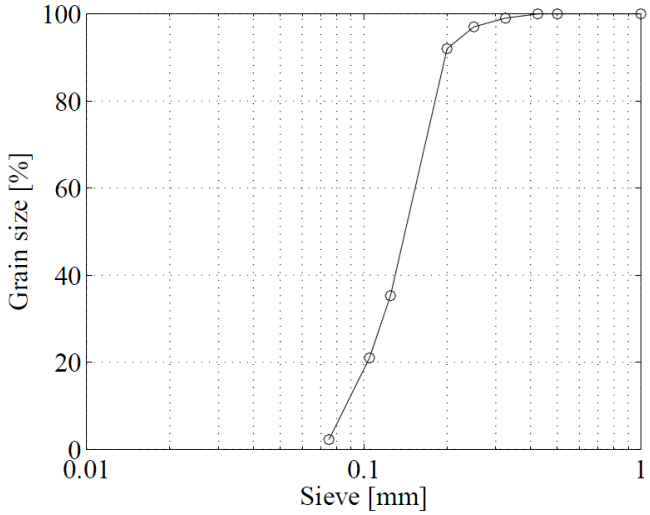

Figure B.9: Distribution of Baaskarp Sand No.15 Found by sieve analysis Ibsen and Bødker (1994)

The material properties for Baaskarp sand No.15 are shown in table B.1:

BAASKARP SAND No. 15	
Specific grain density d_s	2,64
Maximum void ratio e_{max}	0,858
Minimum void ratio e_{min}	0,549
d_{50}	50%-quantile [mm]
U	d_{60}/d_{10}

Table B.1: Material properties for Baskarp Sand No.15, Andersen et al. (1998)

B.5.2 Calculation of the parameters

The properties of Baaskarp sand no. 15 are well known for values of the confining pressure σ_3 ranging from 5 − 800 kPa. The friction angle φ_{tr} and dilatancy angle ψ_{tr}were plotted versus the relative density I_D ,cf. Fig. B.10. Triaxial tests were performed with two different density indices and nine different confining pressures.

The equations are based on the described relationship between relative density and friction angle proposed by Schmertmannn (1978), cf. Figure B.10. The parameters are derived in accordance to Ibsen (2009).

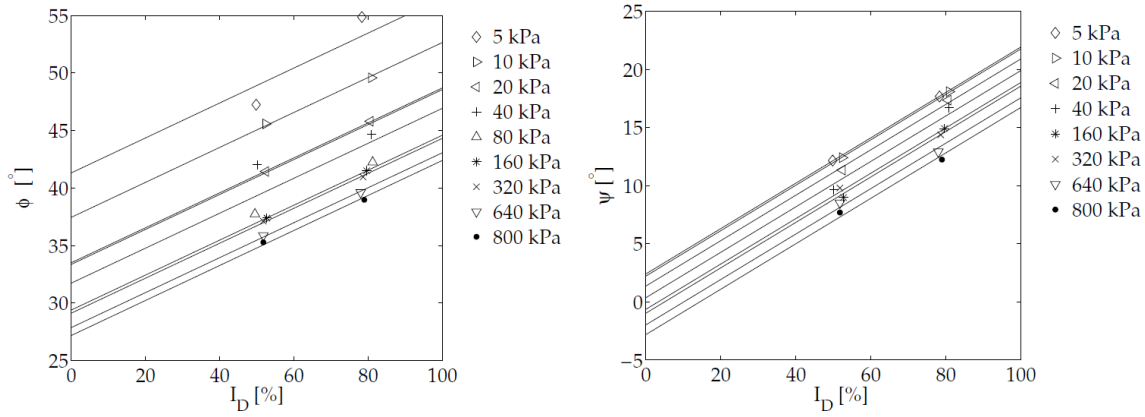

Figure B.1: Friction angle and dilatancy angle versus relative density. The legend displays the nine confining pressures σ_3, Ibsen and Bødker (1994)

Figure B.2: Based on figure B.10, the equations of the friction angle and dilation angle as a function of relative index are as equations B.1 and B.2 state:

$$\varphi_{tr} = 0.152 \cdot I_D + 27.39 \cdot \sigma_3^{'-0.2807} + 23.21 \tag{B.1}$$

$$\psi_{tr} = 0.195 \cdot I_D + 14.86 \cdot \sigma_3^{'-0.09764} - 9.946 \tag{B.2}$$

Equations B.1 and B.2 are based on curve fitting in figure B.10 where it can be seen, that the friction angle and dilation angle versus the relative density are relatively uncorrelated for small confining pressures. Moreover, the limit values of φ_{tr} and ψ_{tr} for $\sigma_3' \rightarrow 0$ are infinity. As the CPT-cone only reaches depths of around 45 cm, σ_3' will reach values between 0-2.5 kPa based on the assumption, that the effective unit weight of the sand is $\gamma' \approx 10$ kN/m^3 and the coefficient of horizontal earth pressure at rest, K_0 is 0.5.

In calculating the friction angle and dilatancy angle, the horizontal effective stress, σ'_3 is set to 5 kPa. This will yield a higher friction angle and dilation angle than the real value. As these soil strength parameters are highly stress dependant this constitutes a problem. However, the problem is assessed by increasing the air pressure in the pressure tank. Therefore, the difference in friction angle and dilation angle is considered admissible.

The relative density index I_D and the effective unit weight γ' are found using equations B.3 to B.6 in an iterative procedure, governed by the expressions:

$$\gamma' = \frac{d_s - 1}{1 + e_{insitu}} \cdot \gamma_w \tag{B.3}$$

$$\sigma_1' = \gamma' \cdot x \tag{B.4}$$

$$I_D = c_2 \cdot \left(\frac{\sigma_1'}{q_c^{c_1}}\right)^{c_3} \quad \text{(B.5)}$$

$$I_D = \frac{e_{max} - e_{insitu}}{e_{max} - e_{min}} \cdot 100 \quad \text{(B.6)}$$

Where:

$\sigma_1^{'}$	Effective vertical stress [kPa]
d_s	Specific grain density [-]
e_{insitu}	In situ void ratio
e_{min}	Minimum void ratio
x	Depth [m]
e_{max}	Maximum void ratio
γ_w	Unit weight of water [kN/m^3]
c_1, c_2, c_3	Fitting constants, $c_1 = 0.75, c_2 = 5.14, c_3 = -0.42$
q_c	Cone resistance [MPa]

In table B.1 the values of the maximum void ratio, minimum void ratio, and the specific grain density obtained in previous triaxial tests have been presented.

The iteration process is initiated by setting $e_{insitu} = e_{min}$, then the effective unit weight is calculated by equation B.3. Afterwards the effective vertical stress is computed by equation B.4. Finally the density index is obtained by equation B.5 and the new e_{insitu} is updated in equation B.6.

The iteration process is continued until the difference between two successive values of e_{insitu} is lower than10^{-4}.

The effective horizontal stress, $\sigma_3^{'}$ can be expressed in terms of the vertical effective stress, $\sigma_1^{'}$ in order to be able to apply equations B.1 and B.2 for friction angle and dilation angle. The dependency of both terms is connected by the coefficient of horizontal earth pressure at rest, K_0 as it is expressed in the next equations:

$$\sigma_3^{'} = \sigma_1^{'} \cdot K_0 \quad \text{(B.7)}$$

Where $\sigma_1^{'}$ can be expressed in terms of unit weight, overburden pressure and depth:

$$\sigma_1^{'} = \left(\gamma^{'} \cdot x + P_0\right) \quad \text{(B.8)}$$

And the coefficient of horizontal earth pressure at rest is:

$$K_0 = (1 - \sin \varphi_{tr}) \quad \text{(B.9)}$$

Finally replacing in B.7, it is obtained:

$$\sigma_3^{'} = \left(\gamma^{'} \cdot x + P_0\right) \cdot (1 - \sin \varphi_{\,tr}) \tag{B.10}$$

Where:

P_0	Overburden pressure [kPa]
K_0	Earth pressure coefficient at rest [-]

The initial stiffness of the soil E_0 is determined, the secant modulus E_{50} is calculated following the equation suggested by Ibsen et al. (2009). Notice that E_0 is not calculated for small confining pressures (0 kPa) due to the inaccuracy of the method explained before. Equations B.11, B.12 are given by Brinkgreve and Swolfs (2007).

$$E_{50} = \left(0.6322 \cdot I_D^{2.507} + 10920\right) \cdot \left(\frac{c \cdot \cos \varphi_{\,tr} + \sigma_3^{'} \cdot \sin \varphi_{tr}}{c \cdot \cos \varphi_{tr} + \sigma_3^{'ref} \cdot \sin \varphi_{tr}}\right)^{0.58} \tag{B.11}$$

$$E_0 = \frac{2 \cdot E_{50}}{2 - R_f} \tag{B.12}$$

Where:

E_{50}	Secant modulus of elasticity [kPa]
E_0	Tangential modulus of elasticity [kPa]
R_f	Ratio between q_f and q_a .The standard value is setting to R_f=0.9 [Brinkgreve and Swolfs (2007)]
$\sigma_3^{'ref}$	Reference pressure set to $\sigma_3^{'ref} = 100\ kPa$
q_f	Ultimate deviatoric stress [kPa]
q_a	Asymptotic value of the shear strength [kPa]

B.5.3 Interpretation of the CPT's

Depth versus Cone resistance is plotted in figure B.11 for the 6 CPT's carried out for the first test, and the dashed line represents the average of the cone resistance for the last 6 tests.

Figure B.11 shows that each CPT reaches similar results independent of the CPT location and similar results obtained in the first test compared to the average of the last 6 tests.

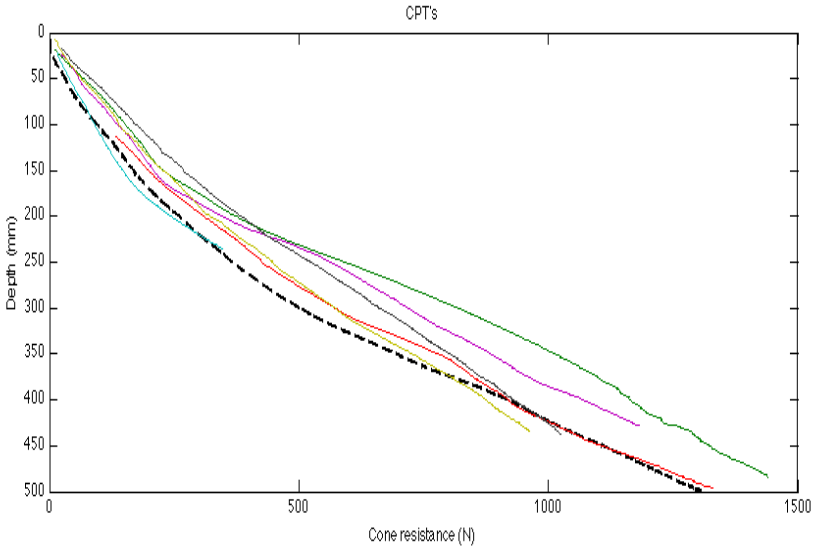

Figure B.3: For test no. 1, the 6 CPT‘s have been plotted, depth versus cone resistance. The discontinuous bold line represents the average of cone resistance obtained for the last 6 tests.

In general, table B.2 shows the average of the soil parameters for every test:

	D [mm]	P_0 [kPa]	φ_{tr} [°]	ψ_{tr} [°]	I_D [%]	γ' [kN/m^3]	E_0 [MPa]
Test 1	40	0	54.4	20.4	91.0	10.4	[-]
Test 2	40	50	50.4	19.1	89.0	10.4	38.6
Test 3	40	100	48.0	18.6	91.0	10.4	57.2
Test 4	60	0	52.6	18.1	79.0	10.2	[-]
Test 5	60	50	48.5	16.9	79.0	10.2	25.4
Test 6	60	100	45.9	16.2	79.0	10.2	41.1
Test 7	80	0	52.6	18.2	83.0	10.3	[-]
Test 8	80	50	49.5	17.9	83.0	10.2	27.6
Test 9	80	100	49.7	17.0	83.0	10.2	44.4
Test 10	80	100	45.5	15.5	76.6	10.1	36.5
Test 11	80	0	52.7	17.0	84.6	10.3	[-]
Test 12	80	50	47.3	15.7	77.9	10.2	25.2
Test 13	80	100	45.7	16.1	79.7	10.2	38.9
Test 14	80	0	52.2	17.5	76.0	10.1	[-]
Test 15	80	50	45.1	15.3	75.0	10.1	37.4
Test 16	80	100	48.3	16.7	78.0	10.1	24.9
Test 17	80	50	48.3	16.1	79.9	10.2	26.1
Test 18	80	100	45.5	15.8	78.6	10.2	38.0
Test 19	100	0	53.7	19.6	86.0	10.3	[-]
Test 20	100	50	49.9	17.6	87.2	10.3	30.0
Test 21	100	50	50.3	19.0	89.0	10.4	38.2
Test 22	100	100	47.7	18.3	90.0	10.4	55.6

Table B.2: Average CPT’s result for each test.

It was not possible to carry out CPT’s in tests 8 to 10 (marked in grey in table B.2),

since the slenderness ratio considered is too small (L/D = 3) and thus, the embedded length is only 240 mm, making it impossible to perform the CPT's. The structure which holds the CPT would hit the pile if the soil was penetrated more than 15 cm. As the 10 first cm are discarded in the soil parameters calculation only 5 cm would be considered, which makes the calculations not reliable.

For this reason, the soil parameters for tests 8 to 10 are computed using an averaged density index, I_D between the maximum and the minimum values reached through the tests. Therefore, the rest of the soil parameters can be computed based on this averaged density index. It is expected to obtain a higher friction angle for 0 kPa than for 50 kPa and 100 kPa.

Furthermore, it can be concluded that the sand is assessed as homogeneous and sufficiently compacted in order for the tests to begin.

APPENDIX C

INTERPRETATION OF TRIAXIAL TEST RESULTS

An interpretation of the triaxial test results is done through this chapter, obtaining the q-ε_1, ε_v- ε_1 and the p'-q plots, in order to compute the called characteristic line, to be able to make an approach to the real friction angle, φ_{cr} and the dilatancy angle, ψ, for Baskpard sand no. 15 used for the small-scale tests at Aalborg University Laboratory. Thus, these results will be useful not to reach the plastic behaviour of the soil, and also for the extrapolation of the small-scale tests to a full-scale prototype.

C.1 Introduction

Some triaxial tests were carried out at Aalborg University Laboratory with the purpose of analysing how the soil behaves when confining pressure is applied. Four different void ratios were employed, corresponding to density indexes of I_D = 1, 0.8, 0.51, 0.025 and many different confining pressures σ_c were applied for each density index.

The maximum q defined as equation C.1 shows, will be also determined for each confining pressure, in order to ensure that the small-scale tests are carried out without reaching a plastic behaviour of the soil staying always inside the elastic limit.

$$q = \sigma_1 - \sigma_3 \tag{C.1}$$

C.2 Triaxial tests description

The purpose of performing this kind of tests is to determine the mechanical properties of the soil assuming that the soil specimen represents the behaviour of the entire soil, and the properties obtained through these tests are reliable enough to extrapolate them to full-scale. In figure C.1 it can be observed how a triaxial test was being carried out.

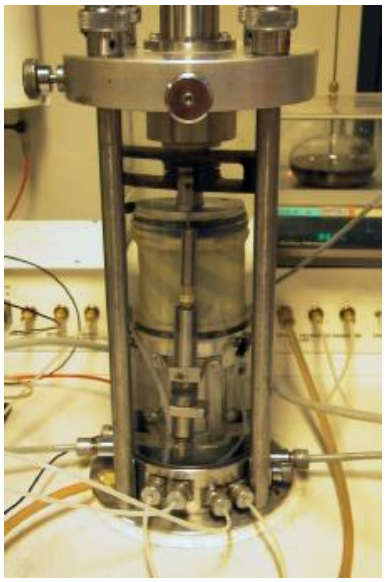

Figure C.1: Triaxial test.

Stress is applied in the three directions, σ_1, σ_2 and σ_3, cf. Figure C.2. Drainage conditions are regulated and changes in volume and strains of the soil are measured, obtaining a complete set of stress-strain data representing the behaviour of the soil.

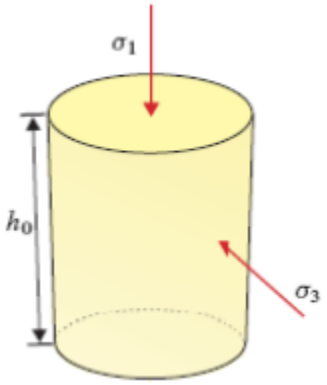

Figure C.2: Specimen of soil submitted to stress in the three directions

At first, the volume of the specimen decreases, reaching a maximum compression, but after that, the volume increases again because of dilation phenomenon.

C.3 Interpretation of triaxial tests results

The test results obtained at Aalborg University for Baaskarp Sand no. 15 are analysed and discussed in order to achieve a good comprehension of the soil behaviour when it is submitted to stress in all the directions.

There are some relations which are interesting to analyse, such as q-ε_1, ε_v-ε_1 to check how the soil deforms when it is submitted to stress and how its volume varies. It is also of high interest to investigate the stress space, q-p' in order to obtain a real value of the friction angle taking into account the dilation of the soil, ψ.

The deviator stress, q and volumetric strain, ε_v, have been plotted together against ε_1 in the same graph to check the stress state corresponding to the maximum volume variation (characteristic state), and also to be able to obtain the maximum dilation experienced by the soil corresponding to a stress status of q_{max} (failure state). For instance, all these parameters can be observed in Figure C.3 and C.4 corresponding to I_D = 1 and σ_c = 200 and 320 kPa.

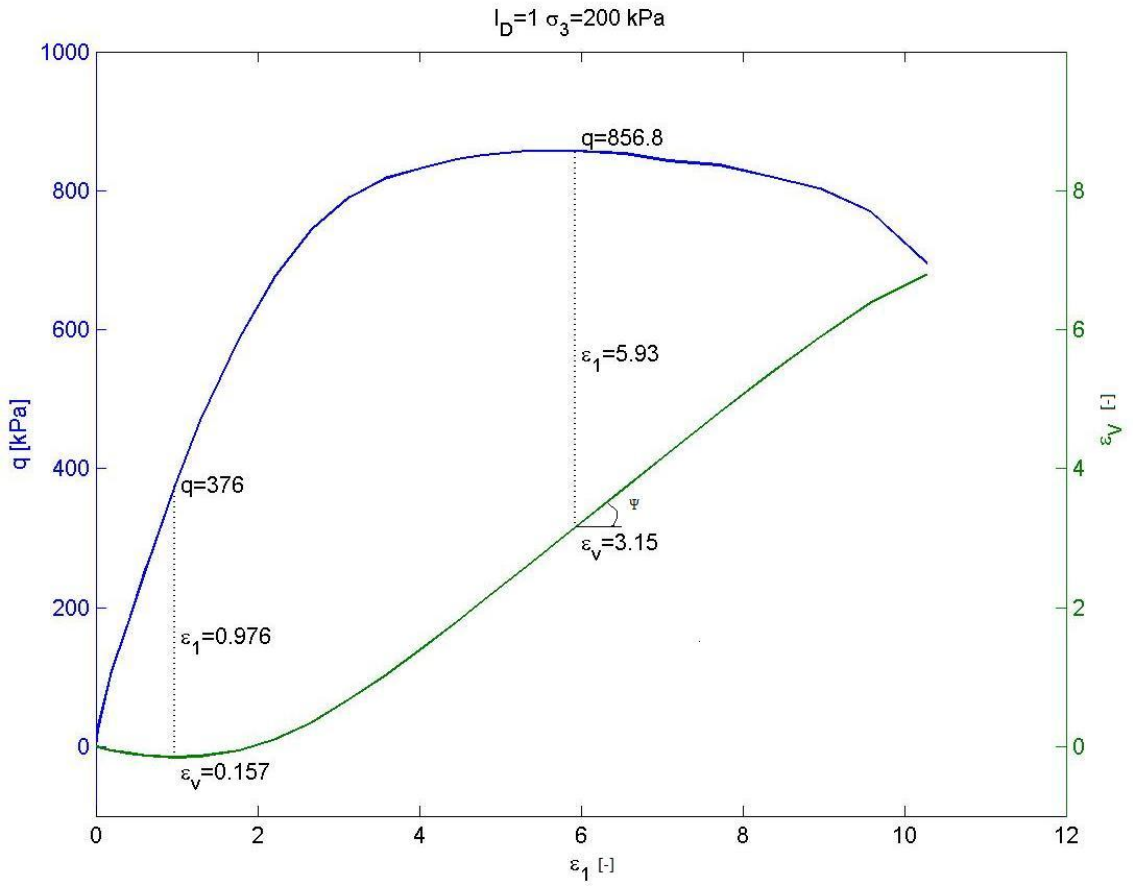

Figure C.3: q-ε_1, ε_v- ε_1, relationships for I_D = 1 and σ_c = 200 kPa

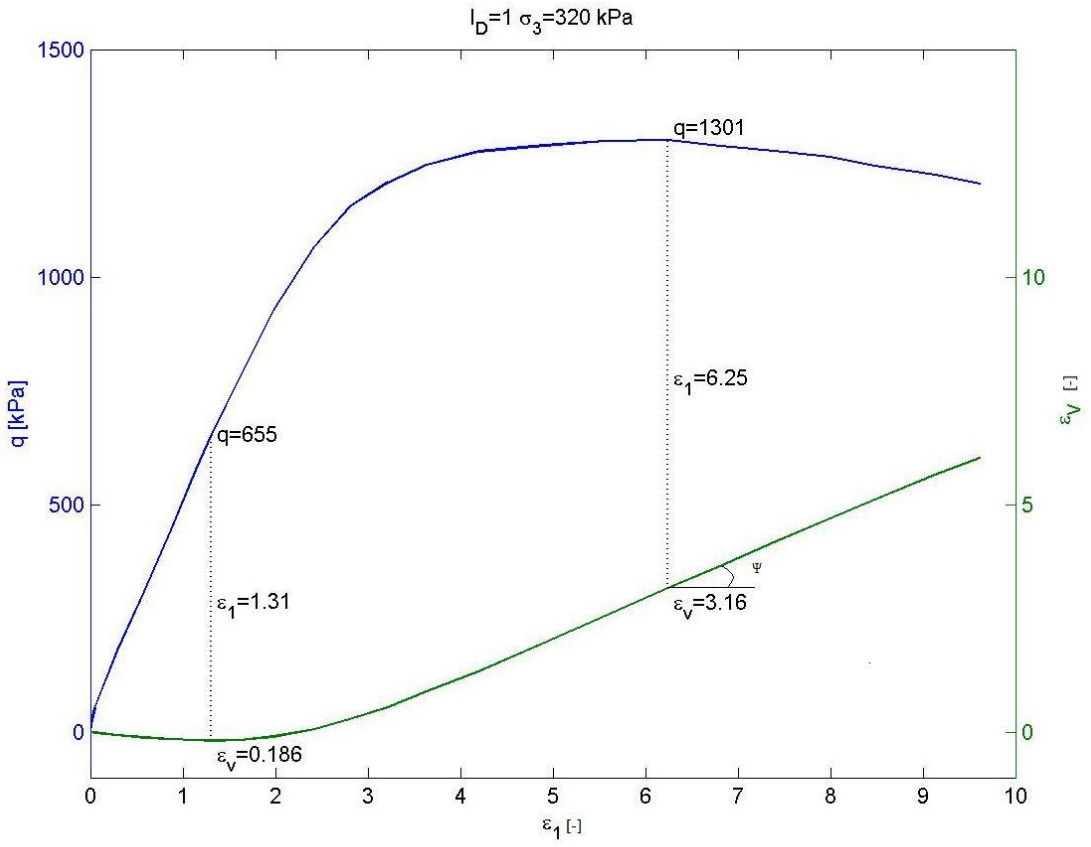

Figure C.4: q-$\varepsilon_{1,}$ ε_{v}- $\varepsilon_{1,}$ relationships for I_D = 1 and σ_c = 320 kPa

As it was expected, the peak of the volumetric strain, ε_v and the deviator stress, q are higher when the confining pressure increases. For the maximum volumetric strain, a value of q is obtained by the straight line plotted in the upward direction. In the stress space, the q corresponding to the maximum ε_v can be plotted against p', obtained as equation C.2 shows, defining a straight line (characteristic line) which represents the transition between an elastic and the plastic behaviour of the soil, cf. Figure C.5.

$$p' = \frac{\sigma_1 + 2 \cdot \sigma_3}{3} \qquad \text{(C.2)}$$

For instance, the q-p' graphs corresponding to the different density indexes are obtained based on triaxial tests realised at different confining pressures. Figure C.5 shows the characteristic line obtained for I_D = 1.

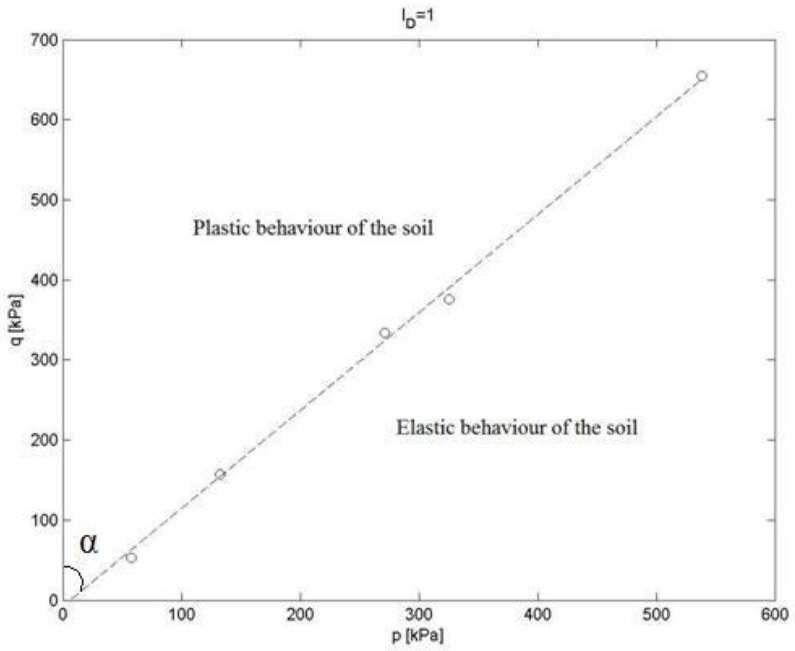

Figure C.5: Characteristic line for I_D = 1, obtained for σ_c = 40, 80, 160, 200, 320 kPa

The real value of the friction angle, called the peak friction angle, is defined as it is shown in equation C.3:

$$\varphi_{peak} = \varphi_{cl} + \psi_{peak} \tag{C.3}$$

Where:

φ_{peak}	Real value of friction angle [°]
φ_{cl}	Characteristic friction angle [°]
ψ	Dilation angle [°]

The characteristic friction angle, φ_{cl} is calculated based on the slope of the characteristic line which defines the border line where the soil experiments a change in its behaviour (from elastic to plastic), cf. Equation C.4.

$$\sin \varphi_{cl} = \frac{3}{1 + 6 \cdot \tan \alpha} \tag{C.4}$$

The maximum dilation of the soil, ψ_{peak} occurs for the peak value of the deviator stress, q_{max} in the q-ε_1 relationship, and q_{max} for the different confining pressures is represented in the stress space, q-p' adopting the form of a curve above the characteristic line, cf. Figure C.6.

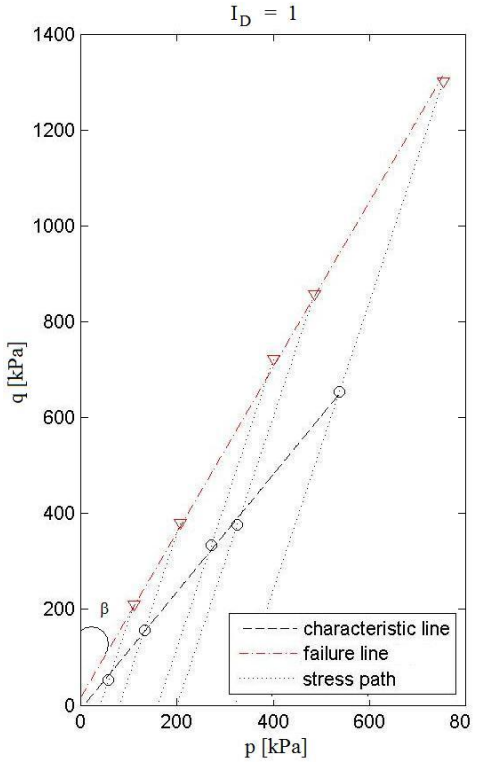

Figure C.6: Failure state line and characteristic state line

As it can be observed in figure C.6, it was obtained empirically that the q_{max} data points and the q data points corresponding to the maximum volumetric strain, ε_v for the same confining pressure can be connected by a straight line which in all cases has a constant slope of 1/3.

Thus, the maximum dilation of the soil can be computed by means of the variation of q_{max} with the confining pressure (red function shown in Figure C.6). Cf. Equations C.5 and C.6.

$$\sin \varphi_{peak} = \frac{3}{1 + 6 \cdot \tan \beta} \tag{C.5}$$

$$\psi_{peak} = \varphi_{peak} - \varphi_{cl} \tag{C.6}$$

Four different values of characteristic friction angle, φ_{cl} 4 peak dilation angles, ψ_{peak} and 4 peak friction angles, φ_{peak} are calculated, depending on the considered density index derived from each void ratio by equation C.7. Cf. Figures C.9, C.10 and tables 1 to 4.

$$I_D = \frac{e_{\max} - e_{insitu}}{e_{\max} - e_{\min}} \cdot 100 \qquad \text{(C.7)}$$

Where:

$e_{\max}$	0.858
$e_{\min}$	0.549

C.4 Triaxial test results

In the following, the graphs showing the q-ε_1, ε_v-ε_1, and q-p' representing the characteristic state and the failure state are presented for the 4 density indexes used for the triaxial tests. The confining stresses used to obtain these graphs are the ones shown in tables 1 to 4.

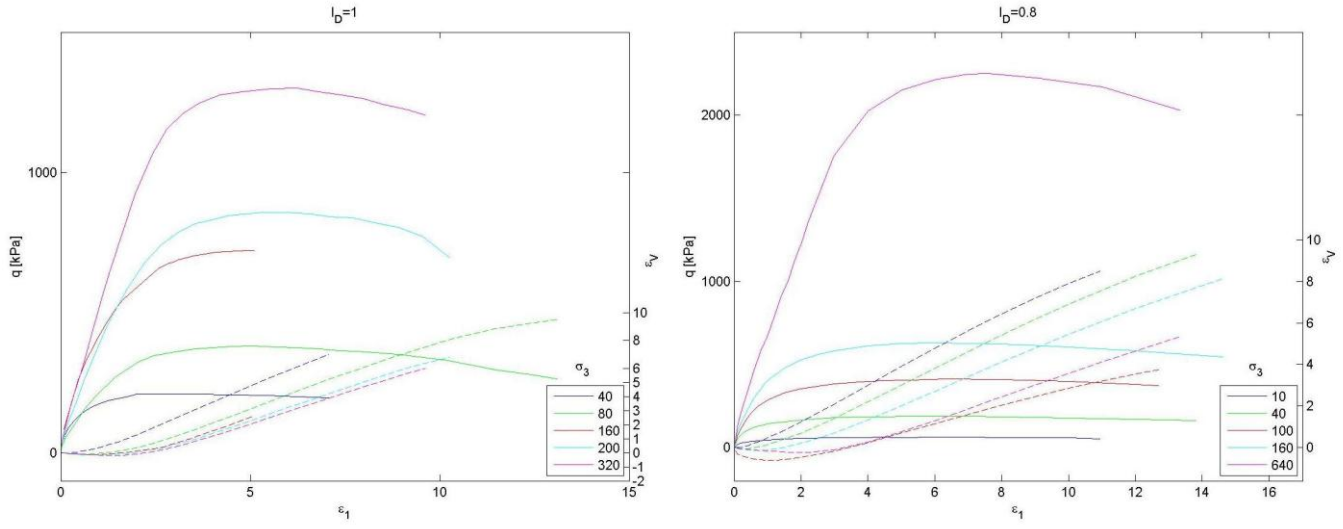

Figure C.7: q-ε_1 and ε_v- ε_1 for I_D = 1 and 0.8

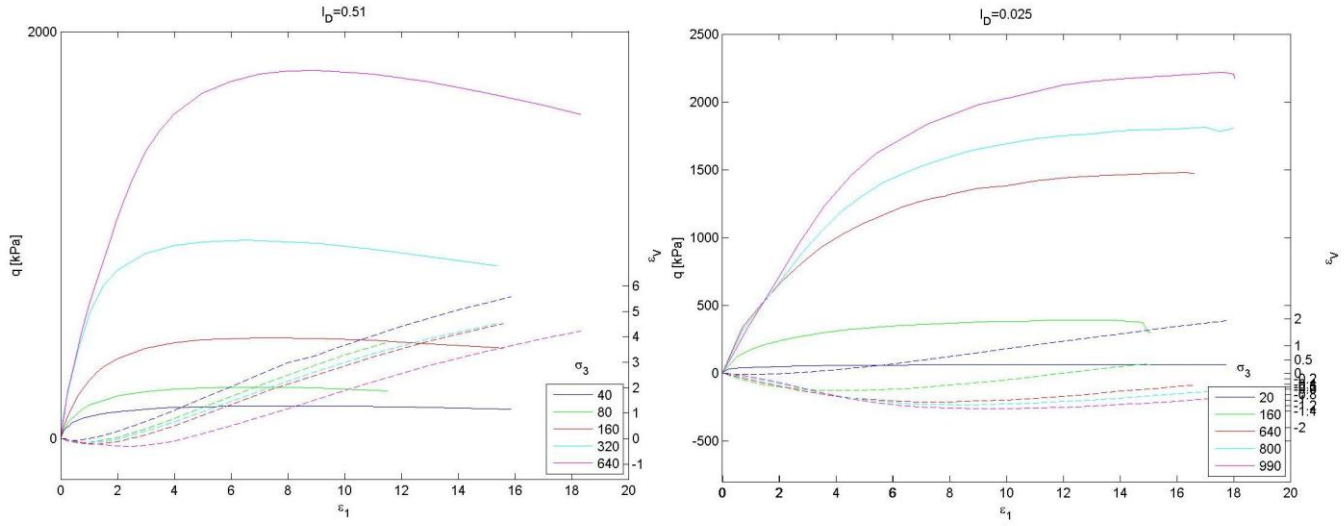

Figure C.8: q-ε_1 and ε_v- ε_1 for I_D = 0.51 and 0.025

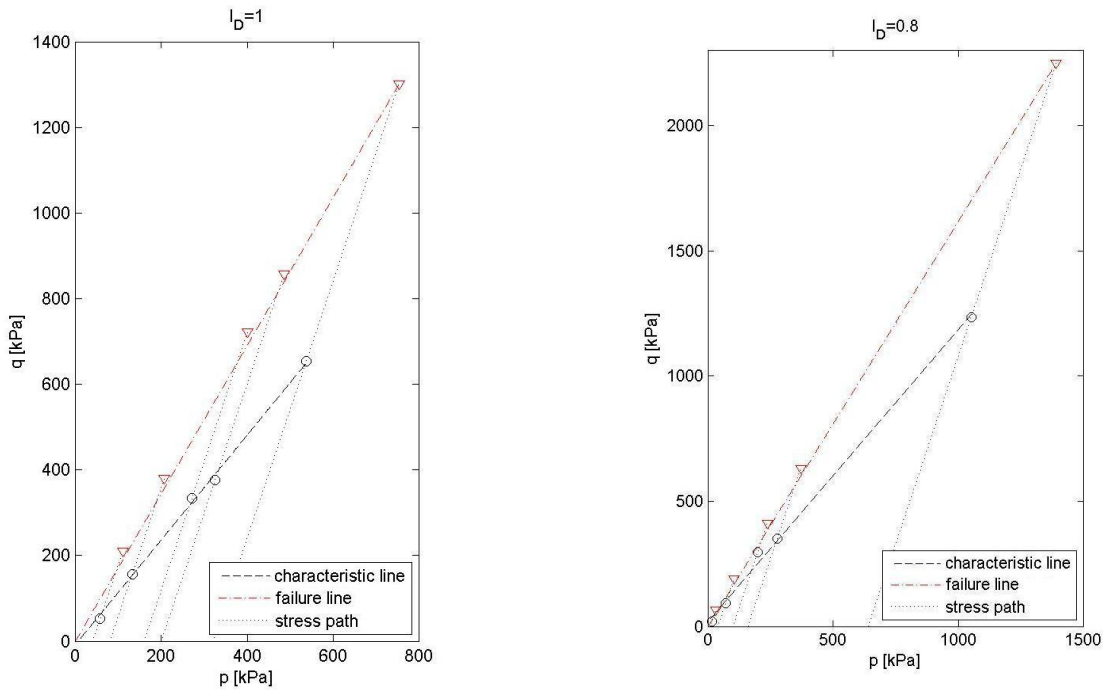

Figure C.9: q-p' for I_D = 1 and 0.8

σ_c [KPa]	φ_{cl} [˚]	φ_{peak} [˚]	Ψ_{peak} [˚]
40	30.5	46.3	15.8
80	30.5	44.8	14.2
160	30.5	43.8	13.3
200	30.5	43	12.5
320	30.5	42.1	11.6

Table 1: Friction angles and dilation angle for I_D = 1

σ_c [KPa]	φ_{cl} [˚]	φ_{peak} [˚]	Ψ_{peak} [˚]
10	29.3	49.7	19.2
40	29.3	44.6	14.1
100	29.3	42.3	11.8
160	29.3	41.6	11.1
640	29.3	39.6	9.1

Table 2: Friction angles and dilation angle for I_D = 0.8

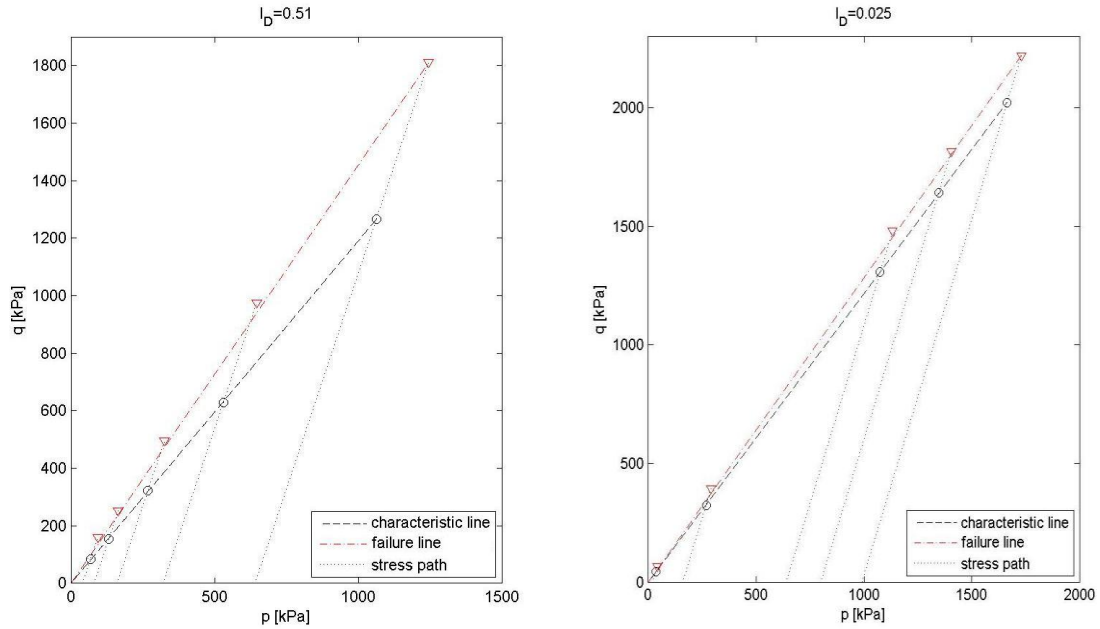

Figure C.10: Stress space, *q-p'* for I_D = 0.51 and 0.025

σ_c [KPa]	φ_{cl} [˚]	φ_{peak} [˚]	Ψ_{peak} [˚]
40	29.8	41.8	12
80	29.8	37.8	8
160	29.8	37.4	7.6
320	29.8	37.1	7.3
640	29.8	35.9	6.1

Table 3: Friction angles and dilation angle for I_D = 0.51

σ_c [KPa]	φ_{cl} [˚]	φ_{peak} [˚]	Ψ_{peak} [˚]
20	30.4	38	7.6
160	30.4	33.4	3.05
640	30.4	32.4	2.05
800	30.4	32.1	1.73
990	30.4	31.9	1.54

Table 4: Friction angles and dilation angle for I_D = 0.025

In conclusion, it can be observed in Figures C.9 and C.10 that the lower density index, the more near the failure line is to the characteristic line, meaning that the dilation angle, ψ decreases for higher void ratios of the soil, *e*.

The characteristic friction angle, φ_{cl} is almost constant and independent of the void ratio, meaning that the characteristic line, and thus the transition from an elastic behaviour of the soil to a plastic behaviour remains constant, cf. Figure C.11. This result is expected, since every kind of soil has its own characteristic friction angle, and the peak friction angle varies depending on the density index or the void ratio.

Moreover, in typical offshore locations, the friction angle is much lower (rarely existing above 40 degrees) than the ones obtained at Aalborg University Laboratory in the small-scale tests. This is due to the fact that the pressure in typical offshore locations is higher than the maximum applied in the pressure tank (100 kPa).

On the other hand, it can be observed in the triaxial tests results that the higher the confining pressure is, the more accurate and reliable the obtained friction angle

becomes. This behaviour is due to the strong relationship between the friction angle and the stress level.

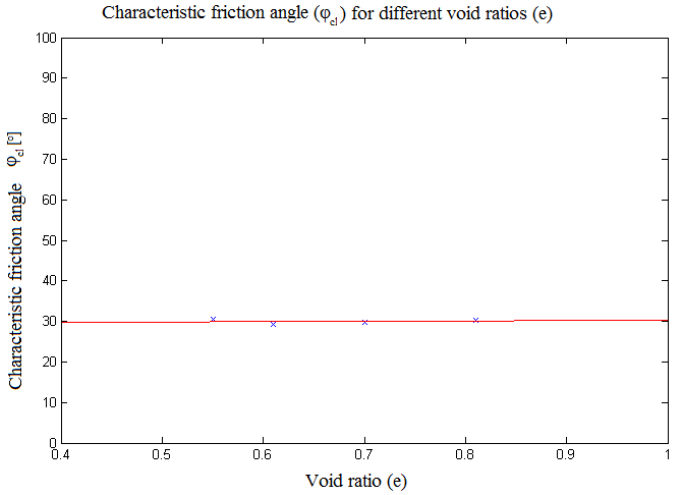

Figure C.11: Constant characteristic friction angle for different void ratios

APPENDIX D

SCALING SMALL-SCALE MODELS OF MONOPILES IN SAND

In this chapter, the techniques and theories used for the scaling and analysis of small-scale models are described in the beginning. Then some assumptions are described followed by the scaling criteria which was applied to the models. Finally some similarity laws and relations are presented in order to extrapolate small-scale models to full-scale models.

D.1 Introduction

Small-Scale modeling is often used to provide accurate and reliable results of phenomenos which occur in reality. These small-scale models are conducted in such a way that small-scale effects are minimised by the help of the pressure tank. Dimensional analysis is necessary when small-scale tests are carried out in the field of Geotechnical Engineering, which means that any phenomenon can be described by a dimensionless group, known as Π-factors. For this reason, it is essential to use a similitude theory in order to be able to provide quantitative results.

There are many similitude theories; however, all of them provide a set of scaling relations to adapt the observed behaviour in a small-scale model to the real-scale behaviour. This similarity is achieved when the model and the prototype's dimensionless group has the same values in both of them.

Some scaling laws will be derived from a dimensional analysis, and the empirical data can be extrapolated to the full-scale model.

D.2 Dimensional analysis and similitude theories

The dimensional analysis of a physical phenomenon is done by representing a set of dimensionally and homogeneous equations among certain significant variables. This equations should not depend on the fundamental units of measurement. If a physical phenomenom can be correctly described by dimensionally homogeneous equations it can be assumed that a complete similarity exists between the phenomenon and the small-scale test. This similarity has to be fulfilled geometrically, kinematically and dinamically. Prosperine K. Peralta (2010).

If similarity exists, the mechanical behaviour of the physical phenomenon can be reproduced by the small-scale model, which means a reduction in time and money, and can be carried out under controlled conditions. Three conditions must be fulfilled to achieve similarity:

- A constitutive law for soil and a load-displacement relationship for monopile foundations must be derived and expressed by dimensionless variables.

- Constitutive law and load-displacement relationship must be identical.

- Constitutive law and load-displacement relationship must be verified by small-scale tests at Aalborg University Laboratory.

Dimensional analysis supports that the significant variables that influence a physical phenomenon can be grouped into a set of dimensionless products that form a solution to the problem, named Π-products.

By grouping the specified significant variables into dimensionless products, a reduction of these variables is obtained, and a solution to the problem can be obtained as a function of the Π-factors.

Some combinations of the variables can be formed and several dimensionless products can be obtained. However, only those which are independent of each other are valid. Buckingham's theorem is used to obtain a complete set of dimensionless products, meaning that all possible combination of variables forming independent dimensionless products have been found.

Based on Buckingham's theorem, the number of dimensionless products in a complete set is equal to the number of the specified variables minus the number of fundamental dimensions in the problem, see equation D.1:

$$f(G) = f(O - P) \tag{D.1}$$

Where:

G	Number of dimensionless products in a complete set.
O	Number of significant variables in the problem.
P	Fundamental dimensions in the problem.

Once a complete set of dimensionless products for an equation defining a physical phenomenon is achieved, quantitative information can be derived by means of a model test whose setup provides independent dimensionless products with similar values for the model than for the prototype.

It can be said that the small-scale model and the prototype are completely similar, and full similitude laws can be enforced on the model.

According to Langhaard (1951), full similarity between a small-scale model and a prototype can be defined as geometric, kinematic or dynamic, however through this project only geometric similarity is possible. Besides, being the soil involved also its properties are considered equal in laboratory and in reality.

D.3 Constitutive Law

A constant problem for engineers is the challenge of finding a scaled equivalent of a prototype soil material, which in many cases is virtually impossible.

A constitutive law for cohesionless soil under cylindrical compression and extension was presented by Gudehus et Hettler (1983) using a more general formulation presented earlier by Hettler (1981).

Their theory was developed for the case of cohesionless soils under monotonic and cyclic loading affirming that similarity can exist when the soil stresses before loading (initial stress state) are identical in both, small-scale model and full-scale model.

Initially, before any load is applied to the soil, the stress path leads to the initial principal stresses: $\sigma_{1,0}$ and $\sigma_{2,0} = K_0 \cdot \sigma_{1,0}$, where K_0 denotes the coefficient of earth pressure at rest.

Further, when the soil is loaded a stress path can be defined by $\Delta\sigma_1$ and $\Delta\sigma_2 = K \cdot \Delta\sigma_1$ where K is another constant different to the coefficient of earth pressure at rest. When a stress path is presented, consequently there are associated strains $\Delta\varepsilon_1$ and $\Delta\varepsilon_2$ which are a function of the Π-products as shown in equations D.2 and D.3:

$$\Delta\varepsilon_1 = f_1\left(\frac{\Delta\sigma_1}{\sigma_{1,0}}, K_0, K\right) \tag{D.2}$$

$$\Delta\varepsilon_2 = f_2\left(\frac{\Delta\sigma_2}{\sigma_{2,0}}, K_0, K\right) \tag{D.3}$$

Notice that f_1 and f_2 can be expressed as functions of Π-products, and the first product should remain constant under any confining pressure. It is important to remark that if the same stress path to a soil medium with different voids ratios, *e* is applied, the strain path varies proportionally.

If a log-log scale is considered when plotting $\Delta\varepsilon_1$ and $\Delta\varepsilon_2$ against $\frac{\Delta\sigma_1}{\sigma_{1,0}}$ and $\frac{\Delta\sigma_2}{\sigma_{2,0}}$ straight lines must be obtained, since a linear relation exists between the initial stress path and the strain, always remaining in an elastic behaviour of the soil without reaching the plastic behaviour.

Taking into account the factors which depend on *K* and K_0, and considering the hypothesis explained before, the corresponding function related to equations D.2 and D.3 can be rewritten as a stress-independent constitutive law with the shape of a potential function:

$$\Delta\varepsilon_1 = f(K_0, K)\cdot\left(\frac{\Delta\sigma_1}{\sigma_{1,0}}\right)^u \tag{D.4}$$

$$\Delta\varepsilon_2 = f(K_0, K)\cdot\left(\frac{\Delta\sigma_2}{\sigma_{2,0}}\right)^u \tag{D.5}$$

D.4 The power law

Based on the constitutive law derived above, it has been chosen a force-displacement relationship named the “power law”. This law was purposed by Hettler (1981) and investigated by Gudehus and Hettler (1983), but it has not been until 2010 when Peralta used this “power law” succeeding in a research regarding piles subjected to cyclic loading.

The power law states that the lateral displacement of any rigid structure is proportional to a power of the normalized horizontal load.

As it was described when obtaining the constitutive law, before applying any load to the system, the soil is considered to be in the state of natural sedimentation, so that at a generic depth x:

$$\begin{aligned}\sigma_{1,0} &= \gamma \cdot x \\ \sigma_{2,0} &= K_0 \cdot \sigma_{1,0}\end{aligned} \tag{D.6}$$

When a lateral load, H is applied to the monopile, displacements in any directions will occur. Taking the horizontal displacement u as main objective through this project, its correspondent horizontal strain is expressed by equation D.7:

$$\Delta\varepsilon_2 = f_s(\frac{u}{L}) \tag{D.7}$$

Where f_s is *a* dimensionless factor dependent on the spatial coordinates, u is the lateral displacement of the monopile and L is the embedded pile length. The horizontal stress $\Delta\sigma_2$ is defined by the power law as shown in equation D.8:

$$\Delta\sigma_2 = \left(\frac{f_s}{f_{k_0,k}} \cdot \frac{u}{L}\right)^k \cdot \sigma_{2,0} \tag{D.8}$$

The lateral force acting on the pile, H discarding shear stresses, is the sum of all horizontal stresses acting on the pile, yielding:

$$\begin{aligned}H &= \int_0^L \int_{-D/2/}^{D/2} \Delta\sigma_2 \cdot dx \cdot dz; \\ H &= \int_0^L \int_{-D/2/}^{D/2} \left(\frac{f_s}{f_{k_0,k}} \cdot \frac{u}{L}\right)^k \cdot K_0 \cdot \gamma \cdot x \cdot dx \cdot dz; \\ H &= \gamma \cdot \left(\frac{u}{L}\right)^k \cdot \int_0^L \int_{-D/2/}^{D/2} \left(\frac{f_s}{f_{k_0,k}}\right)^k \cdot K_0 \cdot x \cdot dx \cdot dz;\end{aligned} \tag{D.9}$$

Thus, the dimensionless lateral displacement can be expressed as:

$$\frac{u}{L} = \left(\frac{H}{\gamma \cdot L^3}\right)^{1/k} \cdot \left(\int_0^L \int_{-D/2/}^{D/2} \left(\frac{f_s}{f_{k_0,k}}\right)^k \cdot K_0 \cdot \frac{x}{L} \cdot \frac{dx}{L} \cdot \frac{dz}{L};\right)^{-1/k} \tag{D.10}$$

Naming *C* the second product and rearranging the equation in dimensionless quantities, equation D.10 is simplified to:

$$\frac{u}{L} = \left(\frac{H}{\gamma \cdot L^3} \right)^k \cdot C \qquad \text{(D.11)}$$

C is a dimensionless product that is a function of the spatial coordinates, soil parameters (*k*, K_0 and *K*), pile geometric parameters and depth (*x/L*).

The dimensionless load-displacement equation shown above is similar to the assumed dimensionless constitutive law of a cohesionless soil, cf. Equation D.5. Hence, one of the essential conditions of the similitude theory has been fulfilled.

Therefore, equation D.11 will be employed as the corresponding function for the load-displacement behaviour of a monopile foundation.

D.5 Π-products derived for the load-displacement equation

Considering a simplified system for the 1-g modelling of laterally-loaded piles in cohesionless soil, the variables chosen to describe the behaviour of a monopile foundation subjected to horizontal static loading are described in figure D.1, where:

H	Value of the lateral Load [F]
L	Embedded length of the pile [L]
D	Diameter of the pile [L]
$E_p I_p$	Pile flexural rigidity [F $\cdot$L^2]
γ	Unit weight of the soil [KN/L^3]
φ	Friction angle of the soil [˚]
K_0	Coefficient of earth pressure at rest

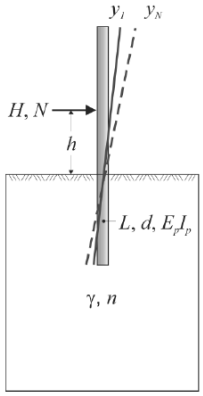

Figure D.1: Sketch of a simplified system and variables in a laterally-loaded pile ,Prosperine K. Peralta (2010)

Thus, the lateral displacement of a pile subjected to lateral static loading can be expressed as:

$$u = fs(H, L, D, E_p I_p, \varphi) \tag{D.12}$$

Notice that the vertical force corresponding to the self-weight is not taken into account, and the friction angle, φ is a function of the void ratio, e and the mean effective stress p'. Furthermore E_pI_p can be disregarded since a rigid system is considered for all the calculations.

There are two fundamental dimensions in Equation D.12: force, F and length, L and five significant variables. Therefore, according to the Buckingham's theorem stated in equation D.1, four homogeneous dimensionless products are needed in a complete set, given as Equation D.13 shows:

$$\frac{u}{L} = g_s\left(\frac{H}{\gamma \cdot L^3}, \frac{D}{L}, \varphi\right) \tag{D.13}$$

g_s represents a generic function which will be found theoretically and thereafter numerically by means of small-scale tests at Aalborg University Laboratory.

Furthermore, a corresponding equation should be found for each dimensionless variable presented in equation D.13, yielding:

$$\frac{u}{L} = g_H \cdot g_D \cdot g_\varphi \tag{D.14}$$

This equation, as it was explained before, remains valid in small-scale and in full-scale only if there is dimensional similarity between the model and the prototype. For further details see Borobia, Mikalauskas and Troya (April, 2011).

D.6 Similitude Laws

In the following, the similitude laws for a laterally static loaded pile are derived. Due to the non-existence of cyclic loading of the soil and the pile structure, dynamic similarity is unnecessary.

Based on the initial stress state of the soil "at rest", the dimensionless lateral displacement y/L of the model can be extracted to the prototype by means of the geometric similarity ratio λ, set to $\lambda = 0.01826$.

The geometrical similarity states that:

$$\frac{L_M}{L_P} = \lambda \tag{D.15}$$

Where the sub-indexes $_M$ and $_P$ are referred to the model and prototype respectively. Then the similitude laws are defined in Equations D.16 to D.20:

$$(L)_M = \lambda (L)_P \tag{D.16}$$

$$(y)_M = \lambda (y)_P \tag{D.17}$$

$$(h)_M = \lambda (h)_P \tag{D.18}$$

$$(H)_M = \lambda^3 (H)_P \tag{D.19}$$

$$(D)_M = \lambda (D)_P \tag{D.20}$$

By the use of the scaling laws, the measured results of small-scale model tests carried out in the lab can be extrapolated to a full-scale prototype.

Notice that the lateral force taken into account in the small-scale model is the one which corresponds to a maximum rotation of 0.25 degrees allowed by API and DNV regulations for the design of offshore wind turbine foundations.

In table D.1 the Π-products and equivalent scaling for the 1-g model pile described in Borobia, Mikalauskas and Troya (April, 2011) for 100 kPa and *L/D* = 5 are shown:

Π-products	Model Pile Parameters	Prototype Parameters
Test 3		
f_d = 0.0033	D = 0.04 m L = 0.2 m	D = 2.2 m L = 10.1 m
f_n = 0.0874	γ = 10.4 kN/m^3	γ = 10.4 kN/m^3
f_H = 4.604	H = 300 N	H = 4.9 MN
Test 6		
f_d = 0.0121	D = 0.06 m L = 0.3 m	D = 3.29 m L = 16.43 m
f_n = 0.0874	γ = 10.2 kN/m^3	γ = 10.2 kN/m^3
f_H = 5.850	H = 1000 N	H = 16.4 MN
Test 13		
f_d = 0.016	D = 0.08 m L = 0.4 m	D = 4.38 m L = 21.9 m
f_n = 0.0874	γ = 10.2 kN/m^3	γ = 10.2 kN/m^3
f_H = 2.675	H = 1300 N	H = 21.3MN
Test 22		
f_d = 0.0173	D = 0.1 m L = 0.5 m	D = 5.48 m L = 27.4 m
f_n = 0.0874	γ = 10.4 kN/m^3	γ = 10.4 kN/m^3
f_H = 2.861	H = 2800 N	H = 45.9MN

Table D.1: Π-products, Model Pile Parameters and Prototype Parameters

APPENDIX E

PRESENTATION OF EXPERIMENTAL RESULTS

In this appendix, an interpretation of the strain gauges measurements is carried out and the experimental results are presented through it. Bending moment distribution, load-deflection plots, and p-y curves are shown for the 10 tests carried out at Aalborg University Laboratory. Notice that for tests 1, 8, 9 and 10 bending moment distribution and p-y curves are not shown, since no strain gauges were used through these tests.

E.1. Interpretation of strain gauge measurements

Once the tests have been conducted, an interpretation of the strain gauges measurements must be carried out. The output file of each test is a matrix with around 80.000 rows and 22 columns which defines the time steps and the strain measurements from the strain gauges, respectively. In order to simplify the calculations, 100 time steps are chosen equally distributed through the test.

At each time step the average strain, ε, is computed for each pair of strain gauges:

$$\varepsilon = \frac{abs(\varepsilon_1 - \varepsilon_2)}{2} \tag{E.1}$$

ε_1, and ε_2 are the single strain gauge measurements at the same level of the pile. For the calculation of the bending moment distribution, calibration factors are used. Bending moment is related to strain by equation E.2:

$$M = k_g \cdot \varepsilon \tag{E.2}$$

where:

M	Bending moment [Nmm]
k_g	Calibration factor [Nmm]
ε	Strain [-]

Since the pile is loaded without reaching the yielding limit, the relation force-displacement is supposed to be linear, thereby Hooke's law is applied, so $\sigma_{xx,i}$ can be computed by equation E.3:

$$\sigma_{xx,i} = E \cdot \varepsilon_i \tag{E.3}$$

With all this, *M(x)* can be computed at 11 different levels (where every couple of strain gauges is placed) at 100 steps of time.

The curvature of the pile can be calculated by equations E.4 to E.6:

$$\sigma = \frac{M}{Izz} \cdot y \tag{E.4}$$

$$E \cdot \varepsilon = \frac{M}{Izz} \cdot r^* \tag{E.5}$$

$$E \cdot \varepsilon = \frac{E \cdot I_{zz} \cdot \kappa}{I_{zz}} \cdot r^* \tag{E.6}$$

Yielding:

$$\kappa = \frac{\varepsilon}{r^*} \tag{E.7}$$

where:

E	Young's modulus of elasticity for the pile [F/L^2]
I_{zz}	Second moment of inertia [L^4]
r^*	Distance from the centre of the pile to the strain gauges [L]
κ	Curvature of the pile [L^{-1}]

Based on the bending moment distribution all over the depth, the p-y curves can be obtained by integrating twice and differentiating the distribution of moment twice along the length of the pile. The deflection of the pile wall, *y(x)*, and the soil resistance *p(x)*, can be obtained by:

$$y(x) = \iint \frac{M(x)}{E \cdot I_{zz}} dx \cdot dx \tag{E.8}$$

$$p(x) = \frac{d^2 M(x)}{dx^2} \tag{E.9}$$

In order to differentiate *M(x)* twice, and obtain the soil resistance *p(x)*, Piecewise Polynomial Curve fitting method will be presented through the next paragraphs. Yang & Liang (2006).

E.1.1. Calculation of soil resistance by piecewise polynomial curve fitting method

Piecewise polynomial curve fitting method employs five points of the measured bending moment in order to determine a polynomial function of third order which fits the points, using the least square technique.

This third degree polynomial function is differentiated twice and evaluated in the middle of the interval to obtain the soil resistance, *p*, at that point.

This step is repeated as many times as possible, depending on the number of data points that are being considered, moving one point lower in the distributed data, or one point upper. For a better understanding of the method see figure E.1.

To evaluate the soil resistance in the points located near to the soil surface, or the deepest points, the function which includes them situated in the border is differentiated twice, and evaluated at those points.

Notice that the moment distribution is zero above where the load is applied, and then varies linearly from that point until the soil surface. A linear regression is used to fit these data points, cf. Figure E.1.

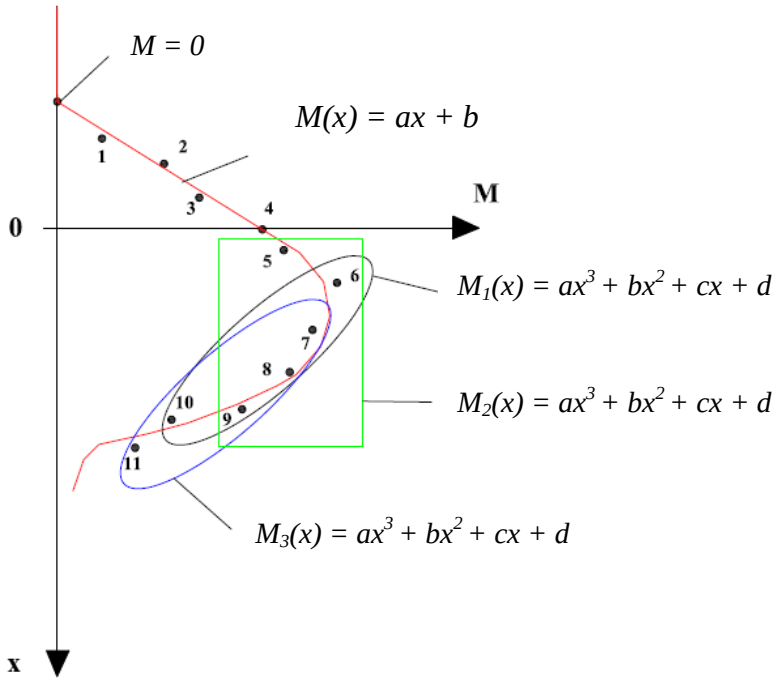

Figure E.1: Piecewise Polynomial Curve Fitting Method for *L/D* = 5

A boundary condition to be able to apply this method must be included: the zero moment at the loading point, or a known value of the moment at the soil surface.

In this project, in all the tests carried out, a pair of strain gauges was placed on the soil surface, with the objective of measuring the strain, and thus calculating the bending moment at that point. This bending moment is then used as boundary condition for the calculations.

E.1.2. Lateral deflection of the pile

The lateral deflection of the pile is differently obtained, depending on which depth is being considered. Two different zones can be differentiated, directly related to the moment distribution, in order to obtain the lateral deflection of the pile, *y*, as it can be observed in figure E.2:

1. Between the load applied and the soil surface (blue line).
2. Under the soil surface (red curve).

The moment distribution can be seen in equation E.10 and graphically shown in figure E.2:

$$M(x) = \begin{cases} M_1 = 0 & -640 \le x \le -370 \\ M_2(x) = a \cdot x + b & -370 \le x \le 0 \\ M_3(x) = a \cdot x^5 + b \cdot x^4 + c \cdot x^3 + d \cdot x^2 + e \cdot x + f & 0 \le x \le 320 \end{cases} \quad \text{(E.10)}$$

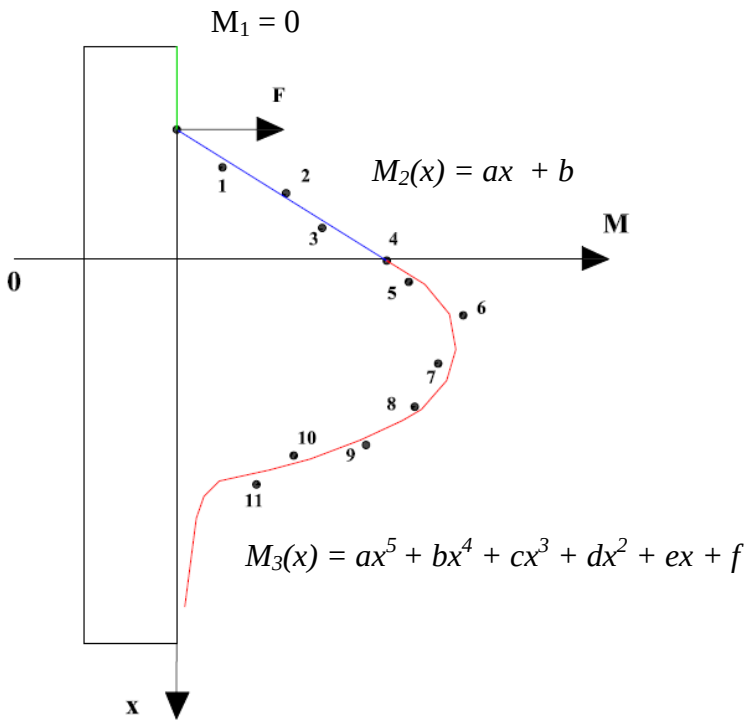

Figure E.2: Moment distribution along the pile

1. Lateral deflection function obtained from the linear distribution moment (blue line defined by equation E.11:

$$M_2(x) = a \cdot x + b \quad \text{(E.11)}$$

$$y_2(x) = \iint \frac{M_2(x)}{E \cdot I_{zz}} dx \cdot dx \Rightarrow \frac{1}{E \cdot I_{zz}} \cdot \left(\frac{a \cdot x^3}{6} + \frac{b \cdot x^2}{2} + C_1 \cdot x + C_2 \right) \quad \text{(E.12)}$$

2. Lateral deflection function obtained from the red distribution of the moment data shown in figure E.2.

$$M_3(x) = a \cdot x^5 + b \cdot x^4 + c \cdot x^3 + d \cdot x^2 + e \cdot x + f \tag{E.13}$$

$$y_3(x) = \iint \frac{M_3(x)}{E \cdot I_{zz}} dx \cdot dx \Rightarrow$$
$$\frac{1}{E \cdot I_{zz}} \cdot \left(\frac{a \cdot x^7}{42} + \frac{b \cdot x^6}{30} + \frac{c \cdot x^5}{20} + \frac{d \cdot x^4}{12} + \frac{e \cdot x^3}{6} + \frac{f \cdot x^2}{2} + C_3 \cdot x + C_4 \right) \tag{E.14}$$

In summary, the lateral deflection function can be defined in two intervals, but has to be a continuous function between the intervals, cf. equation E.15:

$$y(x) = \begin{cases} y_2(x) = \dfrac{1}{E \cdot I_{zz}} \cdot \left(\dfrac{a \cdot x^3}{6} + \dfrac{b \cdot x^2}{2} + C_1 \cdot x + C_2 \right) & -370 \le x \le 0 \\ y_3(x) = \dfrac{1}{E \cdot I_{zz}} \cdot \left(\begin{array}{l} \dfrac{a \cdot x^7}{42} + \dfrac{b \cdot x^6}{30} + \dfrac{c \cdot x^5}{20} + \\ \dfrac{d \cdot x^4}{12} + \dfrac{e \cdot x^3}{6} + \dfrac{f \cdot x^2}{2} + C_3 \cdot x + C_4 \end{array} \right) & 0 \le x \le 320 \end{cases} \tag{E.15}$$

In equation E.15, the coefficients *a*, *b*, *c*, *d*, *e* and *f* have been obtained, fitting the bending moment points in each time step obtained from the strain measurements by the strain gauges.

On the other hand, 4 boundary conditions must be formulated for the calculation of C_1, C_2, C_3, and C_4, to be able to obtain the lateral deflection:

- Constant rotation above second displacement transducer:

$$\theta = \frac{dy_1}{dx} = cte \approx \frac{\Delta y}{\Delta x} = \frac{y_3 - y_2}{x_3 - x_2} \Rightarrow y_1'(x_3) = \frac{y_3 - y_2}{x_3 - x_2} \tag{E.16}$$

- Known lateral deflection y_2, at displacement transducer 2:

$$y_2(x_2) = y_2 \tag{E.17}$$

The function *y(x)* has to be continuous in all its domain, so the rotation, and the displacement has to be the same at the soil surface, since it is a common point for functions $y_2(x)$ and $y_3(x)$:

- Similar rotation in the soil surface:

$$\theta_1 = \theta_2 \Rightarrow y_2'(0) = y_3'(0) \tag{E.18}$$

- Similar displacement in the soil surface:

$$y_2(0) = y_3(0) \tag{E.19}$$

Equations E.16, to E.19 form an equation system which is solved for each time step, obtaining *C1*, *C2*, *C3* and *C4*, and therefore the lateral deflection of the pile for any depth, *x*.

E.2. Test 1 (*D* = 100 mm, *P* = 50 kPa, *L/D* = 5, No gauges)

Load-Displacement Plots

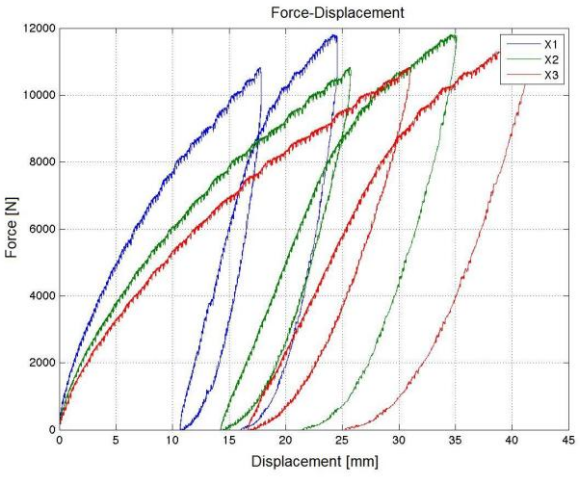

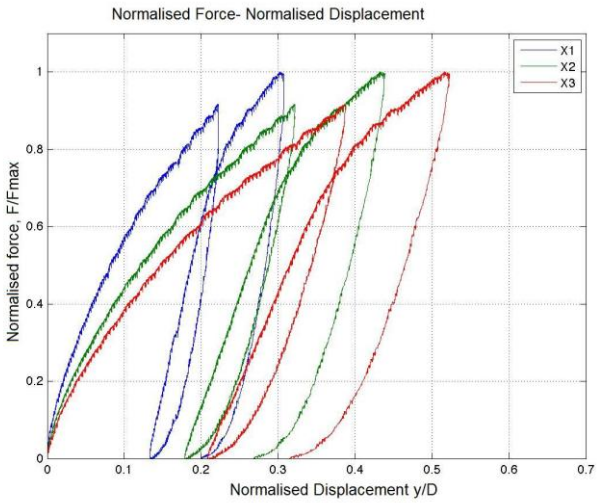

E.3. Test 2 (D = 80 mm, P = 0 kPa, L/D = 5)

Load-Displacement Plots

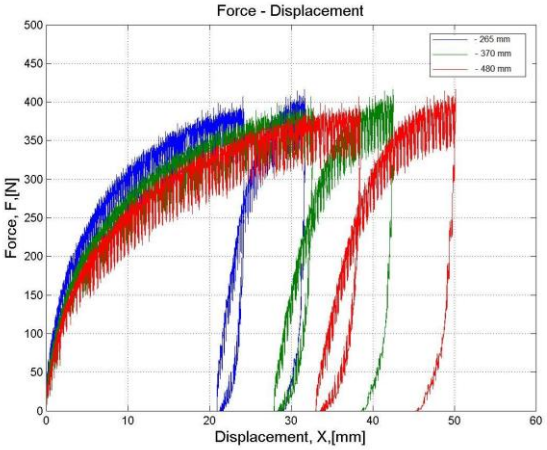

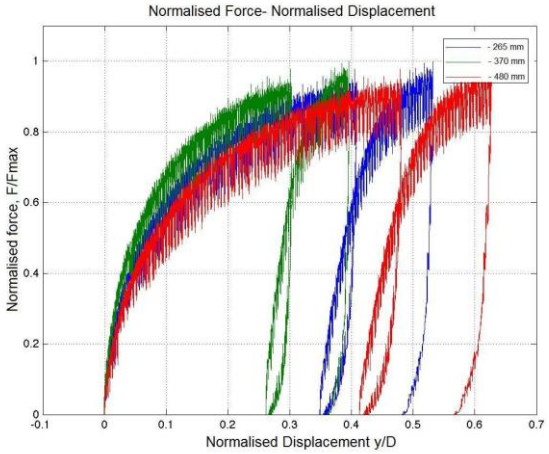

Deflection along the depth.

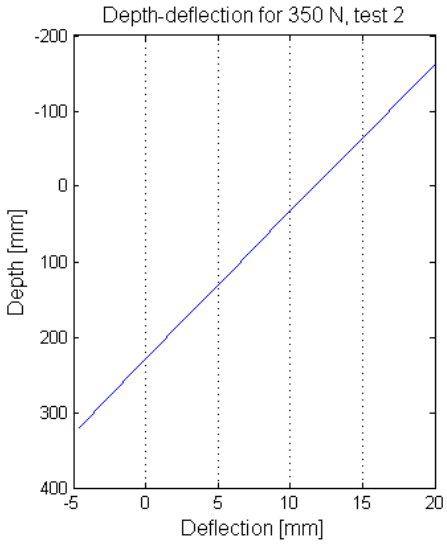

Bending Moment Distribution

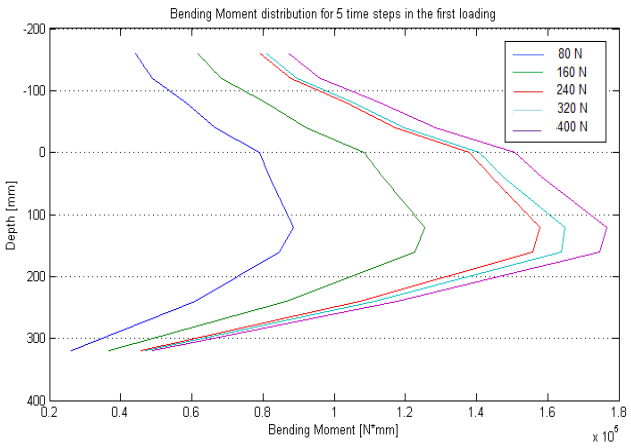

P-y Curves for different depths

Surface

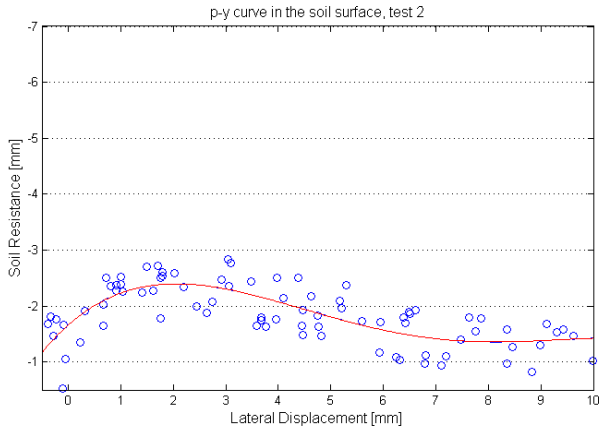

40 mm

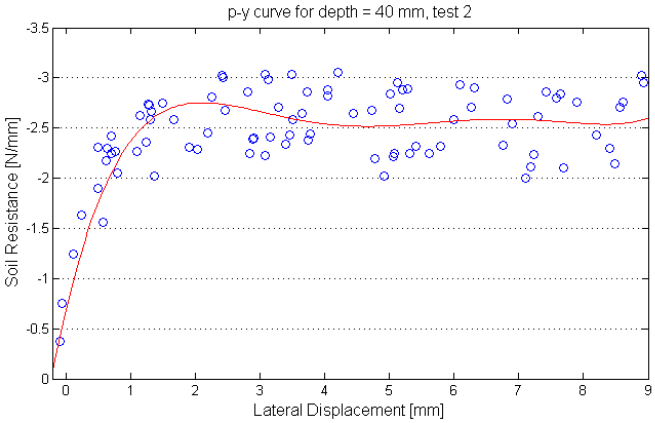

120 mm

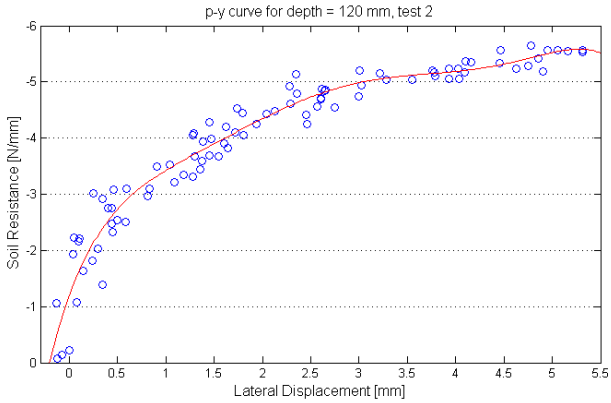

160 mm

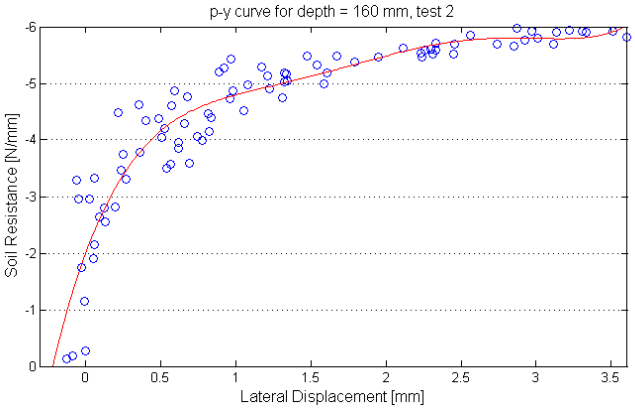

240 mm

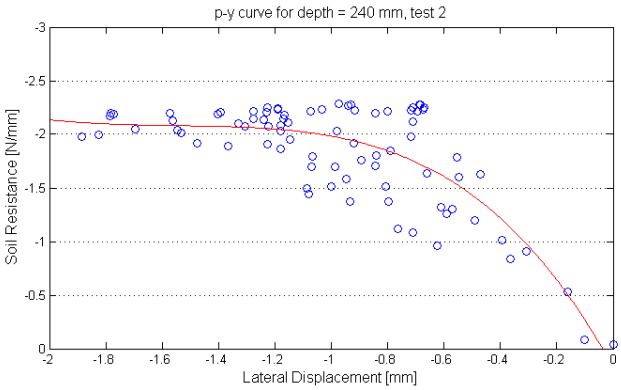

320 mm

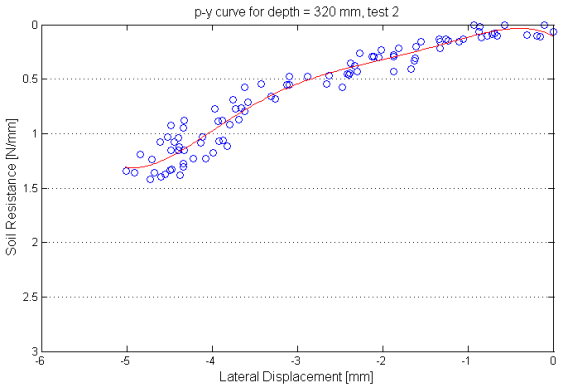

All depths

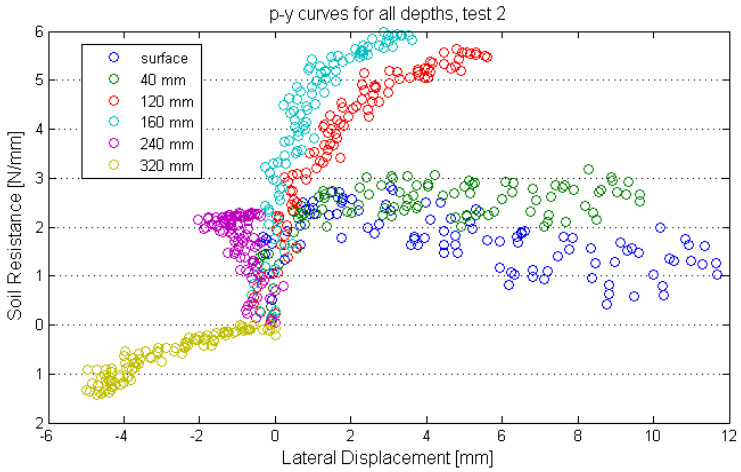

E.4. Test 3 (*D* = 80 mm, *P* = 50 kPa, *L/D* = 5)

Load-Displacement plots

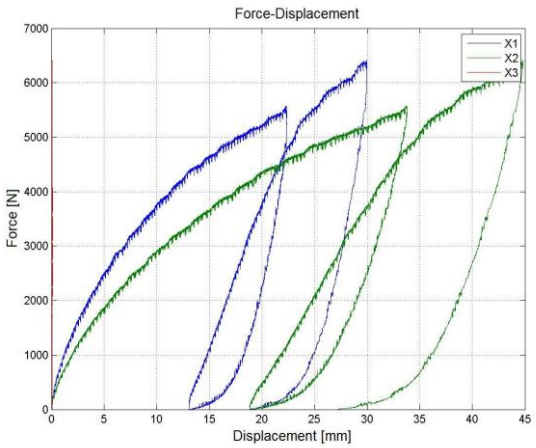

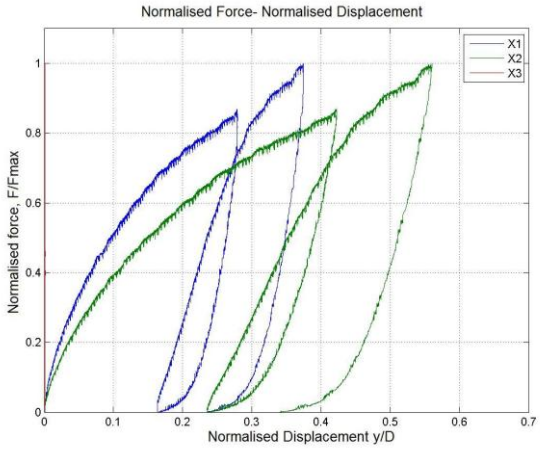

Displacement transducer 1 did not work as expected. Thus, the results are plotted, and it can be observed that the displacements shown by displacement transducer 1 are wrong (very near to 0), cf. Appendix J.

Deflection along the depth

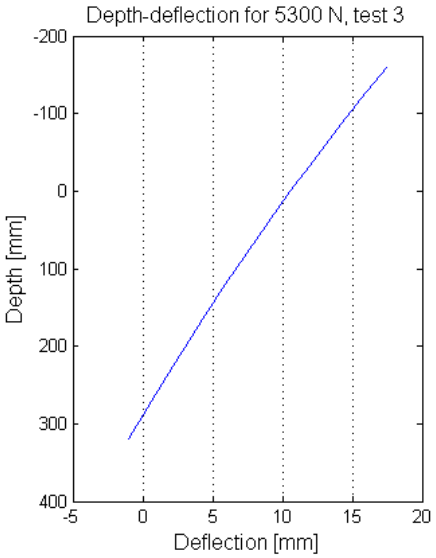

Bending moment distribution

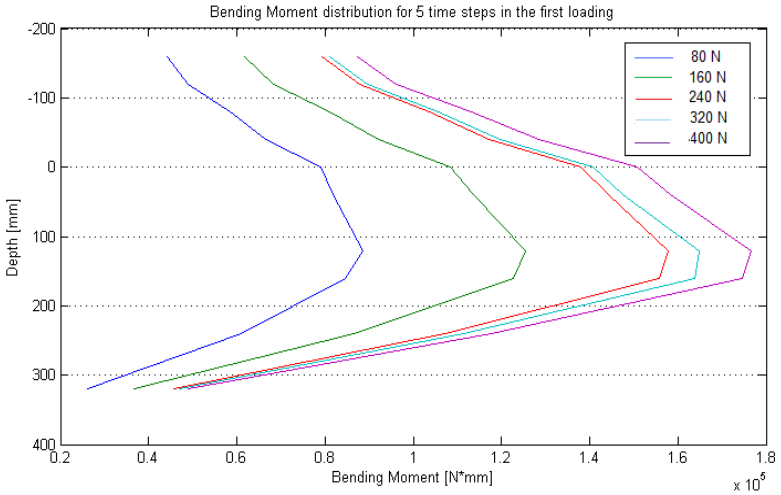

P-y Curves for different depths

Surface

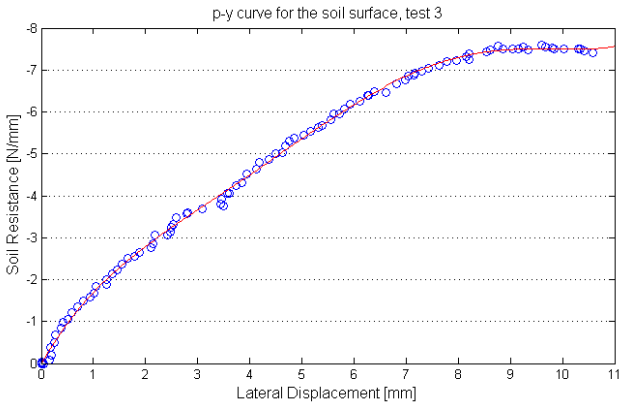

40 mm

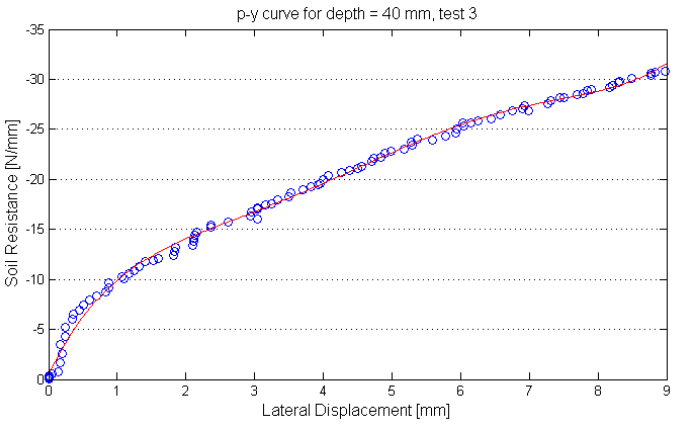

120 mm

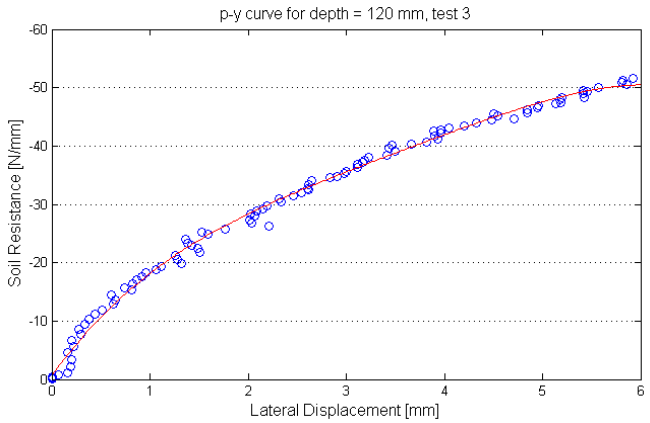

160 mm

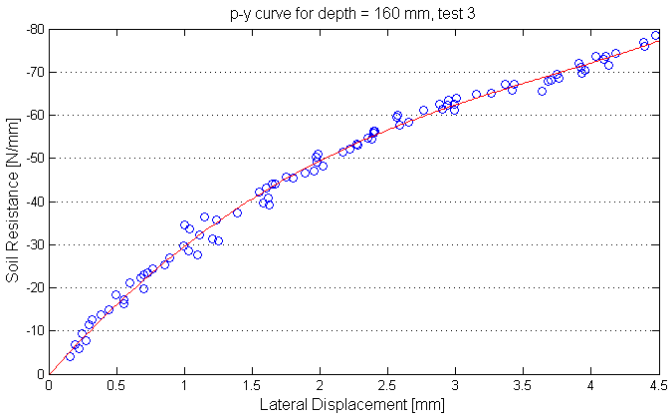

240mm

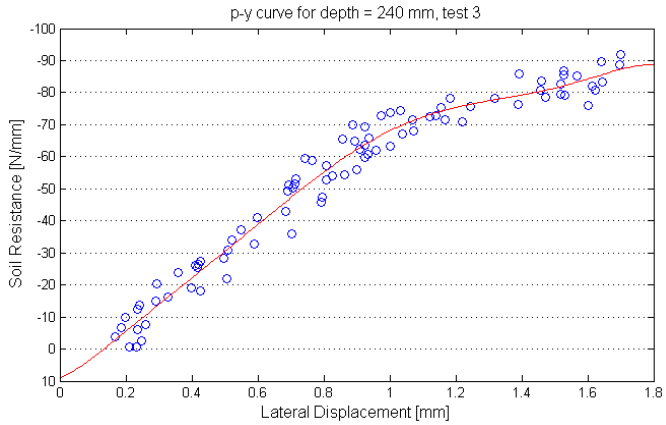

320mm

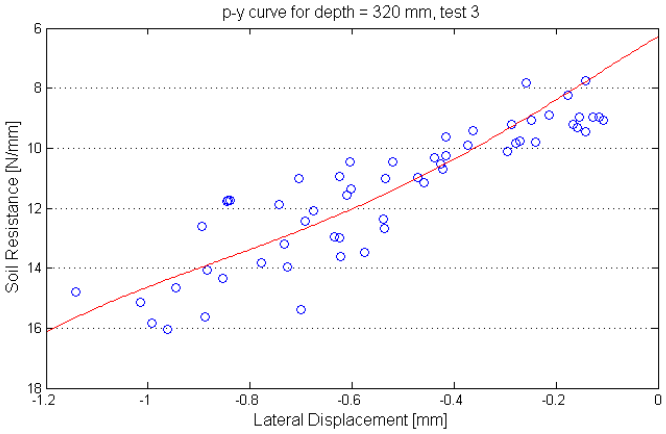

All depths

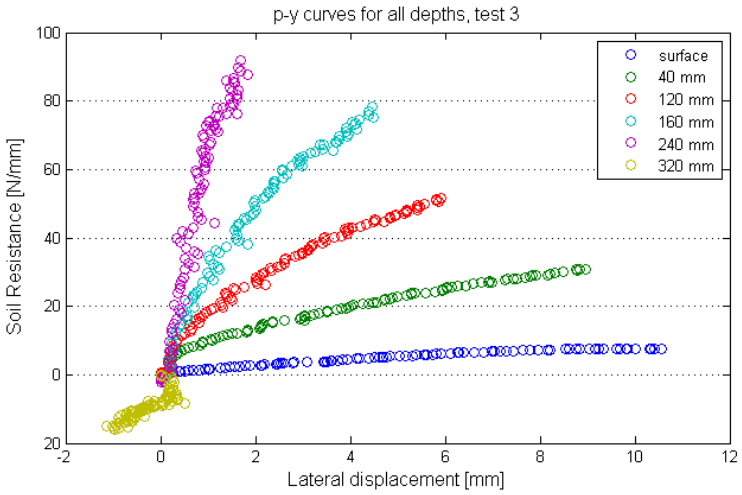

E.5. Test 4 (*D*= 80 mm, *P* = 50 kPa, *L/D* = 6)

Load-Displacement plots

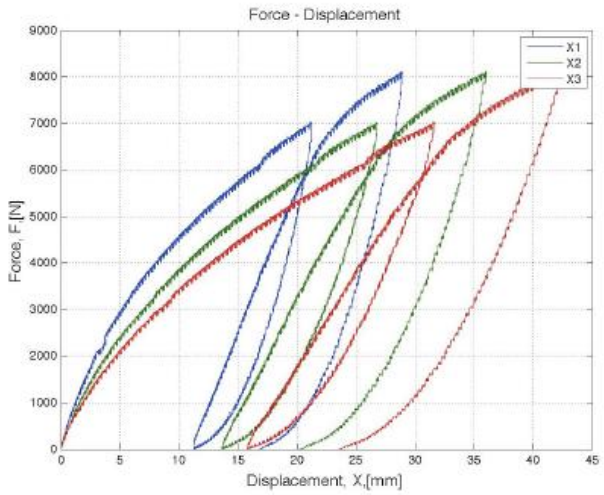

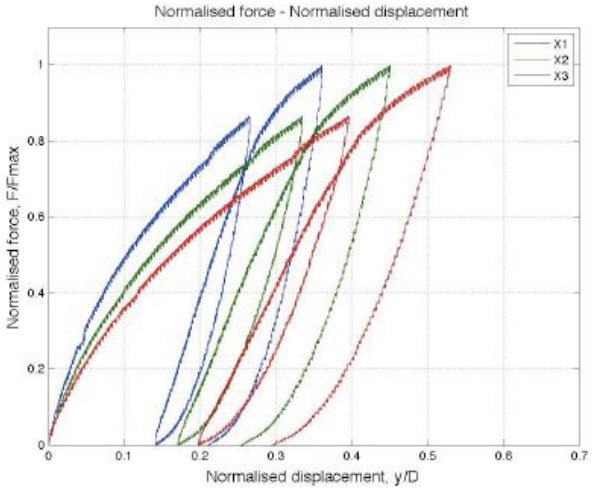

Deflection along the depth

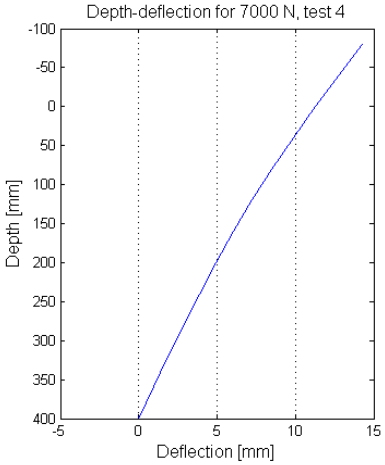

Bending Moment Distribution

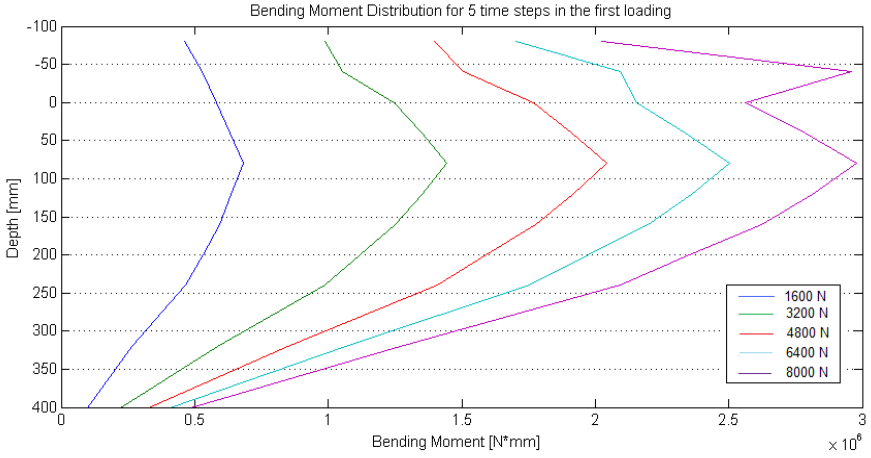

P-y curves for different depths

Surface

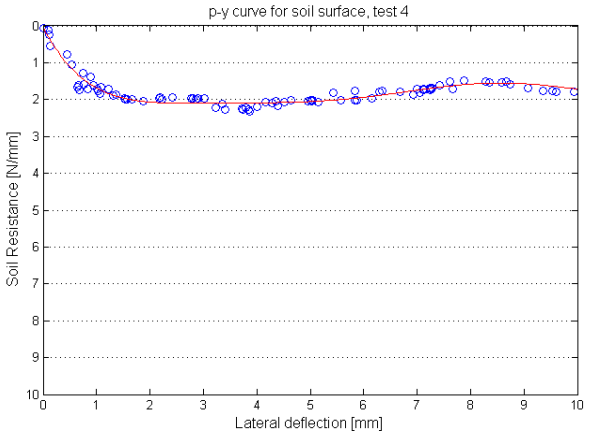

40 mm

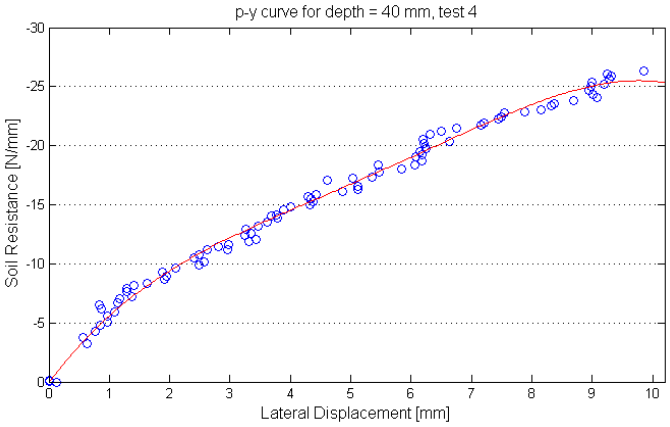

80 mm

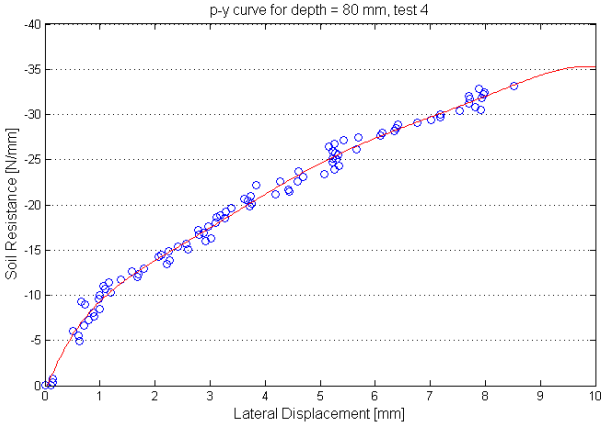

120 mm

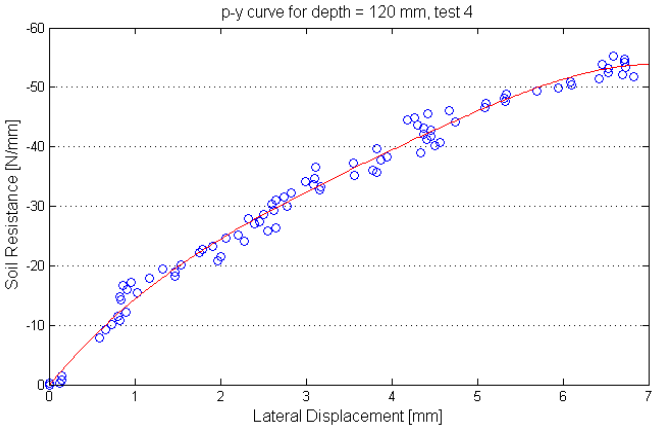

160 mm

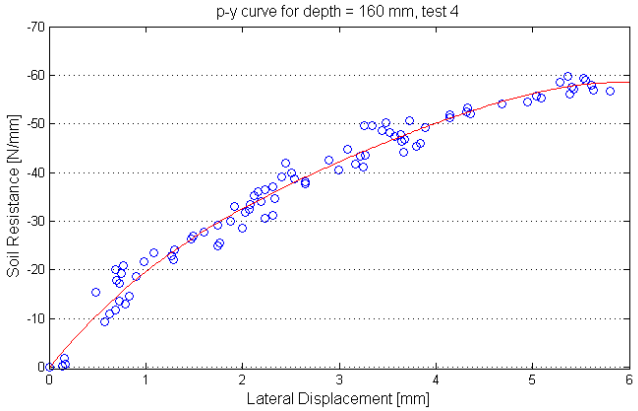

200 mm

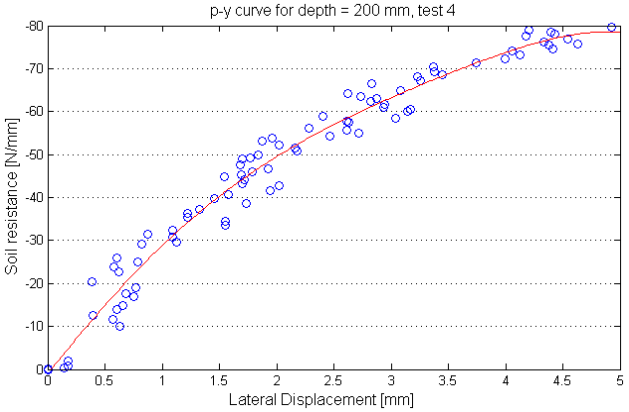

240 mm

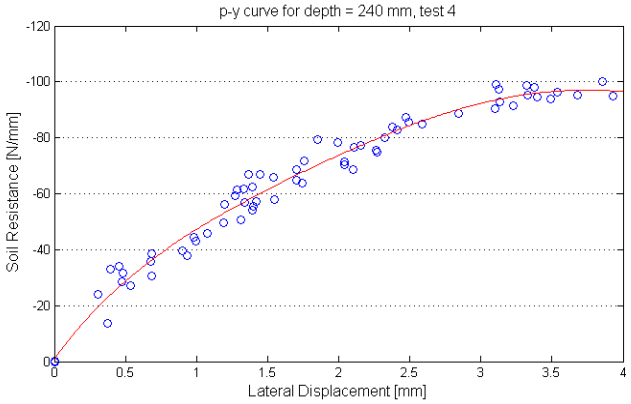

320 mm

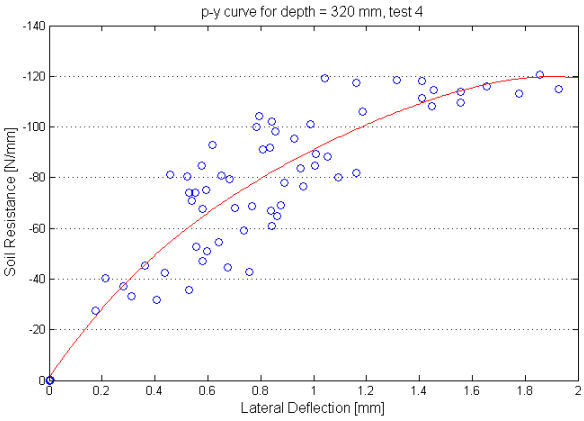

400 mm

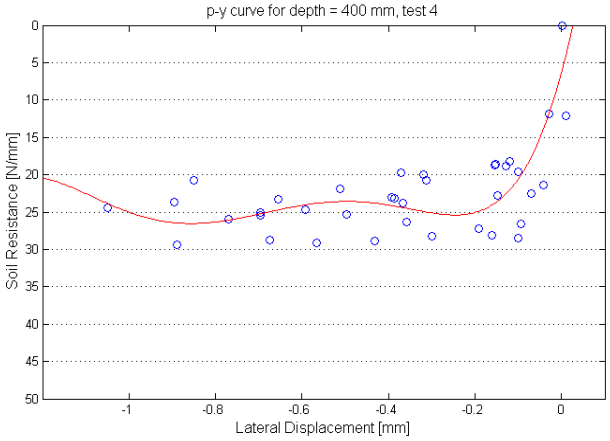

All depths

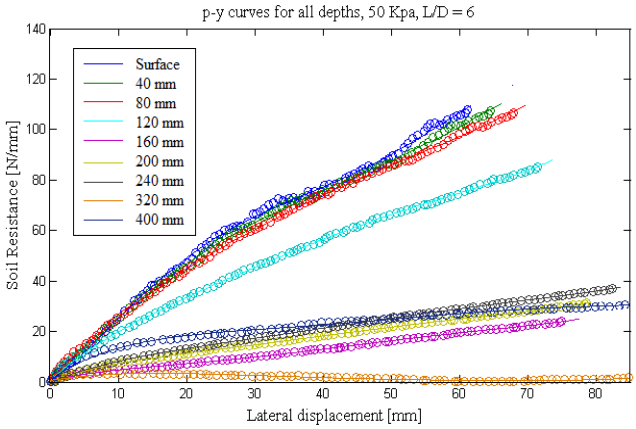

E.6.Test 5 (*D*= 80 mm, *P* = 100 kPa, *L/D* = 4)

Load-Displacement plots

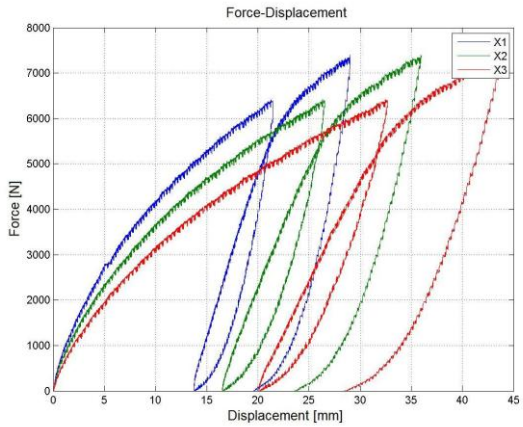

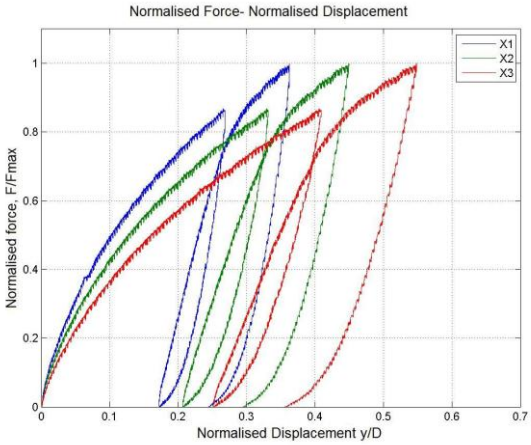

Deflection along the depth

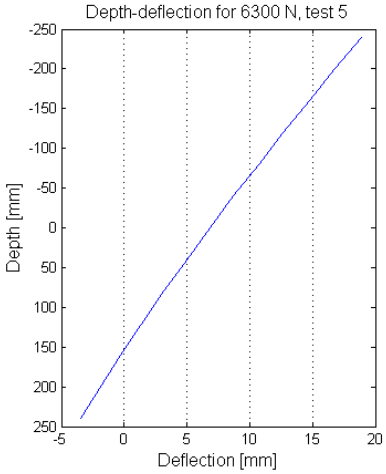

Bending Moment Distribution

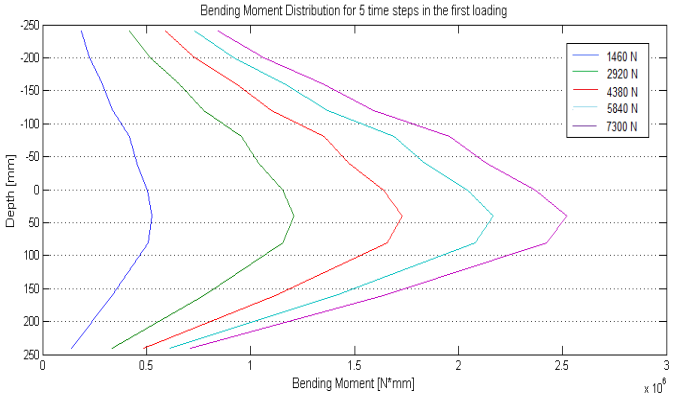

P-y Curves for different depths

Surface

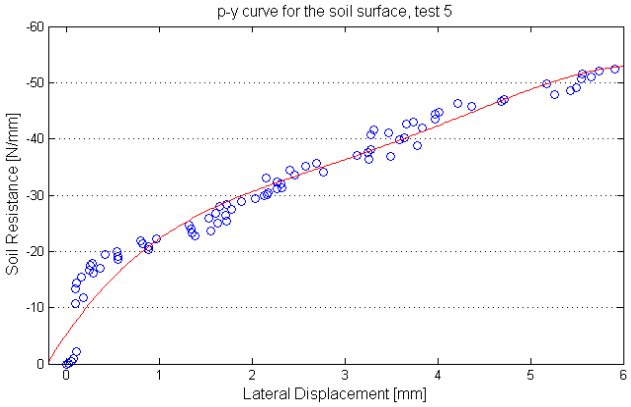

40 mm

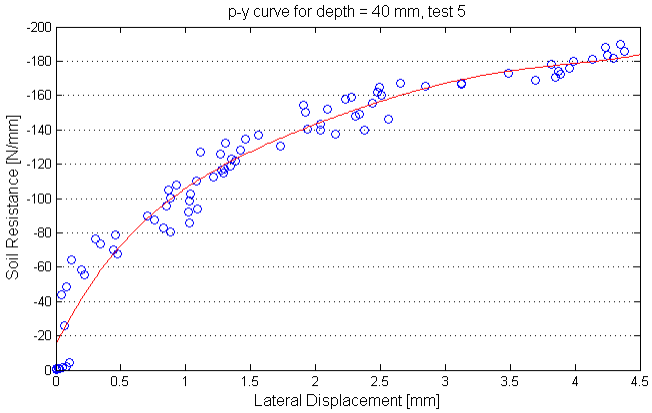

80 mm

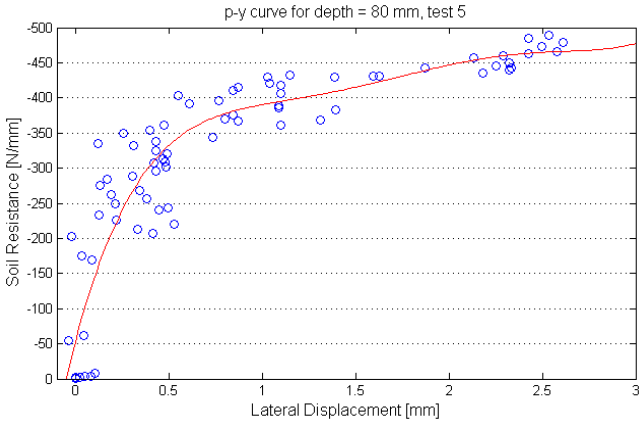

160 mm

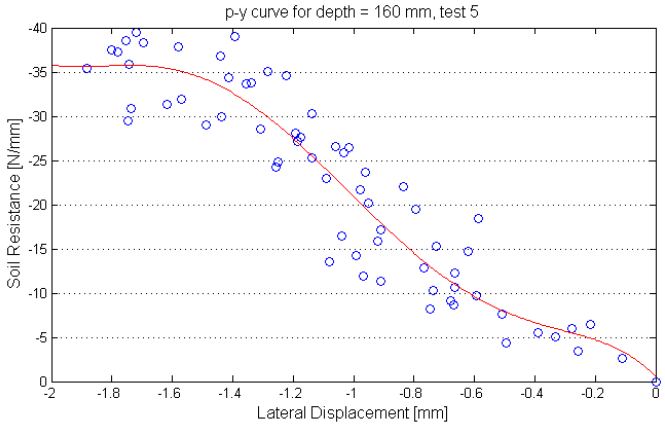

240 mm

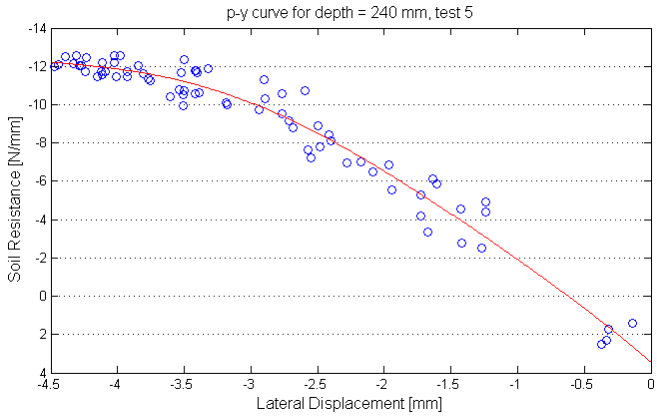

All depths

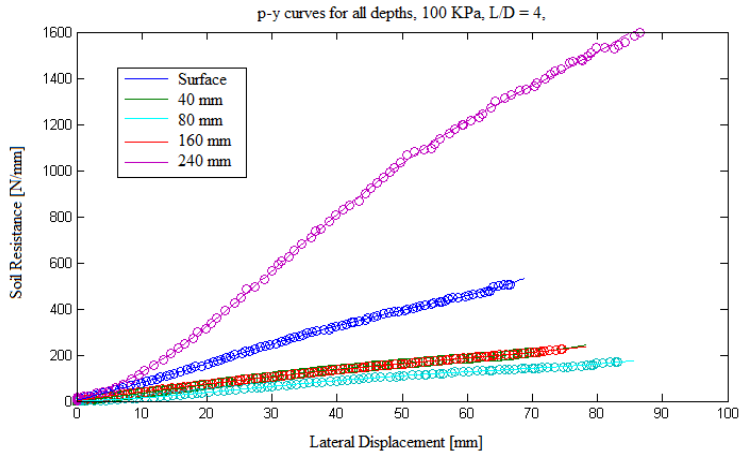

E.7. Test 6 (*D*= 80 mm, *P* = 100 kPa, *L/D* = 5)

Load-Displacement Plots

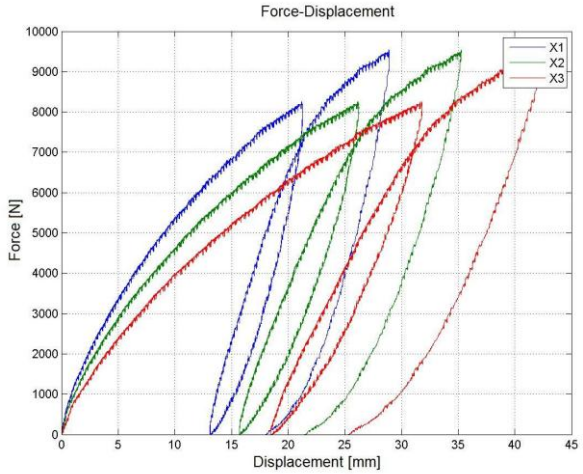

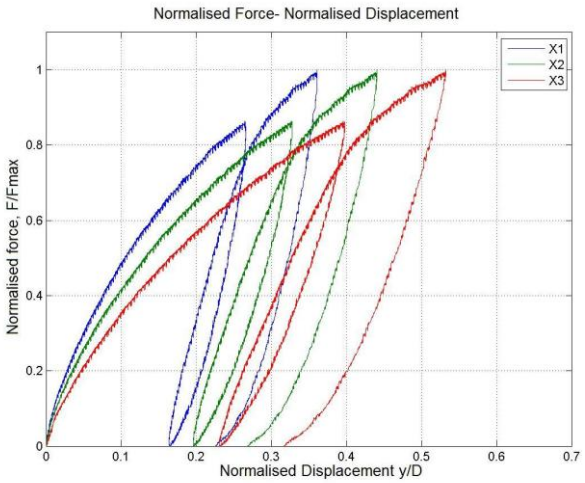

Deflection along the depth

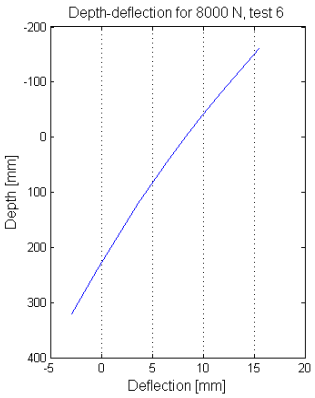

Bending moment distribution

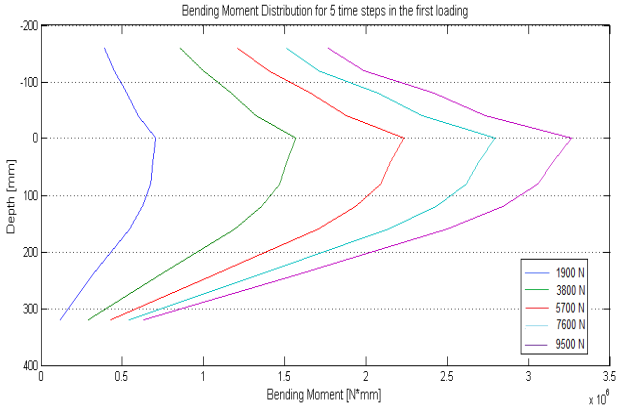

P-ý Curves for different depths

Surface

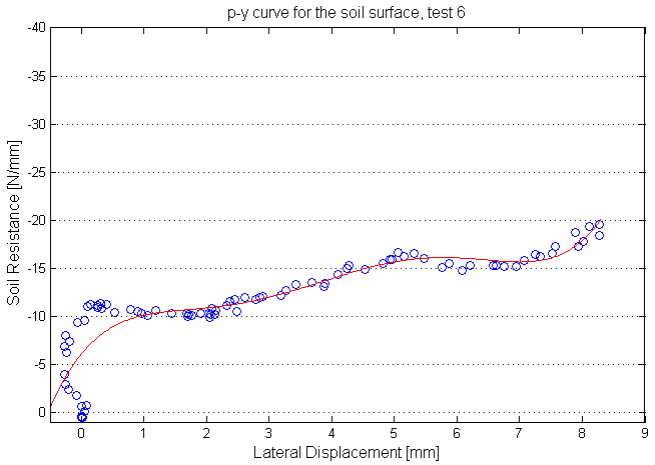

40 mm

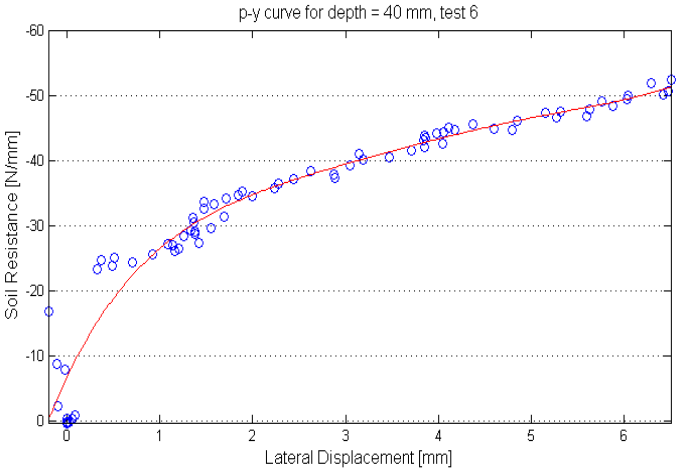

80 mm

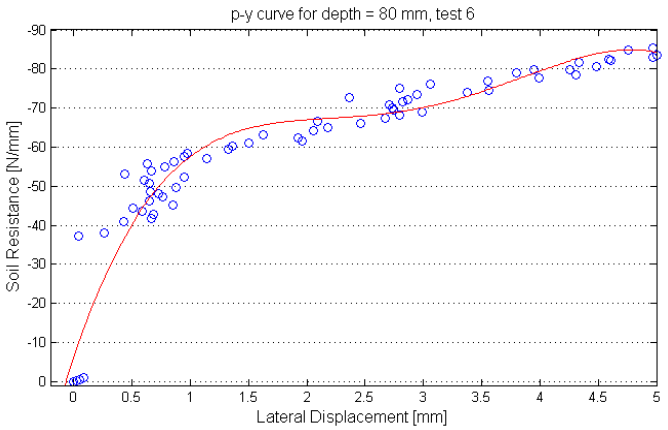

120 mm

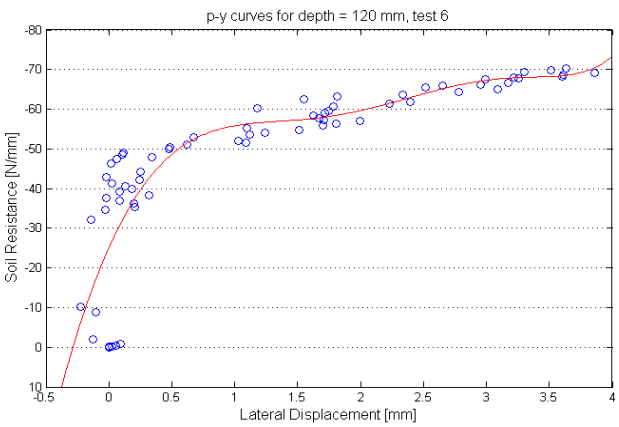

160 mm

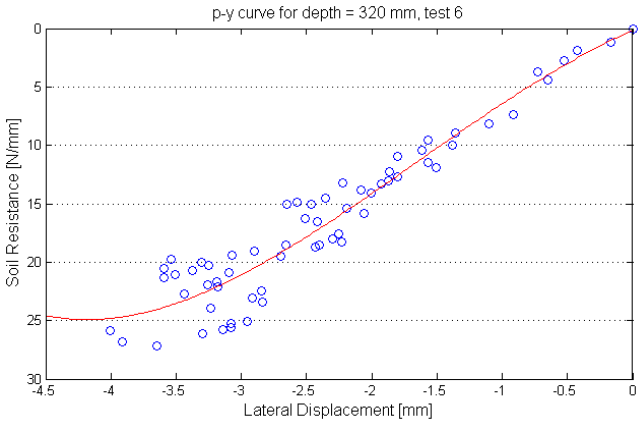

240 mm

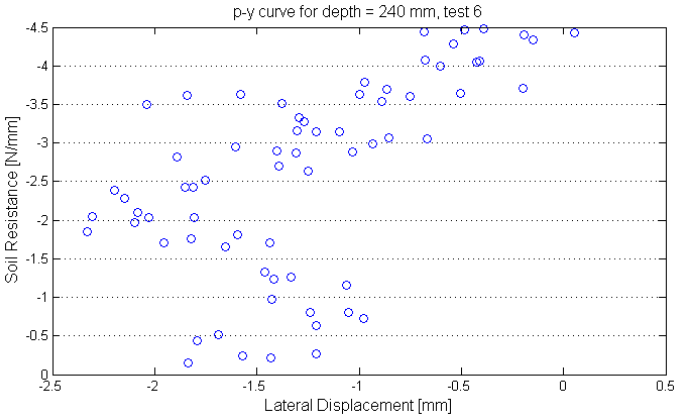

320 mm

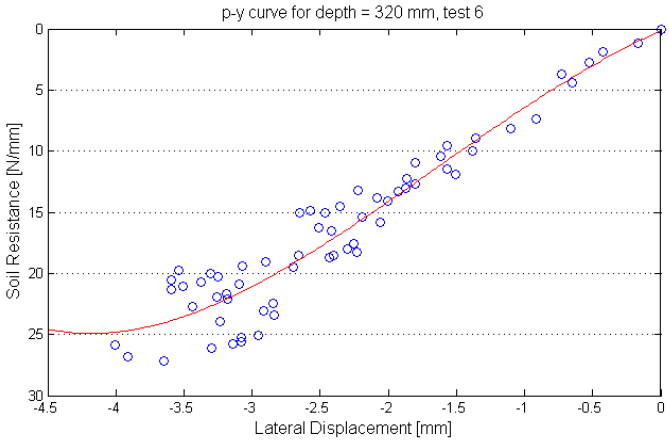

All depths

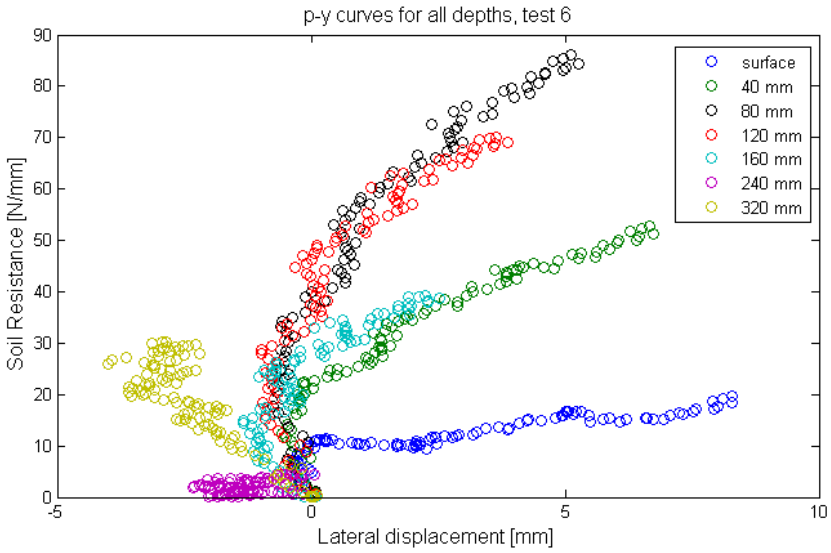

E.8. Test 7 (*D*= 80 mm, *P* = 100 kPa, *L/D* = 6)

Load-Displacement plots

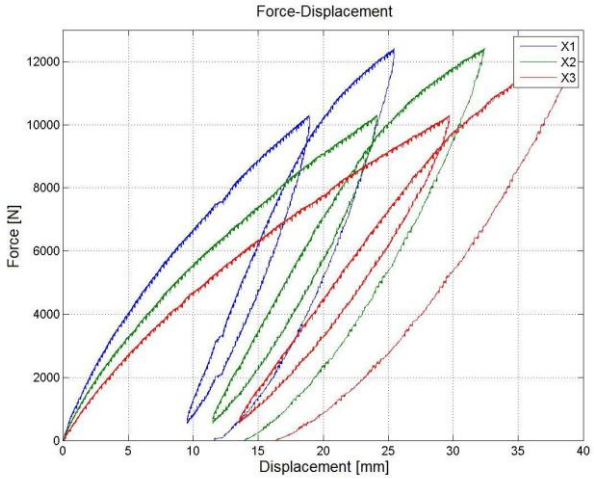

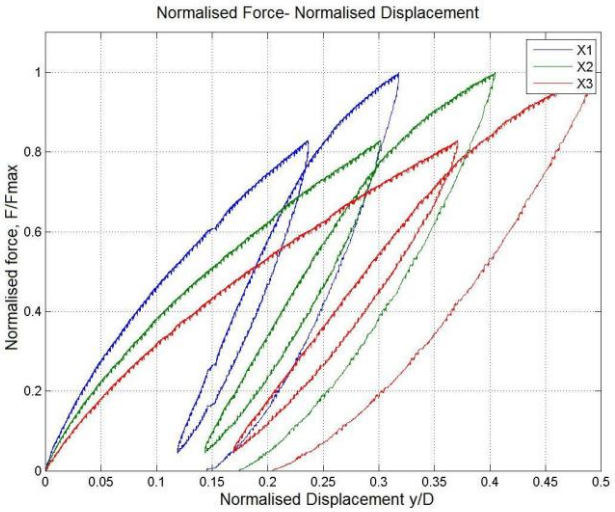

Deflection along the depth

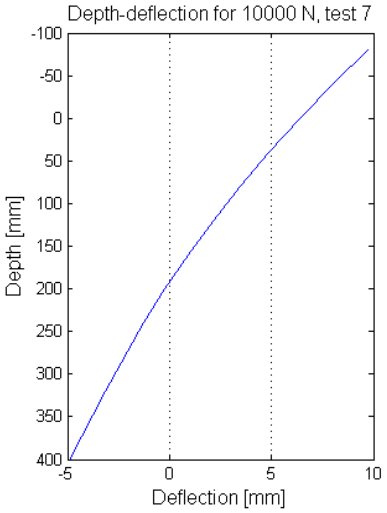

Bending Moment Distribution

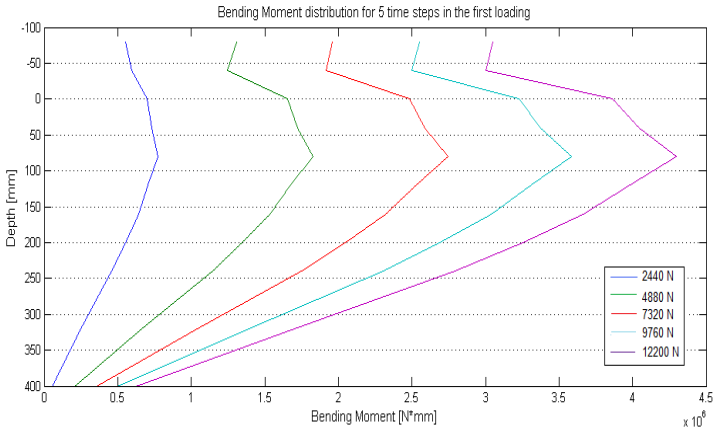

P-y Curves for all depths

Surface

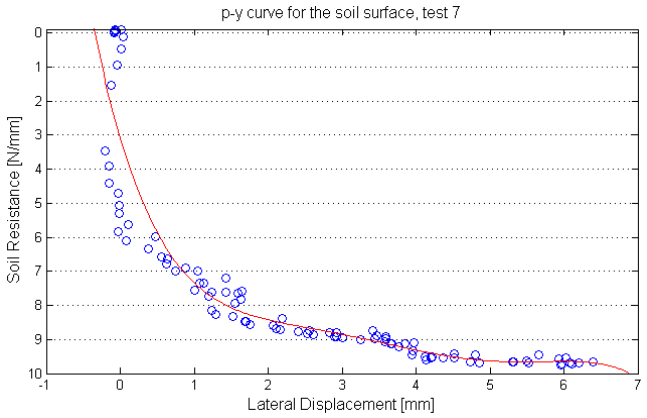

40 mm

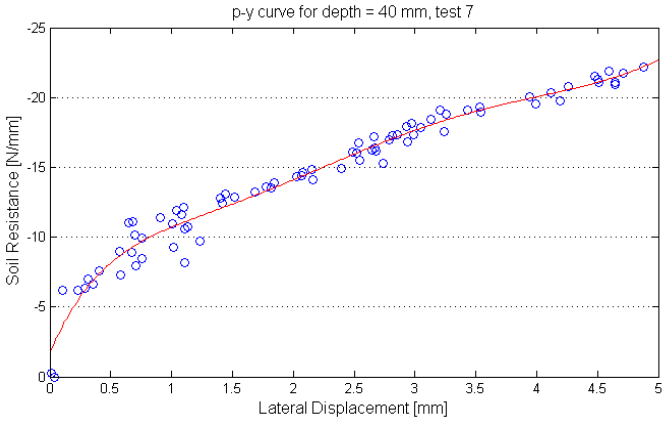

80 mm

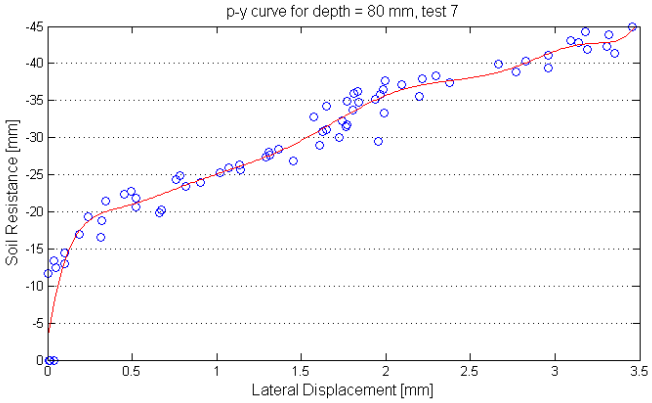

120 mm

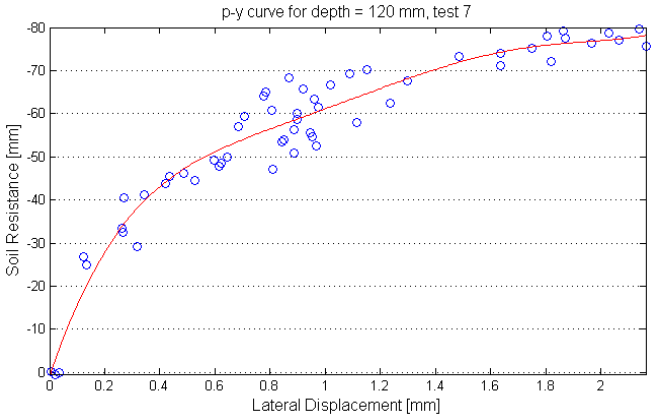

160 mm

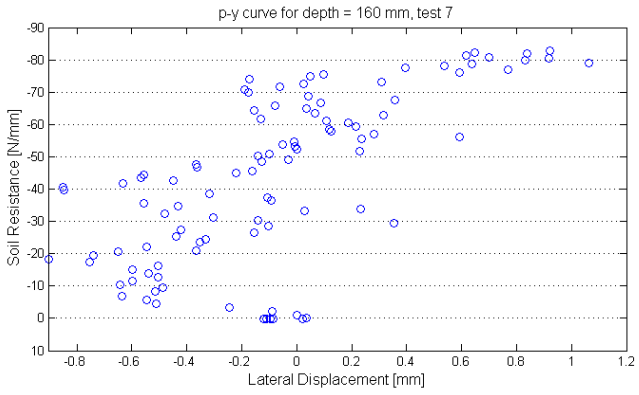

200 mm

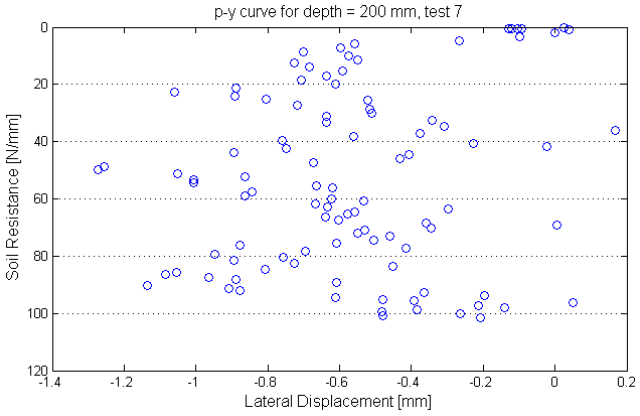

240 mm

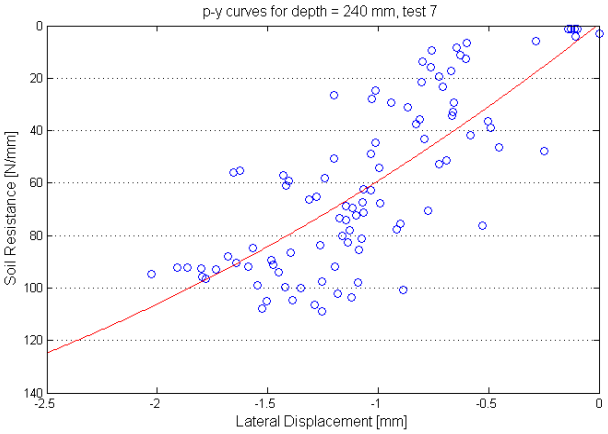

320 mm

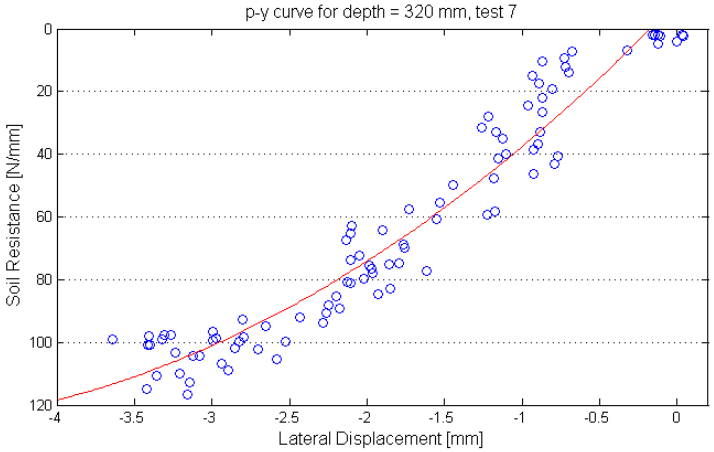

400mm

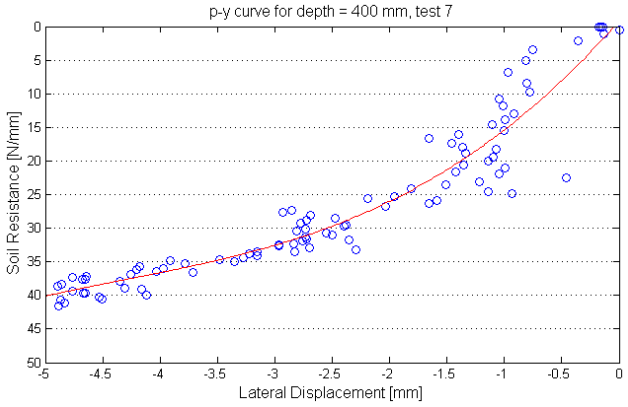

All Depths

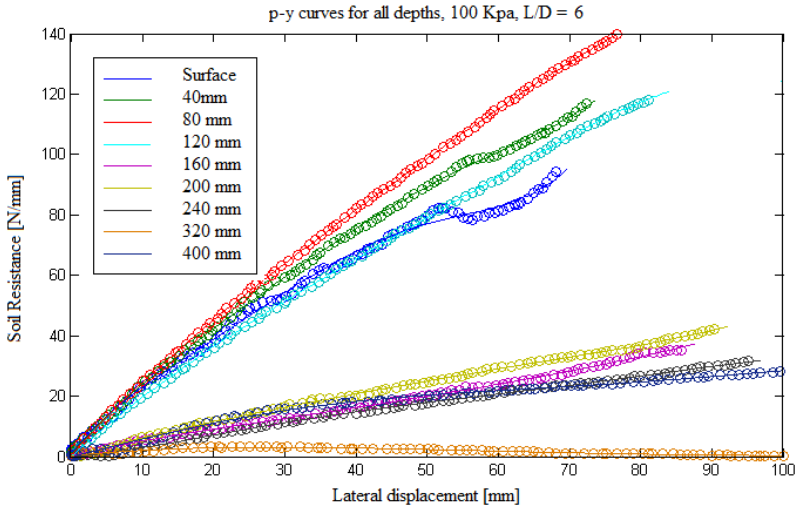

E.9. Test 8 (D = 80 mm, P = 50 kPa, L/D = 3)

Load-displacement plots

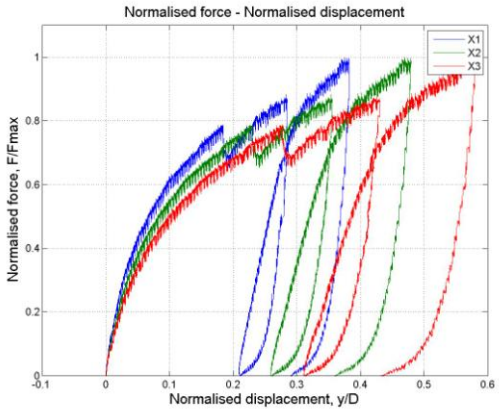

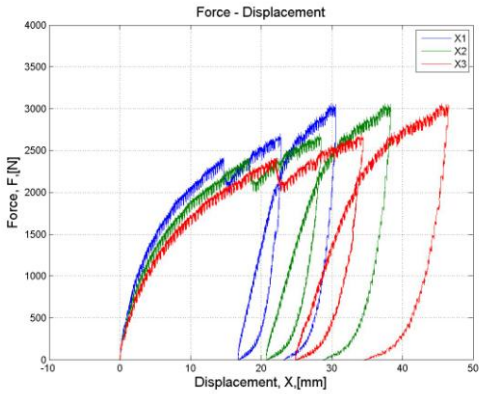

E.10. Test 9 (D = 80 mm, P = 0 kPa, L/D = 3)

Load-displacement plots

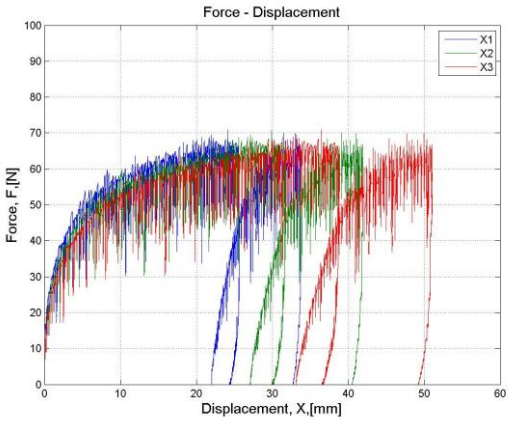

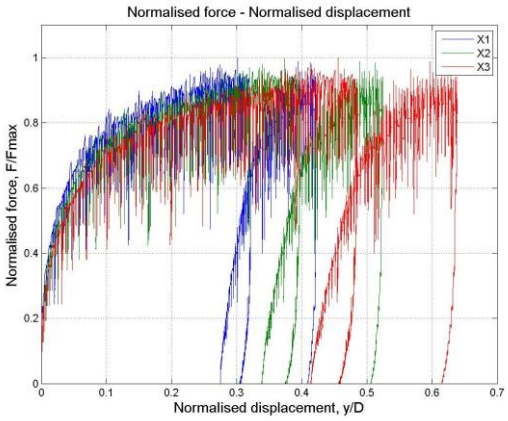

E.11. Test 10 (D = 80 mm, P = 100 kPa, L/D = 3)

Load-displacement plots

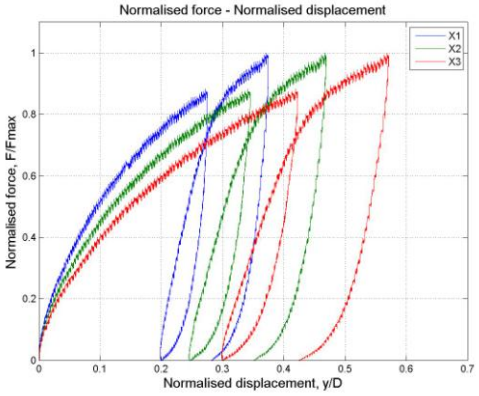

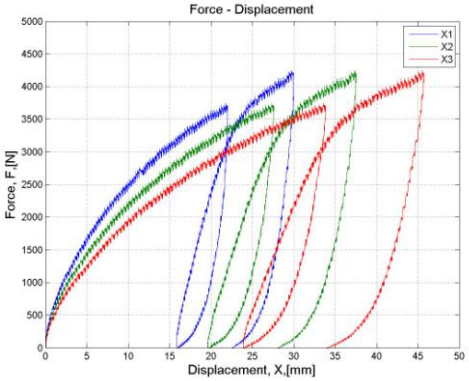

APPENDIX F

GENERATION OF FLAC^{3D} MODELS

The goal of the chapter is to describe the numerical modelling in more detail with a short introduction to the FLAC^{3D} 4.0, generation of the models and the description of employed elements.

F.1 General Introduction to FLAC^{3D}

FLAC^{3D} is a numerical modelling program for advanced geotechnical problems where continuum analysis is necessary in three dimensions. The program utilizes an explicit Finite Difference formulation that can model complex mechanical behaviour not suitable for Finite Elements method, such as large displacements and strains, non-linear material behaviour and unstable systems like cases of yield or failure over large areas or total collapse. [FLAC^{3D} manual]

The materials are represented by polyhedral elements within a 3D mesh that can be adjusted to fit the shape of the modelled object. Each of these elements behave according to linear or nonlinear stress/strain law.

The program carries out Lagrangian calculations process and the "mixed-discretization" of each zone, this makes it possible to obtain accurate plastics behaviour in the model.

The advantages of FLAC^{3D} compared to Finite Elements numerical method are:

The laws of motion for the continuous medium are transformed into discrete forms of Newton's law at the nodes, resulting an ordinary differential equations system, which is solved numerically using explicit finite difference approach in time.

The explicit solution used can follow arbitrary nonlinear behaviour, whereas implicit solutions can take significantly longer time to solve nonlinear problems. Moreover it is possible to work with large number of elements and large deformations. Furthermore it is seen that linear simulations run more slowly than nonlinear. Large-strain problems or situations physically unstable. [FLAC^{3D} manual]

Another advantage of FLAC^{3D} is the graphic facilities. The user-friendly interface makes it possible to make plots not only at the end of the process, but also while processing the model. There is a large range of possibilities like generating two dimensional planes of cross sections and obtaining the parameters needed at that part of the model. [FLAC^{3D} manual]

F.2 Model generation steps

Generation of the model and carried out calculations are briefly described step by step:

- Geometry generation and material properties assignment;
- Boundary conditions and initial stress assignment;
- Bringing model to equilibrium with assigned sand material properties both to the sand and the pile;
- Real material and boundary condition assignment. Bringing model to equilibrium again.
- Load application
- During the analysis total force, displacements, bending moments and pressures are recorded.

More detailed descriptions of each step are given in the next sections.

F.3 Geometry generation

Geometry is modelled to match the exact conditions as in the laboratory test. As the geometry is symmetrical, only a half of test setup is modelled to have smaller number of elements. Different parts of the model are generated by using zone elements which have specific primitive shapes. At first only a quarter of the test setup is created and the other part is generated by reflecting the first one. To have correct model conditions an interface is generated at the sand-pile interaction.

	D [mm]	L/D	P_0 [kPa]
Test 1	100	5	50
Test 2	80	5	0
Test 3	80	5	50
Test 4	80	6	50
Test 5	80	4	100
Test 6	80	5	100
Test 7	80	6	100

Table F.1: Tests' geometries and overburden pressures

F.3.1 Soil generation

The soil is generated with cylindrical shell elements. At first the part around the pile is generated, then the part below it. The sand near the pile is meshed into smaller elements as the stresses have greater variation in this zone.

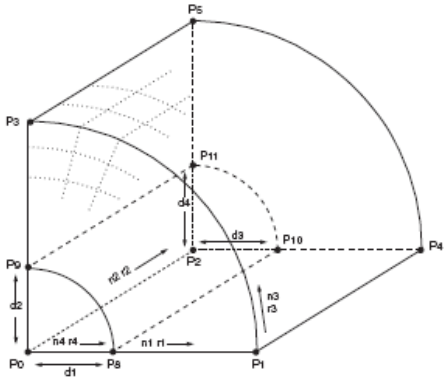

Figure F.1: Cylindrical shell zone. FLAC^{3D} 4.0 manual (2009)

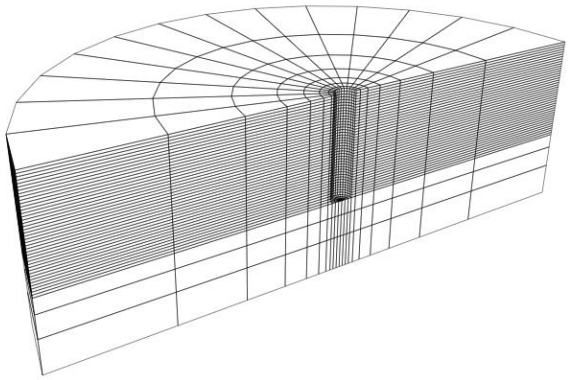

Figure F.2: Generated soil elements

Soil properties are defined the same as found from the laboratory tests.

	D [mm]	P_0 [kPa]	φ_{tr} [˚]	ψ_{tr} [˚]	I_D [%]	γ' [kN/m^3]	E_0 [MPa]
Test 1	100	50	50,26	17.56	87.20	10.33	29.96
Test 2	80	0	49,77	17.03	84.57	10.27	-
Test 3	80	50	48,63	15.70	77.91	10.15	25.15
Test 4	80	50	48,90	16.09	79.85	10.18	26.12
Test 5	80	100	48,30	15.45	76.60	10.12	36.54
Test 6	80	100	48,86	16.06	79.66	10.18	38.85
Test 7	80	100	48,66	15.84	78.59	10.15	38.00

Table F.2: Soil properties for each test

The horizontal earth pressure coefficient at rest (K_0), the shear modulus (G) and the bulk modulus (K) are calculated by equations F.1 to F.3.

$$K_0 = 1 - \sin(\varphi_{tr}) \quad \text{(F.1)}$$

$$K = \frac{E}{3 \cdot (1 - 2 \cdot \upsilon)} \quad \text{(F.2)}$$

$$G = \frac{E}{2 + 2 \cdot \upsilon} \quad \text{(F.3)}$$

Where:

φ_{tr}	is the internal angle of friction [˚]
E	is the elasticity modulus [F/L^2]

F.3.2 Interface generation

By using the interface command pile-sand interaction is modelled. This allows separation and sliding between two materials. Interfaces are represented as a set of triangular elements, which are defined by three interface nodes. These elements are attached to the face of a zone surface. On the appearance of a contact with another

element surface each interface node characterizes sliding properties, normal and shear stiffnesses between the materials. Each interface node has a representative area and the relationship between interface elements and interface nodes is illustrated in figure F.3. As it is shown in figure F.4 the interface is generated in two parts – vertical and horizontal.

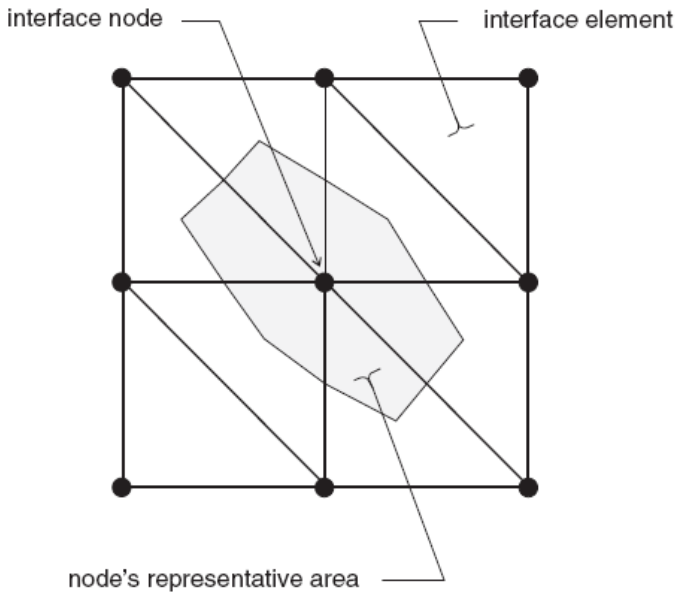

Figure F.3: Distribution of representative areas to interface nodes FLAC^{3D} 4.0 manual (2009)

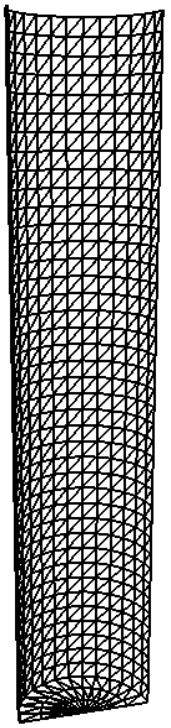

Figure F.4: Generated interface elements

The interface properties have a great influence in the results. They are described by the following parameters given in table F.3. The values of the parameters were chosen to match the results form laboratory tests.

Friction angle	φ_{tr}' [°]	36.81 – 38.73
Cohesion	c_{int} [kPa]	0.001
Dilitation	ψ_{tr} [°]	0
Normal stiffness	k_n [MPa]	100 x E_0
Shear stiffness	k_n [MPa]	100 x E_0

Table F.3: Average CPT result for each test.

Friction angle is calculated by formula F.4:

$$\varphi_{tr}' = \tan^{-1}\left(2/3 \cdot \tan\left(\varphi_{tr}\right)\right) \qquad \text{(F.4)}$$

Where:

φ_{tr} | is the internal angle of friction for the sand[°]

F.3.3 Pile generation

In the laboratory test closed-ended hollow piles are used, however in the FLAC^{3D} models a solid pile is used cf. Fig. F.7. The pile geometry is generated by using the cylinder elements cf. Fig. F.5.

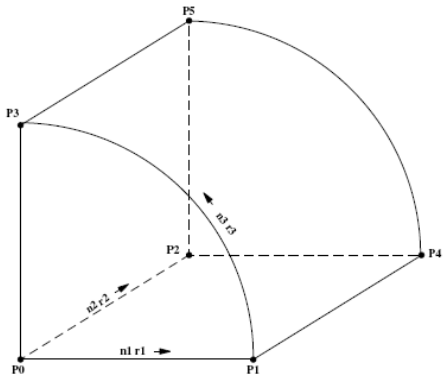

Figure F.5: Cylinder zone. FLAC^{3D} 4.0 manual (2009)

The pile is created by 4 different parts: a part which will be embedded in the soil, a part between the soil and the first displacement transducer, a part between the first and the second transducers, a part between the second and the third transducer. The elements are generated above the soil surface. This is done so it would be possible to select only the pile nodes, when it is embedded in the soil. This way of selection makes it easier to operate only the pile nodes when obtaining the test parameters.

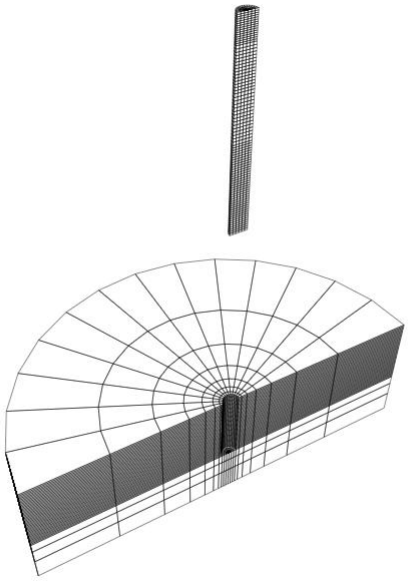

Figure F.6: Generation of the pile

As a solid pile is used instead of a hollow, equivalent Young's modulus and density have to be used cf. Eq. F.5 and F.6.

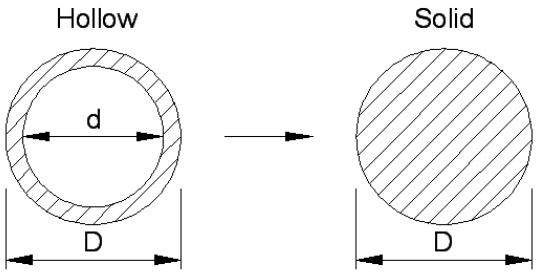

Figure F.7: Hollow and solid pile cross-sections

$$E_{solif} = \frac{E_{hollow} \cdot I_{hollow}}{I_{solid}} \quad \text{(F.5)}$$

$$\rho_{solif} = \frac{\rho_{hollow} \cdot A_{hollow}}{A_{solid}} \quad \text{(F.6)}$$

Where:

E_{hollow}	is the Young's modulus of the aluminium (7.2×10^4 MPa) according to Teknisk Ståbi [Jensen and Olsen, 2007]
E_{solid}	is the Young's modulus of the solid pile
I_{hollow}	is the moment of inertia of the hollow pile cross -section
I_{solid}	is the moment of inertia of the solid pile cross -section
ρ_{hollow}	is the density of the aluminium (2700 kg/m^3) according to Teknisk Ståbi [Jensen and Olsen, 2007]
ρ_{solid}	is the density of the solid pile
A_{hollow}	is the area of hollow pile cross-section
A_{solid}	is the area of solid pile cross-section

The Poisson's ratio for aluminium ($\nu = 0{,}33$) is not scaled due to negligible effect to the results.

F.4 Pile installation

The pile is embedded in the soil after generating all the elements. The final model geometry is shown in figure F.8.

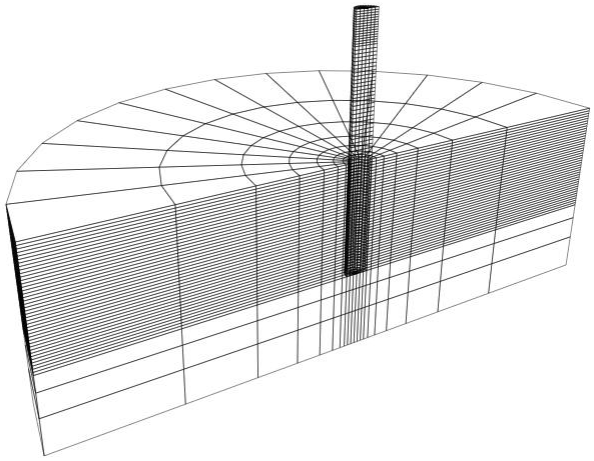

Figure F.8: Final model geometry

F.5 Material models

There are thirteen basic models in FLAC^{3D}: one null, three elastic and nine plastic models. Different material models are used for different parts of the model.

The Mohr-Coulomb material model with tension cut-off is used to represent relations in the sand, cf. Figure F.9. This model describes the stress-strain behaviour of the soil in an elastic-plastic state. The elastic part is described by Hooke's law whereas in the plastic part the strain is described as a sum of elastic and plastic strains, cf. Figure F.10.

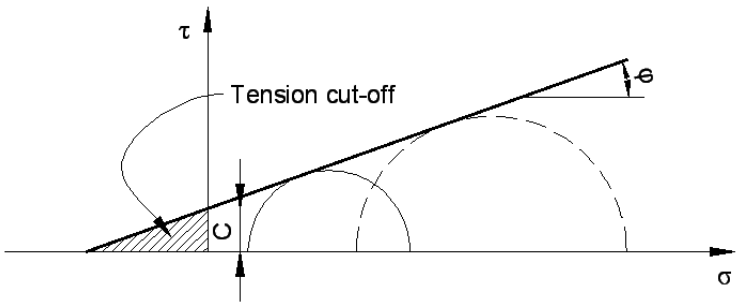

Figure F.9: Graphical representation of the Mohr-Coulomb failure criteria

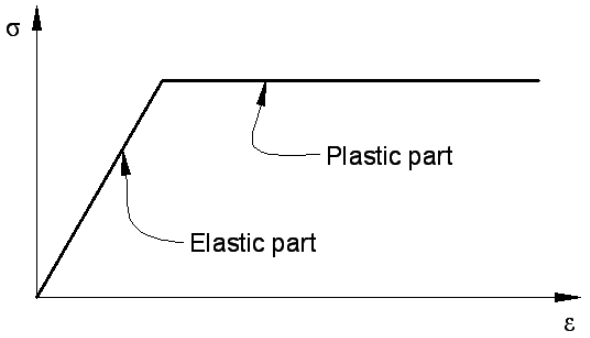

Figure F.10: Elastic-plastic stress-strain curve

Elastic, isotropic model is used for the monopole. In this case stress-strain relationship is described by the law of Hooke.

Null model is used for the rest of the volume – the part above the soil. In this type of material stresses are automatically set to zero.

F.6 Boundary and initial conditions

Boundary conditions are modelled to match the real conditions in the tank. Three different conditions are assigned to different parts of the model, cf. Figure F.11.

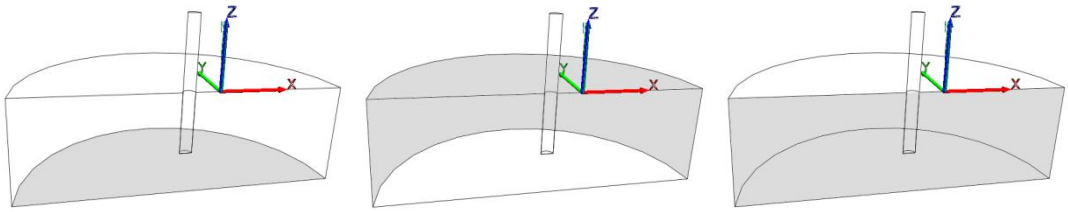

Figure F.11: Model boundaries

All nodes in the bottom of the model are fixed in x, y and z directions. Nodes in vertical part which simulate the pressure tank walls are fixed in x and y directions. Nodes in the symmetry plane are fixed in the y direction.

Initial conditions are assigned by applying densities, gravity loading and overburden pressure for model elements. The horizontal pressure is defined by use of horizontal earth pressure coefficient K_0=1-$sin(\varphi_{tr})$.

At first the soil properties are assigned for the whole volume and the model. This is done to avoid stress concentrations around the pile. The friction in the interface between the pile and the soil is set to zero and then the whole model is brought to equilibrium. After that, correct interface and pile properties are set the damping is used to get the equilibrium state in the soil and to initialize stresses in the interface between the soil and the monopile.

It is seen in figure F.12 that in the model without the overburden pressure the horizontal stresses vary depending on the depth, however in figure F.13 which represents the model with overburden pressure the stress variation is small in comparison with the overall pressure.

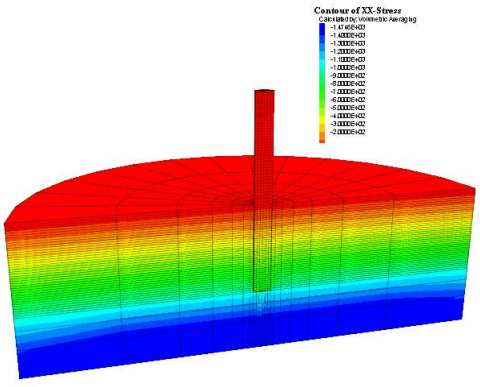

Figure F.12: Initial horizontal stresses without overburden pressure

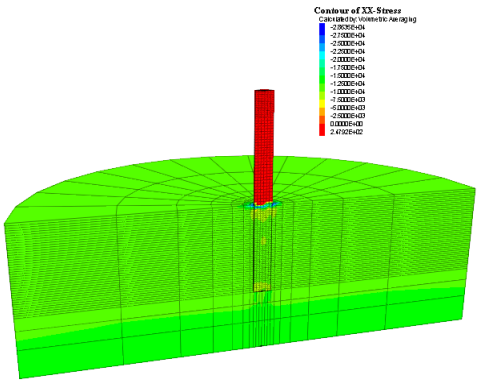

Figure F.13: Initial horizontal stresses with overburden pressure P_0=50 kPa

F.7 Damping

To ensure static or quasi-static solution of the model, motion equations have to be damped. There are two different damping mechanisms in FLAC^{3D}: local damping by default or combined damping.

Local damping is based on the sign variation of the velocity component. However in this case significant uniform motion is apparent as velocity loading is applied and in the velocity will not change sign in most of the nodes. Therefore the combined damping is used. In this mechanism damping depends of the unbalanced force sign variation and it is more appropriate for rigid-body motion systems as well as oscillatory motion dissipation.

F.8 Numerical stability

In order to get valid results from finite difference equations numerical scheme has to be stable. The ideal medium is a set of points with applied masses connected by springs with stiffness k. The whole systems eigenperiod is related to the critical timestep and stable result is obtained if it is greater than the chosen timestep.

It‘s impractical to have global eigenvalue analysis, so variety of local stability analysis are performed where unit timestep Δt = 1 is applied for the whole system.

For infinite series of masses and springs the limit-stability criterion is:

$$m = k(\Delta t)^2 \qquad \text{(F.7)}$$

By selecting unit timestep Δt = 1, system will be stable if the point mass is eaqual or greater than spring stiffness. Validity in equation F.7 is extended to tetrahedron in the local analysis by interpreting m and k in local nodes as the nodal mass contribution and nodal stiffnes contribution respectiveley. The critical timestep is obtained according to the system stiffness.

F.9 Deflection application

As in the laboratory tests the deflection is applied to the pile instead of the force. Velocity is applied to the nodes at 370mm height above the soil surface. It is increased slowly to avoid any dynamic response in the model which would make the inertia effects dominant. A steady-state response is achieved in the system by using more than a million time steps.

F.10 Bending moment and soil resistance calculation

Bending moments, *M*, are calculated at different levels of embedded pile by equation:

$$M = \sigma_{zz,i} \cdot A_i \cdot x_i \qquad \text{(F.8)}$$

Where:

$\sigma_{zz,i}$	is the vertical normal stress for element i
A_i	is the the area of the element i
x_i	is the x coordinate of the center of the element i

The *x*-component of all stresses in the interface points is equal to soil resistance per unit length. Total stress in each of these nodes can be calculated by equation F.9.

$$T_x = \sigma_{xx}' \cdot n_x + \sigma_{xy}' \cdot n_y + \sigma_{xz}' \cdot n_z \qquad \text{(F.9)}$$

Where:

T_x	is the x-component of the total stress
n_x, n_y, n_z	are unit normal components

The soil resistance along the pile, p_x, is calculated by equation F.10.

$$p_x = \int T_x dC \qquad \text{(F.10)}$$

Where:

C	is the interface circumference

APPENDIX G

NUMERICAL MODELLING BY PLAXIS3D

In the following appendix, a numerical analysis of the monopile foundation is carried out using numerical finite element commercial software Plaxis 3D 2010. The aim is to evaluate and compare the results in Plaxis 3D 2010 with the ones obtained by the numerical explicit finite element program FLAC^{3D} using the experimental tests performed at Aalborg University laboratory as a model.
Initially, a short description of Plaxis 3D is presented, then the procedure to create the model geometry and the calculation phases are explained.
Load-displacement relationships, p-y curves, zero deflection point and moment distribution along the monopile are obtained, depending on the different soil characteristics and test setup of each test.
Plaxis 3D manual (2010) has been followed as bibliography and the results are shown in Appendix H

G.1 Introduction to Plaxis3D 2010

Plaxis3D 2010 is a commercial three dimensional finite element program used to perform deformation and stability analysis for various types of geotechnical structures such as foundations, anchors and sheet piles. The program uses a convenient graphical user interface that enables users to generate a geometry model and a finite element mesh quickly and easily.

Plaxis 3D is an implicit element solver relating forces and displacements by demanding equilibrium in every point in the model. From the equations of equilibrium the weak formulation of the continuum problem is obtained by means of virtual work. A difference between FLAC^{3D} and Plaxis 3D is that the last one is a static solver, meaning that inertial forces are omitted.

The generation of a three-dimensional finite element model is based on the model geometry such as volumes, surfaces, lines and points. To create the soil stratigraphy different boreholes can be defined. Boreholes are locations in the drawn area at which the information on the position of soil layers and the water table is given. The program will interpolate the soil layer position between each borehole.

The sign convention used by Plaxis 3D, is based on the Cartesian coordinate system cf. figure G.1. Compressive stresses and forces, including pore pressures, are taken to be negative, whereas tensile stresses and forces are taken to be positive. The international system criterion is used for the unit and dimensions.

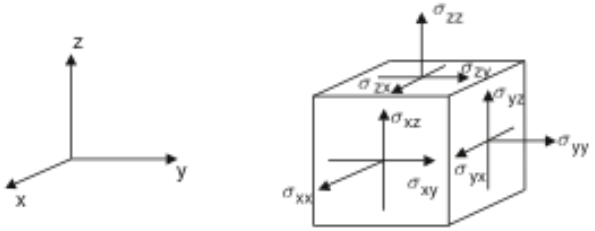

Figure G.1: Sign convention in Plaxis 3D

In models that involve pore pressure, the input of the water unit weight is required to determine the effective stresses and pore pressure. In these models is set by default to 10 kN/m^3.

Plaxis 3D provides four predefined materials models. The Mohr-Coulomb tension cut-off for drained conditions is used in this numerical approach, as is also used in the $FLAC^{3D}$ models. The tension cut-off model considers that the soil can only be submitted to compression and it cannot resist tension.

The creation of the model basically consists of two parts, generation of the model and calculation phase. The model geometry is a composition of boreholes and work planes. Only one borehole is created in the numerical modelling, as no information on the soil stratigraphy at the site is available, i.e. the soil layers are assumed to be horizontal and homogenous. The work planes are used in order to define loads and structures at different vertical levels.

Soil and material properties can be added using material library in Plaxis 3D, where standards values of the material properties of construction materials can be found. For these numerical approaches, the soil material is assignment depending on the soil properties obtained from the CPT's made in the geotechnical laboratory for each test.

The program offers a three-dimensional mesh generation feature, which can be carried out for various mesh densities in different surfaces. A convergence test is made in order to establish the optimal density mesh with which the horizontal displacement remains constant if the mesh density increases.

After the mesh creation, the calculation phase is built. The initial situation, plates and interfaces, overburden pressure load and the lateral load are defined in different calculation phases.

G.2 Generation of the model

G.2.1 Model geometry

The numerical model has to fit properly the laboratory test setup; therefore the outer boundary of the geometry model is set to the dimension of the soil volume in the pressure tank.

The boundary conditions are similar to the ones employed in the FLAC^{3D} model, except that no boundary restrictions are attached to the plane of symmetry, since there are no symmetry simplifications in the Plaxis 3D model. Moreover, in discordance with FLAC^{3D}, Plaxis 3D does not allow curved outer boundaries, only square boundaries. Therefore, a whole model is created in Plaxis 3D, where the diameter of the inner walls of the pressure tank corresponds to the side length of the model. Therefore, the side length is 2.10 meters and the depth of the soil is set to 0,58 meters. In the calculation of the convergence test for the mesh density it has been proved that the soil model is big enough to ensure that the boundaries do not affect the displacement and the behaviour of the monopile, when is submited to horizontal loads.

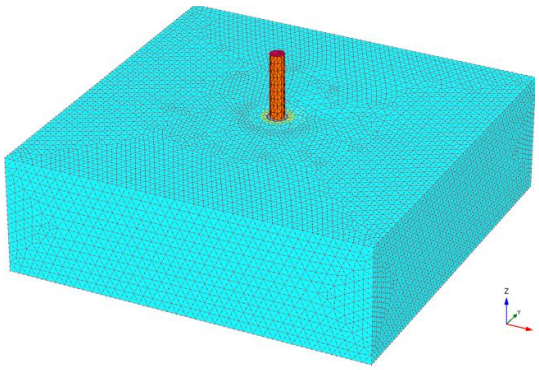

Figure G.2: Model geometry

The monopile is generated importing a vertical hollow cylinder from the Plaxis 3D volumes and surfaces library. The dimensions of the monopile are set equal to the small-scale monopile used in the laboratory tests.

The surfaces of the monopile can be discomposed into simple surfaces; each surface can be modelled as a plate or as a geogrid. In this model the surfaces are modelled as a plate and then the material properties of the monopile can be added to the plates.

G.2.2 Model boundary fixities

Along all boundaries Plaxis 3D automatically imposes a set of fixities corresponding to a free ground surface and a fully fixed bottom. All vertical boundaries are fixed in the direction of their normal.

The soil volume:

- Vertical model boundaries with their normal in x-direction are fixed in x-direction (U_x=0) and free in y and z-direction.
- Vertical model boundaries with their normal in y-direction are fixed in y-direction (U_y=0) and free in x and z-direction.
- The model bottom boundary is fixed in all directions (U_x=U_y=U_z=0)
- The surface is free in all directions.

It is important for the full-scale model, that the bottom and vertical boundaries are located in a distance from the foundations large enough to avoid interference with the failure zone around the foundation. If the boundaries would interfere with the failure zone it would strengthen the soil. This issue has been examined for the full-scale test; in conclusion, the purpose is that the chosen geometry does not pose any problems in this regard. However for the small-scale test it has not been studied because the propose is to model as accurate and similar as possible to the laboratory test, and no changes of geometry are considered.

G.2.3 Interface

In order to achieve a good relationship between the pile structure and the soil volume, an interface is created. Interfaces are joint elements to be added to the surfaces to allow for a proper modelling of soil-structure interaction. Interfaces are used to simulate the contact between a plate (from the pile structure surfaces) and the surrounding soil. An interface can be created next to the plate or geogrid elements or between two soil volumes. In the model the interface is created next to the pile plates. The thickness of the interface is zero, which means that the pair of nodes are located with the same coordinates, however, a virtual thickness is used automatically by the program to calculate the stiffness and cannot be modified.

The interface consists of 16 nodes quadrilateral shaped elements. Interface elements are numerically integrated using 3 Gauss integration points. Cf. Figure G.3, for the position of the nodes and integration points.

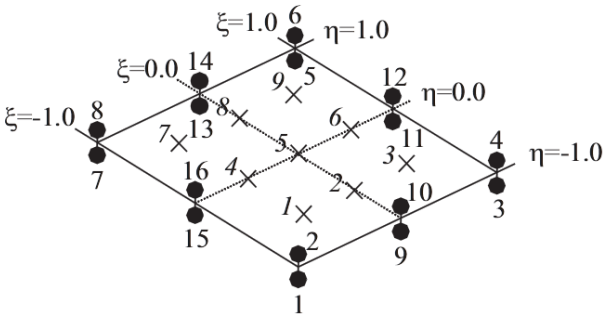

Figure G.3: Local position of nodes (bold dots) and integration points (crosses) in a 16 nodes interface element.

The interface elements have pairs of nodes instead of single nodes. The distance between the two nodes of a node pair is zero. Each node has three translational degrees of freedom (U_x, U_y, U_z). The aim of these interface nodes is to allow for differential displacements between the node pairs slipping and gapping.

A positive interface (the side of the surface at the positive local z-direction) is created between the mantle part of the pile and the surrounding sand. A negative interface (the side of the surface at the negative local z-direction) is created for the inner wall of the cylinder. A positive interface is created for the toe pile, which is embedded in the sand for a better interaction between soil and toe pile due to the expected toe-kick effect caused by the rigid motion of the pile.

The sign of an interface is only used to enable distinguishing interfaces at either side or at the surface, but it does not affect its behaviour.

The interface stiffness and strength can be defined depending on the kind of analysis, and it is controlled by the parameter R_{inter}.

A rigid interface, perfectly rough soil-structure, is used when the interface should not have a reduced strength with respect to the strength in the surrounding soil. It is not intended for soil-structure interaction and should not have reduced strength properties. The strength of these interfaces should be assigned as rigid (which corresponds to R_{inter} = 1.0).

The value of R_{inter} can be entered manually. In general, for real soil-structure interaction the interface is weaker and more flexible than the surrounding soil, which means that the value of R_{inter} should be less than 1. As a recommendation it may be assumed that R_{inter} is of the order of 2/3. However, it is possible to find out a suitable value of R_{inter} by the following relationships cf. Equations G.1 to G.3. Plaxis 3D manual (2010).

$$\tan(\varphi_i) = R_{inter} \cdot \tan(\varphi_s) \quad \text{(G.1)}$$

$$E_i = R_{inter}^2 \cdot E_s \quad \text{(G.2)}$$

$$G_i = R_{inter}^2 \cdot G_s \quad \text{(G.3)}$$

Where:

φ_i	Friction angle of the interface [º] Set to 29º by recommendation
φ_s	Friction angle of the soil [º]
E_i	Young's Modulus interface [kN/m^2]
E_s	Young's Modulus soil [kN/m^2]
G_i	Shear Modulus interface [kN/m^2]
G_s	Shear Modulus soil [kN/m^2]

When the interface is elastic, then both slipping (relative movement parallel to the interface) and gapping or overlapping (i.e. relative displacements perpendicular to the interface) could be expected to occur.

G.2.4 Material assignment

G.2.4.1. Mohr-Coulomb model

As previously mentioned, it has been chosen Mohr-Coulomb tension cut-off, cf. Figure G.4. The model is chosen in drained conditions in which stiffness and strength are defined in terms of effective properties.

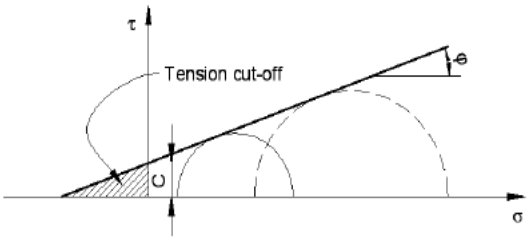

Figure G.4: Mohr-Coulomb tension cut off model.

A perfectly plastic model is a constitutive model with a fixed yield surface, i.e. a yield surface that is fully defined by model parameters and not affected by plastic straining. The basic principle of elastoplasticity is that strains and strain rates are decomposed into an elastic part, ε^e, and a plastic part ε^p.

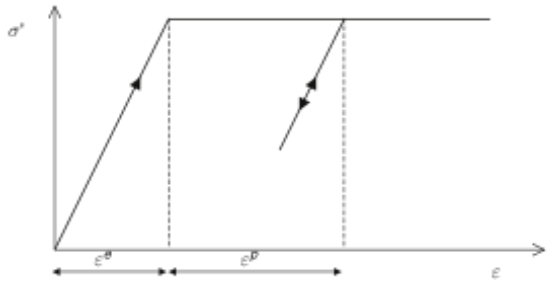

Figure G.5: Basic idea of elastic perfectly plastic model by Plaxis3D manual (2010)

In the Mohr-Coulomb model five parameters are required. These five parameters are basic geotechnical parameters that can be obtained by CPT's. The five parameters can be found in table G.1.

Geotechnical Parameters Mohr Coulom		
E	Young's Modulus	[kN/m^2]
υ	Poisson ratio	[-]
φ	Friction angle	[º]
ψ	Dilatancy angle	[º]
c	Cohesion	[kN/m^2]

Table G.1: Geotechnical parameters used in the Mohr-Coulomb model.

For further information of the Mohr-Coulomb model see Appendix I, Materials models.

In the models, a unique borehole is placed in the drawn area of the model. The assigned depth is the pressure tank depth, 0.58 m and the head of the water table is set to zero due to the aim is to increase the effective stresses of the soil and not the pore pressure.

The material properties of the Baaskarp sand and the CPT's results for each test are created in the Plaxis's library and assigned to the borehole. The soil properties and parameters are considered homogenous along the depth. See table G.2 and G.3:

Parameter	Name	Sand	Interface	Unit
General				-
Material Model	Model	Mohr-Coulomb	Mohr-Coulomb	-
Type of material behaviour	Type	Drained A	Drained A	-
Parameters				-
Poisson's ratio	υ	0,23	0,23	-
Cohesion	$C_{u,ref}$	0,001	0,001	kN/m^2
Increase in stiffness	E'_{inc}	0	0	kN/m^2/m
Increase in cohesion	$S_{u,inc}$	0	0	kN/m^2/m
R_{inter}		Table H.3	1	-

Table G.2: Constants input parameters for the sand and interface according to Plaxis3D input

Test no.	P_0 [kN/m^2]	φ_{tr}[°]	ψ_{tr}[°]	γ' [kN/m^3]	E_0 [MPa]	$R_{inter\ for\ interface}$	$K_{0,x}$, $K_{0,y}$
1	50	49.92	17.56	10.33	29.96	0.4664	0.2349
2	0	52.70	17.03	10.27	9	0.4223	0.2045
3	50	47.26	15.70	10.15	25.15	0,5122	0.2656
4	50	48.26	16.09	10.18	26.12	0.4946	0.2538
5	100	45.46	15.45	10.12	36.54	0.5455	0.2872
6	100	45.67	16.06	10.18	38.85	0,5415	0,2847
7	100	45.54	15.84	10.15	38.00	0.5440	0.2863

Table G.3: Sand input parameters in Plaxis3D Foundation for each test obtained from experimental CPT's at the laboratory.

The material model is computationally light and recommended when obtaining an initial numerical analysis of soil behaviour. It is a first order model that does not take into account stress dependency or stress path dependency on stiffness. The model describes the failure state quite well when using effective values, friction angle and cohesion. Moreover the model limitations are more apparent when undrained behaviour is considered, but in this case, only drained conditions are considered.

G.2.4.2. Hardening soil model

As an alternative model to Mohr-Coulomb material model, the Hardening Soil model has been considered. The small-scale tests have been simulated using the Hardening soil model due to the fact that a better approach of the load-displacement relationship is expected using this model.

The Hardening Soil model is, like the Mohr-Coulomb model, a failure criterion, which can be used to model the soil. The principal difference between both material models can bee appreciated in figure G.6.

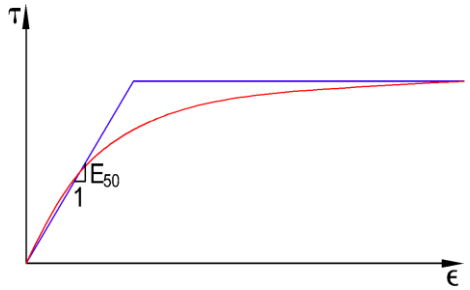

Figure G.6: Basic difference between Mohr Coulomb (Blue line) and Hardening soil (Red curve) models

The Mohr-Coulomb model is a linear-elastic, perfect plastic model (blue line) and the Hardening Soil model describes work curve of the soil in a more realistic manner (red curve). In contrast to an elastic perfectly-plastic model, the yield surface of a hardening plasticity model is not fixed in principal stress space, but it can expand due to plastic straining.

For further details of Hardening soil model used, a deeper explanation of the theory and the procedure for obtaining the parameters of the model is written in Appendix I, Material models.

The basic parameters necessary to describe the Hardening soil model are:

Geotechnical Parameters Hardening soil model		
E_{50}^{ref}	Secant stiffness in standard drained triaxial test	[kN/m^2]
E_{ur}^{ref}	Unloading/reloading stiffness	[kN/m^2]
E_{oed}^{ref}	Tangent stiffness for primary oedometer loading	[kN/m^2]
m	Power for stress level dependency of stiffness	[-]
υ	Poisson ratio	[-]
φ	Friction angle	[º]
ψ	Dilatancy angle	[º]
c	Cohesion	[kN/m^2]

Table G.4: Input parameters for Hardening soil model.

The values of the input parameters for every test, following the procedure explained in Appendix I, are shown in table G.5. The friction angle and dilatancy angle are the values obtained from the CPT's in table G.3.

Test no.	σ'_3 [kN/m^2]	E_{50}^{ref} [kN/m^2]	E_{ur}^{ref} [kN/m^2]	m [-]	E_{oed}^{ref} [kN/m^2]
1	11.74	57235	171706	0.58	44027
2	5	53812	161438	0.58	41394
3	13.20	45840	137521	0.58	35262
4	12.70	48061	144184	0.58	36970
5	28.70	44386	133160	0.58	34143
6	28.50	47840	143520	0.58	36800
7	28.60	46609	139828	0.58	35854

Table G.5: Input parameters for Hardening soil model.

G.2.4.1. Hardening soil small strain model

This is an elastoplastic type of hyperbolic model, similar to the Hardening Soil model. Moreover, this model incorporates strain dependent stiffness modulus, simulating the different reaction of soil in small strain state.

The original Hardening Soil model assumes elastic material behaviour during unloading and reloading. However, the strain range in which soils can be considered truly elastic, i.e. where they recover from applied straining almost completely, is very small. With increasing strain amplitude, soil stiffness decays nonlinearly.

For further details of Hardening soil small strain model, a deeper explanation of the theory and the procedure for the obtained parameters of the model can be found in Appendix I.

The basic necessary parameters to describe the Hardening soil small strain model are the ones from Table G.4 within the additional parameters shown in Table G.6:

Geotechnical Parameters Hardening soil small strains model		
G_0^{ref}	Reference shear modulus at very small strains	[kN/m^2]
G_s	Secant shear modulus	[kN/m^2]
υ_{ur}	poission ratio for unloading and reloading	[-]
$\gamma_{0,7}$	Shear strain at which $G_s = 0.722 G_0$	[-]

Table G.6: Extra input parameters for Hardening soil small strains model.

The calculated values (Cf. Appendix I for the calculation procedure) for the additional parameters for each test are:

Test no.	G_0^{ref} [kN/m^2]	G_s [kN/m^2]	$\gamma_{0,7}$ (10^{-5}) [-]
1	82454	17185	28,4
2	82354	10462	21,7
3	82104	18316	27.63
4	82177	17926	27.87
5	82057	28722	35.95
6	82170	28645	35.97
7	82130	28690	35.96

Table G.7: Extra input parameters for Hardening soil small strains model.

G.2.5 Mesh generation

The model is meshed using the automatic mesh generation tool in Plaxis 3D 2010. The mesh is generated using different types of elements depending on the body being meshed. In Plaxis 3D the soil is modelled by means of 10-node tetrahedral elements. This type of element provides a second-order interpolation of displacements, cf. Figure G.7. Plaxis 3D uses three local coordinates (ξ, η, ζ), the shape functions have the property that the function value is equal to unity at node i, and zero at the other nodes. This type of element has three translational degrees of freedom in each node and is generated from 6 nodes triangular wedge elements, suitable for a two-dimensional mesh.

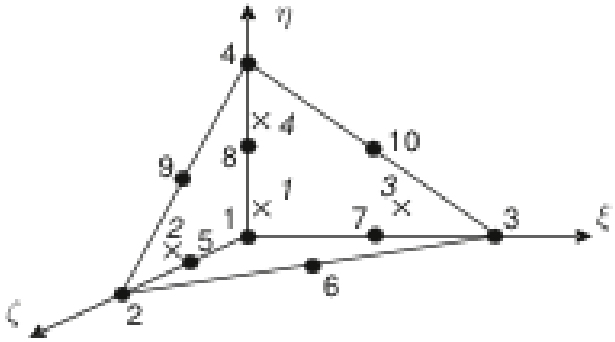

Figure G.7: Local numbering and positioning of nodes (•) and integration points (x) of a 10-node wedge element in Plaxis 3D. Plaxis 3D manual (2010)

The monopile is modelled as a hollow pile and meshed using 6 node triangle plate elements, see figure G.8. This type of element has six degrees of freedom in each node, i.e. three translational (U_x, U_y, U_z) and three rotational degrees of freedom (ϕ_x , ϕ_y , ϕ_z).

These elements are directly integrated over their cross section and numerically integrated using 3 point Gaussian integration. The position of the nodes (bold dots) and integration points (crosses) can be observed in figure G.8.

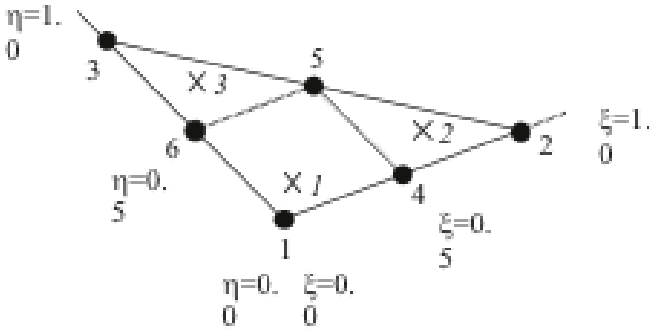

Figure G.8: Local numbering and positioning of nodes and integration points of a 6 nodes plate element used to model the monopile in Plaxis 3D. [Plaxis 3D manual, 2010]

The top plate, where the lateral load is applied, has been created stiffer than the top plate of the monopile in the laboratory, in order to have punctual load distributed evenly in pile circumference and to avoid having any deformation in the cross section.

G.2.6 Convergence test

To evaluate the optimal number of necessary elements in the finite element mesh and the behaviour of the pile depending on the mesh density, a convergence test is carried out for test number 7, with 100 kPa of overburden pressure. The lateral load has been applied in the centre point of the cross section of the top pile and the maximum total horizontal displacement is evaluated for the same load step within different mesh densities. The result, cf. Figure G.9, shows that the lateral displacement becomes constant (around 31.5 mm) with a number of elements of around 25000. The mesh density around the pile is higher than in the soil in order to obtain more data in the plate and interface nodes to compile the *p-y* curves and moment distribution.

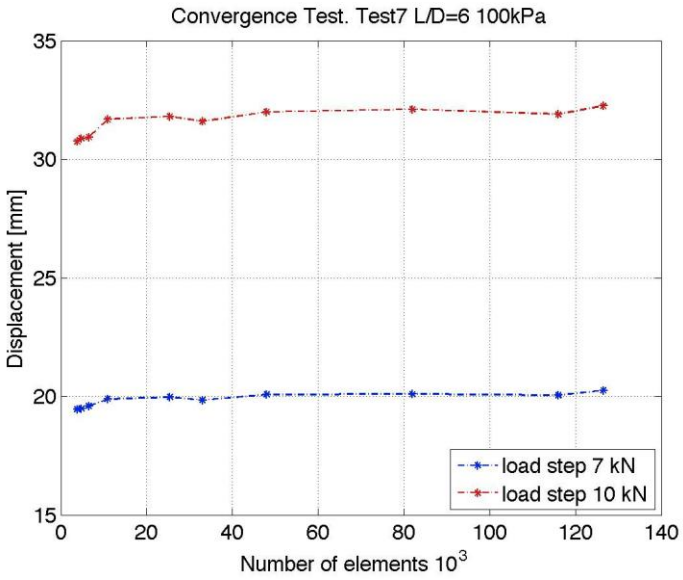

Figure G.9: Convergence test for two different load steps and maximum horizontal deflection of the top pile.

Therefore, according with the convergence test, the tests are modelled with an average of 25000 elements, which is considered accurate enough and the calculations stages are not very complex.

The next step is the calculation phase, which is explained in the following.

G.2.7 Calculation phase

At this phase the construction of the model and loads applied are staged. The first phase is the initial phase, where the initial stresses in the soil are computed using the K_0-procedure. In this procedure the initial vertical stresses are computed using submerged soil unit weight. Then, related horizontal stresses are computed using the coefficient of lateral earth pressure at rest, $K_0 = 1 - sin(\varphi)$ assuming normally consolidated soil. Following the initial phase, a second phase, called the installation phase, is initiated. In the installation phase the foundation is "constructed", the plate and interface surfaces are activated. The 3rd phase involves the creation of the distributed load on the soil surface, which corresponds to the overburden pressure simulation. Afterwards, the lateral load is applied in the centre of the top plate of the pile. The load is applied using different intervals of load, and each interval corresponds to a different phase. The calculation phase is staged in this order, because the displacements are reset to zero after the initial stresses have been calculated and the foundation has been installed. This is done to calculate the displacements solely created by the applied loads. The staging is summarised below:

1. Calculation of initial stresses using the K_0 procedure.

2. The interface and the plates are activated and the monopile is installed.

3. Surface load is applied; the model is brought to equilibrium setting the displacements to zero.

4. The horizontal load is applied in different phases corresponding to increments of load.

G.3 Generation of the full scale model

A full-scale model is generated in Plaxis 3D 2010. The same model is modelled in FLAC3D and ABAQUS. The aim is to compare the results of load-displacement relationship with the ones obtained in FLAC3D and ABAQUS in order to analyze the reliability of the numerical models using different finite element programs.

The input data is obtained from L. Kellezi and P. B. Hansen (2003).

The material properties for the soil are assigned based on the offshore geotechnical investigation carried out at Horns Rev. The geometry and material properties for the pile are based on a preliminary pile design which consists of a 4 m diameter and 22 m pile length.

The extreme static horizontal load is H = 2503 kN and the bending moment M = 84983 kNm, acting at the seabed level. In order to simulate the same conditions, a lateral force is applied at an eccentricity of 34 meters above the soil surface creating a moment of the

same magnitude. To be able to apply the load at that specific eccentricity, the pile is extended until 34 meters above the soil surface, giving low values of density to the extra section of the pile to make the weight of the foundation as minimum as possible. The stiffness of the extended pile section is used as in section 1, cf. Table G.8.

The pile is modelled as a hollow steel pile tube close ended. It is considered to behave linearly elastic and modelled as a cylindrical structure. Different values of wall thickness are set to the different sections, cf. Table G.8.

	Depth (m)	E_{steel} (kN/m^2)	γ_{steel} (kN/m^3)	υ	Walls thickness (mm)
Section 1	1.4	210E6	78.5	0.3	50
Section 2	9.1	210E6	78.5	0.3	54
Section 3	12.4	210E6	78.5	0.3	50
Section 4	14.7	210E6	78.5	0.3	40
Section 5	22	210E6	78.5	0.3	30

Table G.8: Mechanical input data for the pile geometry

In figure G.10 the 5 different sections can be observed for a better understanding of the pile geometry.

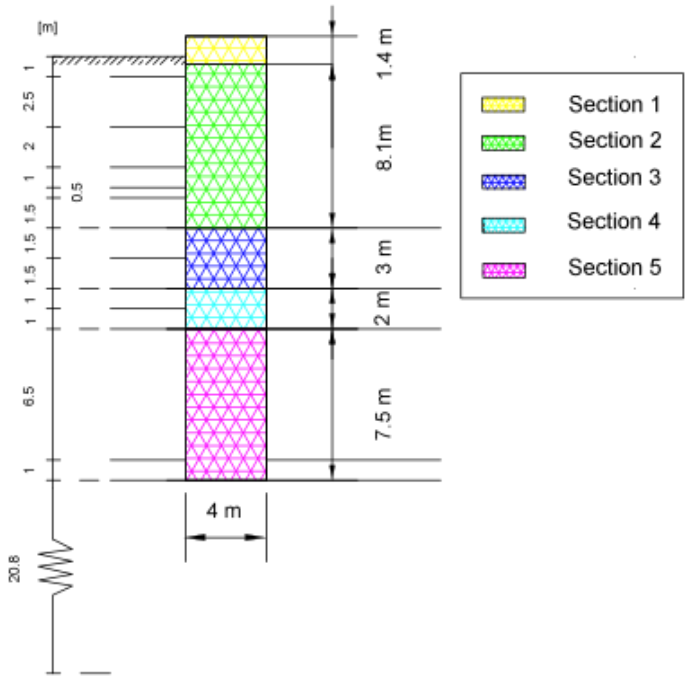

Figure G.10: Sketch of pile sections and the different soil layers creating in the model.

The soil profile is modelled with 13 different layers with derived designed parameters taken as averaged values as shown in table G.9 as it has been modelled in the ABAQUS model. From the soil profile it can be noted that at depth 13.5 m to 20 m a layer of

organic sand is located having rather low value of the friction angle. Different interfaces are created for each soil layer in order to make the soil-structure interaction the most possibly accurate. Values of R_{inter} are calculated for each interface following the criteria explained in equations G.1 to G.3.

Soil layer	Name	Depth (m)	E (kN/m^2)	γ/γ' (kN/m^3)	φ (º)	ψ (º)	R_{inter}	υ
Layer 1	Sand	1	31800	20/10	42	12	0.6156	0.3
Layer 2	Sand	3.5	57100	20/10	43.5	13.5	0.584	0.3
Layer 3	Sand	5.5	52534	20/10	42.5	12.5	0.604	0.3
Layer 4	Sand	6.5	44100	20/10	41.7	11.7	0.622	0.3
Layer 5	Sand	7	58200	20/10	43.2	13.2	0.590	0.3
Layer 6	Sand	8.5	72170	20/10	44.3	14.3	0.568	0.3
Layer 7	Sand	10	52950	20/10	43.1	13.1	0.592	0.3
Layer 8	Sand	11.5	35400	20/10	40.3	10.3	0.653	0.3
Layer 9	Sand	12.5	23530	20/10	37.2	7.2	0.730	0.3
Layer 10	Sand	13.5	13600	20/10	33.8	3.8	0.828	0.3
Layer 11	Org.sand	20	3135	17/7	21.6	0	1	0.3
Layer 12	Org.sand	21	12950	17/7	31.2	1.2	0.915	0.3
Layer 13	Sand	41.8	36800	20/10	37.8	7.8	0.714	0.3

Table G.9: Geometric and mechanical input data for the pile soil

Figure G.11 shows the different layers of soil and interface around the pile for each layer of soil.

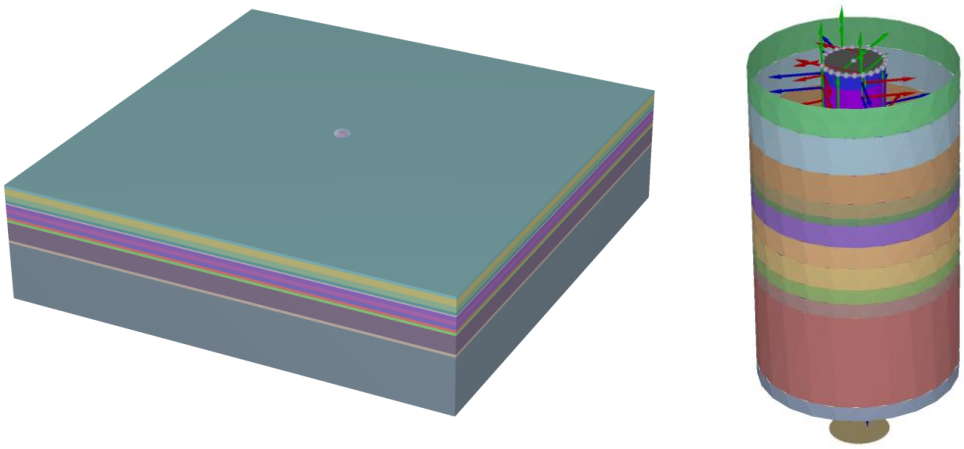

Figure G.11: Left: Soil geometry. Right: Different interface for each soil layer.

The mesh and number of elements has been created with the same mesh factors than the ones using in the convergence test. Calculation procedure has the same procedure as followed in the simulation of the small-scale test.

G.4 Post processing of results

Once Plaxis 3D has finished the calculation stages, an output window with all the results is displayed. In the next, the basic analysis of the output is shown as it has been used for the calculation of *p-y* curves and bending moment.

In figure G.12 the deformed mesh can be observed for the ultimate applied load. Plaxis 3D allows the user to select different parts of the model, being possible to select only the plates corresponding to the pile and the interface attached to the embedded part of the monopile. An output of total horizontal displacement, forces acting in the monopile plates and stresses in the interface are obtained for every load step in each node of each element.

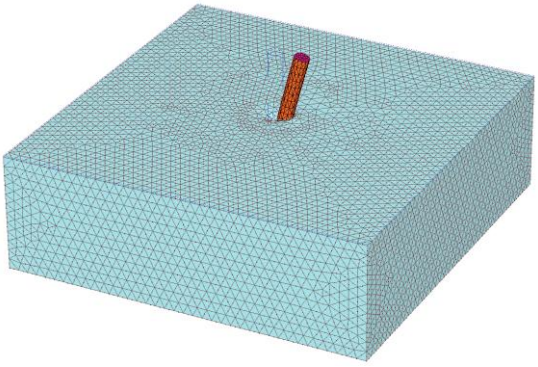

Figure G.12: Deformed mesh, test number 7 L/D = 6 P_0 = 100kPa. Maximum applied lateral load 10 kN corresponding to a total displacement of 32 mm.

In phase number 2, the interface and plates are installed, the model is brought to equilibrium and the displacements are set to zero. The difference in the soil stress distribution between phase 2 and phase 3 (when the overburden pressure is applied) can be observed in figures G.13 and G.14 which correspond to test number 7, L/D = 6 and P_0 = 100 kPa.

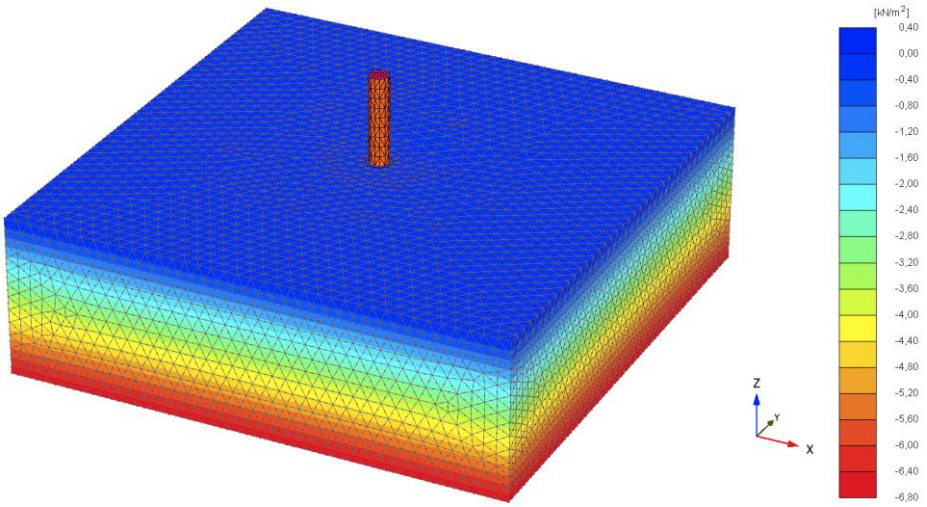

Figure G.13: Steady state of the pore pressure before the overburden pressure is applied.

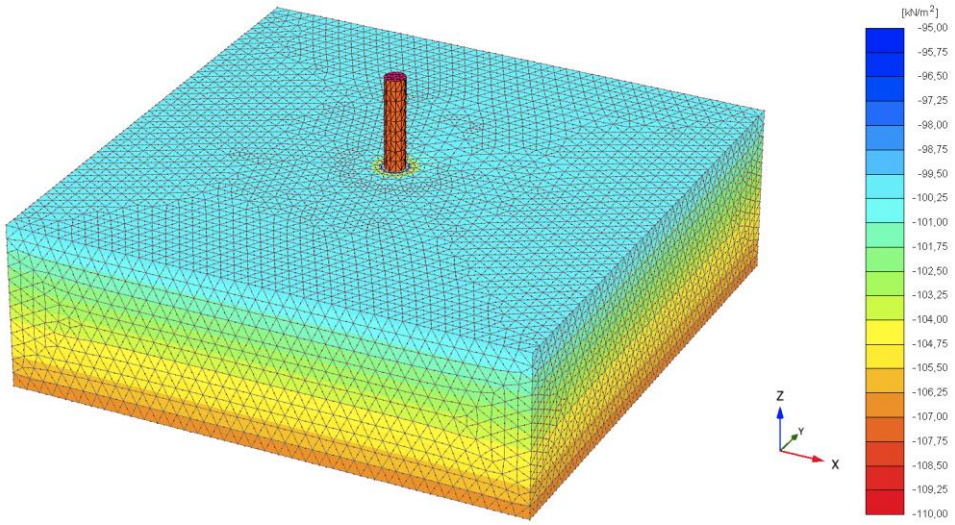

Figure G.14: Cartesian total stress distribution in z-direction when an overburden pressure of 100kPa is applied.

The program allows obtaining the stress and forces distribution along the pile in the 3 Cartesian axes and it can show it graphically for a better understanding. In figure G.15 on the left, can be observed the stress distribution when the pile is bended for the ultimate load step 10 kN. It can be appreciated the tension and compression along the monopile and the stress distribution in the toe-pile due to the shear forces.

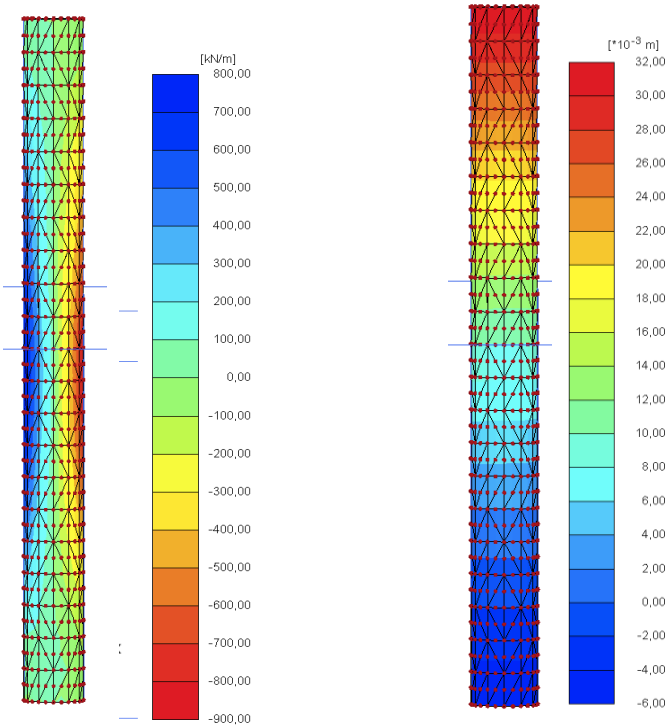

Figure G.15: Left: Axial stress distribution along the pile for 10 kN. Right: Lateral displacement of the pile for 10 kN.

In figure G.15 on the right, for the same stress state the lateral displacement along the pile is plotted. It is interesting to appreciate the zero deflection point near the bottom of the pile, as it is expected to have a rigid-body motion for a non-slender pile.

G.5 Bending moment and soil resistance calculation

Soil resistance for a pile subjected to lateral load is computed directly by integrating the stresses in the soil elements around the circumference of the pile. Chia-Chenmg Fan, James H. Long (2005).

In Plaxis 3D, the Gauss points closest to the pile have the same coordinates as the interface nodes, therefore the interface nodes are taken as the soil stresses between the pile and soil.

The soil resistance per unit length along the pile is the x-component of the total stress acting on the interface circumference. The x-component stress at a point in an interface element can be represented by traction vector, T_x, as follows in equation G.4:

$$T_x = \sigma'_{xx} n_x + \sigma'_{xy} n_y + \sigma'_{xz} n_z \tag{G.4}$$

Where n_x and n_y are components of unit normal along the x-, y-directions, respectively, and are expressed as:

$$n_x = \cos\theta_x = \frac{x_g}{\sqrt{x_g^2 + y_g^2}} \tag{G.5}$$

$$n_y = \cos\theta_y = \frac{y_g}{\sqrt{x_g^2 + y_g^2}} \tag{G.6}$$

Notice that n_z is zero because the unit normal is on a horizontal plane.

The soil resistance is computed as:

$$dp_x = T_x dA \tag{G.6}$$

To calculate the total soil resistance, p_x, per unit length along the pile, the soil resistance is integrated over the circumference:

$$p_x = \int T_x dL \tag{G.7}$$

Where L corresponds to the perimeter of the pile.

The p-y relationship at a given depth is obtained by relating the soil resistances, *p*, to the corresponding lateral deflections, *y*, of the pile at that depth.

The bending moment in the pile is computed through the forces at the plate nodes which conform the pile:

$$dM_i = x_g \cdot N_{zi} \cdot dL \tag{G.8}$$

The total Bending moment for a level z becomes:

$$M_i = \int x_g \cdot N_{zi} \cdot dL \tag{H.9}$$

Where N_{zi} is the vertical force at the node.

A value of the *p-y* curve per unit length, bending moment distribution, load-deflection relationship and zero deflection point of the monopile is obtained. Results are shown in Appendix H and in Chapter 4 and the analysis and conclusion of the numerical model are discussed.

APPENDIX H

NUMERICAL RESULTS

In the following appendix all the numerical results obtained by means FLAC^{3D} and Plaxis 3D 2010 and comparison between them and experimental results are presented.

H.1 FLAC^{3D} results (not calibrated)

H.1.1 Test 1 D=100 mm, L/D=5, P_0 = 50 kPa

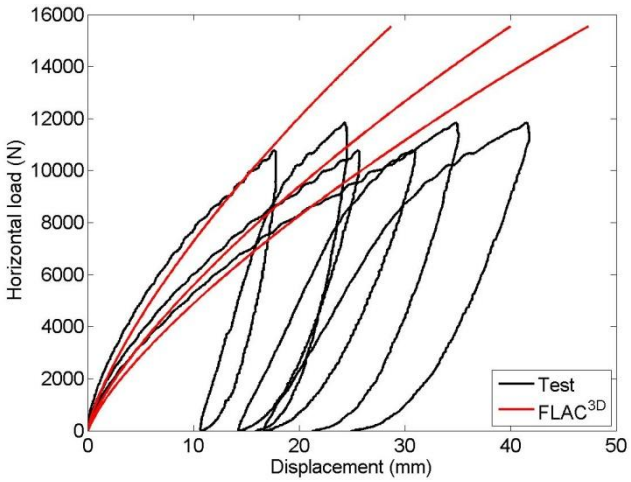

Figure H.1: Load-displacement curves obtained by numerical modelling and small scale test

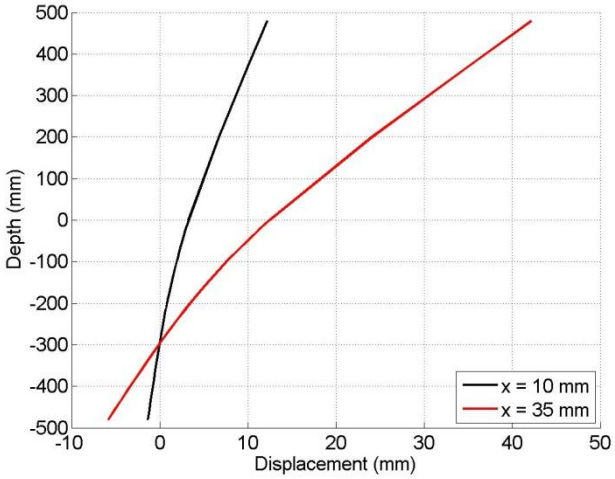

Figure H.2: Displacement distribution along the pile depth

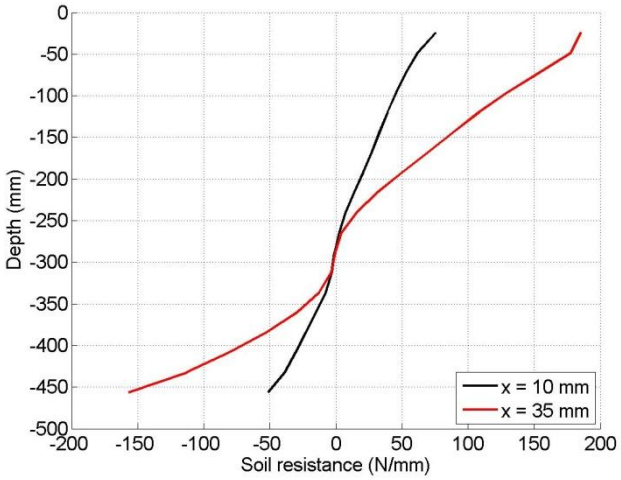

Figure H.3: Soil resistance distribution along the pile depth

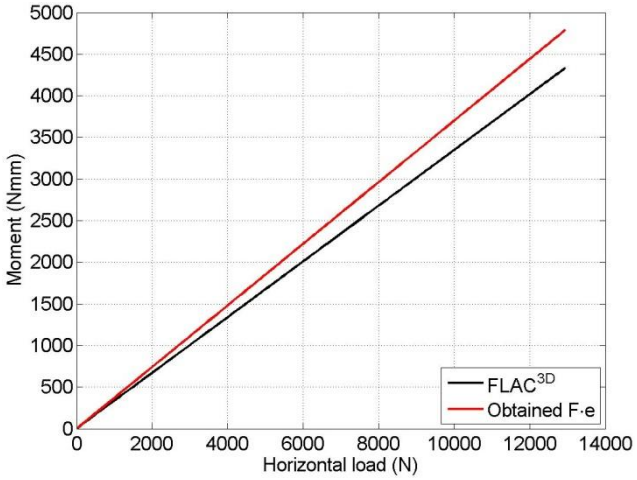

Figure H.4: Comparison of bending moments at the soil surface, obtained by multiplying the applied force with the eccentricity and computed by FLAC^{3D}

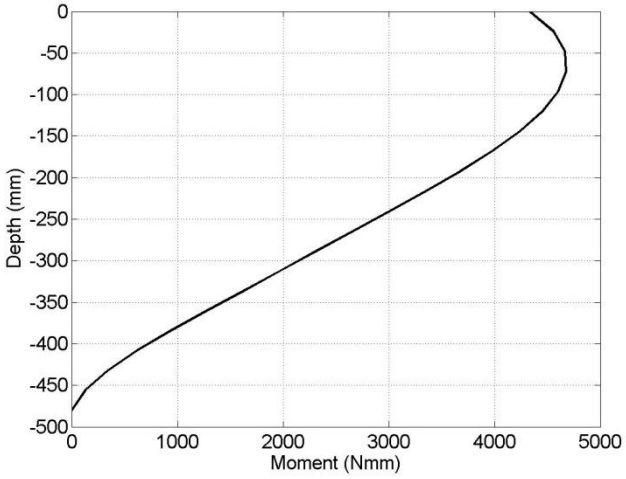

Figure H.5: Bending moment distribution along the pile depth in the final step

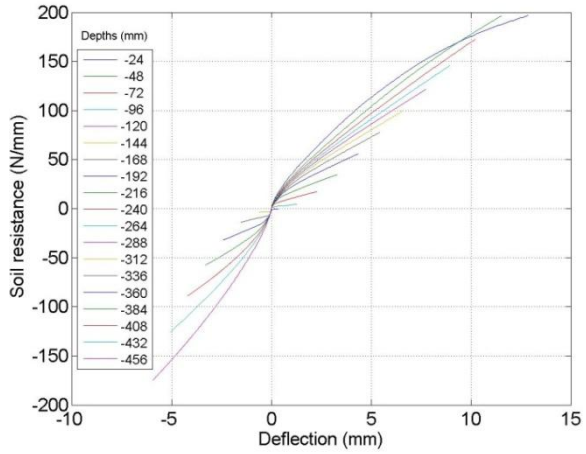

Figure H.6: p-y curves for different depths

H.1.2 Test 2 D=80 mm, L/D=5, P_0 = 0 kPa

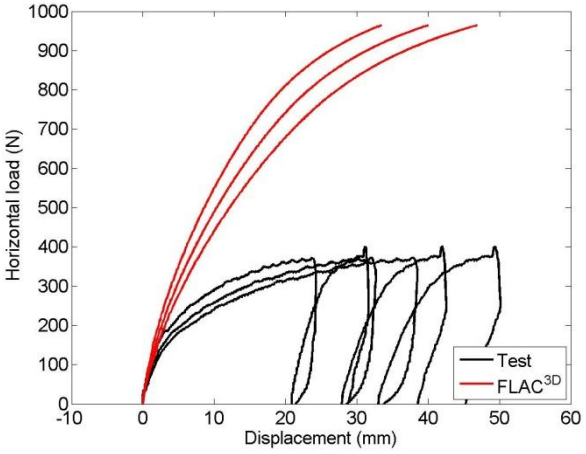

Figure H.7: Load-displacement curves obtained by numerical modelling and small scale test

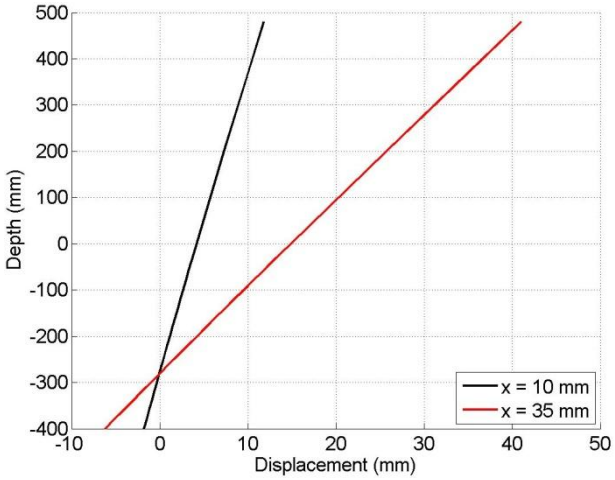

Figure H.8: Displacement distribution along the pile depth

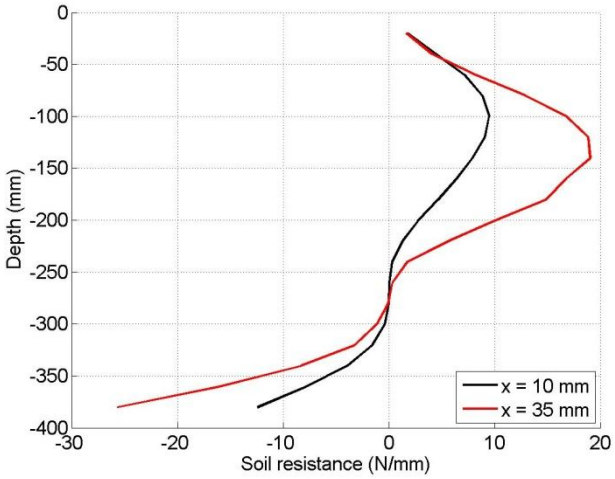

Figure H.9: Soil resistance distribution along the pile depth

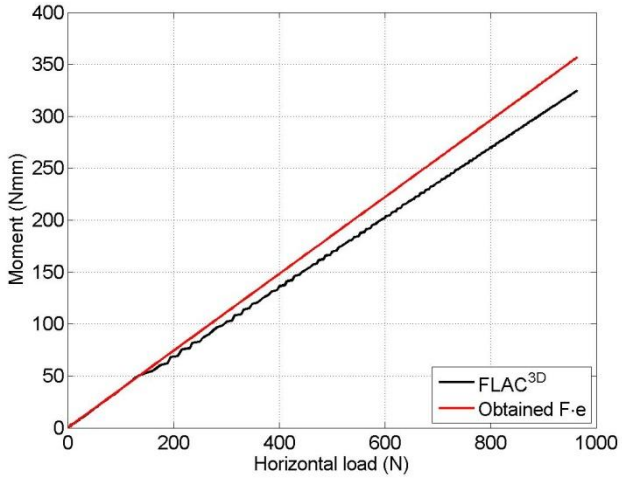

Figure H.10: Comparison of bending moments at the soil surface, obtained by multiplying the applied force with the eccentricity and computed by FLAC^{3D}

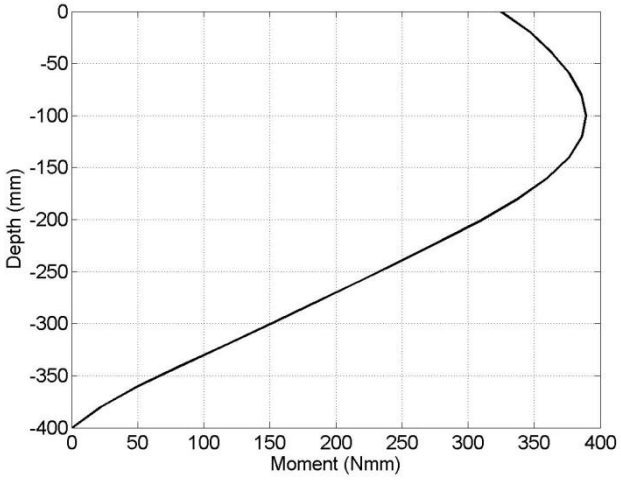

Figure H.11: Bending moment distribution along the pile depth in the final step

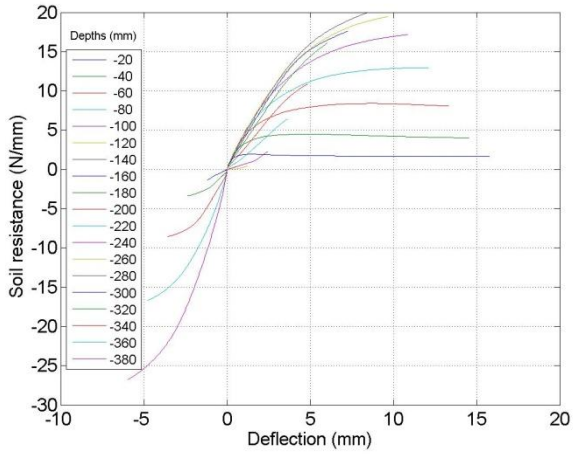

Figure H.12: p-y curves for different depths

H.1.3 Test 3 D=80 mm, L/D=5, P_0 = 50 kPa

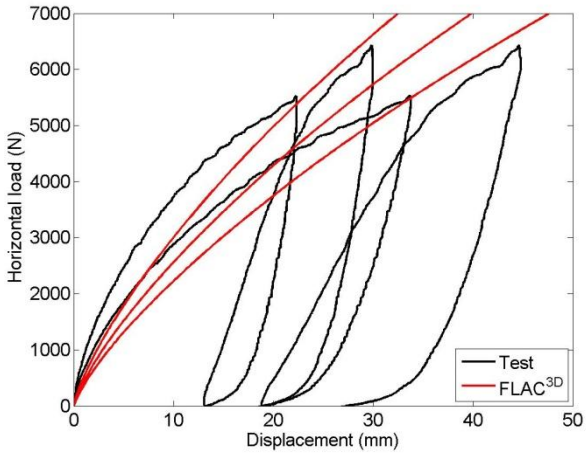

Figure H.13: Load-displacement curves obtained by numerical modelling and small scale test

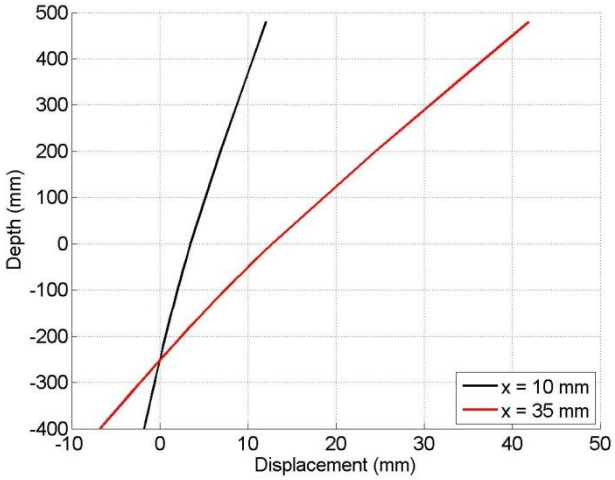

Figure H.14: Displacement distribution along the pile depth

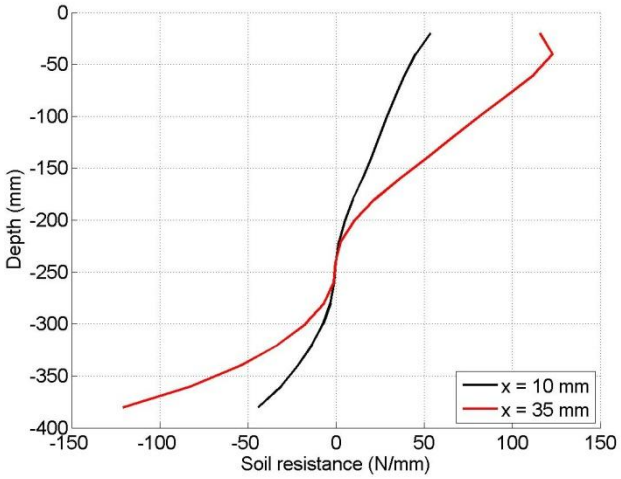

Figure H.15: Soil resistance distribution along the pile depth

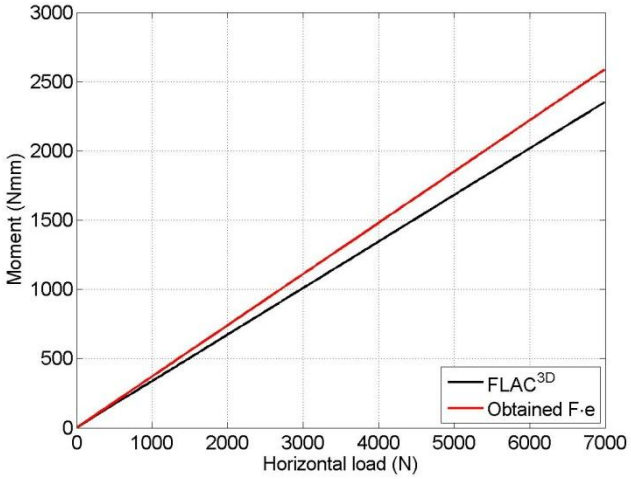

Figure H.16: Comparison of bending moments at the soil surface, obtained by multiplying the applied force with the eccentricity and computed by FLAC^{3D}

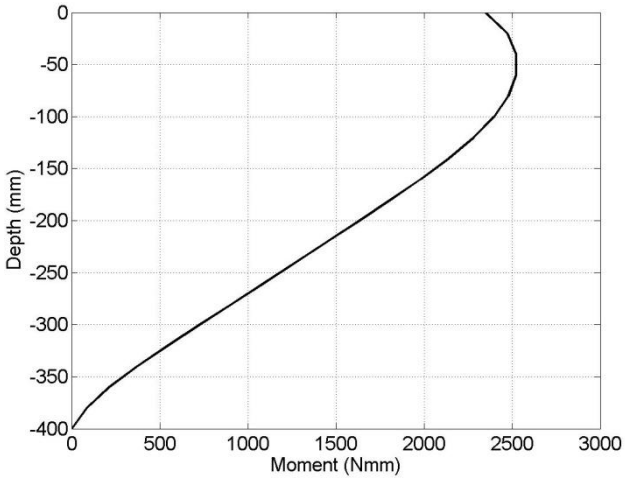

Figure H.17: Bending moment distribution along the pile depth in the final step

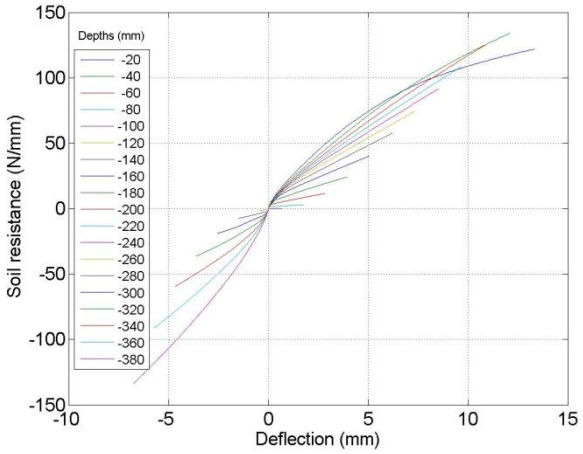

Figure H.18: p-y curves for different depths

H.1.4 Test 4 D=80 mm, L/D=6, P_0 = 50 kPa

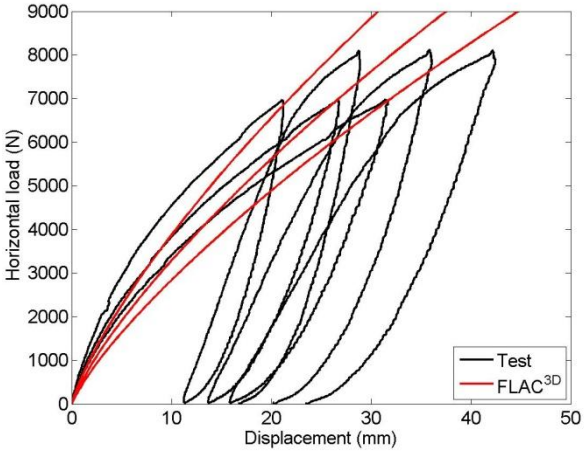

Figure H.19: Load-displacement curves obtained by numerical modelling and small scale test

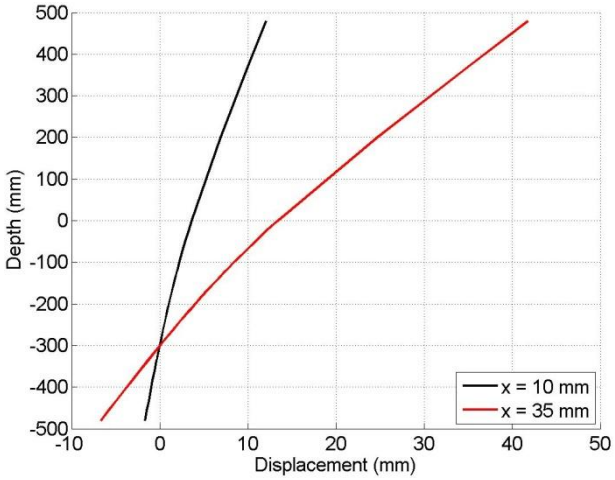

Figure H.20: Displacement distribution along the pile depth

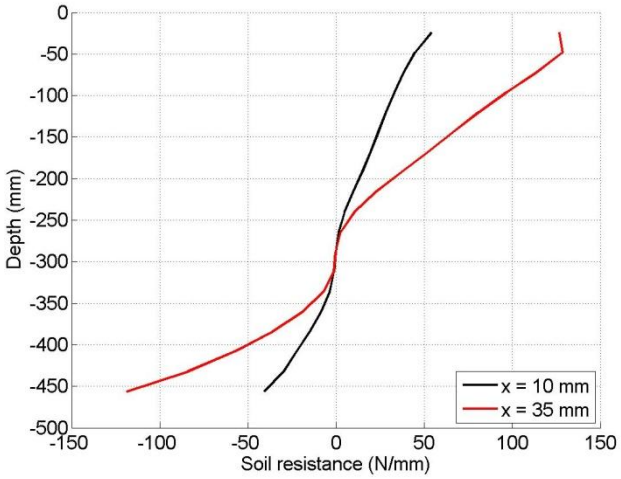

Figure H.21: Soil resistance distribution along the pile depth

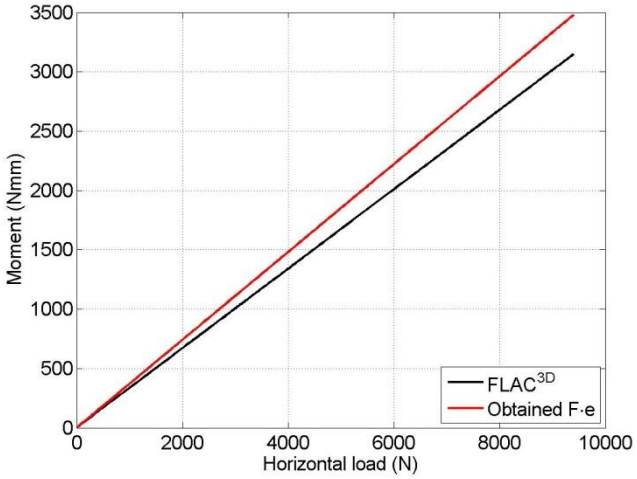

Figure H.22: Comparison of bending moments at the soil surface, obtained by multiplying the applied force with the eccentricity and computed by FLAC^{3D}

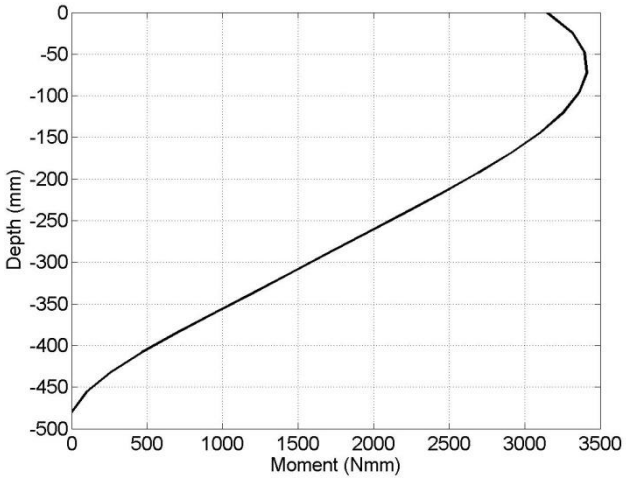

Figure H.23: Bending moment distribution along the pile depth in the final step

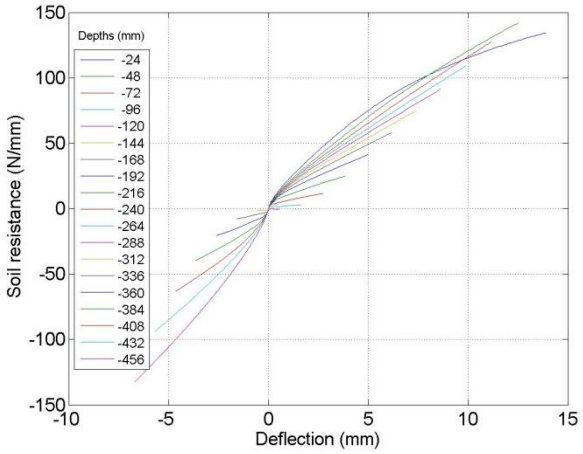

Figure H.24: p-y curves for different depths

H.1.5 Test 5 *D*=80 mm, *L/D*=4, P_0 = 100 kPa

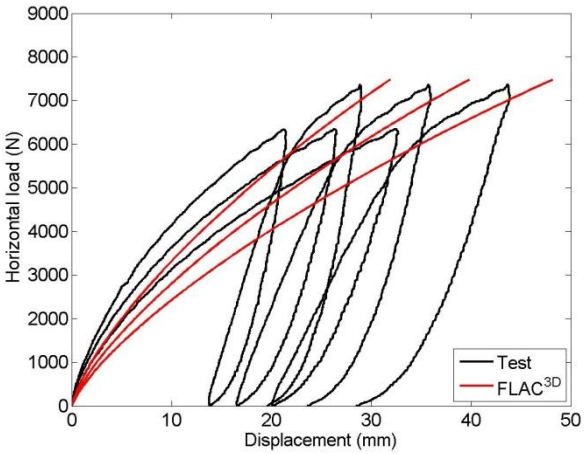

Figure H.25: Load-displacement curves obtained by numerical modelling and small scale test

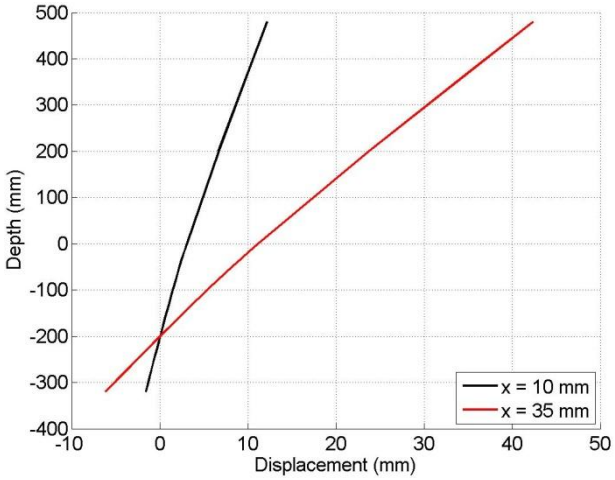

Figure H.26: Displacement distribution along the pile depth

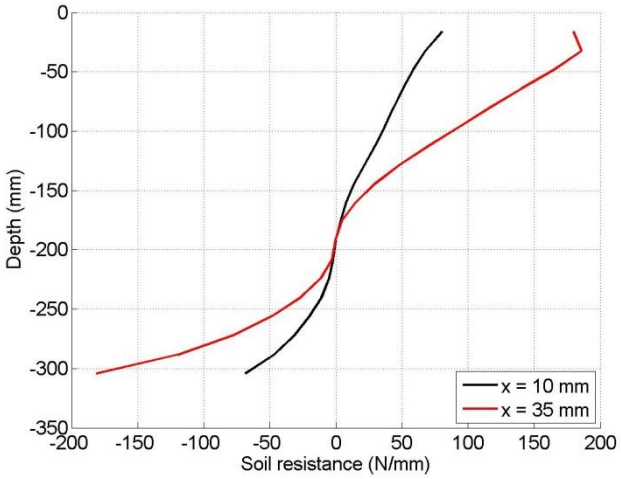

Figure H.27: Soil resistance distribution along the pile depth

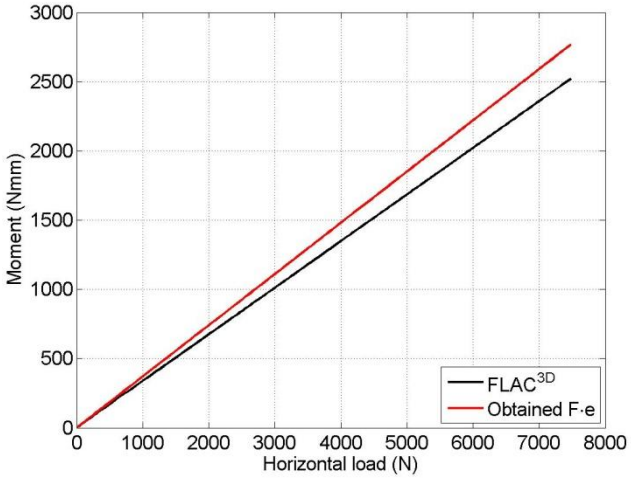

Figure H.28: Comparison of bending moments at the soil surface, obtained by multiplying the applied force with the eccentricity and computed by FLAC^{3D}

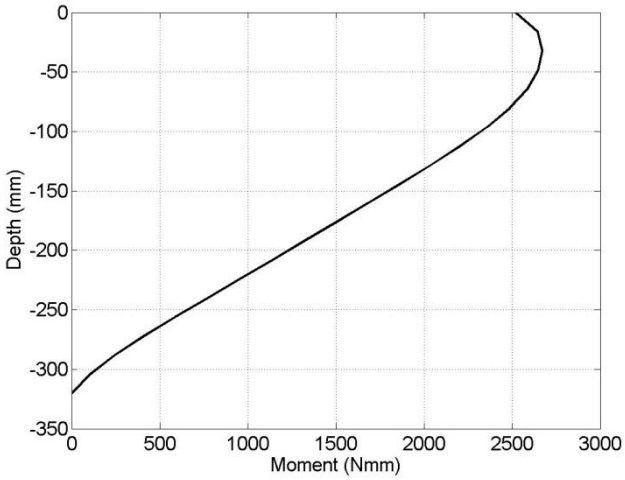

Figure H.29: Bending moment distribution along the pile depth in the final step

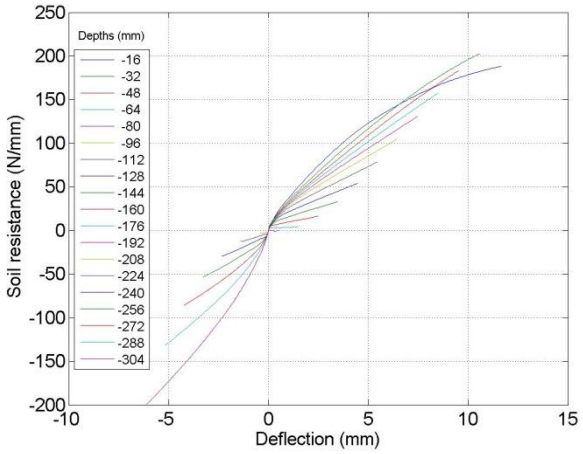

Figure H.30: p-y curves for different depths

H.1.6 Test 6 D=80 mm, L/D=5, P_0 = 100 kPa

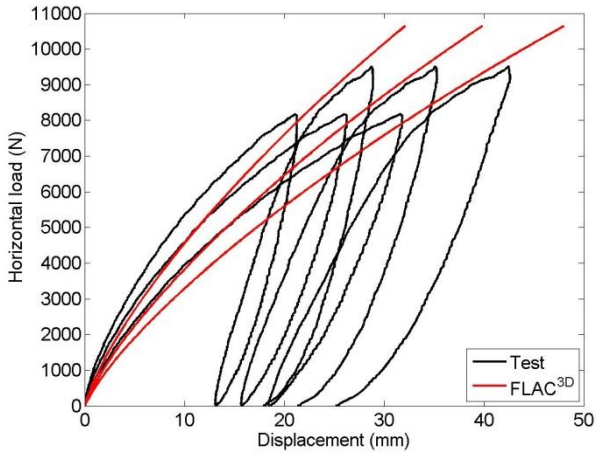

Figure H.31: Load-displacement curves obtained by numerical modelling and small scale test

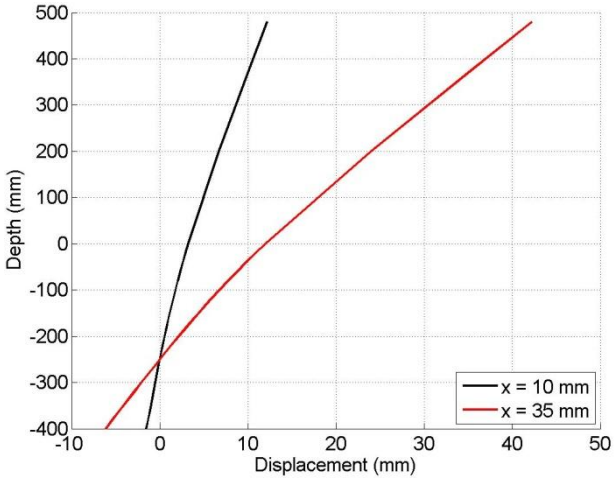

Figure H.32: Displacement distribution along the pile depth

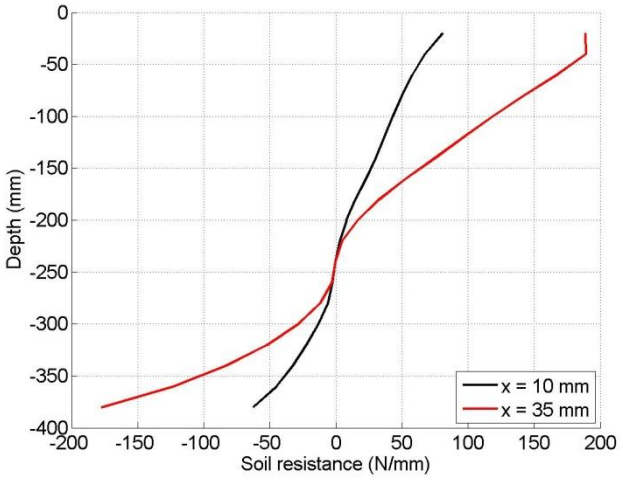

Figure H.33: Soil resistance distribution along the pile depth

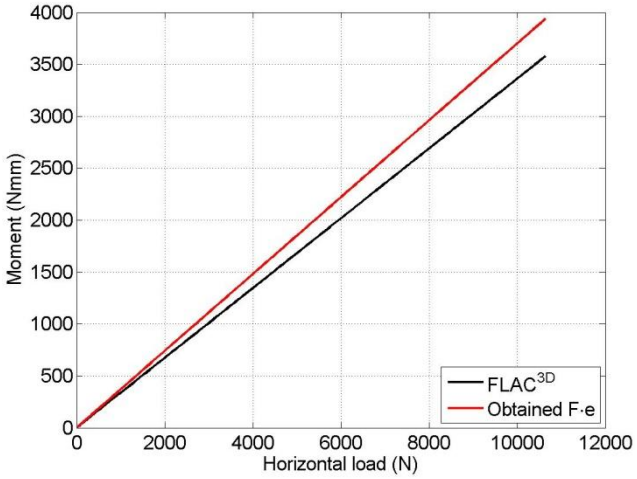

Figure H.34: Comparison of bending moments at the soil surface, obtained by multiplying the applied force with the eccentricity and computed by FLAC^{3D}

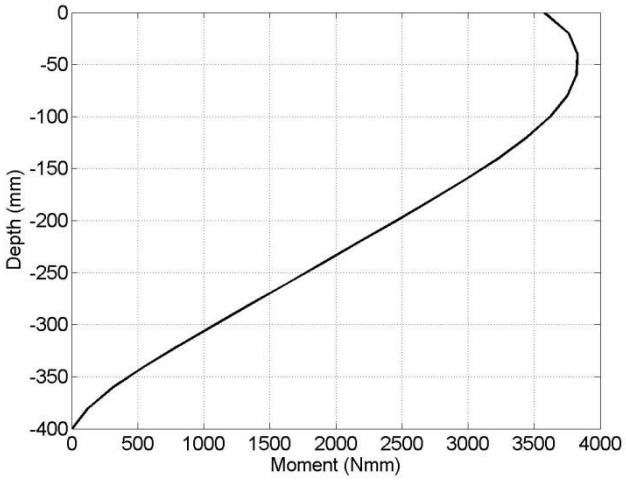

Figure H.35: Bending moment distribution along the pile depth in the final step

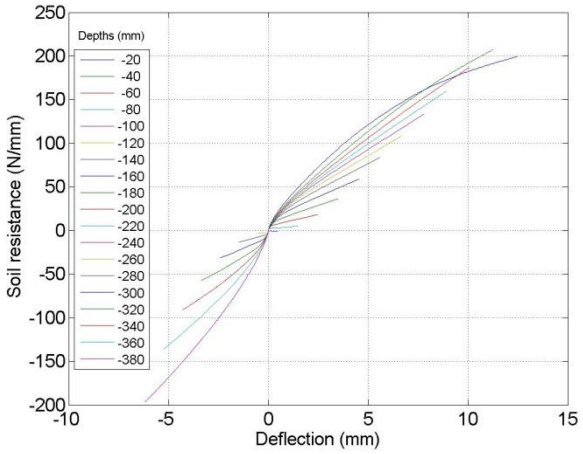

Figure H.36: p-y curves for different depths

H.1.7 Test 7 D=80 mm, L/D=6, P_0 = 100 kPa

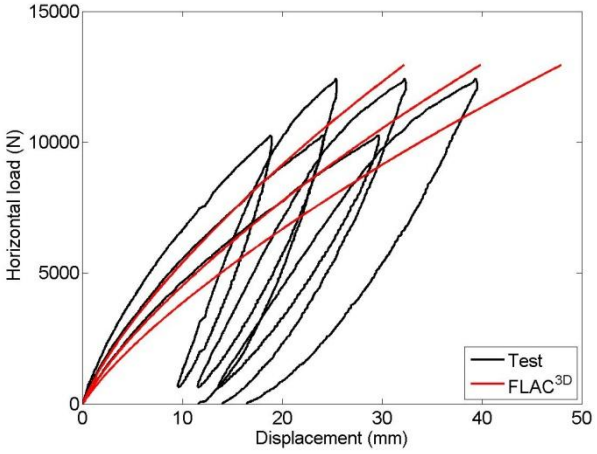

Figure H.37: Load-displacement curves obtained by numerical modelling and small scale test

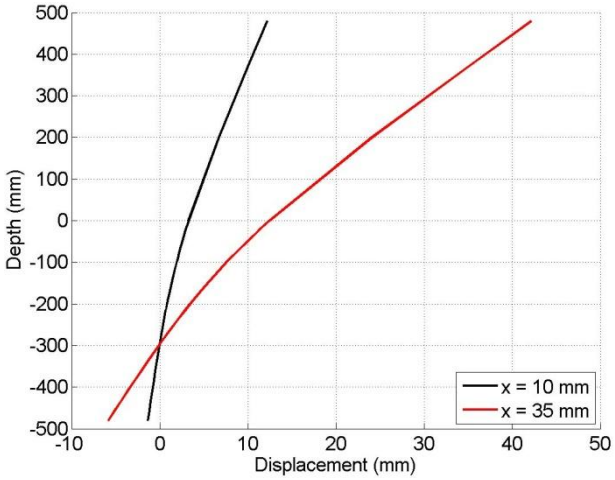

Figure H.38: Displacement distribution along the pile depth

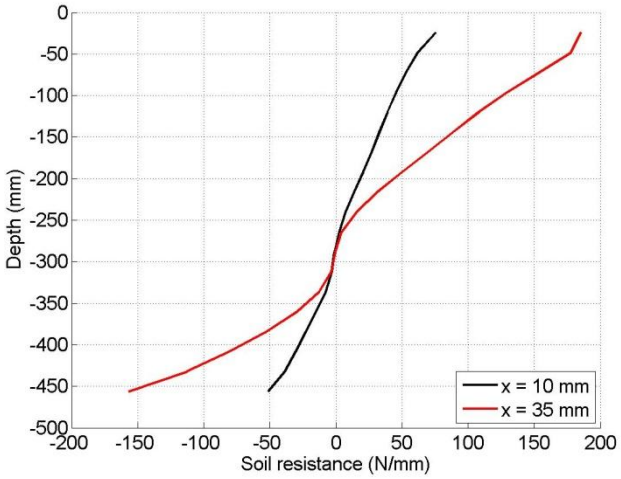

Figure H.39: Soil resistance distribution along the pile depth

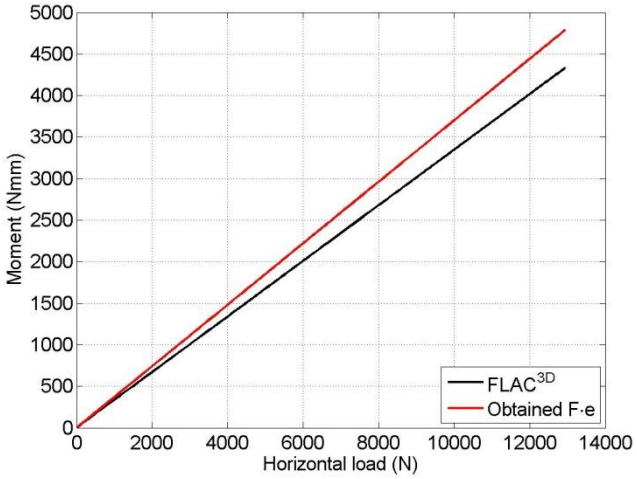

Figure H.40: Comparison of bending moments at the soil surface, obtained by multiplying the applied force with the eccentricity and computed by FLAC^{3D}

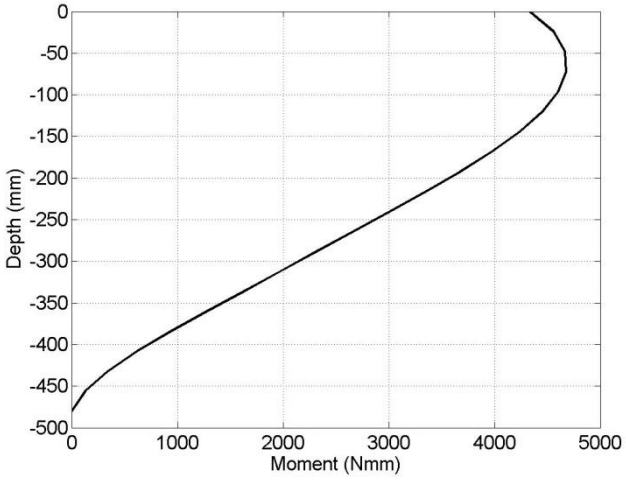

Figure H.41: Bending moment distribution along the pile depth in the final step

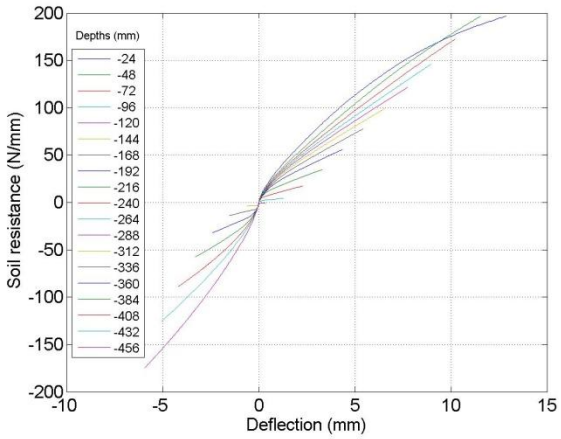

Figure H.42: p-y curves for different depths

H.2 FLAC^{3D} results (calibrated)

H.2.1 Test 1 D=100 mm, L/D=5, P_0 = 50 kPa

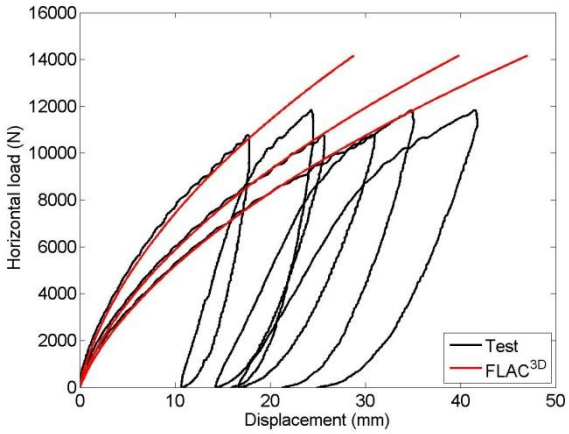

Figure H.43: Load-displacement curves obtained by numerical modelling and small scale test

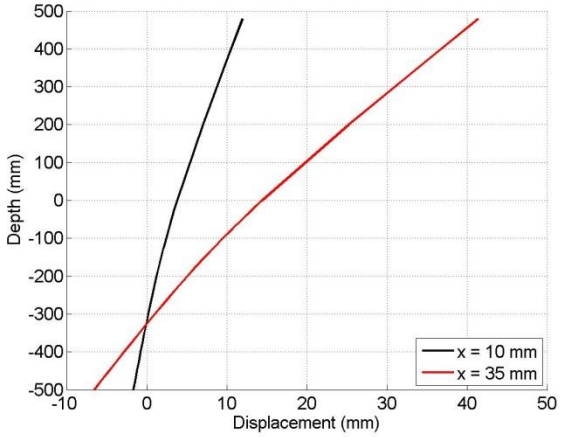

Figure H.44: Displacement distribution along the pile depth

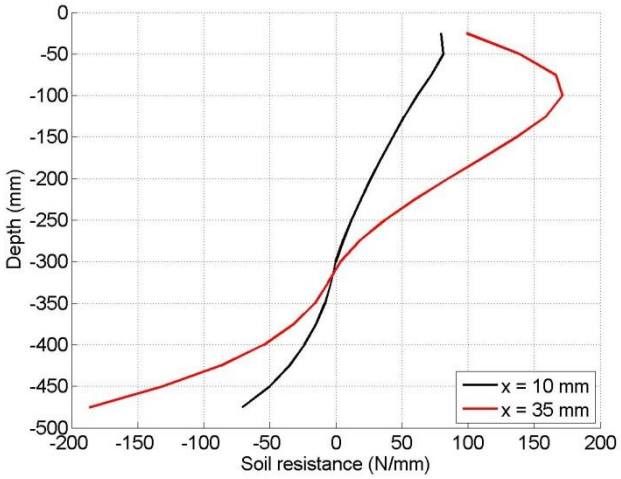

Figure H.45: Soil resistance distribution along the pile depth

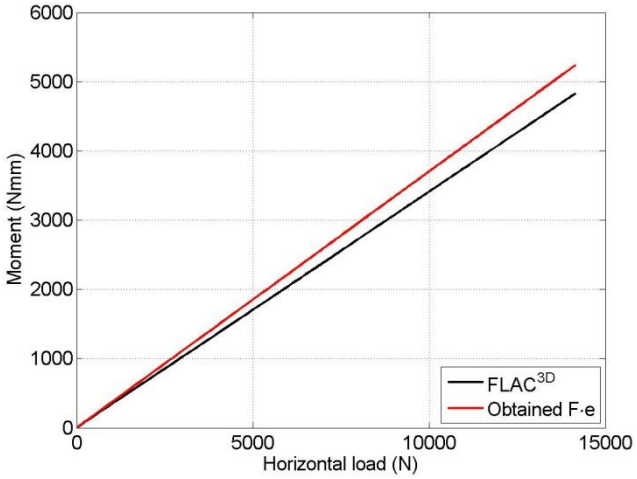

Figure H.46: Comparison of bending moments at the soil surface, obtained by multiplying the applied force with the eccentricity and computed by FLAC^{3D}

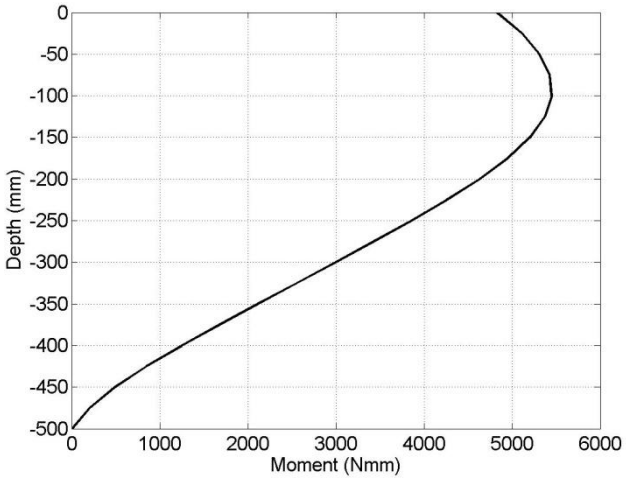

Figure H.47: Bending moment distribution along the pile depth in the final step

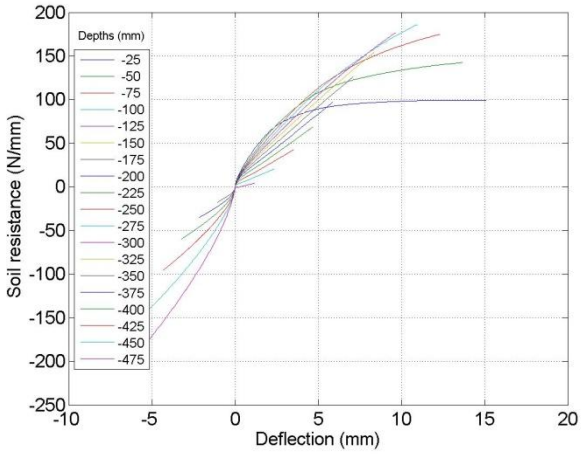

Figure H.48: p-y curves for different depths

H.2.2 Test 2 D=80 mm, L/D=5, P_0 = 0 kPa

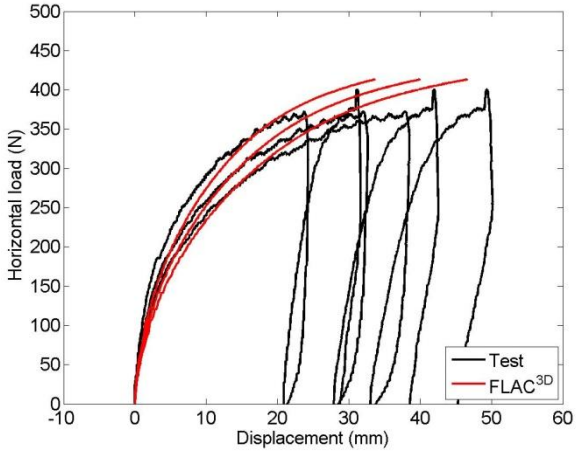

Figure H.49: Load-displacement curves obtained by numerical modelling and small scale test

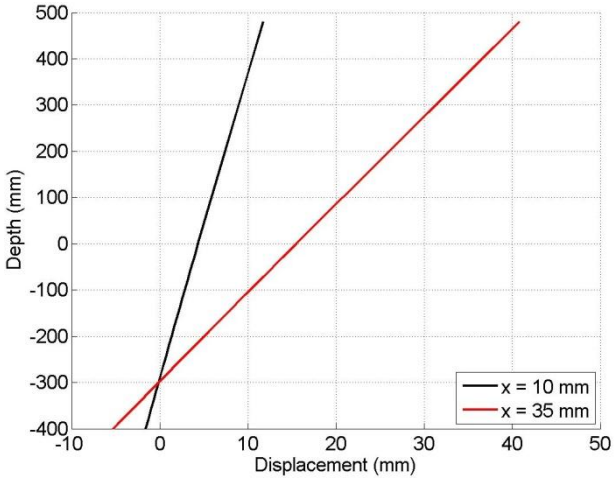

Figure H.50: Displacement distribution along the pile depth

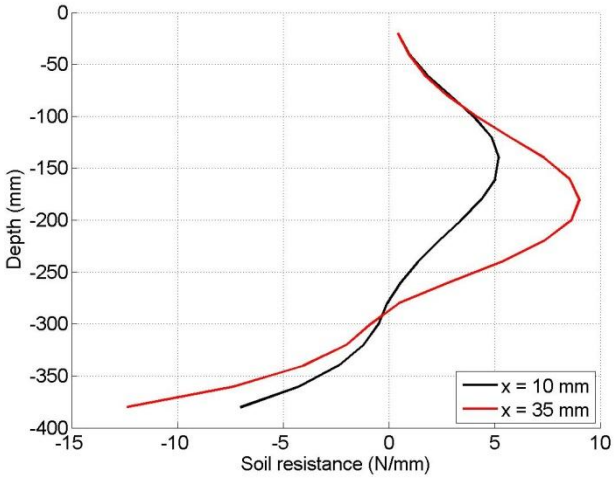

Figure H.51: Soil resistance distribution along the pile depth

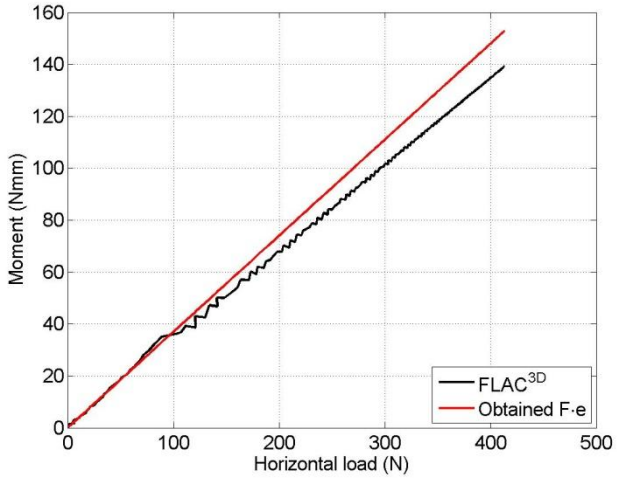

Figure H.52: Comparison of bending moments at the soil surface, obtained by multiplying the applied force with the eccentricity and computed by FLAC^{3D}

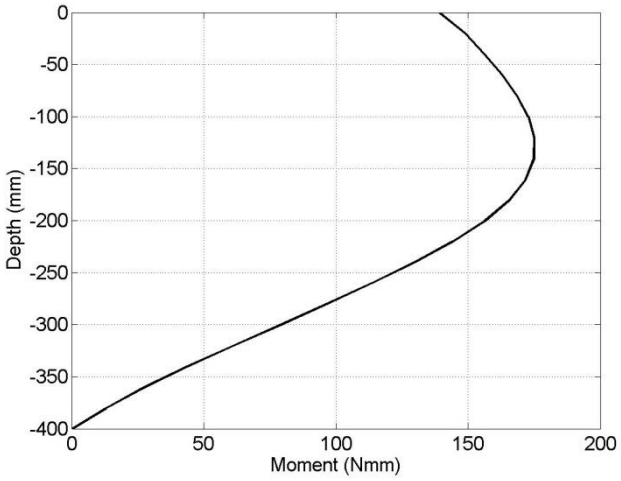

Figure H.53: Bending moment distribution along the pile depth in the final step

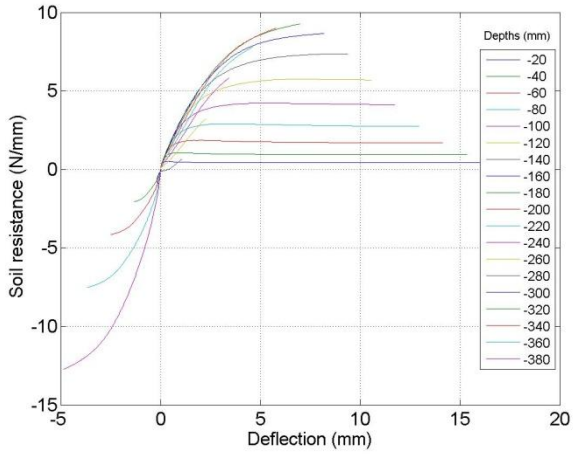

Figure H.54: *p-y* curves for different depths

H.2.3 Test 3 D=80 mm, L/D=5, P_0 = 50 kPa

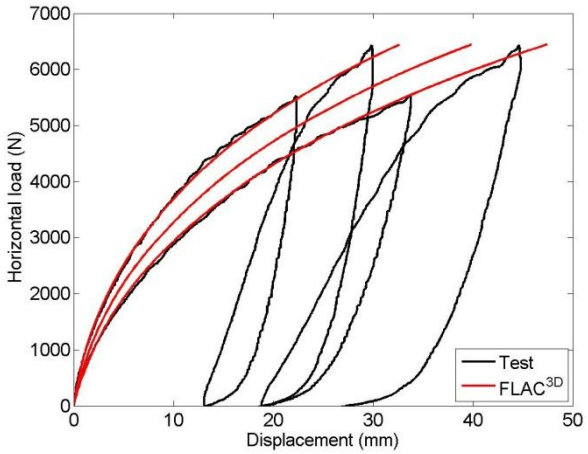

Figure H.55: Load-displacement curves obtained by numerical modelling and small scale test

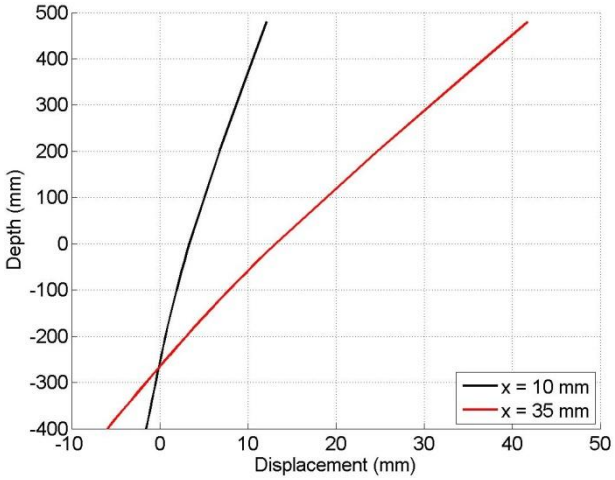

Figure H.56: Displacement distribution along the pile depth

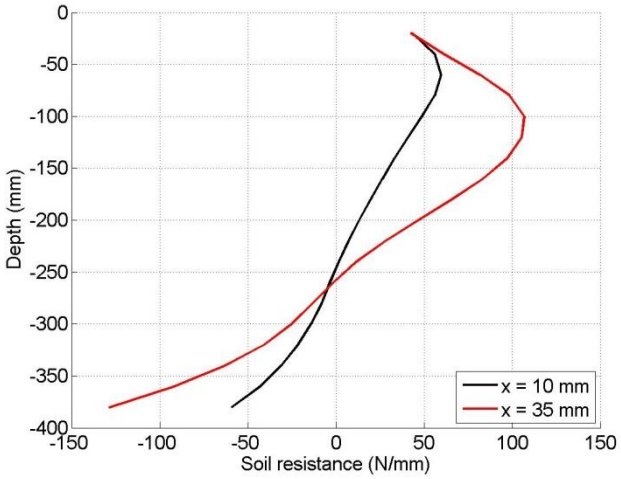

Figure H.57: Soil resistance distribution along the pile depth

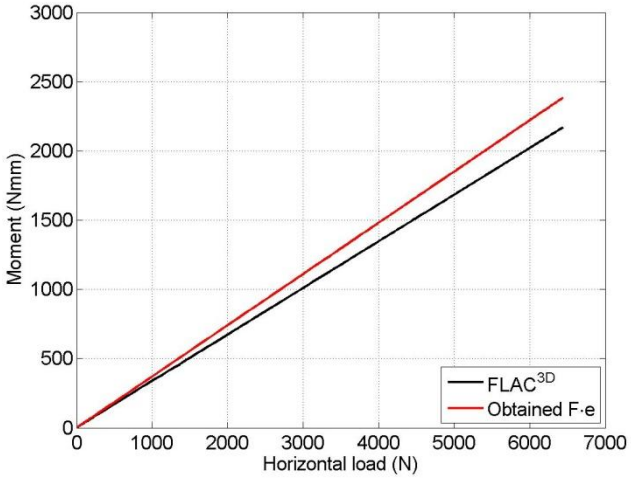

Figure H.58: Comparison of bending moments at the soil surface, obtained by multiplying the applied force with the eccentricity and computed by FLAC^{3D}

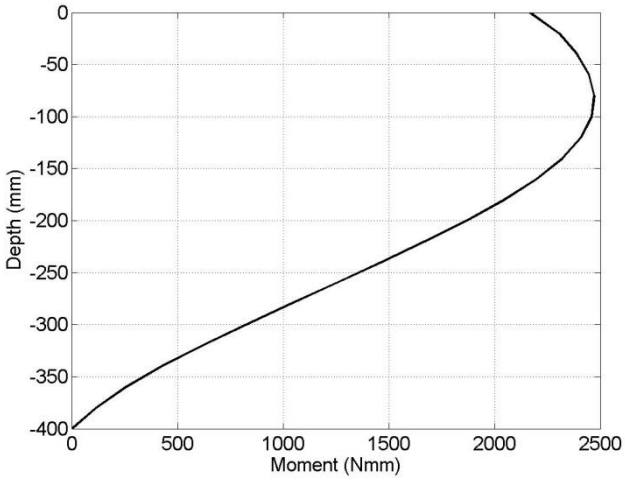

Figure H.59: Bending moment distribution along the pile depth in the final step

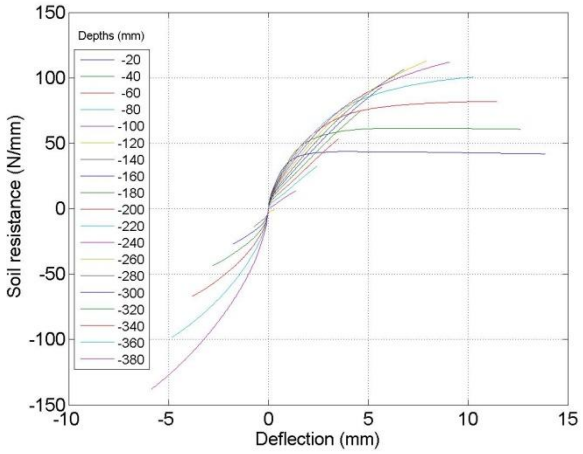

Figure H.60: *p-y* curves for different depths

H.2.4 Test 4 *D*=80 mm, *L/D*=6, P_0 = 50 kPa

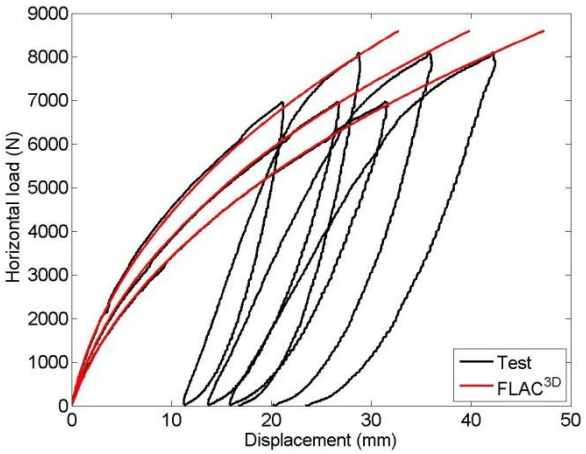

Figure H.61: Load-displacement curves obtained by numerical modelling and small scale test

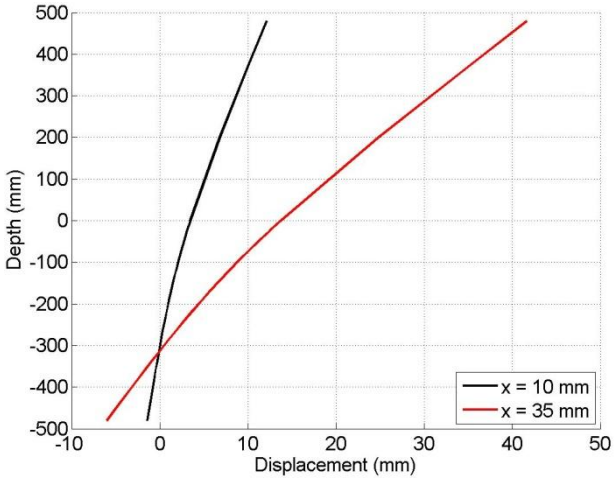

Figure H.62: Displacement distribution along the pile depth

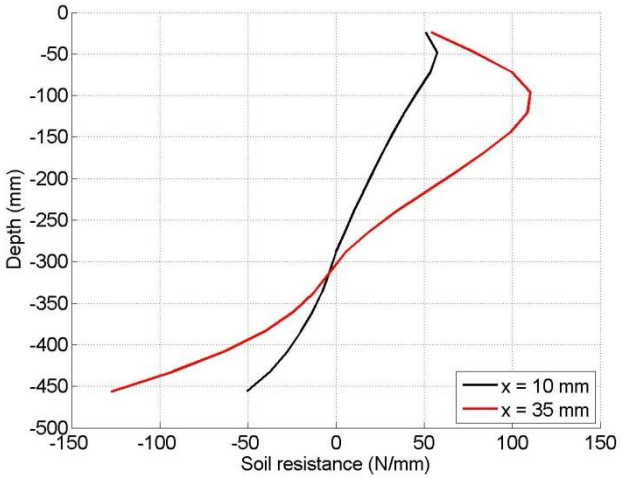

Figure H.63: Soil resistance distribution along the pile depth

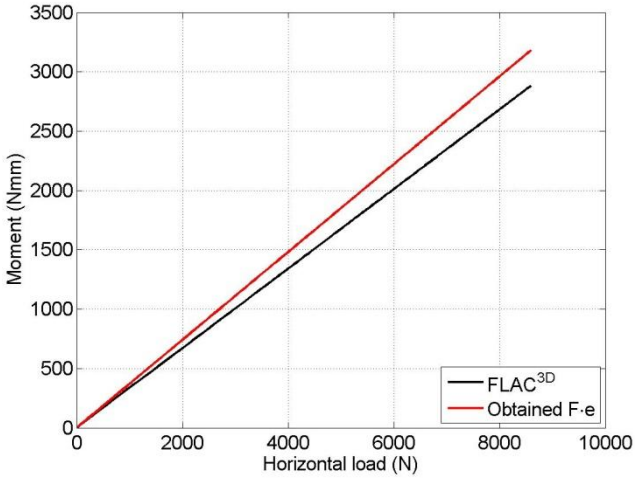

Figure H.64: Comparison of bending moments at the soil surface, obtained by multiplying the applied force with the eccentricity and computed by FLAC^{3D}

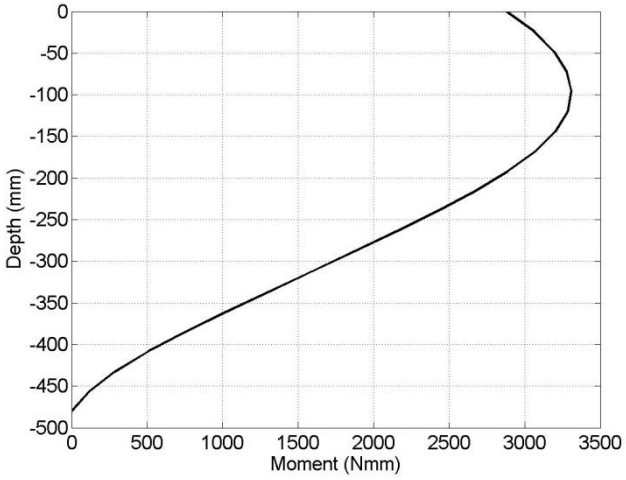

Figure H.65: Bending moment distribution along the pile depth in the final step

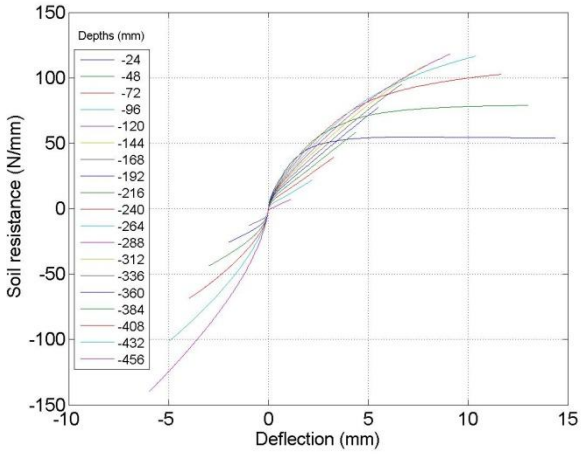

Figure H.66: *p-y* curves for different depths

H.2.5 Test 5 *D*=80 mm, *L/D*=4, P_0 = 100 kPa

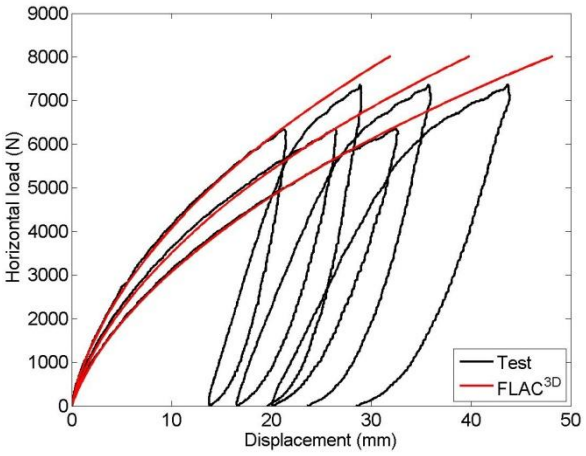

Figure H.67: Load-displacement curves obtained by numerical modelling and small scale test

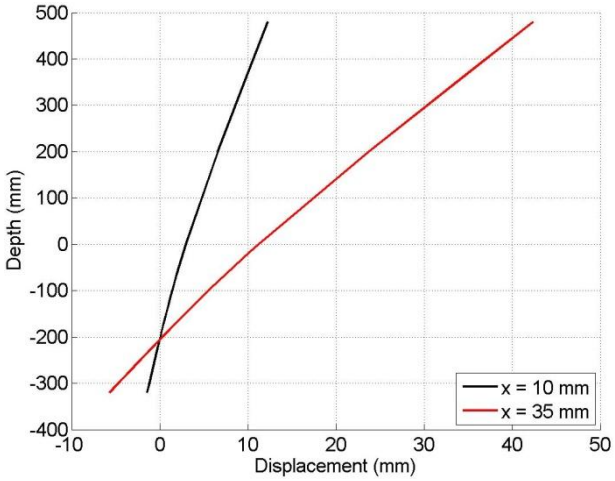

Figure H.68: Displacement distribution along the pile depth

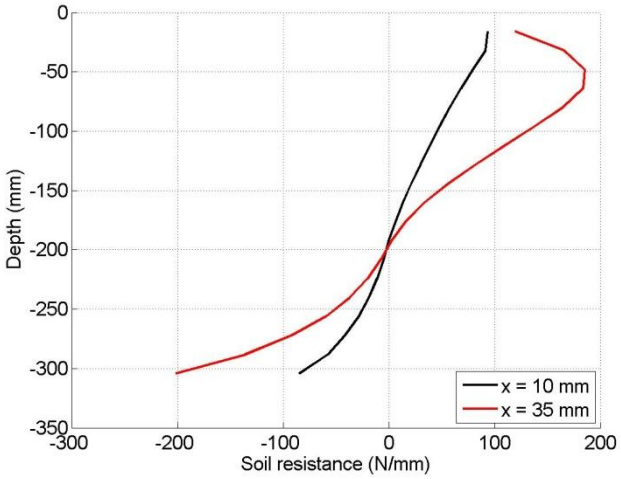

Figure H.69: Soil resistance distribution along the pile depth

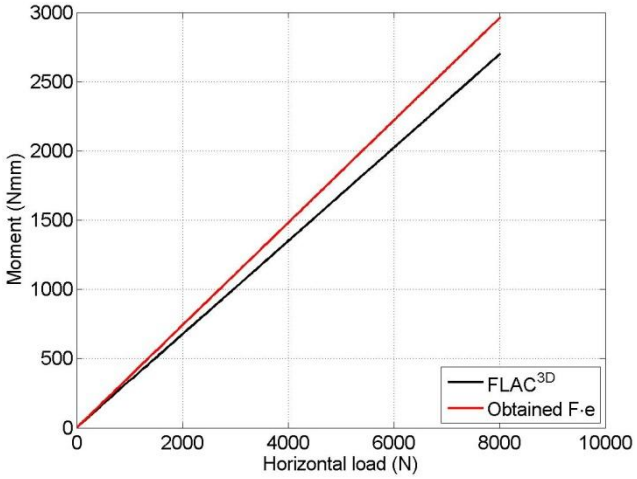

Figure H.70: Comparison of bending moments at the soil surface, obtained by multiplying the applied force with the eccentricity and computed by FLAC^{3D}

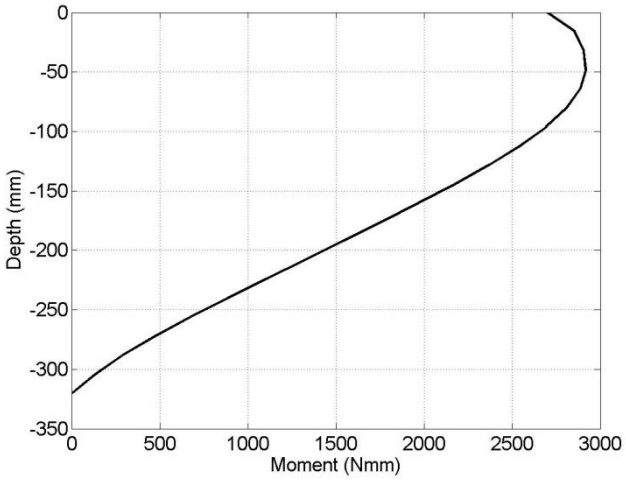

Figure H.71: Bending moment distribution along the pile depth in the final step

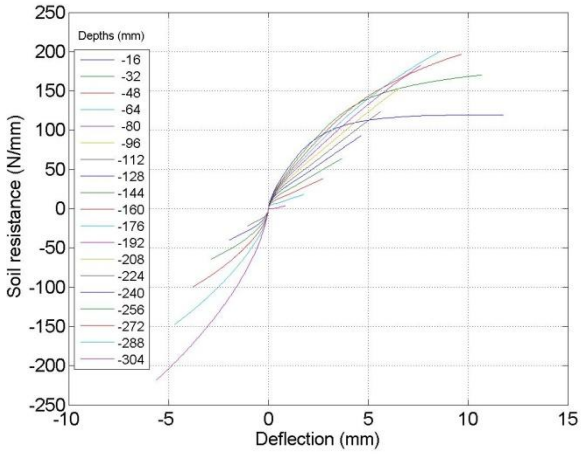

Figure H.72: *p-y* curves for different depths

H.2.6 Test 6 *D*=80 mm, *L/D*=5, P_0 = 100 kPa

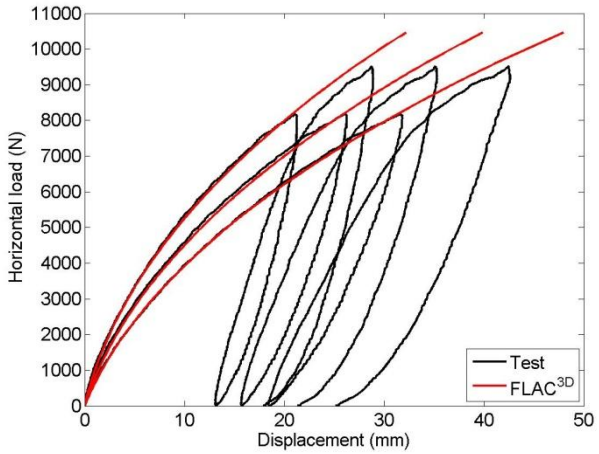

Figure H.73: Load-displacement curves obtained by numerical modelling and small scale test

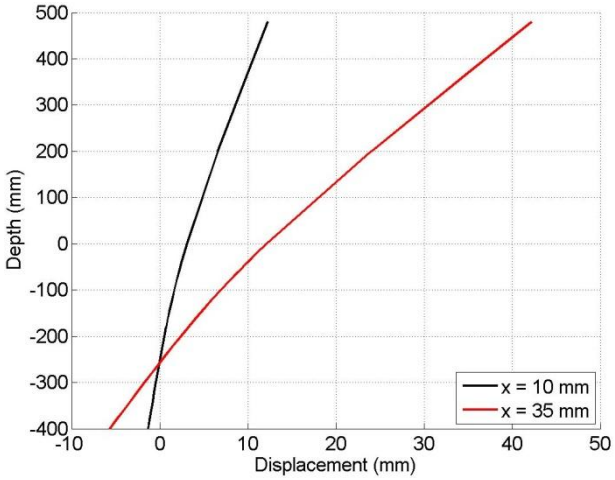

Figure H.74: Displacement distribution along the pile depth

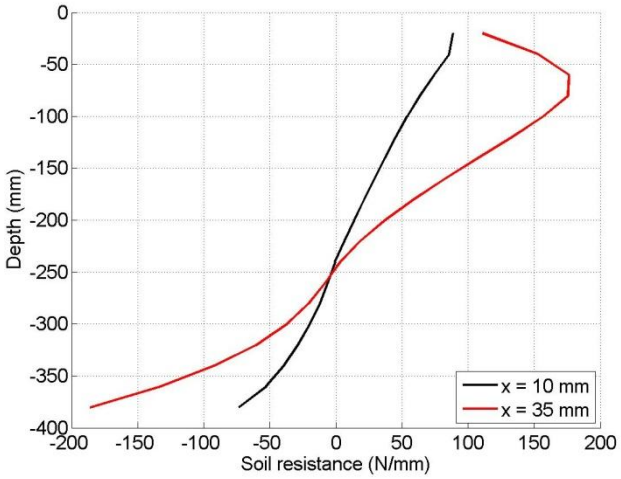

Figure H.75: Soil resistance distribution along the pile depth

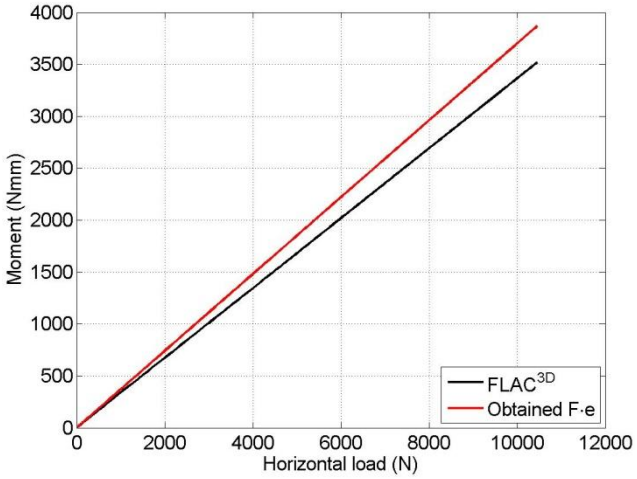

Figure H.76: Comparison of bending moments at the soil surface, obtained by multiplying the applied force with the eccentricity and computed by FLAC^{3D}

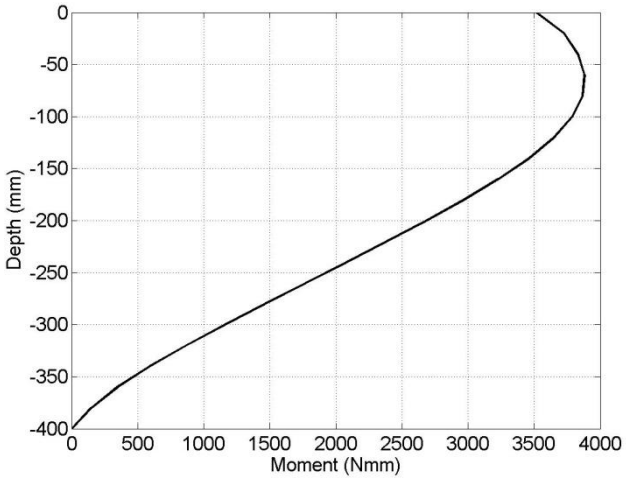

Figure H.77: Bending moment distribution along the pile depth in the final step

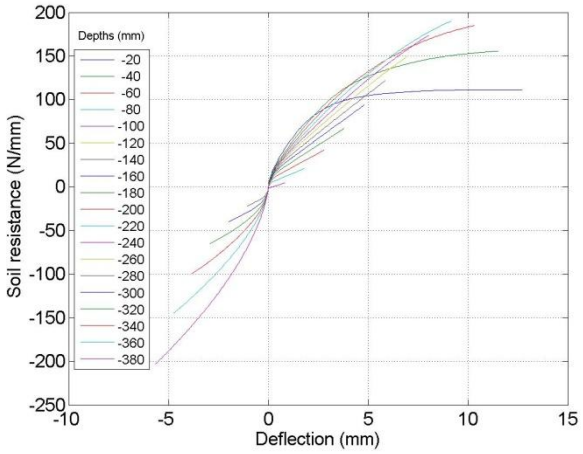

Figure H.78: *p-y* curves for different depths

H.2.7 Test 7 *D*=80 mm, *L/D*=6, P_0 = 100 kPa

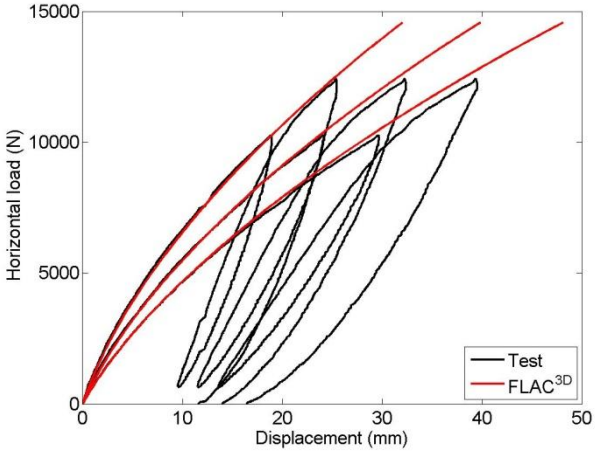

Figure H.79: Load-displacement curves obtained by numerical modelling and small scale test

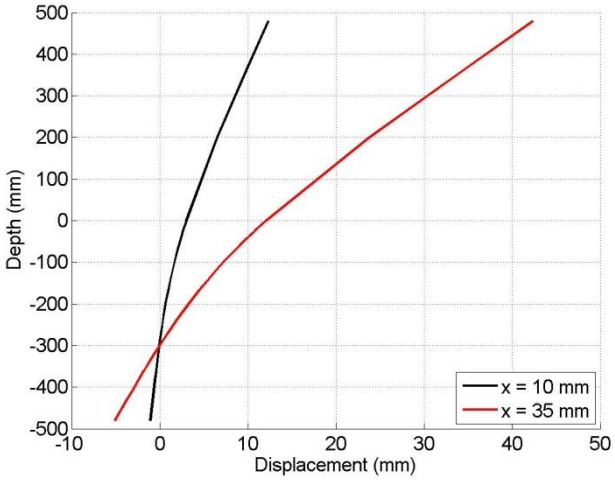

Figure H.80: Displacement distribution along the pile depth

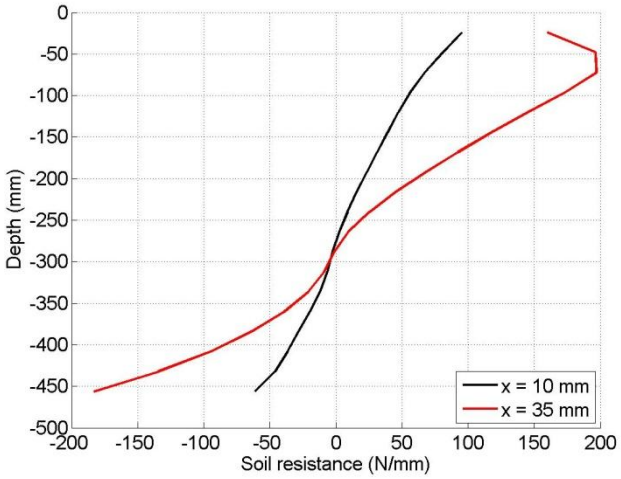

Figure H.81: Soil resistance distribution along the pile depth

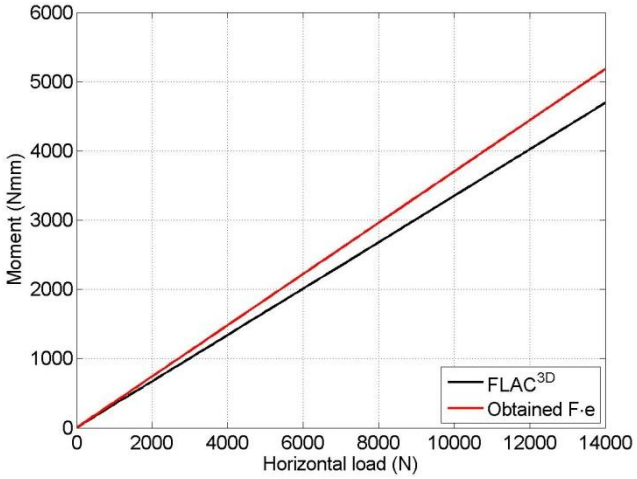

Figure H.82: Comparison of bending moments at the soil surface, obtained by multiplying the applied force with the eccentricity and computed by FLAC^{3D}

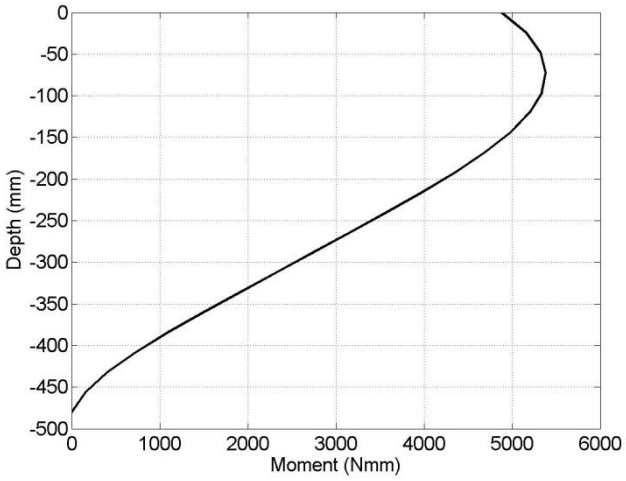

Figure H.83: Bending moment distribution along the pile depth in the final step

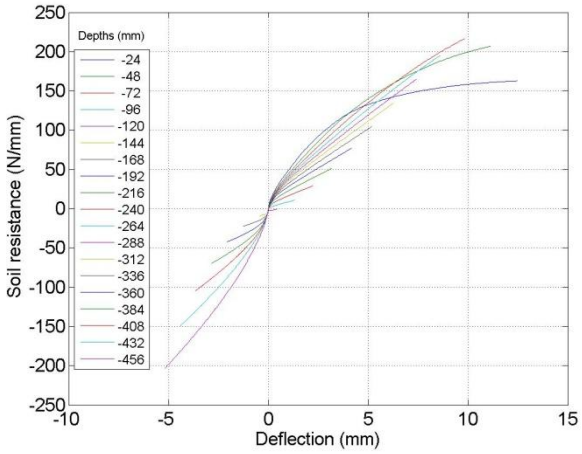

Figure H.84: *p-y* curves for different depths

H.3 Numerical results by Plaxis 3D 2010

H.3.1 Test 1 D=100 mm, L/D=5, P_0 = 50 kPa

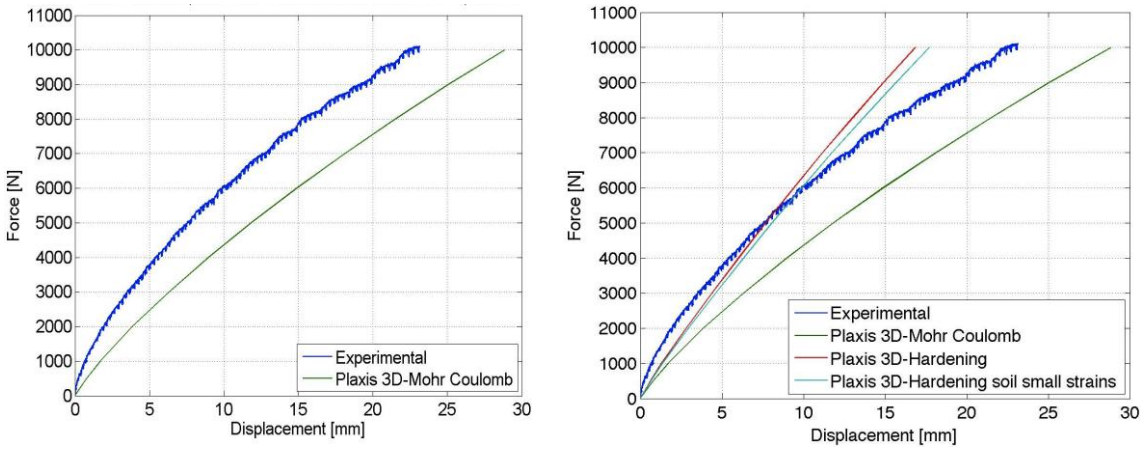

Figure H.85: Comparison of load-deflection curves obtained by numerical modelling and small scale test

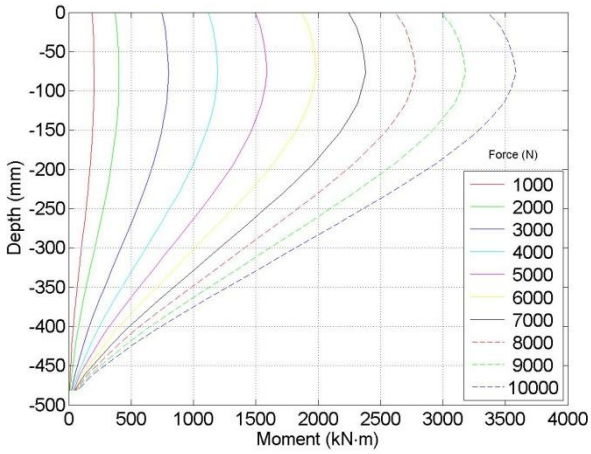

Figure H.86: Bending moment distribution along the embedded pile length

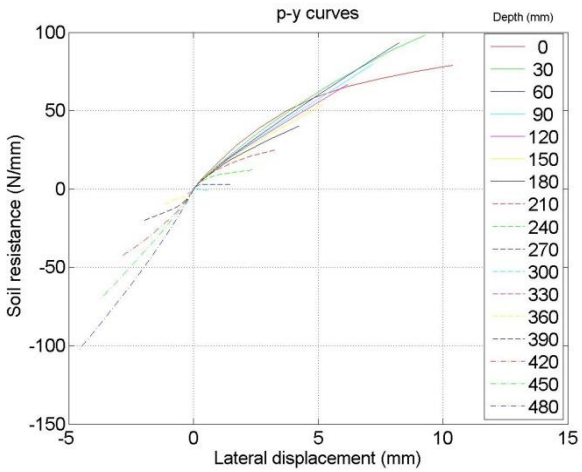

Figure H.87: *p-y* curves for different depths

H.3.2 Test 2 *D*=80 mm, *L/D*=5, P_0 = 0 kPa

No results are obtained for the test without overburden pressure, due to the fact that in Plaxis 3D, cohesion is necessary as an input. Having it as almost zero value in the model without overburden pressure leads to disconvergence.

H.3.3 Test 3 *D*=80 mm, *L/D*=5, P_0 = 50 kPa

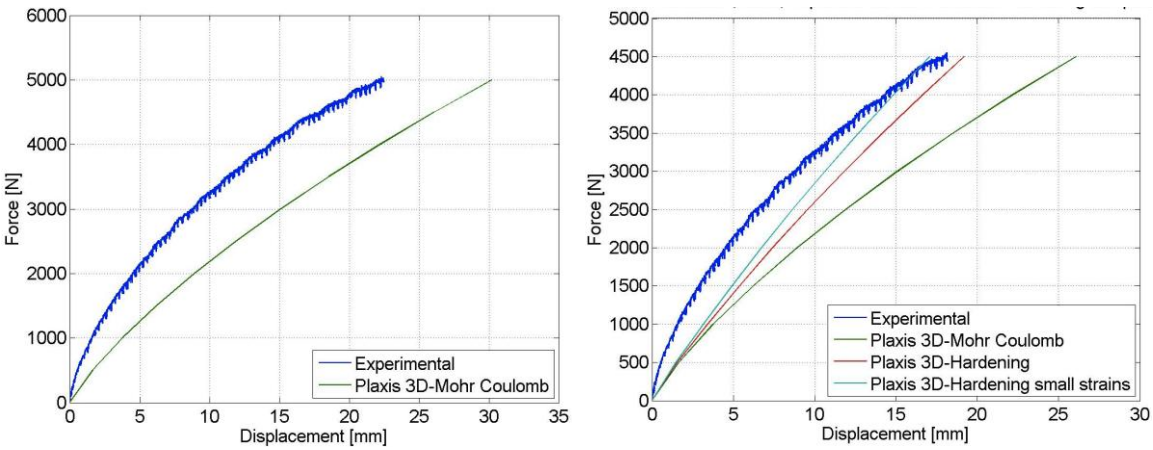

Figure H.88: Comparison of load-deflection curves obtained by numerical modelling and small scale

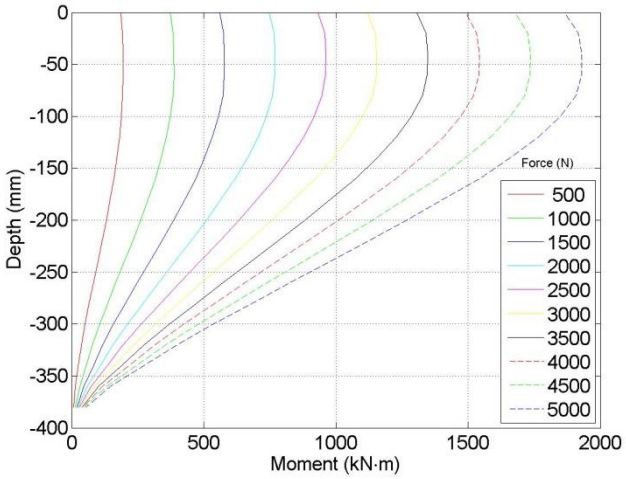

Figure H.89: Bending moment distribution along the embedded pile length

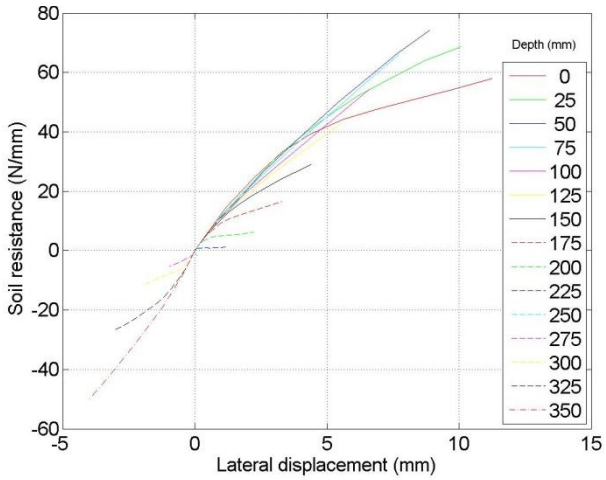

Figure H.90: *p-y* curves for different depths

H.3.4 Test 4 *D*=80 mm, *L/D*=6, P_0 = 50 kPa

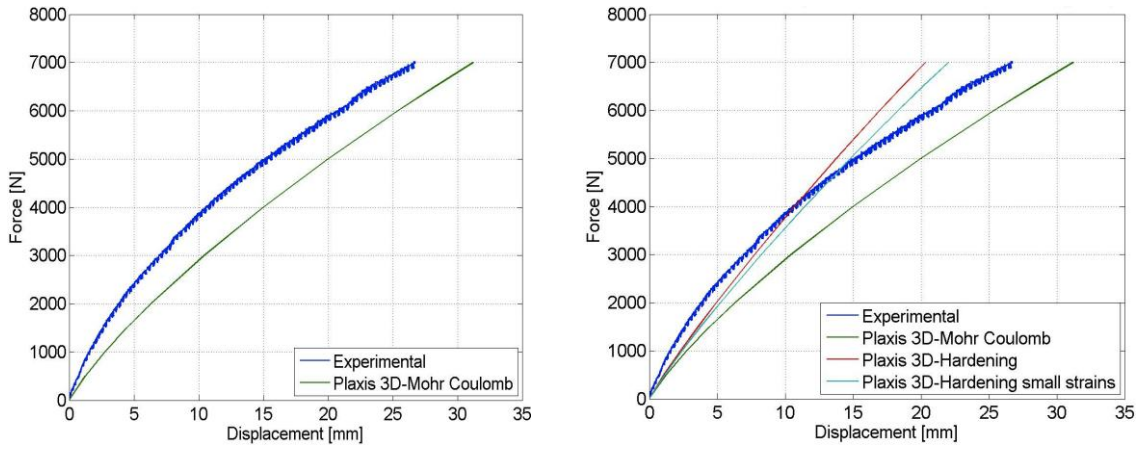

Figure H.91: Comparison of load-deflection curves obtained by numerical modelling and small scale

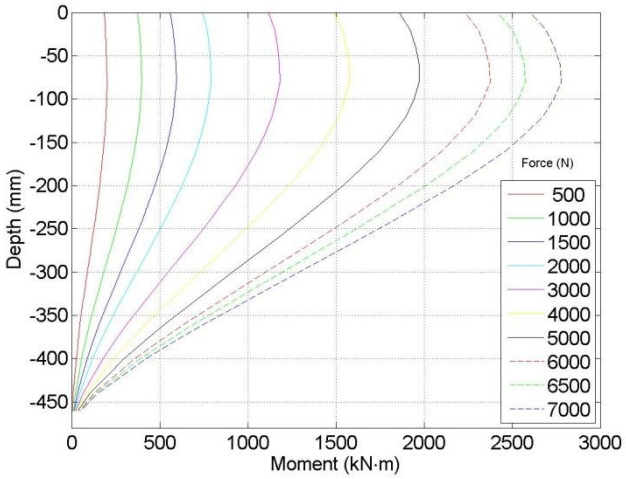

Figure H.92: Bending moment distribution along the embedded pile length

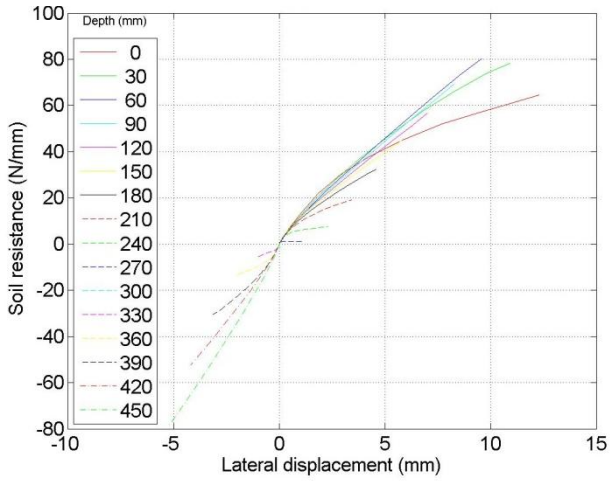

Figure H.93: *p-y* curves for different depths

H.3.5 Test 5 *D*=80 mm, *L/D*=4, P_0 = 100 kPa

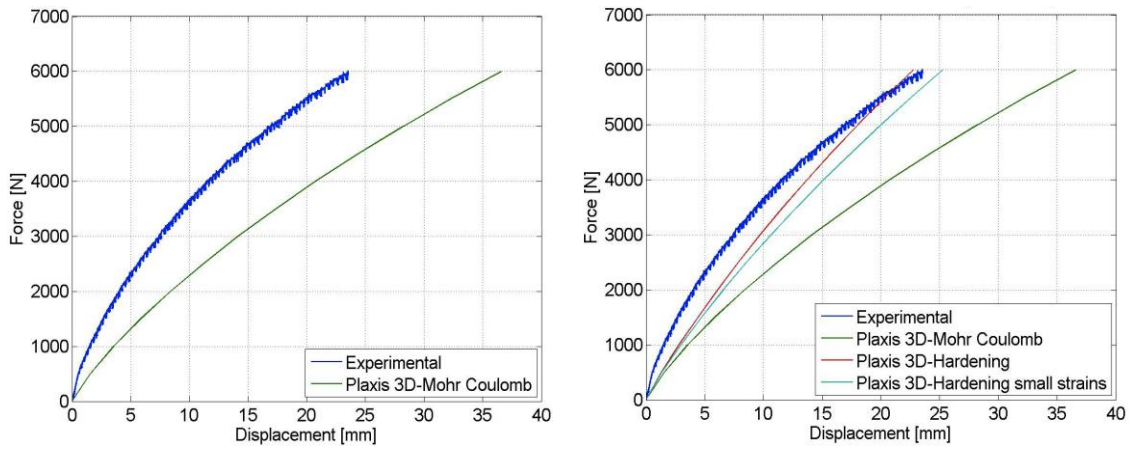

Figure H.94: Comparison of load-deflection curves obtained by numerical modelling and small scale

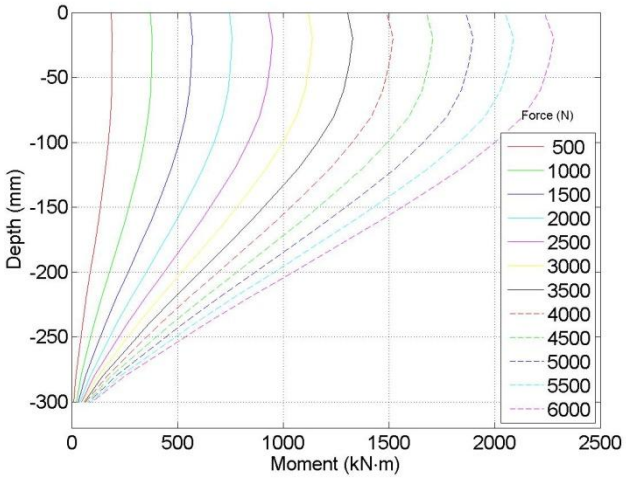

Figure H.95: Bending moment distribution along the embedded pile length

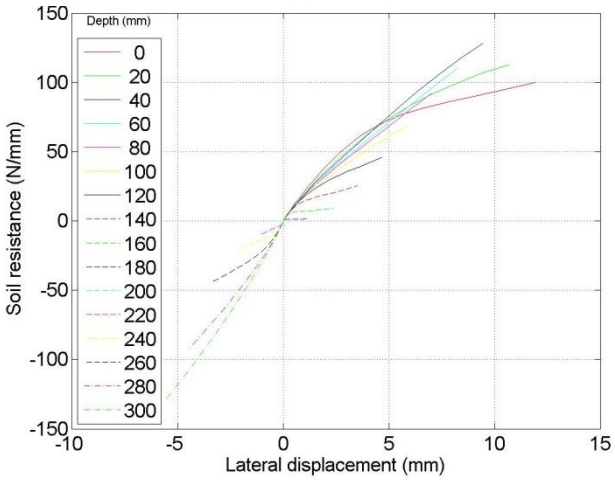

Figure H.96: *p-y* curves for different depths

H.3.6 Test 6 *D*=80 mm, *L/D*=5, P_0 = 100 kPa

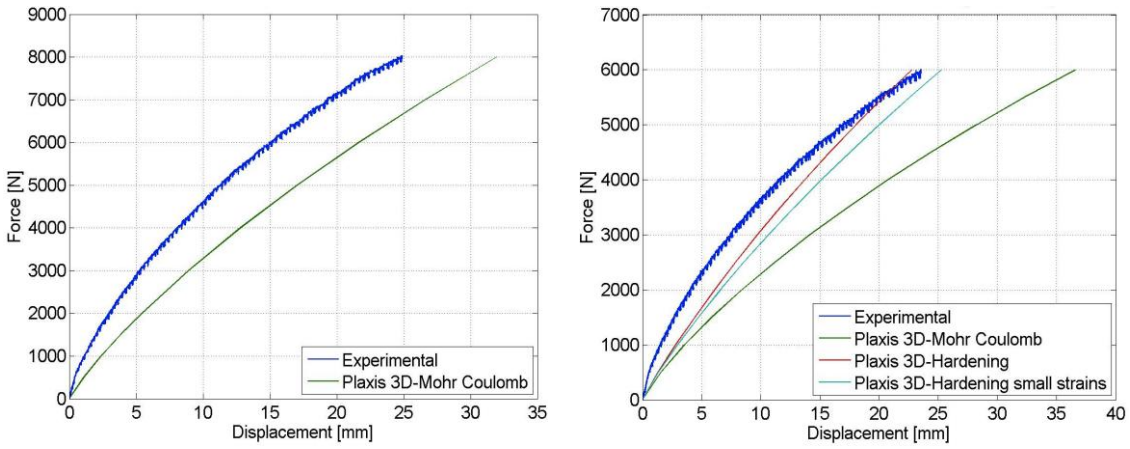

Figure H.97: Comparison of load-deflection curves obtained by numerical modelling and small scale

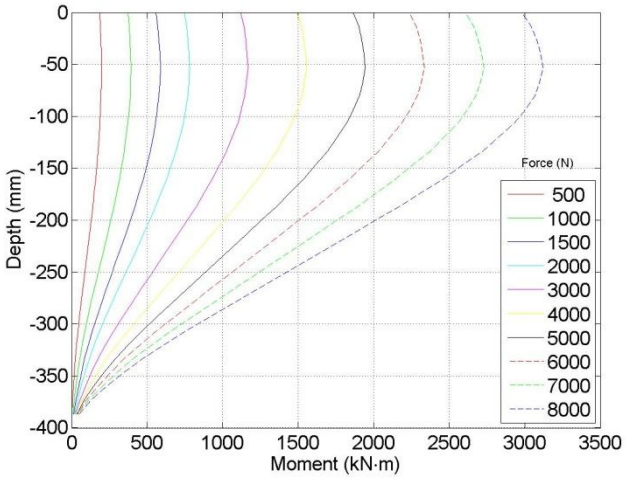

Figure H.98: Bending moment distribution along the embedded pile length

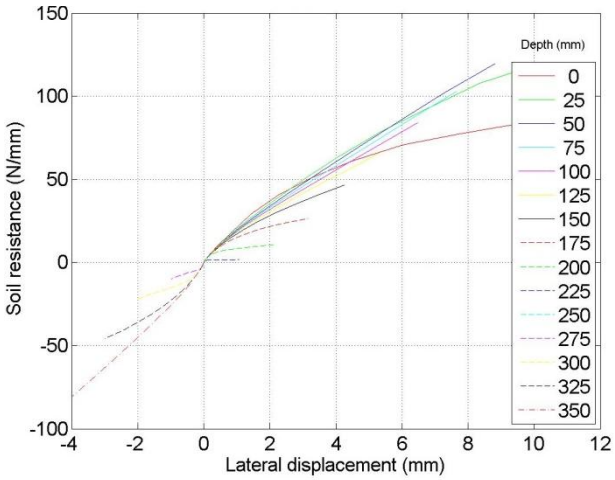

Figure H.99: *p-y* curves for different depths

H.3.7 Test 7 *D*=80 mm, *L/D*=6, P_0 = 100 kPa

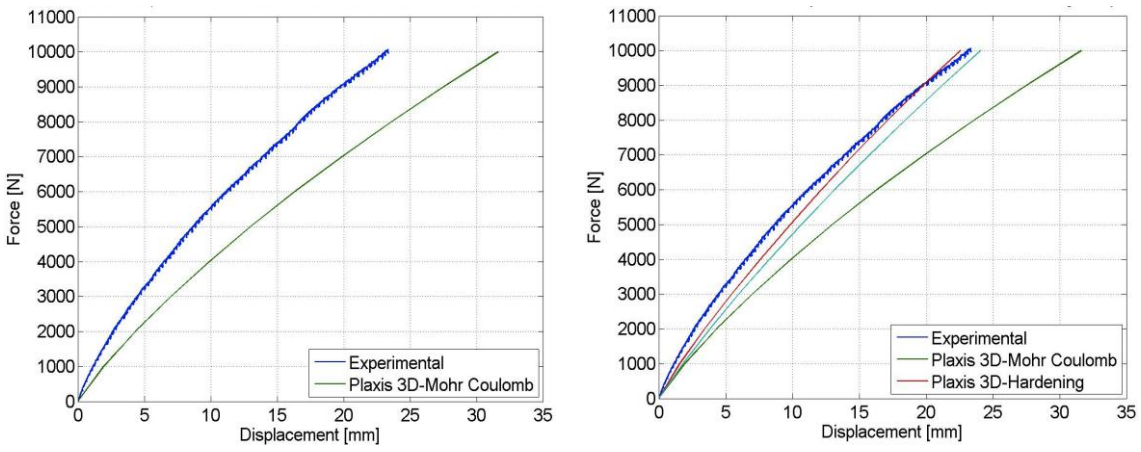

Figure H.100: Comparison of load-deflection curves obtained by numerical modelling and small scale

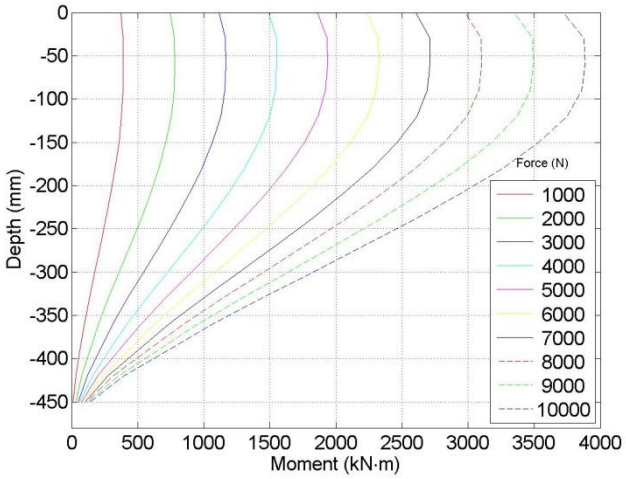

Figure H.101: Bending moment distribution along the embedded pile length

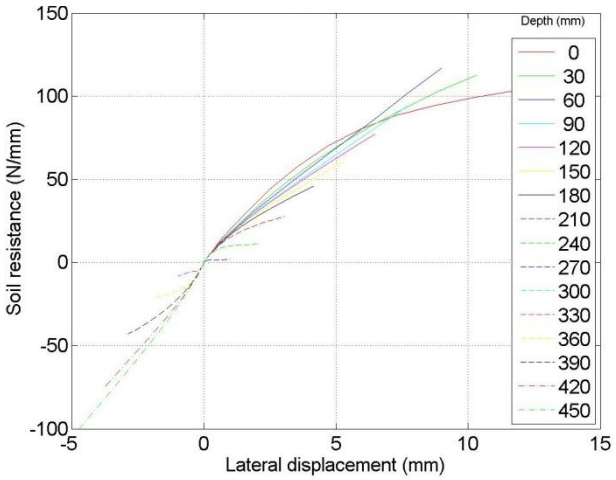

Figure H.102: *p-y* curves for different depths

H.4 Comparison of FLAC^{3D} and Plaxis 3D

H.4.1 Test 1 D=100 mm, L/D=5, P_0 = 50 kPa

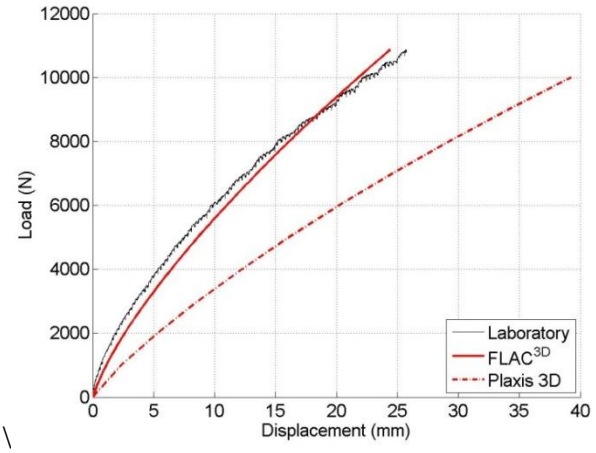

Figure H.103: Comparison of load-displacement curves

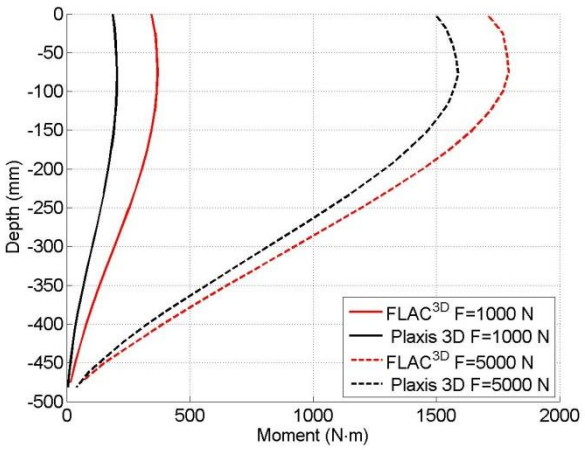

Figure H.104: Comparison of bending moment distribution along the embedded pile

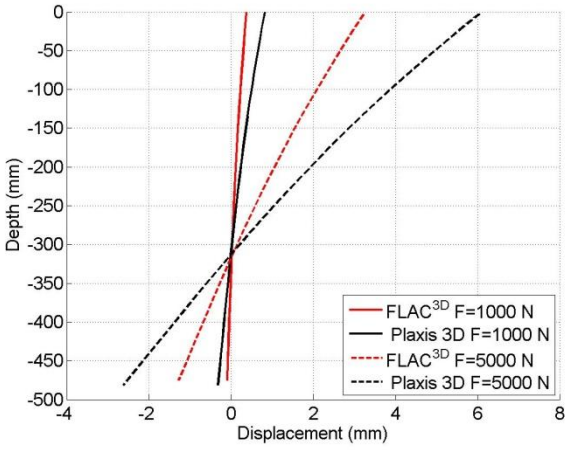

Figure H.105: Comparison of displacement distribution along the embedded pile

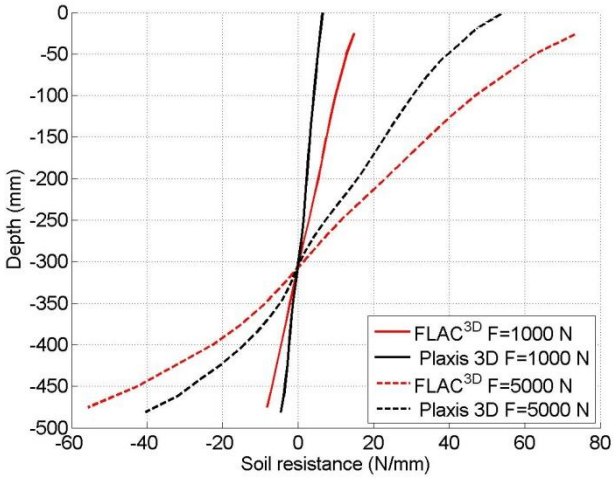

Figure H.106: Comparison of soil resistance distribution along the embedded pile

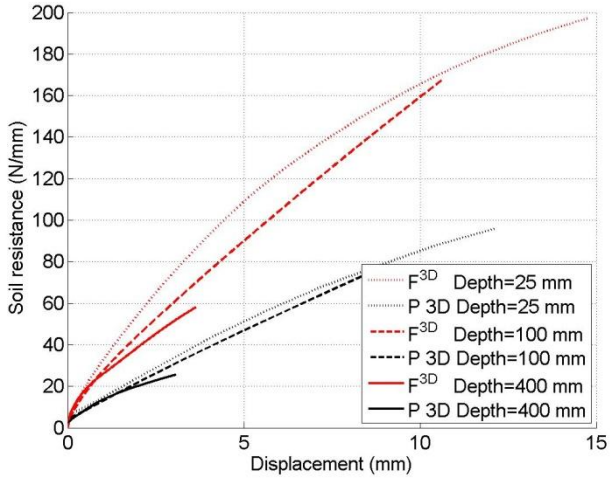

Figure H.107: Comparison of *p-y* curves

H.4.2 Test 2 *D*=80 mm, *L/D*=5, P_0 = 0 kPa

Due to the reasons mentioned in section H 3.2, the comparison of the graphs for test 2 could not be performed.

H.4.3 Test 3 D=80 mm, L/D=5, P_0 = 50 kPa

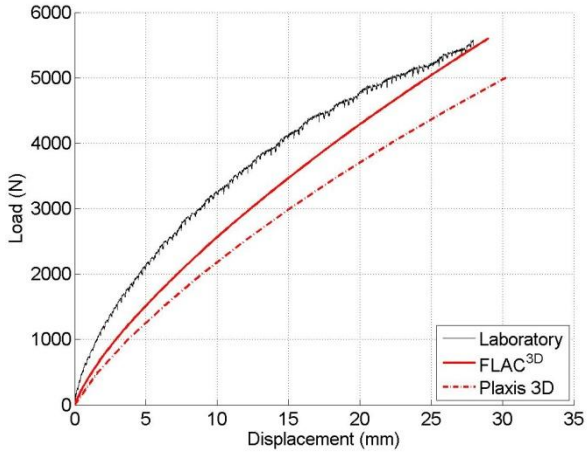

Figure H.108: Comparison of load-displacement curves

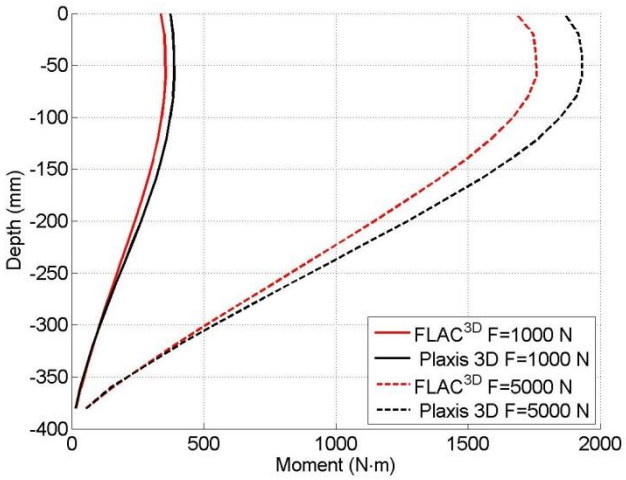

Figure H.109: Comparison of bending moment distribution along the embedded pile

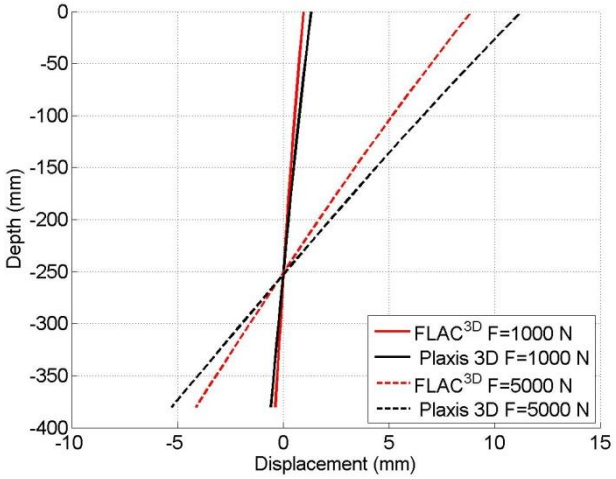

Figure H.110: Comparison of displacement distribution along the embedded pile

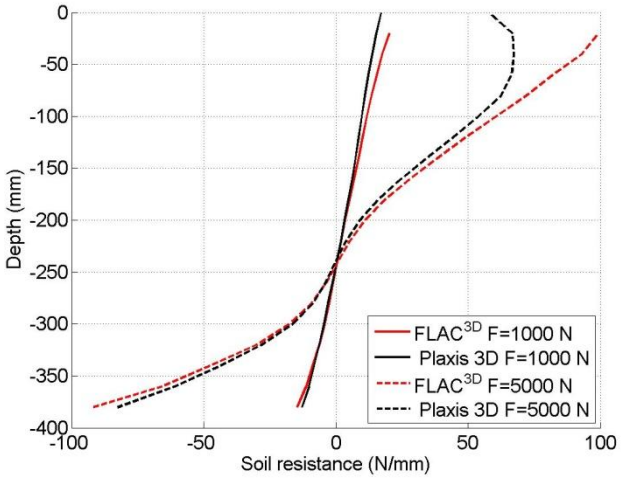

Figure H.111: Comparison of soil resistance distribution along the embedded pile

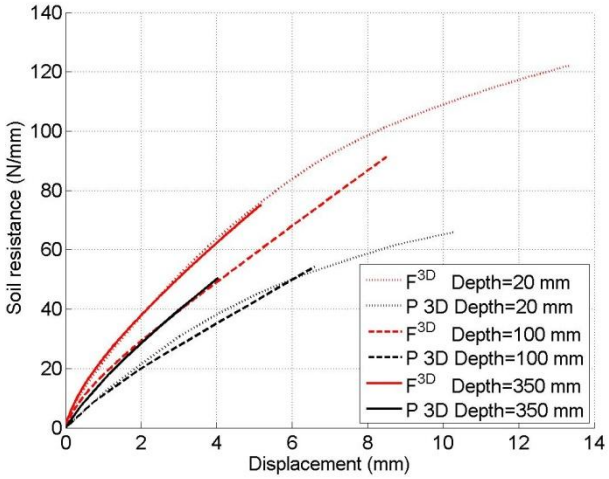

Figure H.112: Comparison of *p-y* curves

H.4.4 Test 4 *D*=80 mm, *L/D*=6, P_0 = 50 kPa

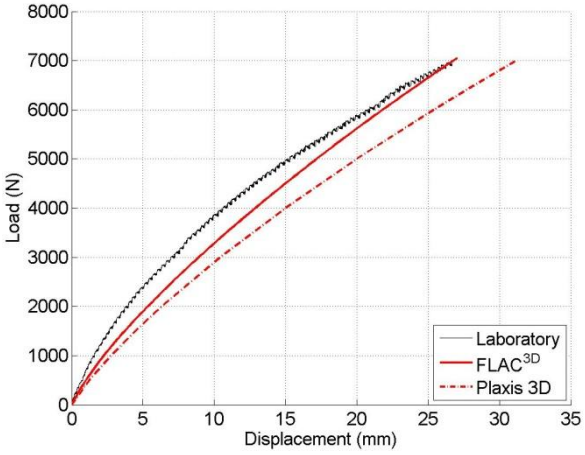

Figure H.113: Comparison of load-displacement curves

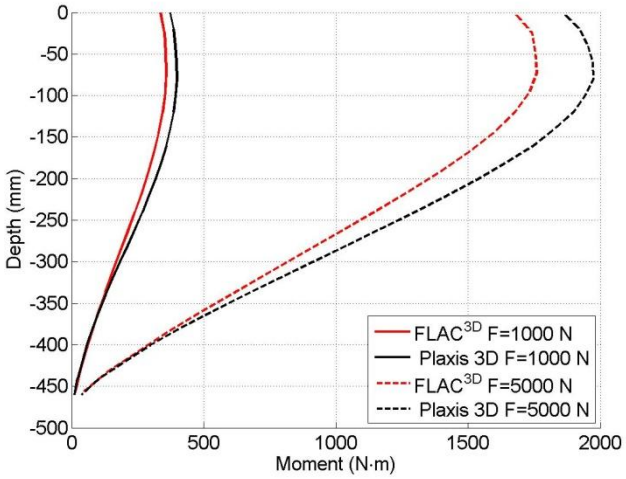

Figure H.114: Comparison of bending moment distribution along the embedded pile

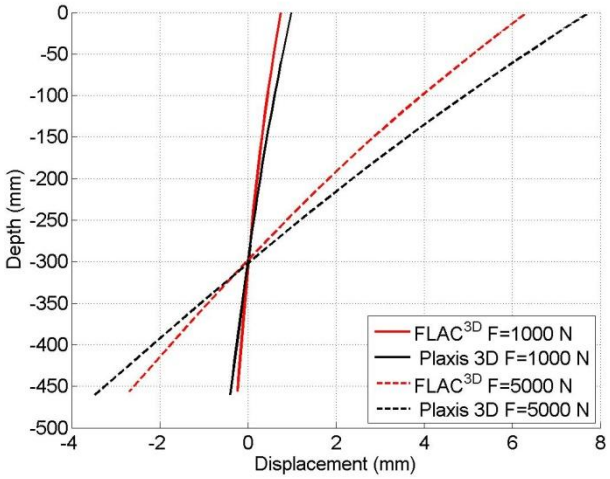

Figure H.115: Comparison of displacement distribution along the embedded pile

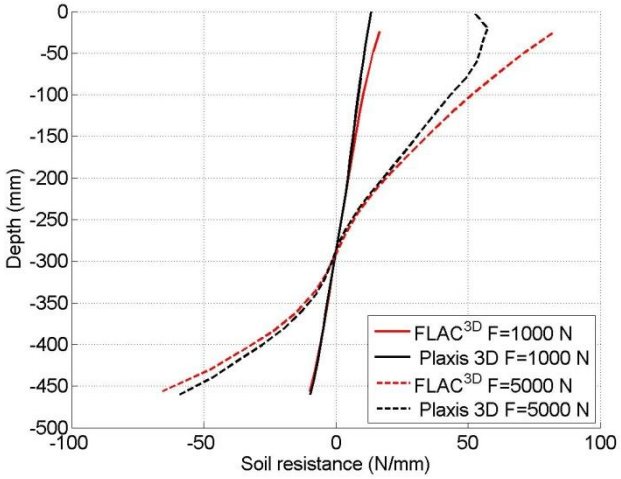

Figure H.116: Comparison of soil resistance distribution along the embedded pile

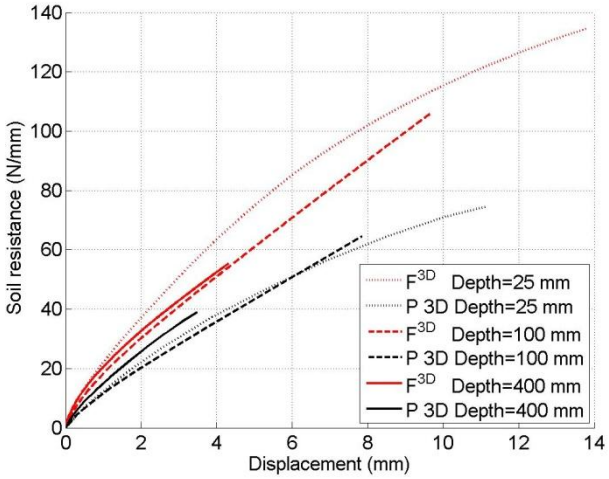

Figure H.117: Comparison of *p-y* curves

H.4.5 Test 5 *D*=80 mm, *L/D*=4, P_0 = 100 kPa

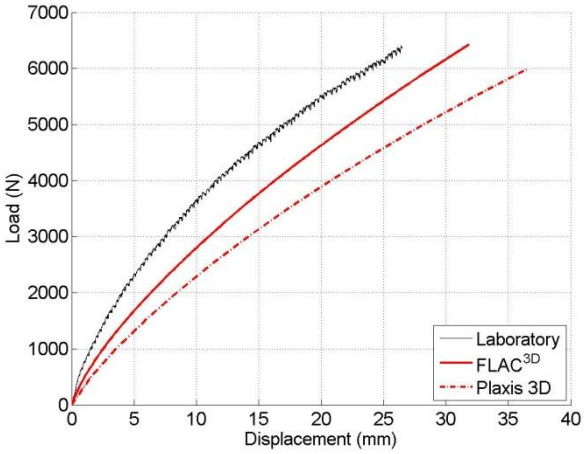

Figure H.118: Comparison of load-displacement curves

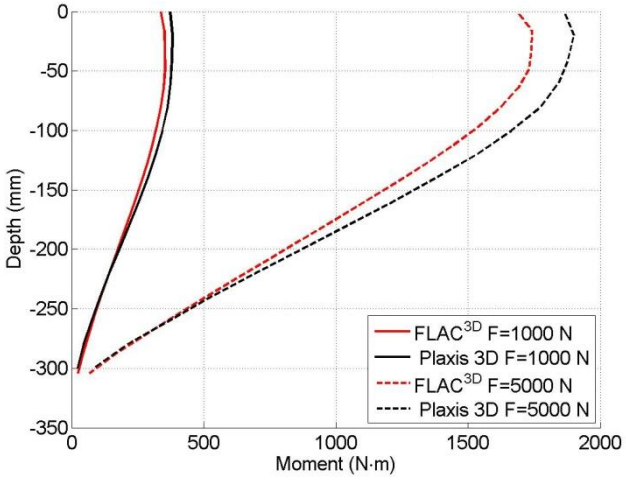

Figure H.119: Comparison of bending moment distribution along the embedded pile

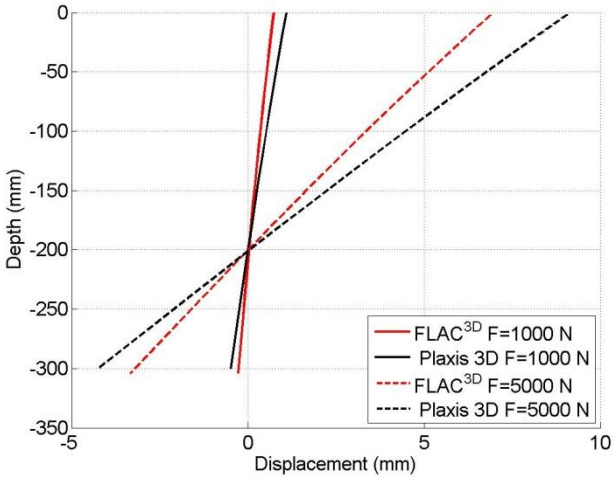

Figure H.120: Comparison of displacement distribution along the embedded pile

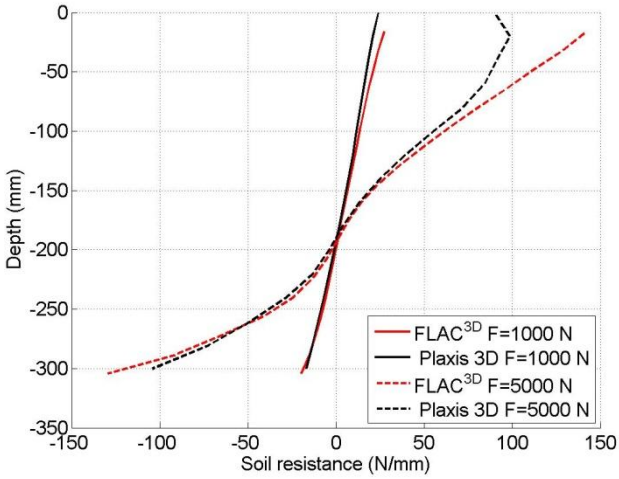

Figure H.121: Comparison of soil resistance distribution along the embedded pile

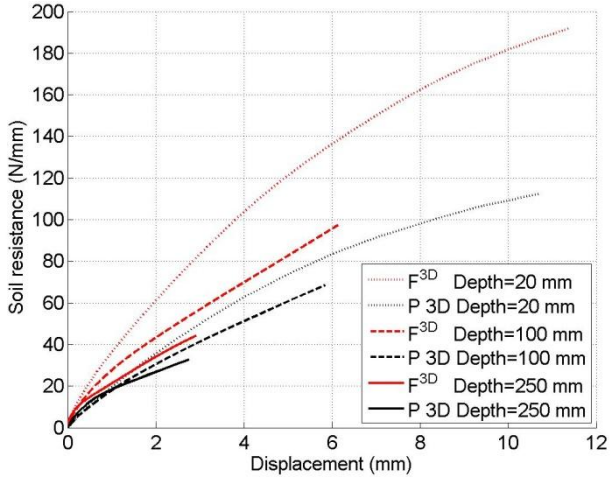

Figure H.122: Comparison of *p-y* curves

H.4.6 Test 6 D=80 mm, L/D=5, P_0 = 100 kPa

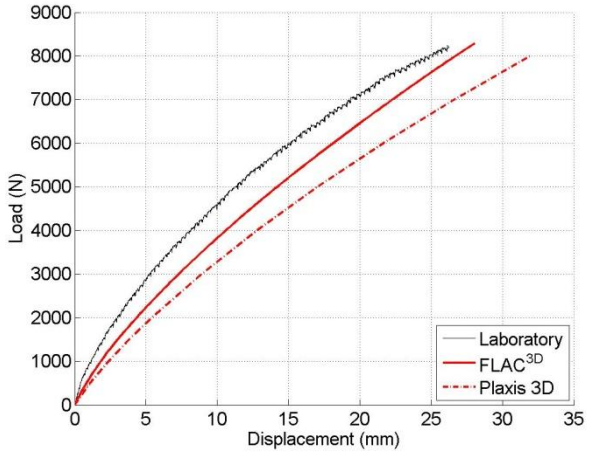

Figure H.123: Comparison of load-displacement curves

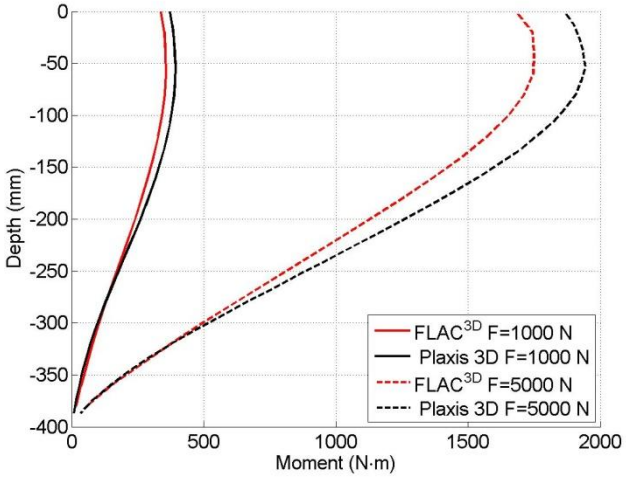

Figure H.124: Comparison of bending moment distribution along the embedded pile

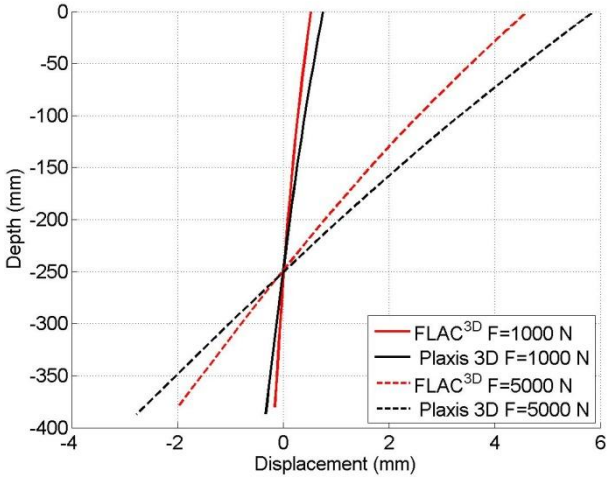

Figure H.125: Comparison of displacement distribution along the embedded pile

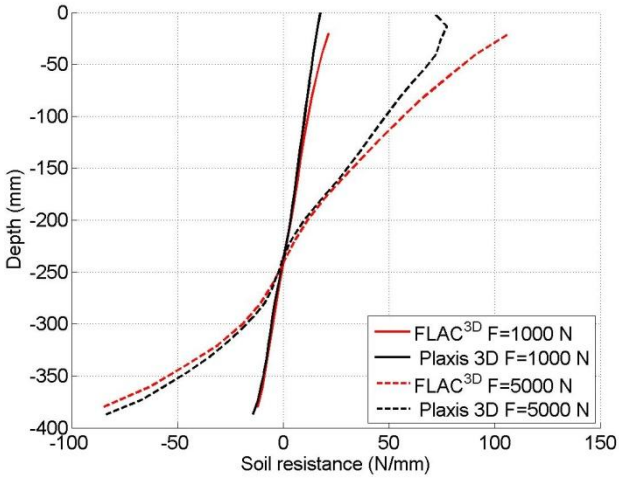

Figure H.126: Comparison of soil resistance distribution along the embedded pile

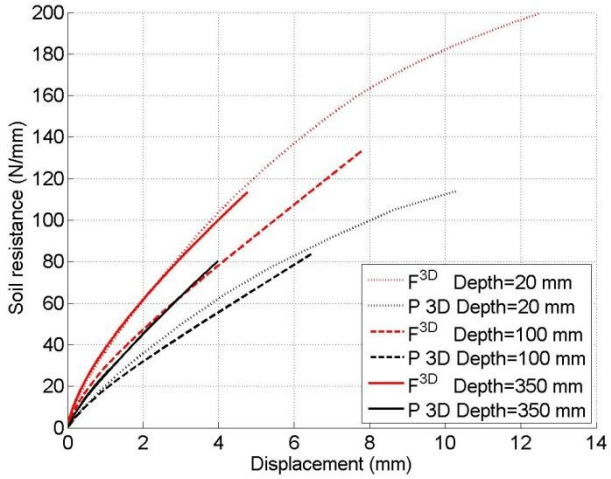

Figure H.127: Comparison of *p-y* curves

H.4.7 Test 7 *D*=80 mm, *L/D*=6, P_0 = 100 kPa

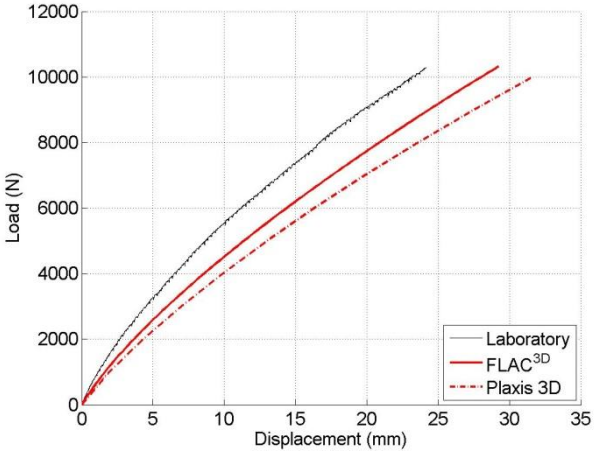

Figure H.128: Comparison of load-displacement curves

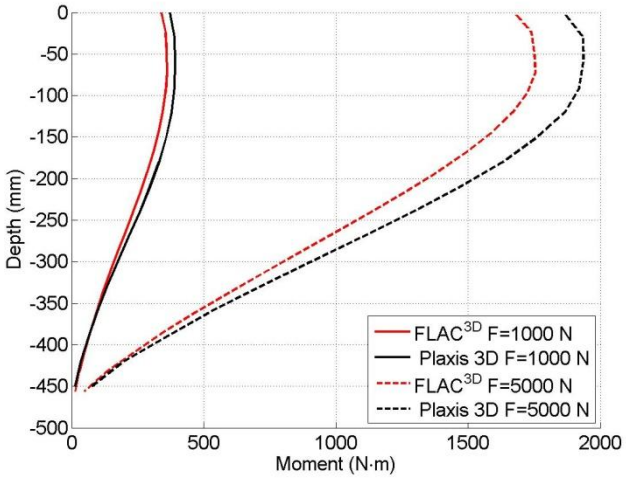

Figure H.129: Comparison of bending moment distribution along the embedded pile

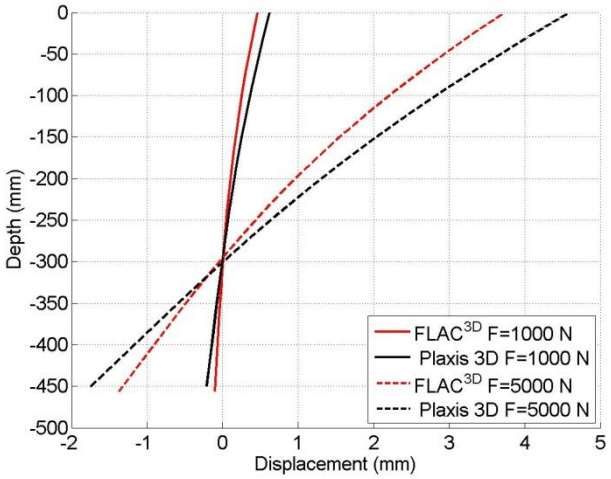

Figure H.130: Comparison of displacement distribution along the embedded pile

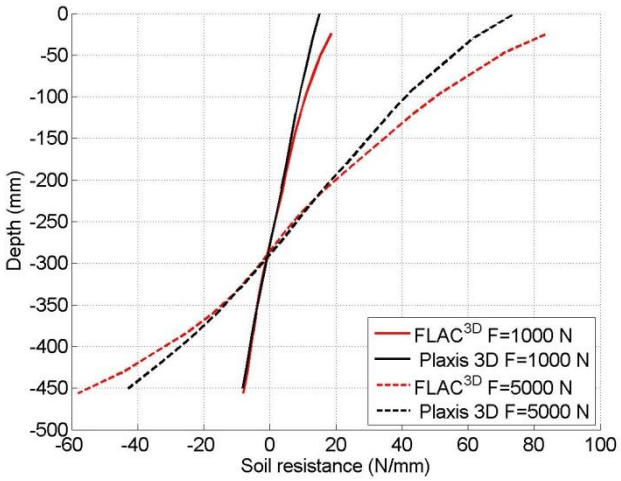

Figure H.131: Comparison of soil resistance distribution along the embedded pile

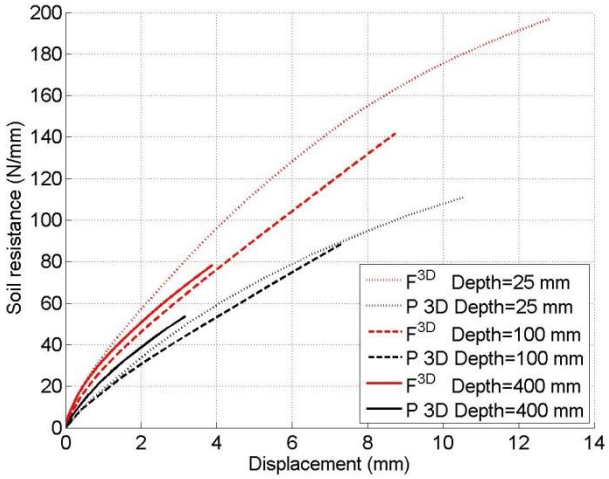

Figure H.132: Comparison of *p-y* curves

H.5 Comparison of FLAC^{3D} and experimental results

H.5.1 Evaluation of bending moments distribution

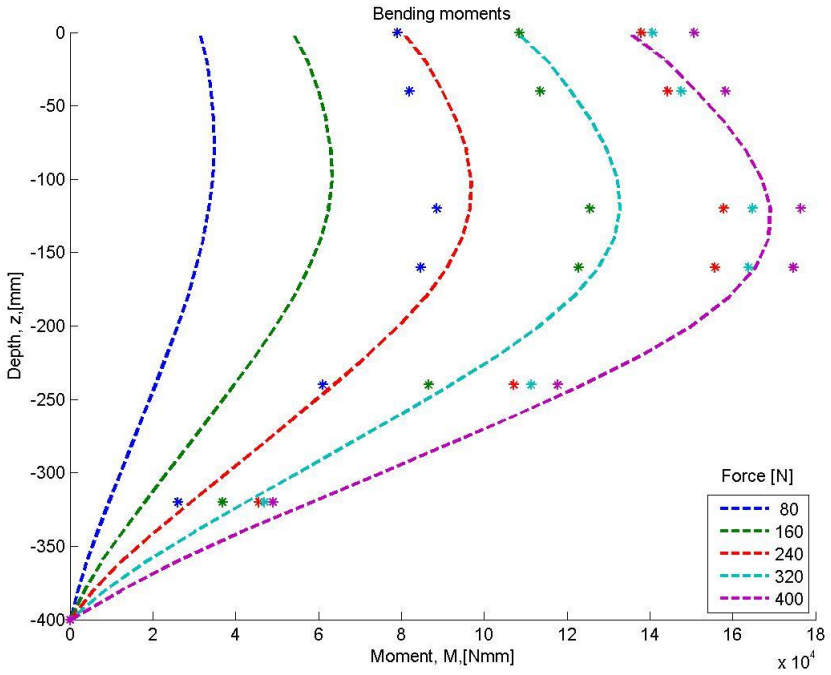

Figure H.133: Moment distribution along depth at different force levels for test 2 (dots represent the results from the experimental tests)

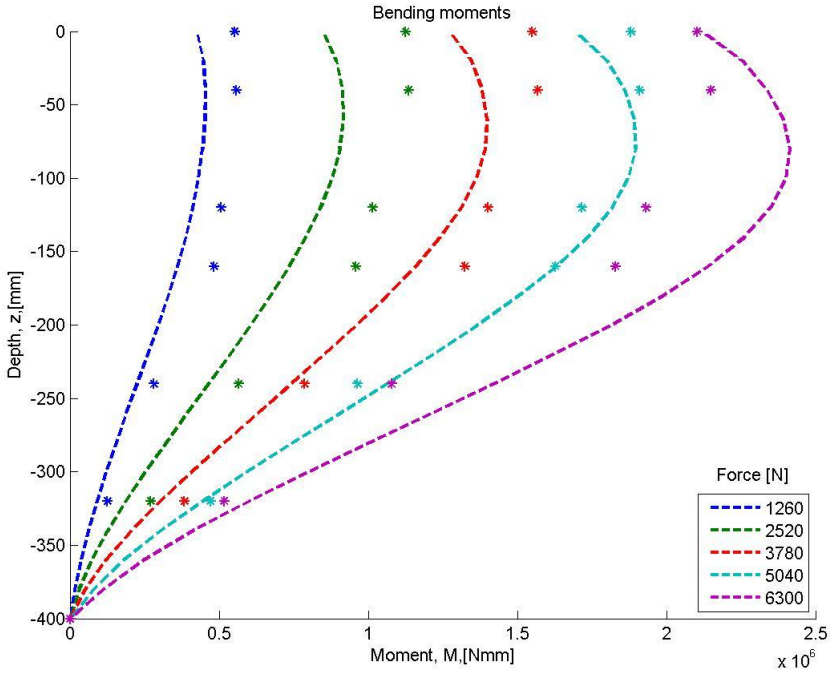

Figure H.134: Moment distribution along depth at different force levels for test 3 (dots represent the results from the experimental tests)

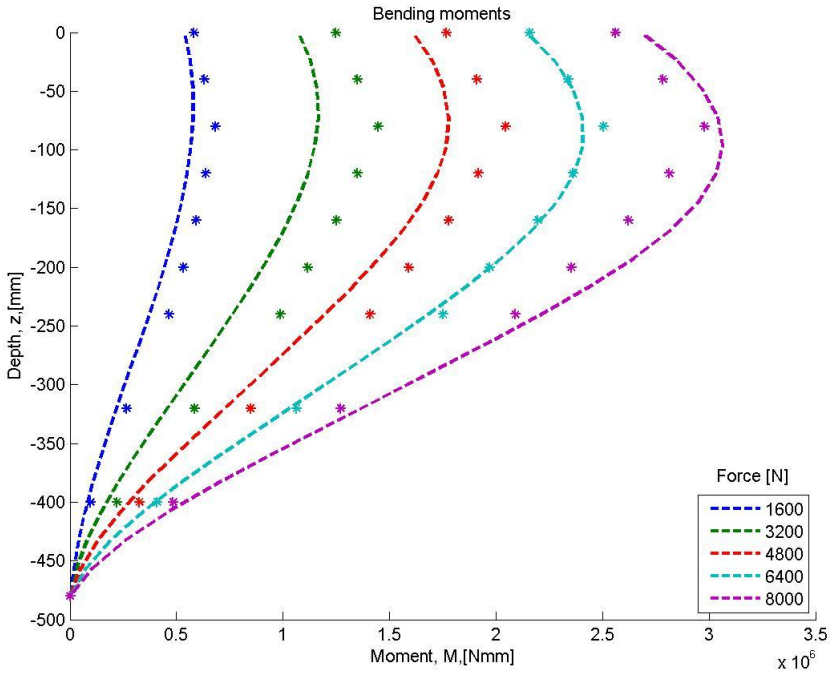

Figure H.135: Moment distribution along depth at different force levels for test 4 (dots represent the results from the experimental tests)

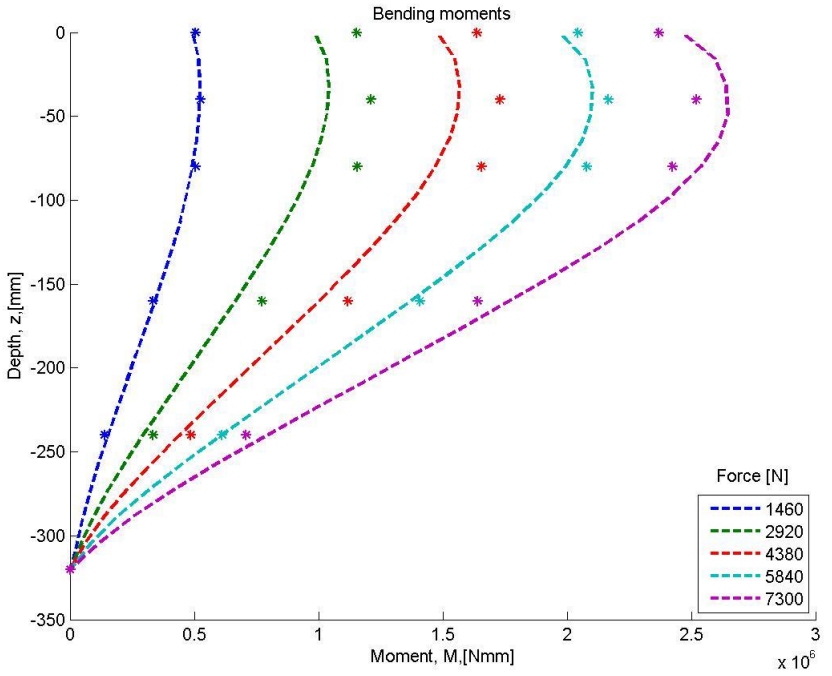

Figure H.136: Moment distribution along depth at different force levels for test 5 (dots represent the results from the experimental tests)

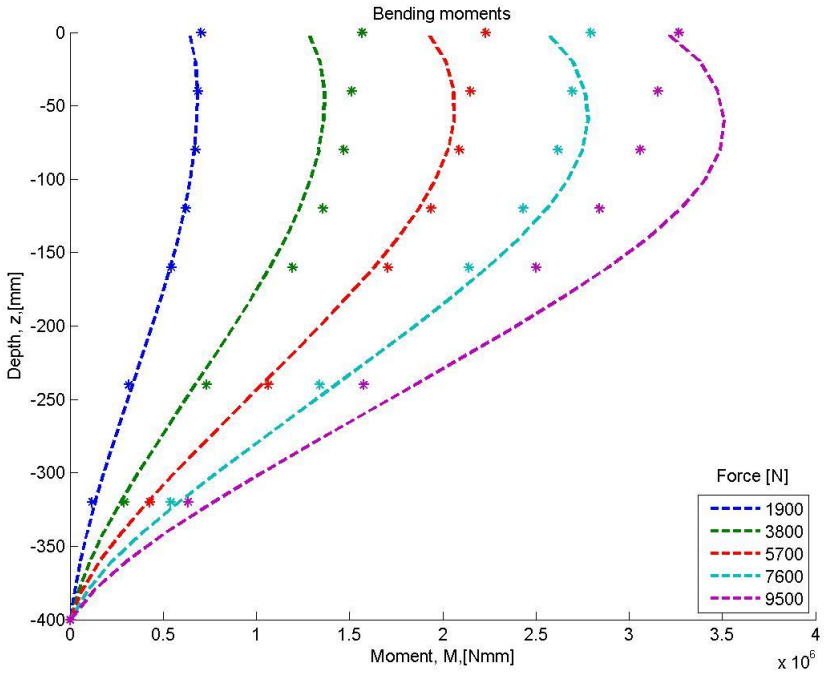

Figure H.137: Moment distribution along depth at different force levels for test 6 (dots represent the results from the experimental tests)

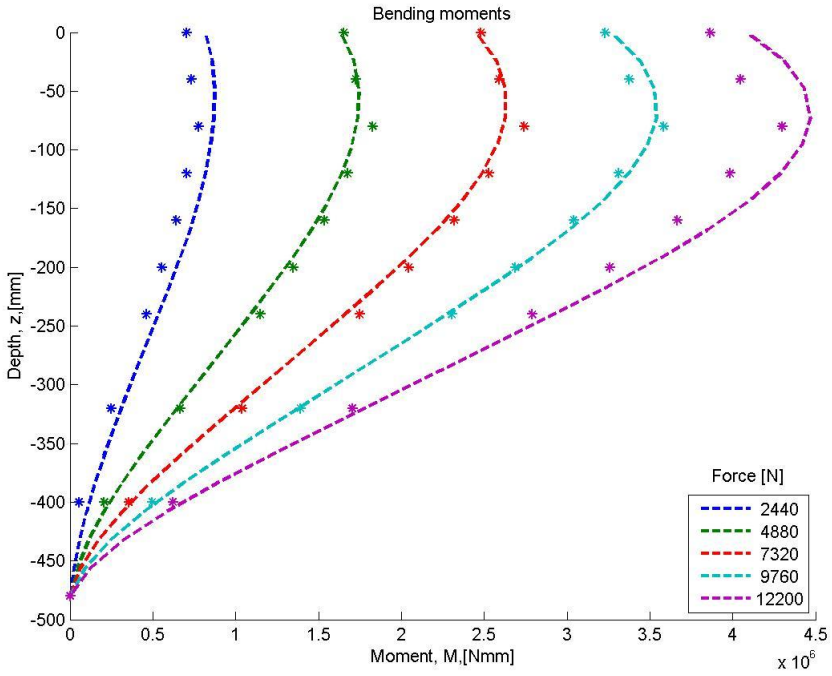

Figure H.138: Moment distribution along depth at different force levels for test 7 (dots represent the results from the experimental tests)

H.5.2 Evaluation of deflection distribution

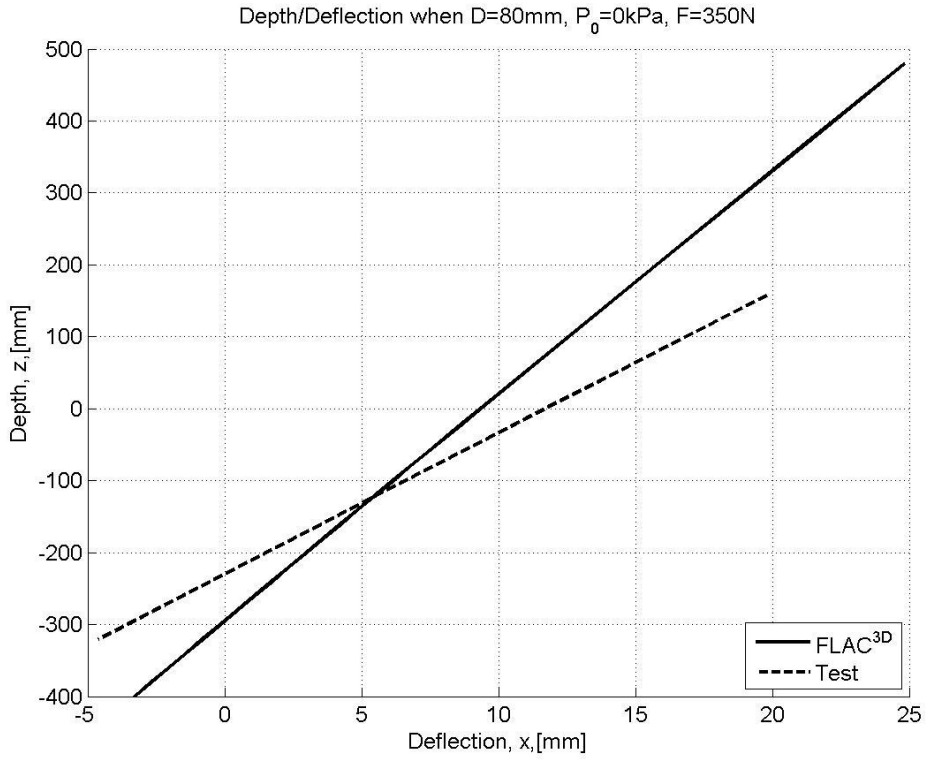

Figure H.139: Deflection distribution along depth at maximum force for test 2

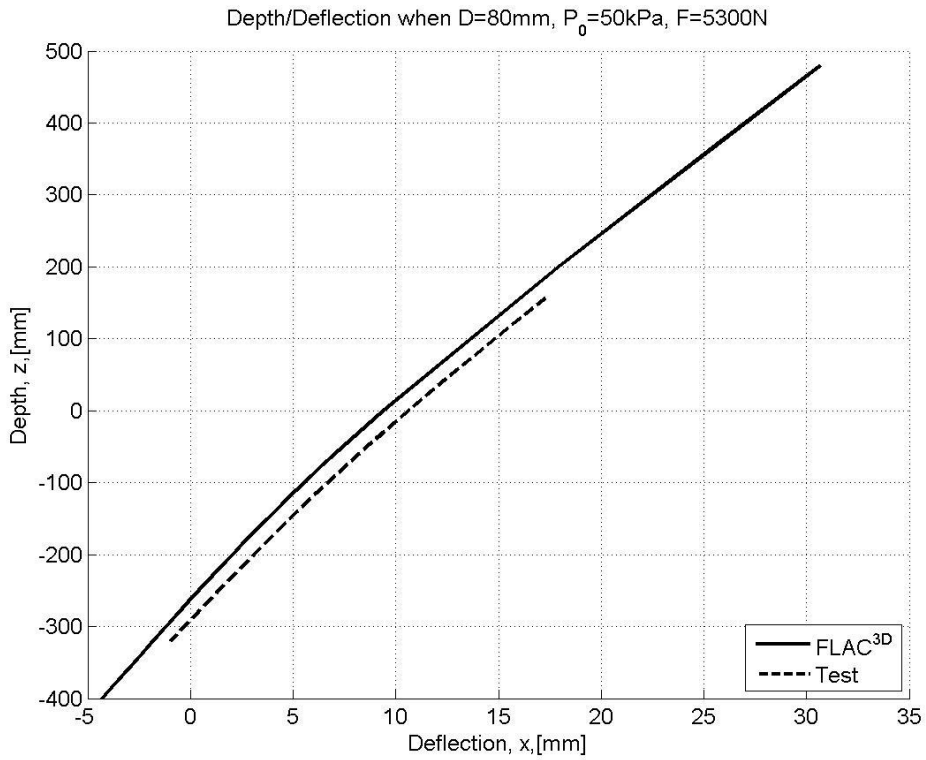

Figure H.140: Deflection distribution along depth at maximum force for test 3

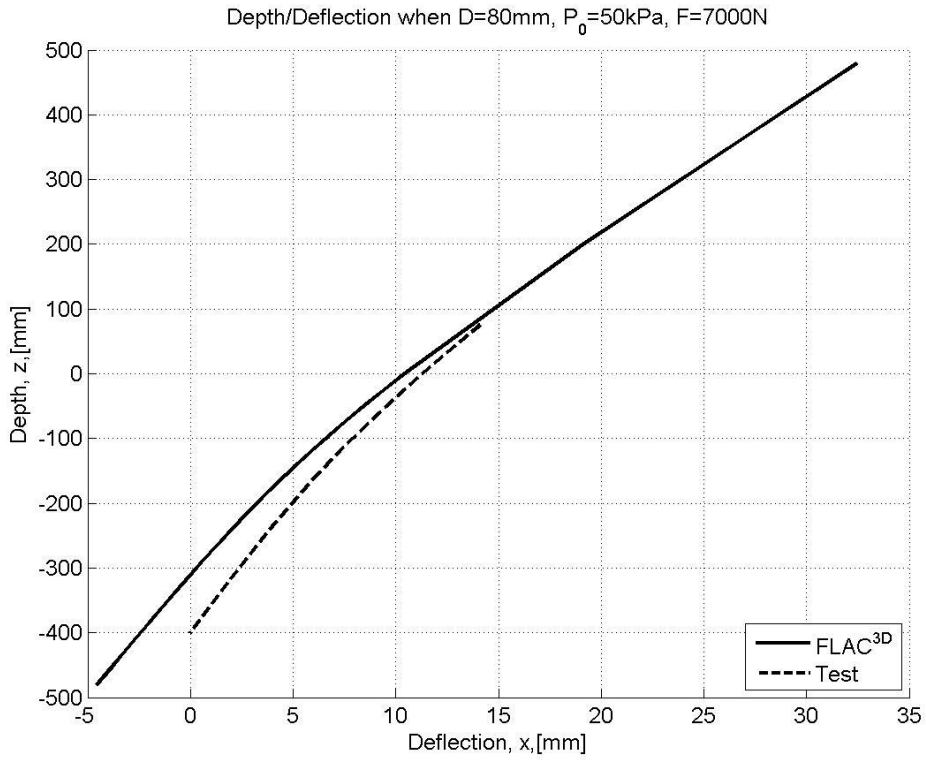

Figure H.141: Deflection distribution along depth at maximum force for test 4

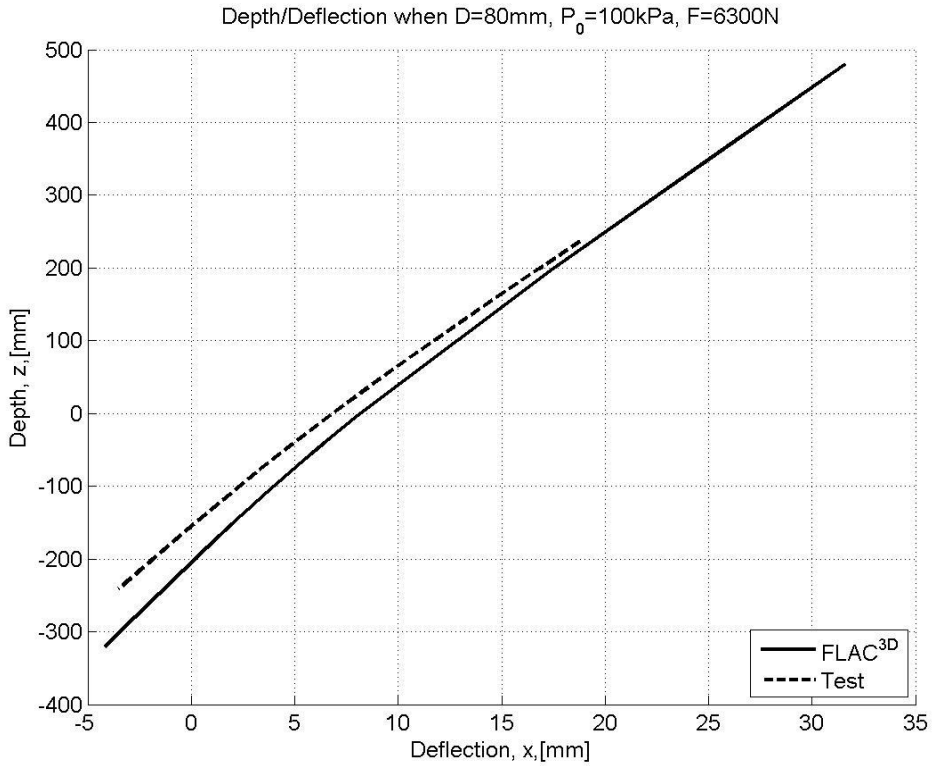

Figure H.142: Deflection distribution along depth at maximum force for test 5

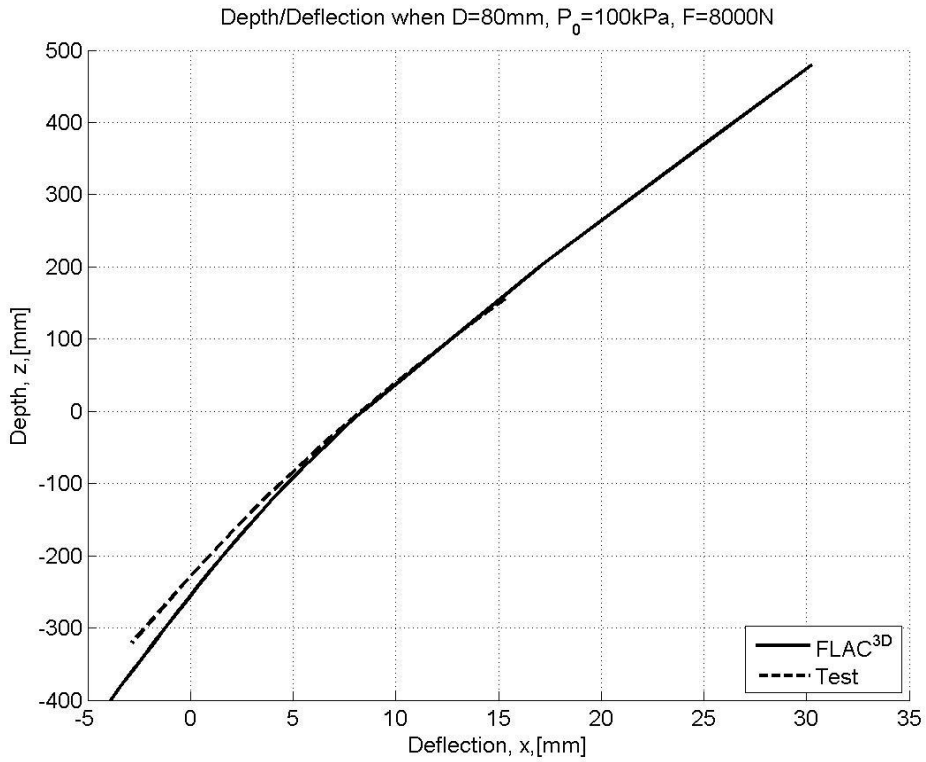

Figure H.143: Deflection distribution along depth at maximum force for test 6

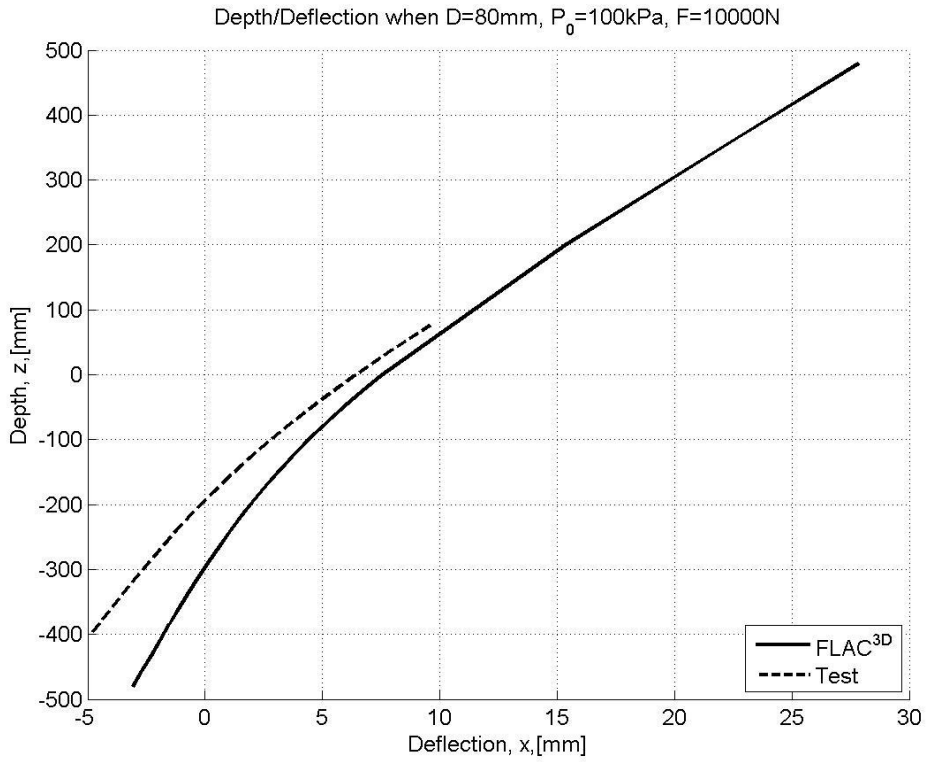

Figure H.144: Deflection distribution along depth at maximum force for test 7

H.5.3 Evaluation of *p-y* curves

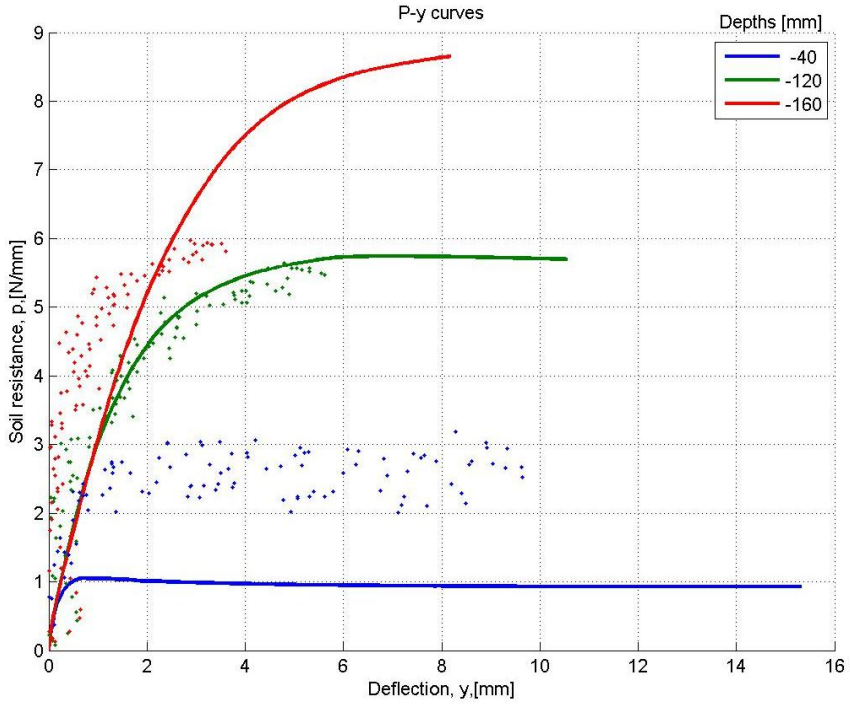

Figure H.145: *p-y* curves for test 2

(dots represent the results from the experimental tests)

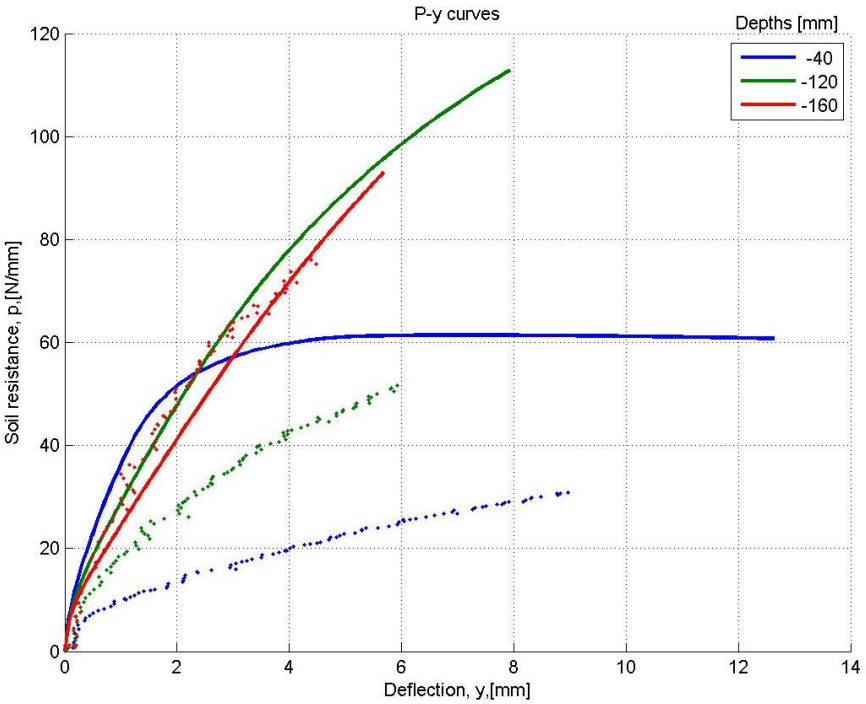

Figure H.146: *p-y* curves for test 3

(dots represent the results from the experimental tests)

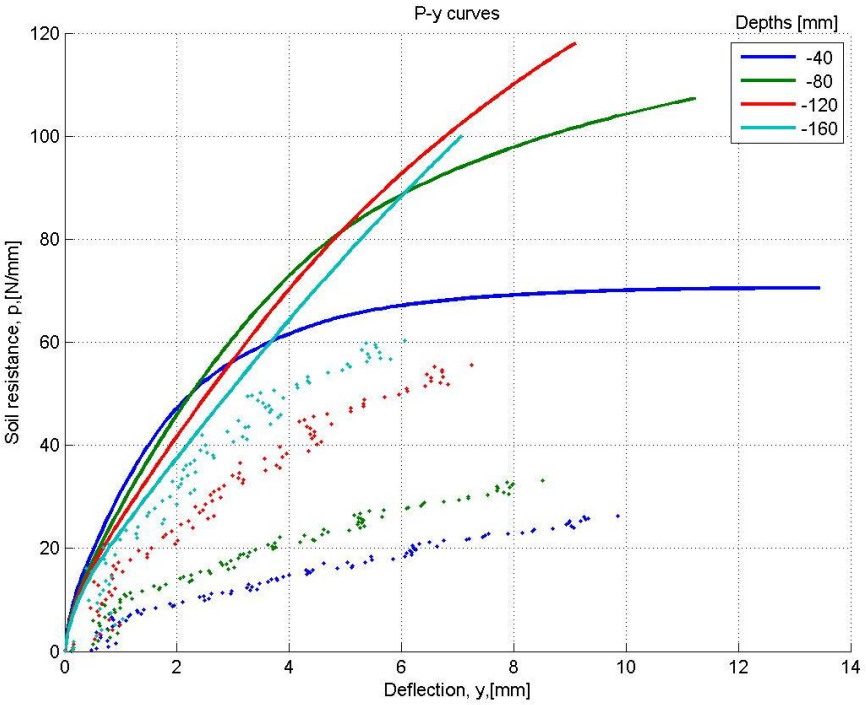

Figure H.147: *p-y* curves for test 4

(dots represent the results from the experimental tests)

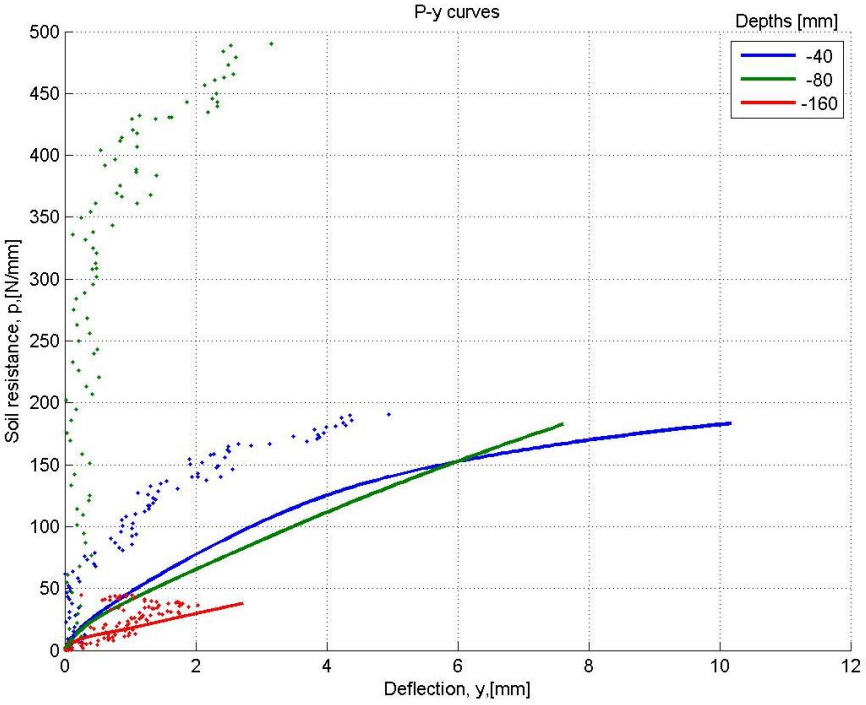

Figure H.148: *p-y* curves for test 5

(dots represent the results from the experimental tests)

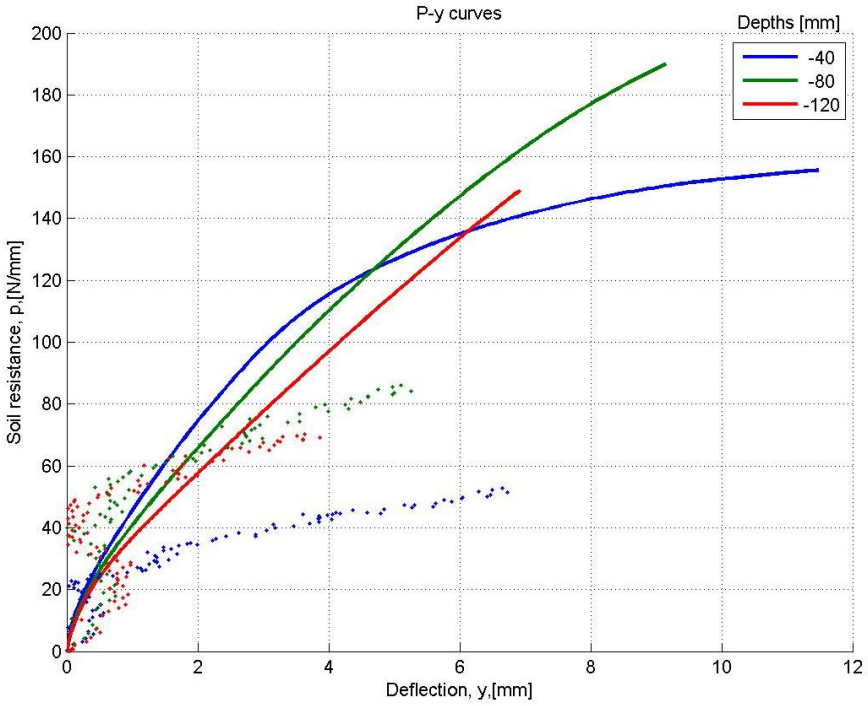

Figure H.149: *p-y* curves for test 6

(dots represent the results from the experimental tests)

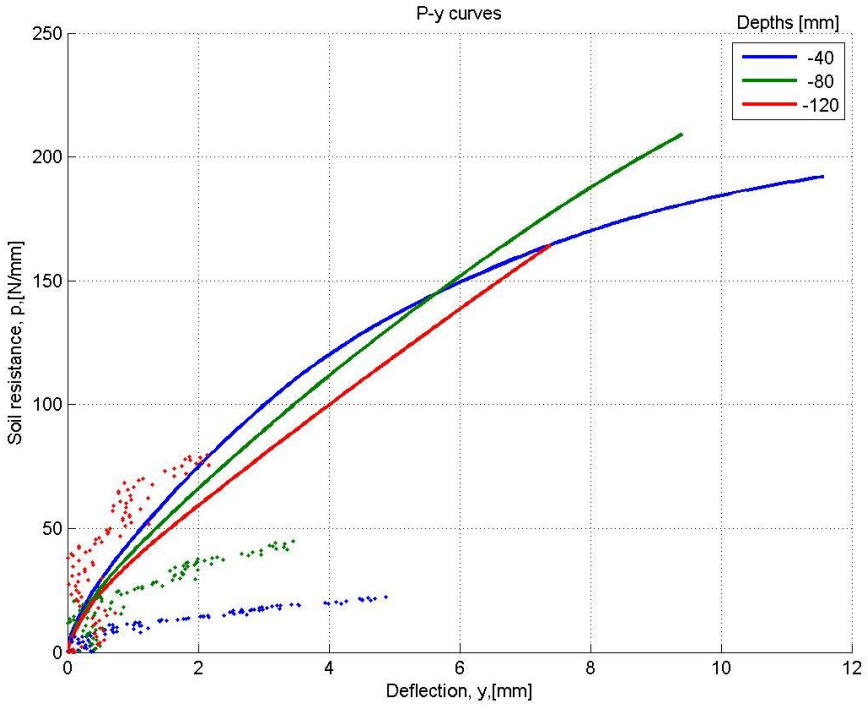

Figure H.150: *p-y* curves for test 7

(dots represent the results from the experimental tests)

APPENDIX I

MATERIAL MODELS

In this appendix, the material models used in the numerical modelling by means of FLAC^{3D} and PLAXIS^{3D} are presented. A description of Mohr-Coulomb tension cut-off model and Hardening soil model is presented through the appendix. The source used through the Appendix is Plaxis 3D manual (2010).

I.1 Mohr-Coulomb tension cut-off model

As mentioned in Chapter 4, in the numerical modelling of the laboratory tests, the Mohr-Coulomb model with tension cut-off has been employed, cf. Figure I.1. The strength and stiffness of the soil have been defined in terms of effective properties as the soil was in drained conditions during the laboratory tests.

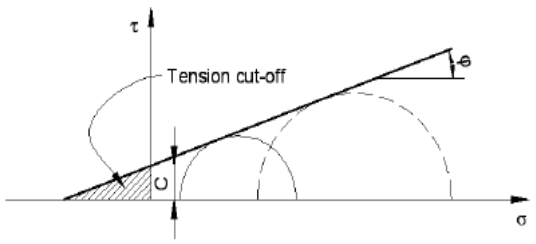

Figure I.1: Mohr-Coulomb tension cut off model.

Mohr-Coulomb failure criterion is a perfectly plastic model, meaning that it is a constitutive model with a fixed yield surface, i.e. a yield surface that is fully defined by model parameters and not affected by plastic straining, cf. Figure I.2.

The basic principle of elastoplasticity is that strains and strain rates are decomposed into an elastic part, ε^e and a plastic part ε^p.

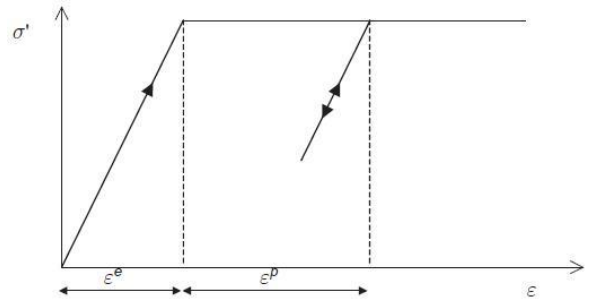

Figure I.2: Basic idea of elastic perfectly plastic model ,Plaxis 3D manual (2010)

In the Mohr-Coulomb model five parameters are required. These five parameters are basic geotechnical parameters that can be obtained by triaxial tests. The five parameters can be seen in table I.1.

Geotechnical Parameters		
E	Young's Modulus	[kN/m^2]
υ	Poisson ratio	[-]
φ	Friction angle	[º]
ψ	Dilatancy angle	[º]
c	Cohesion	[kN/m^2]

Table I.1: Geotechnical parameters used in the Mohr-Coulomb model.

The Mohr-Coulomb model is a failure criterion, which is used to model the soil. The failure criterion is used to combine principle stresses to verify, whether the stresses result in failure in the soil. In two-dimensional analysis, the Mohr-Coulomb failure criterion is an envelope determined by the straight line $\tau_f = c+tan(\varphi) \cdot \sigma_f$, where τ_f is the shear stress at failure and σ_f is the stress at failure.

In three dimensions the Mohr-Coulomb failure criterion spans a hexagonal failure surface in the principle stress space, cf. Figure I.3. Extending Coulomb's friction law for general stress states creates the Mohr-Coulomb yield condition, cf. Equation I.1 to I.6. This ensures that Coulomb's friction law is used in all planes in the soil. Due to a tension cut-off model, three extra yield-functions usually appear. Plaxis 3D manual (2010).

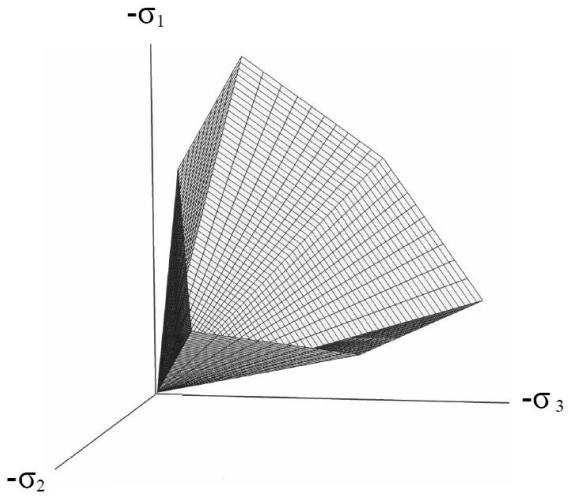

Figure I.3: Yield surface in the principal stress space for the Mohr-Coulomb for a cohesion set

$$f_{1a} = \frac{1}{2}(\sigma_2 - \sigma_3) + \frac{1}{2}(\sigma_2 + \sigma_3) \cdot \sin\varphi - c \cdot \cos\varphi \leq 0 \qquad \text{(I.1)}$$

$$f_{1b} = \frac{1}{2}(\sigma_3 - \sigma_2) + \frac{1}{2}(\sigma_3 + \sigma_2) \cdot \sin\varphi - c \cdot \cos\varphi \leq 0 \qquad \text{(I.2)}$$

$$f_{2a} = \frac{1}{2}(\sigma_3 - \sigma_1) + \frac{1}{2}(\sigma_3 + \sigma_1) \cdot \sin\varphi - c \cdot \cos\varphi \leq 0 \qquad \text{(I.3)}$$

$$f_{2b} = \frac{1}{2}(\sigma_1 - \sigma_3) + \frac{1}{2}(\sigma_1 + \sigma_3) \cdot \sin\varphi - c \cdot \cos\varphi \leq 0 \qquad \text{(I.4)}$$

$$f_{3a} = \frac{1}{2}(\sigma_1 - \sigma_2) + \frac{1}{2}(\sigma_1 + \sigma_2) \cdot \sin\varphi - c \cdot \cos\varphi \leq 0 \qquad \text{(I.5)}$$

$$f_{1a} = \frac{1}{2}(\sigma_2 - \sigma_1) + \frac{1}{2}(\sigma_2 + \sigma_1) \cdot \sin\varphi - c \cdot \cos\varphi \leq 0 \qquad \text{(I.6)}$$

Plasticity is associated with the development of irreversible strains. In order to evaluate whether or not plasticity occurs in a calculation, a yield function, *f*, is introduced as a function of stress and strain. Plastic yielding is related with the condition $f = 0$. This condition can often be presented as a surface in principal stress space. For stress states represented by points within the yield surface, the behaviour is purely elastic and all strains are reversible. Thus, six plastic potential functions are defined for the Mohr-Coulomb Model, cf. Equations I.7 to I.12. These equations define the directions of the plastic strains.

$$g_{1a} = \frac{1}{2}(\sigma_2 - \sigma_3) + \frac{1}{2}(\sigma_2 + \sigma_3)\cdot \sin\psi \quad \text{(I.7)}$$

$$g_{1b} = \frac{1}{2}(\sigma_3 - \sigma_2) + \frac{1}{2}(\sigma_3 + \sigma_2)\cdot \sin\psi \quad \text{(I.8)}$$

$$g_{2a} = \frac{1}{2}(\sigma_3 - \sigma_1) + \frac{1}{2}(\sigma_3 + \sigma_1)\cdot \sin\psi \quad \text{(I.9)}$$

$$g_{2b} = \frac{1}{2}(\sigma_1 - \sigma_3) + \frac{1}{2}(\sigma_1 + \sigma_3)\cdot \sin\psi \quad \text{(I.10)}$$

$$g_{3a} = \frac{1}{2}(\sigma_1 - \sigma_2) + \frac{1}{2}(\sigma_1 + \sigma_2)\cdot \sin\psi \quad \text{(I.11)}$$

$$g_{3b} = \frac{1}{2}(\sigma_2 - \sigma_1) + \frac{1}{2}(\sigma_2 + \sigma_1)\cdot \sin\psi \quad \text{(I.12)}$$

I.2 Hardening soil model

The Hardening Soil model is an advanced model for simulating the behaviour of different types of soil, both soft soils and stiff soils. When subjected to primary deviatoric loading, soil shows a decreasing stiffness and simultaneously irreversible plastic strains develop.

Hardening soil model is like Mohr-Coulumb model, a failure criterion which can be used to model the soil. Unlike the Mohr-Coulomb model, the Hardening Soil model ascribes a changing stiffness of the soil depending on the strain in the soil. This is illustrated in figure I.4.

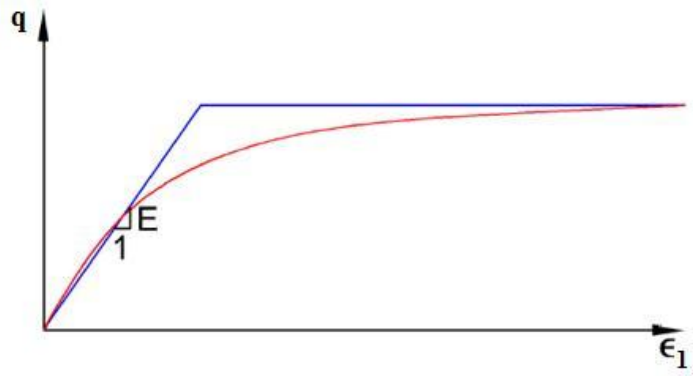

Figure I.4: The work curve for soil modelled with the Mohr-Coulomb model (blue) and Hardening soil model (red).

I.2.1 Hyperbolic Relationship for standard drained triaxial tests

A basic idea in the formulation of the Hardening Soil model is the hyperbolic relationship between the vertical strain, ε_1, and the deviatoric stress, q, in primary triaxial loading, cf. Figure I.5, q_a represents the asymptotic value of the shear strength and E_i is the initial stiffness. E_{50} is defined as the confining stress dependent stiffness modulus for primary loading, and it can be obtained graphically for a 50% of the ultimate deviatoric stress, q_f.

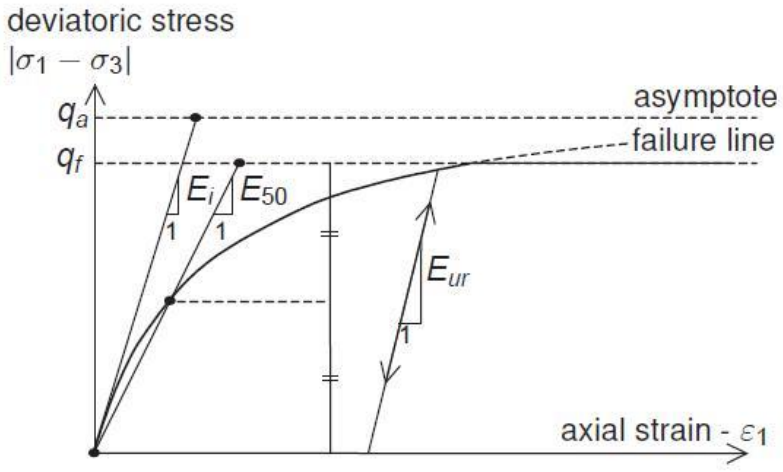

Figure I.5: Hyperbolic stress-strain relation in primary loading for a standard drained triaxial test.

E_{50} is dependent on the confining stress and it is defined by equation I.13:

$$E_{50} = E_{50}^{ref} \cdot \left(\frac{c \cdot \cos\varphi - \sigma_3 \cdot \sin\varphi}{c \cdot \cos\varphi + p^{ref} \cdot \sin\varphi} \right)^m \qquad \text{(I.13)}$$

Where E_{50}^{ref} is a reference stiffness modulus corresponding to the reference confining pressure p^{ref} = 100 kPa. The actual stiffness depends on the minor principal stress, σ_3, which is the confining pressure in a triaxial test. The amount of stress dependency is given by the power m. Notice that since in this project a cohesionless soil is used for the experiments, the cohesion can be neglected and thus $c \approx 0$.

The ultimate deviatoric stress, q_f, and the quantity, q_a, are derived from Mohr-Coulomb criterion and are defined as:

$$q_f = (c \cdot \cot\varphi - \sigma_3) \cdot \frac{2 \cdot \sin\varphi}{1 - \sin\varphi} \tag{I.14}$$

$$q_a = \frac{q_f}{R_f} \tag{I.15}$$

For unloading-reloading stress paths, another stress-dependent stiffness modulus is used, cf. Equation I.16.

$$E_{ur} = E_{ur}^{ref} \cdot \left(\frac{c \cdot \cos\varphi - \sigma_3 \cdot \sin\varphi}{c \cdot \cos\varphi + p^{ref} \cdot \sin\varphi} \right)^m \tag{I.16}$$

Where E_{ur}^{ref} is the reference Young's modulus for unloading and reloading, corresponding to the reference pressure p^{ref}. However, through this project only data corresponding to the primary loading in the triaxial tests has been proportioned, thus the recommendation given by Plaxis Material Models Manual (2010) is followed, cf. Equation I.17.

$$E_{ur}^{ref} = 3 \cdot E_{50}^{ref} \tag{I.17}$$

I.2.2 Approximation of the hyperbola by the Hardening Soil Model

It is assumed that $\sigma_2 = \sigma_3 < \sigma_1$, and that $q < q_f$, as it is shown in figure I.5. In this section it will be explained how this model gives virtually the hyperbolic stress-strain curve when considering stress paths of standard drained triaxial tests. Plastic strains are considered, and it is defined a hardening yield function of the form:

$$f = \overline{f} - \gamma^p \tag{I.18}$$

Where $\overline{f}$ is a function of stress and γ^p is a function of plastic strains:

$$\overline{f} = \frac{2}{E_i} \cdot \frac{q}{1 - q/q_a} - \frac{2 \cdot q}{E_{ur}} \tag{I.19}$$

$$\gamma^p \approx -2 \cdot \varepsilon_1^p \tag{I.20}$$

An essential feature of the above definitions for $\overline{f}$ is that it matches the well-known hyperbolic law represented in figure I.5. In order to verify this statement, one has to consider primary loading, which implies the yield condition $f = 0$. Then it yields $\gamma^p = \overline{f}$ and ε_1^p can be expressed as:

$$\varepsilon_1^p \approx \frac{1}{2}\overline{f} = \frac{1}{E_i}\cdot\frac{q}{1-q/q_a} - \frac{q}{E_{ur}} \qquad \text{(I.21)}$$

Plastic strains develop in primary loading alone, but elastic strains develop both, in primary loading and unloading-reloading. For drained triaxial test stress paths with σ_2 = σ_3 = constant, the elastic Young's modulus E_{ur} remains constant and the elastic strains are given by the equations:

$$-\varepsilon_1^e = \frac{q}{E_{ur}} \qquad \text{(I.22)}$$

$$-\varepsilon_2^e = \varepsilon_3^e = -\upsilon_{ur}\cdot\frac{q}{E_{ur}} \qquad \text{(I.23)}$$

Where υ_{ur} is the unloading-reloading Poisson's ratio. Strains that develop during the first stage of the test are not considered. For the deviatoric loading stage of the triaxial test, the axial strain is the sum of an elastic component given by equation I.22 and a plastic component defined by equation I.23. Thus it can be concluded:

$$\varepsilon_1 = \varepsilon_1^e + \varepsilon_1^p \approx \frac{1}{E_i}\cdot\frac{q}{1-q/q_a} \qquad \text{(I.24)}$$

For this relationship it has been considered absence of plastic volumetric strains, i.e. $\varepsilon_v^p = 0$. However, plastic volumetric strains will never be precisely equal to zero, but for hard soils, plastic volume changes tend to be small when they are compared with the axial strain so that this formulation yields a hyperbolic stress-strain curve under triaxial testing conditions.

The input parameters considered for the input in Plaxis 3D and are the ones shown in Table I.2:

Parameters	Description	Units
c	Cohesion	[kN/m^2]
φ	Angle of internal friction	[˚]
ψ	Angle of dilatancy	[˚]
E_{50}^{ref}	Secant stiffness in standard drained triaxial test	[kN/m^2]
E_{oed}^{ref}	Tangent stiffness for primary oedometer loading	[kN/m^2]
E_{ur}^{ref}	Unloading/Reloading stiffness	[kN/m^2]
m	Power for stress-level dependency of stiffness	[-]
e_{init}	Initial void ratio	[-]

Table I.2: Parameters of the Hardening Soil Model

The elastoplastic Hardening Soil model does not involve a fixed relationship between the drained triaxial stiffness E_{50} and the oedometer stiffness E_{oed} for one-dimensional compression. These stiffnesses are inputted independently. The oedometer stiffness can be defined by equation:

$$E_{oed} = E_{oed}^{ref} \cdot \left(\frac{c \cdot \cos\varphi - \frac{\sigma_3}{K_0^{nc}} \cdot \sin\varphi}{c \cdot \cos\varphi + p^{ref} \cdot \sin\varphi} \right)^m \qquad \text{(I.25)}$$

The initial oedometer stiffness, E_{oed}^{ref} is the tangent stiffness at a vertical stress of $\sigma_1 = \frac{\sigma_3}{K_0^{nc}} = p^{ref}$, as it can be observed in figure I.6. However, since no data of oedometric tests have been proportioned for this project, an approximation of $E_{oed} = E_{50}/1.30$ is assumed, based on the relation suggested by Plaxis 3D manual (2010) and Marta Auleda Catalá (2005).

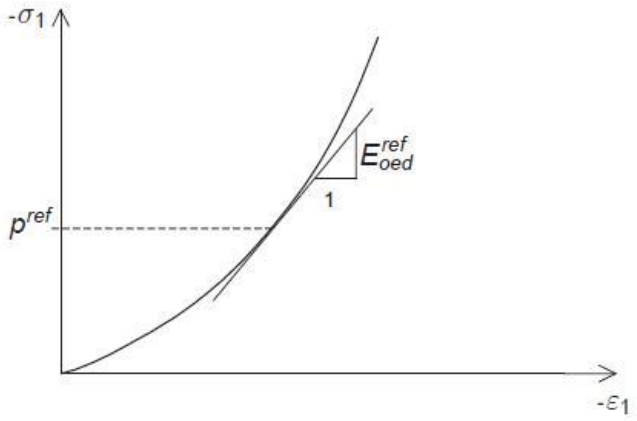

Figure I.6: Definition of E_{oed}^{ref} in oedometer test results

There are some alternative stiffness parameters, such as the compression index, swelling index and initial void ratio. In reality, the first two parameters depend on the actual void ratio, however, in Plaxis 3D it is assumed a constant initial void ratio. These two parameters are obtained as follows:

$$C_c = \frac{2.3 \cdot (1 + e_{init}) \cdot p^{ref}}{E_{oed}^{ref}} \tag{I.26}$$

$$C_S = \frac{2.3 \cdot (1 + e_{init}) \cdot (1 + \upsilon) \cdot (1 - 2\upsilon) \cdot p^{ref}}{(1 - \upsilon) \cdot E_{ur}^{ref}} \tag{I.27}$$

I.2.3 Plastic Volumetric Strain for triaxial states of stress

The plastic volumetric strain, $\dot{\varepsilon}_v^p$, is a function of the plastic shear strain defined before in equation I.20, represented by the linear form of the hardening flow rule:

$$\dot{\varepsilon}_v^p = \sin\psi_m \, \dot{\gamma}^p \tag{I.28}$$

Where ψ_m is the mobilised dilatancy angle, which is defined as equation I.29 states:

For $\sin \varphi_m < 3/4 \sin \varphi$: $\psi_m = 0$

For $\sin \varphi_m \geq 3/4 \sin \varphi$ and $\psi = 0$: $\sin \psi_m = \max\left(\frac{\sin \varphi_m - \sin \varphi_{cv}}{1 - \sin \varphi_{m\cdot} \cdot \sin \varphi_{cv}}, 0 \right)$ (I.29)

For $\sin \varphi_m \geq 3/4 \sin \varphi$ and $\psi \leq 0$: $\psi_m = \psi$

If $\varphi = 0$ $\psi_m = 0$

φ_{cv} is defined as the critical state friction angle, being a material constant independent of density index or void ratio, and φ_m is the mobilized friction angle defined as:

$$\sin \varphi_m = \frac{\sigma_1 - \sigma_3}{\sigma_1 + \sigma_3 - 2c \cdot \cot \varphi} \quad \text{(I.30)}$$

For small mobilized friction angles and for negative values of ψ_m, as long as the dilatancy angle ψ is positive, ψ_m is taken zero. Furthermore, in all cases when $\varphi = 0$, ψ_m is set equal to zero.

The essential property of the stress-dilatancy theory is that the material contracts for small stress ratios $\varphi_m < \varphi_{cv}$, whilst dilatancy occurs for high stress ratios $\varphi_m > \varphi_{cv}$. At failure, when the mobilized friction angle equals the failure friction angle, φ, it is found that:

$$\sin \psi = \frac{\sin \varphi - \sin \varphi_{cv}}{1 - \sin \varphi \cdot \sin \varphi_{cv}} \quad \text{(I.31)}$$

I.2.4 Dilatancy cut-off

Initial void ratio, e_{init}, and the maximum void ratio, e_{max} must be defined as general parameters, since a dilatancy cut-off model is taken into account to run the models in Plaxis 3D. As soon as the volume results change in a state of maximum void ratio, the mobilised dilatancy angle is automatically set to zero, as it is represented in figure I.7. Two zones are diferenciated:

For $e < e_{max}$:

$$\sin\psi_m = \frac{\sin\varphi_m - \sin\varphi_{cv}}{1 - \sin\varphi_m \cdot \sin\varphi_{cv}} \tag{I.32}$$

Where:

$$\sin\varphi_{cv} = \frac{\sin\varphi - \sin\psi}{1 - \sin\varphi \cdot \sin\psi}$$

For $e \geq e_{max}$:

$$\psi_m = 0$$

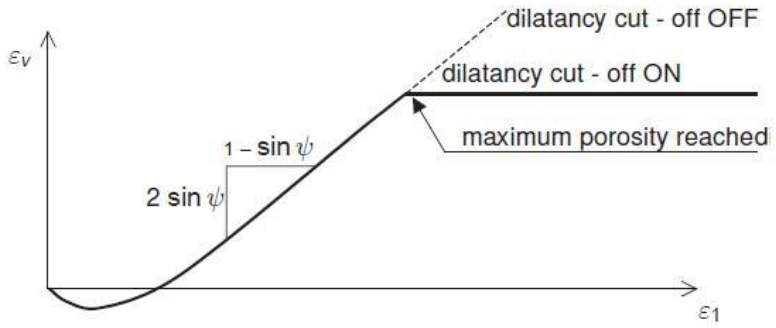

Figure I.7: Strain curve for a drained triaxial test including dilatancy cut-off

The void ratio is related to the volumetric strain, ε_v, by the relationship:

$$-\left(\varepsilon_V - \varepsilon_V^{init}\right) = \ln\left(\frac{1+e}{1-e_{init}}\right) \tag{I.33}$$

I.2.5 Yield Surface in the Hardening Soil Model

To explain the plastic volumetric strain in isotropic compression, a second yield surface closes the elastic region in the direction of the p-axis. While the shear yield surface is mainly controlled by the triaxial modulus, the oedometer modulus controls the cap yield surface. This can be defined:

$$f^c = \frac{\beta}{1-m} \cdot \left(\frac{p_p}{p_{ref}}\right)^{1-m} \tag{I.34}$$

The volumetric cap strain is the plastic volumetric strain in isotropic compression. Another constant, β, is introduced. The following relationships are used in Plaxis 3D to get the input parameters:

$$\begin{aligned} \alpha &\leftrightarrow K_0^{nc} \\ \beta &\leftrightarrow E_{oed}^{ref} \end{aligned} \tag{I.35}$$

The cap has the shape of an ellipse in the $p-\tilde{q}$ plane. p_p determines the magnitude of the ellipse and α its aspect ratio; high values of α lead to steep caps underneath the Mohr-Coulomb line, and small values generate much more pointed caps. This ellipse is also a plastic potential and it still has the hexagonal shape of the Mohr-Coulomb criteria, cf. Figures I.8 and I.9.

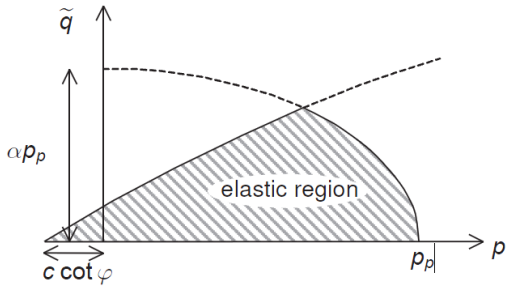

Figure I.8: 2D Yield Surface

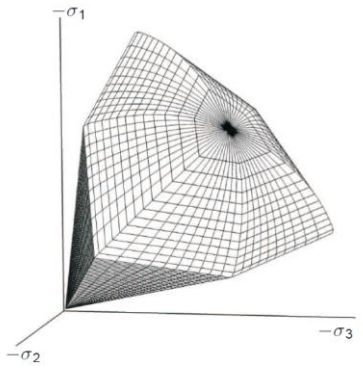

Figure I.9: Total yield contour

I.2.6 Hardening Soil Model with Small-Strain Stiffness

The soil stiffness that should be used in the analysis of geotechnical structures is not the one that relates to the strain range at the end of the construction. Instead, very small-strain soil stiffness and its non-linear dependency on strain amplitude should be properly taken into account.

The Hardening Soil model with small-strain stiffness implemented in Plaxis 3D is based on the Hardening Soil model and uses the same input parameters plus two additional parameters to describe the variation of the stiffness with strain:

- The initial or very small-strain shear modulus G_0
- The shear strain level $\gamma_{0.7}$ at which the secant shear modulus G_S is reduced to about 70% of G_0.

A number of factors influence the small-strain parameters G_0 and $\gamma_{0.7}$. Most importantly they are influenced by the material's actual state of stress and void ratio e. In the Hardening Soil model with Small-Strain stiffness, the stress dependency on the shear modulus G_0 is taken into account with the power law defined by:

$$G_0 = G_0^{ref} \cdot \left(\frac{c \cdot \cos\varphi - \sigma_{3.} \cdot \sin\varphi}{c \cdot \cos\varphi + p^{ref} \cdot \sin\varphi} \right)^m \qquad \text{(I.36)}$$

Where G_0^{ref} is a function of the void ratio defined as:

$$G_0^{ref} = \frac{(2.97 - e)^2}{1 + e} \cdot 33[MPa] \qquad \text{(I.37)}$$

Shear strain level $\gamma_{0.7}$ can be related to the shear modulus by means of Figure I.10:

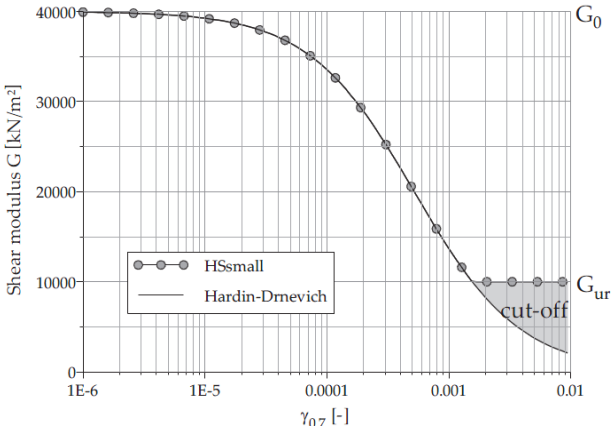

Figure I.10: Relationship between the Shear modulus G_0 and shear strain level $\gamma_{0.7}$

The shear strain level can also be obtained analytically, adopting the Mohr-Coulomb criterion and a hyperbolic law for larger strains, cf. Equation I.37, Plaxis 3D manual (2010).

$$\gamma_{0.7} \approx \frac{1}{9 \cdot G_0} \cdot \left[2c \cdot 1 + \cos(2\varphi)) - \sigma_1 \cdot (1 + K_0) \cdot \sin(2\varphi)\right] \qquad \text{(I.37)}$$

APPENDIX J

DIFFICULTIES WHEN CONDUCTING TESTS

In this appendix, the difficulties while the tests were being carried out are described. Some of these difficulties made impossible to rely on the test, and it had to be repeated, and some of the difficulties introduced uncertainties in the test results.

A summary of the tests realised at Aalborg University laboratory during 2010 and 2011 is shown in table J.1 with the corresponding difficulties occurred during their process.

Test	Pile Diameter [mm]	Pressure [kPa]	L/D	Gauges	Difficulties
Test 1	100	50	5	No	-
Test 2-*0*	80	0	5	Yes	Wire too tight
Test 2-*I*	80	0	5	Yes	Strain gauge 16 broken
Test 3-*0*	80	50	5	Yes	Membrane damaged
Test 3-*I*	80	50	5	Yes	High flow through the membrane due to gaps.
Test 3-*II*	80	50	5	Yes	No mouldings in the new membrane caused a high flow through it.
Test 3-*III*	80	50	5	Yes	Strain gauge 16 broken and displacement transducer 1 did not work as expected.
Test 4-*0*	80	50	6	Yes	High leak in the fire hose.
Test 4-*I*	80	50	6	Yes	Snapped screw from the pile while the piston was pulling.
Test 4-*II*	80	50	6	Yes	-
Test 5	80	100	4	Yes	-
Test 6	80	100	5	Yes	-
Test 7	80	100	6	Yes	-
Test 8	80	50	3	No	Displacement transducer 3 did not work as expected
Test 9-0	80	0	3	No	High scatter in the hydraulic piston
Test 9-I	80	0	3	No	-
Test 10	80	100	3	No	High leak in the fire hose.

Table J.1: Overview and difficulties observed in the 10 tests carried out in the laboratory.

Test 1 (D = 100 mm, P_0 = 50 kPa, L/D = 5)

Everything worked as it was supposed to. A water flow velocity through the gaps of the membrane of *80 l/hour* was estimated for this test.

Test 2 (D = 80 mm, P_0 = 0 kPa, L/D = 5)

Two tests were conducted to be able to obtain reliable results. In test *0*, the initial force was very high. It was observed when the force-deflection graphs were plotted. The initial force did not start in zero, as it was supposed to. This was caused because the wire from the hydraulic piston which is plugged to the pile was too tight. It was decided to conduct the test again.

In test I strain gauge 16 stopped measuring at the beginning of the test, but the test was carried out, since the decision of skipping that measuring level for the calculation of the bending moment was taken. This fact can be accepted, as 22 strain gauges were placed on the pile, forming 11 depth levels, which are considered enough, in order to compute the moment distribution of the pile.

Test 3 (D = 80 mm, P_0 = 50 kPa, L/D = 5)

A total of 4 tests were carried out in order to obtain reliable results for this test.

In test 0, the pile was plugged, the soil vibrated and all the set up prepared. When the pressure of 50 kPa was being added to the pressure tank, the water velocity through the gaps of the membrane was very high, reaching 240 l/h. So, the test had to be stopped, the membrane was removed and it was clearly seen that it was damaged at some points, cf. Figure J.1.

Figure J.1: Damaged membrane after test 0

The membrane was repaired with plastic glue at that point. A second attempt, test I, was tried without succeeding. The water velocity through gaps was still very high, reaching 200 l/h.

In test II, a new membrane was used, with the objective of minimizing the water flow velocity through gaps. The problem with the new membrane it was that it did not have any mouldings glued to it, which caused that the water could pass this time between the wall and the membrane, reaching a water velocity of 180 l/h, which was still too high to run the test.

A compressible moulding was attached to the new rubber membrane, cf. Figure J.2. After that, test III was run solving the problem with the high water flow through gaps. However, two more problems were found while this test was running: strain gauge 16 failed again, and displacement transducer no. 2 did not show correct results.

Figure J.2: New membrane with the moulding attached to it

This test was considered reliable, because 10 more levels of strain measurement and 2 more displacement transducers remained measuring at two different levels in the pile. This was considered enough to obtain accurate results.

Test 4 (D= 80 mm, P_0 = 50 kPa, L/D = 6)

Three tests were realised due to obtain accurate results for this test.

In test 0 the fire hose was leaking too much air before starting to run the test, which caused a high water velocity through the membrane and the pressure tank wall, since it was not compressing the mouldings enough. A new joint was installed in the fire hose.

With the new joint already installed in the fire hose, test I, was being run without any problems, but at some point during the test, the screw was snapped. This was due to the fact that the screw thread was damaged, as it can be observed in figure J.3:

Figure J.3: Damaged screw thread

This problem was solved by welding the screw to the steel plate which is pulled by the piston, cf. Figure J.4. Test II was carried out without any problems.

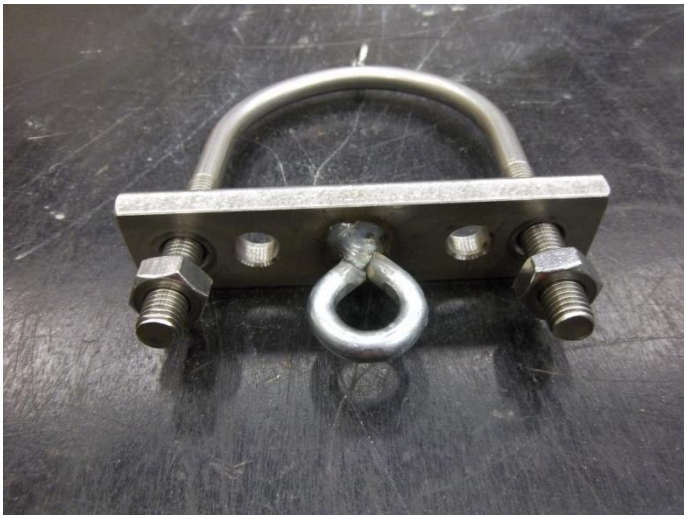

Figure J.4: Screw welded to the thin steel plate

Test 5 (D= 80 mm, P_0 = 100 kPa, L/D = 4)

Test 5 worked as it was supposed to, with a water flow velocity through gaps of 30 l/h.

Test 6 (D= 80 mm, P_0 = 100 kPa, L/D = 5)

Test 6 worked as it was supposed to, reaching a water flow velocity through gaps of 40 l/h.

Test 7 (D= 80 mm, P_0 = 100 kPa, L/D = 6)

Test 7 worked as it was supposed to, with a water flow velocity through gaps of 50 l/h.

Test 8 (D= 80 mm, P_0 = 50 kPa, L/D = 3)

Everything worked as it was supposed to, except for the top displacement transducer (no. 3), which did not measure properly. It showed a constant value of 711 mm, which is discarded, since it is impossible to reach such a high lateral displacement.

Test 9 (D= 80 mm, P_0 = 0 kPa, L/D = 3)

Everything worked as it was supposed to, but it was observed a high scatter in the force applied by the hydraulic piston, reason for why it was decided to repeat it and worked successfully in the second attempt. The water flow velocity through gaps was about 8 l/h.

Test 10 (D= 80 mm, P_0 = 100 kPa, L/D = 3)

Test 10 worked as it was supposed to, with an approximate water flow velocity through gaps of 6 l/h.

BIBLIOGRAPHY

Andersen, A.E. Madsen, and Schaarup-Jensen 1998. *Eastern Scheldt Sand. Baaskarp Sand no.15*. Data Report 9701.

API 1993. *Recommended practice for Planning, Designing and Constructing Fixed Offshore Platforms - Working Stress design*. American Petroleum Institute.

Borobia A., Mikalauskas L. and Troya J. L. 2011. *Small-Scale testing of Static Laterally loaded Non-Slender Monopiles in Cohesionless Sand*. Department of Civil Engineering. Aalborg University.

Chia-Chen Fang, James H. Long. 2005. *Assesment of existing methods for predicting soil response of laterally loaded piles in sand.*

Cox et al. 1974. *Field testing of laterally loaded piles in sand*

DNV. 1992. Foundations. Det Norske Veritas. Classification Notes No. 30.4

Danish Wind Power Association Copyright. 1997-2003. *Danish Wind Industry Association* Updated 10 May 2003
http://www.windpower.org/en/tour/rd/gravitat.htm

FLAC^{3D} 3.1 manual 2006. FLAC^{3D} *Fast Lagrangian Analysis of Continua in 3 Dimensions* Itasca Consulting Group Inc Minneapolis, Minnesota, USA.

G. Gudehus and A. Hettler. 1983. *Model Studies of Foundations in Granular Soil.*

Hanne R. Roesen, Kristina Thomassen. 2010. *Small-Scale Laterally Loaded Non-Slender Monopiles.* Aalborg University.

H. Poulus, T. Hull. 1989. *The Role of Analytical Geomechanics in Foundation Engineering*, Foundation Engineering: Current principles and Practices, 2, 1578-1606.

Ibsen L. B. Hanson, M. Hjort. T. and Thaarup. M. 2009. MC-Parameter Calibration for Baaskarp Sand no.15.

Kellezi L. and Hansen P. B. 2003. *Static and dynamic analysis of an offshore mono-pile windmill foundation*. Lingby. Denmark.

Lars Bo Ibsen, 2009. *Soil Testing.* Aalborg University

L.B Ibsen, P.V. Lade. 1998. *The role of the characteristic line in static soil behavior.*

Murchinson and O'neill. 1984. *Evaluation of p-y relationships in sand.*

Marta Auleda Catalá. May, 2005. *Excess pore pressure generation due to pseudostatic tests in saturated sand.*

Møller M., Brødbæk K. T. and S. P. H. Sørensen. 2009. *Numerical Evaluation of Load-Displacement Relationships for Non-Slender Monopiles in Sand*. Department of Civil Engineering. Aalborg University.

Plaxis 3D 2010 Manual, Brinkgreve R. B. J., Engin E. and Swolfs W. M. (edt.).

Prosperpine K. Peralta. 2010. *Investigations on the behavior of large diameter piles under long-term lateral cyclic loading in cohesionless soil.*

Reese, L. C. and W. F. Van Impe. 2001. *Single Piles and Pile Groups under Lateral Loading*.

Søren P. H. Sørensen and Kristian T. Brødbæk and Martin Møller. *Evaluation of Load-Displacement Relationships for Large-Diameter Piles.* Aalborg University,

Thomassen K., Roesen H. R., Ibsen L. B., and S. P. H. Sørensen. 2010. *Small-Scale Testing of Laterally Loaded Non-Slender Monopiles in sand.* Department of Civil Engineering. Aalborg University.

Yang and Liang .2006. *Methods for deriving p-y curves from instrumented lateral load tests.*